Micro-Cantilever Printing Based Devices and Applications

A Thesis

submitted for the award of the degree of

DOCTOR OF PHILOSOPHY

By

Vimal Kumar Singh Yadav

DEPARTMENT OF ELECTRONICS AND ELECTRICAL ENGINEERING

INDIAN INSTITUTE OF TECHNOLOGY GUWAHATI

GUWAHATI - 781 039, INDIA

January, 2020

DECLARATION

This is to certify that the thesis entitled "**Micro-Cantilever Printing Based Devices and Applications**", submitted by me to the *Department of Electronics and Electrical Engineering, Indian Institute of Technology Guwahati* for the award of the degree of **Doctor of Philosophy**. This is an original research work carried out by me under the supervision of **Prof. Roy P. Paily**. The contents of this thesis, in full or in parts, have not been submitted to any other Institute or University for the award of any degree or diploma.

Signed:

Vimal Kumar Singh Yadav
Department of Electronics & Electrical Engineering,
Indian Institute of Technology Guwahati,
Guwahati-781039, Assam, India.

Date:

CERTIFICATE

This is to certify that the thesis entitled "**Micro-Cantilever Printing Based Devices and Applications**", submitted by **Vimal Kumar Singh Yadav** (146102016), a research scholar in the *Department of Electronics and Electrical Engineering, Indian Institute of Technology Guwahati*, for the award of the degree of **Doctor of Philosophy**, is a record of an original research work carried out by him under my supervision and guidance. The thesis has fulfilled all requirements as per the regulations of the institute, and in my opinion has reached the standard needed for submission. The results embodied in this thesis have not been submitted to any other University or Institute for the award of any degree or diploma.

Signed:

Prof. Roy P. Paily
Department of Electronics & Electrical Engineering,
Indian Institute of Technology Guwahati,
Guwahati-781039, Assam, India.

Date:

Dedicated to

My Babuji **Late Shri. Suryadev Singh Yadav**

Acknowledgements

I am highly privileged to take this opportunity to express my sincere and honest gratitude to my thesis supervisor, Prof. Roy Paily Palathinkal, for his guidance, support and motivation through the entire course of my research work. It would not be out of place to mention that it was his clear vision and constant support that allowed me to work on an emerging research area like printed electronics and fabrication of electronic devices using micro-cantilever printing technology for sensing applications.

I would like to thank Dr. Gayatri Natu for helpful suggestions, discussions, adding important insights to my experimental work and co-authoring my research papers. I am thankful to my doctoral committee members Prof. Harshal B. Nemade (Chairman), Dr. Nagarjuna Nallam, and Dr. John Jose for sparing their valuable time to evaluate the progress of my research work and provide pertinent suggestions leading to improvement in my thesis. I am also thankful to Dr. Amitabh Chatterjee and Dr. Ratul Kumar Baruah in helping me to understand the concepts related to modeling and simulation of advanced nanoscale devices. I thank the Head of the Electronics and Electrical Engineering Department and the other faculty members for their courteous help and support throughout my research work. I am grateful to the technical and office staff of the Department from their time to tome help. My special thanks goes to Mrs. S. Josephine, Technical Officer, who has helped us to utilize the lab resources efficiently.

I am thankful to the Head of Centre for Nanotechnology (CNT) and Centre For Excellence In Nanoelectronics and Theranostic Devices (CENTD), IIT Guwahati and other faculty members associated with this centre for providing us the opportunity to utilize the high-end instruments for fabrication and characterization of our devices. My sincere thanks goes to Central Instruments Facility (CIF), IIT Guwahati for permitting me to carry out material characterization using scanning electron microscopy (SEM), transmission electron microscopy (TEM) and X-ray diffraction (XRD) and Department of Physics to allow me to utilize profilometer. I am also thankful to Dr. P.S.G. Pattader for their help in the measurement of contact angle using goniometer. It is well known that the research in the nanotechnology area is based on sophisticated equipment. In this regard, I put my sincere thanks to all the operators of the instruments in-housed in CNT, CIF or other departments, which were used in my entire research work. My special thanks goes to Manjay for helping me in the replacements of various gas cylinders during my gas sensing experiments with air pollutants.

My sincere thanks goes to Mrs. Emlin E. Abraham and Reena Dey from CNT, who have helped me in numerous ways in the form of fruitful technical and friendly discussions, in the purchase of materials, chemicals, plastic, glassware and so on, proofreading my manuscripts and always motivating me as a sincere colleague. I thank Milan Hazarika for his immense help in SEM experiments and Dr. Suramoni Borthakur for explaining me the concepts of different kinds of vacuum pumps and helping me in low-temperature I-V measurements using liquid nitrogen. I feel delighted to express my heart-bottom thanks to all of my colleagues and friends at IIT Guwahati. I am highly thankful to Satyajit and Birjit, who have been more than colleagues but as brothers to me and helped me tremendously in resolving my technical queries, providing insightful and honest suggestions relate to my research and providing me with all sorts of help at technical and non-technical fronts. I am highly thankful to Thomas and Raveesh S. for helping me in all the gas sensing experiments and sharing the burden of write-up being the co-authors of my research papers apart from being honest friends and vital helping hands to me in all sorts of experiments in the last phase of my thesis work. I would like to express my thanks to my lab mates Siddhanta, Indrajit, Rajan, Manorajan Minz, Hari and Deepjyoti for helping me technically and Pralay, Rahul, Kamlesh, Prateek, and Mridul for maintaining a healthy atmosphere in the lab. My special thanks also goes to my seniors, Dr. Brajesh Rawat, Dr. Vinaya M M, Dr. Saroj Mondal, Dr. Pavan Kumar Manchi, Dr. Ujjwol Barman, Dr. Namami Goswami, Dr. Nagesh C H, Dr. Gaurav Saxena, who have bestowed me with their experience and suggestions from time to time.

The acknowledgement section is incomplete without mentioning my teachers, parents, buaji and family elders who have torched my progress in all the walks of my life. My heart deepest thanks to my dear wife, Rani and my little son OM who share the doctoral credit equally with me and have been patient enough to spend most of the hours during my research days in my absence especially in nights. I also want to thank my sister, Suman, my brother, Ravi, and my nephew Anuj, who have always been a helping hand to me. Finally, I am indebted to Government of India for providing an opportunity, resources and financial support to carry out this research work and implicitly to the people of India who have helped indirectly in many sense to my research efforts.

Vimal Kumar Singh Yadav

Abstract

Printing (additive manufacturing) of micrometer-to-nano scale patterns of metal and semiconductor particles, for the fabrication of electronic devices at room temperature, is receiving significant attention due to its potential as an inexpensive alternative to top-down fabrication of silicon microelectronic devices. The electronic devices fabricated with printed electronics have been successfully applied in the field of sensors, display technology, solar cells, electronic circuits and memory-devices. However, an in-depth understanding of physico-chemical interactions between the liquid ink droplets and the substrate would help in the improvisation of the printed devices.

The prime focus of the thesis is to optimize micro-cantilever based printing (MCP) technology by printing stable and reliable devices and a systematic investigation of the challenges involved. As the first contribution of the thesis, the analysis of the interactions between liquid dispersions of polyaniline emaraldine salt (PANI-ES) and silver nanoparticles (AgNP) over various substrates such as silicon, glass, indium tin oxide (ITO), polyethylene terephthalate (PET) and poly vinyl alcohol (PVA) surfaces has been performed. This analysis has been carried out in terms of concentration of the dispersion, particle size, solvophilic or solvophobic nature of the substrate, evaporation rate of solvents, ambient humidity and post-processing. Substantially low ratios of printed dot feature size to suspended particle size have been obtained, indicating that the MCP can provide a much finer print resolution for flexible and printed electronic circuit components as compared to traditional inkjet, screen or gravure printing.

The second contribution of thesis is the fabrication and electrical characterisation of printed micro-resistors of AgNPs using three different printing techniques based on MCP technology. These printing techniques are referred to as spot overwrite printing (SOP), dip-ink printing with spot overwrite printing (DIPSOP) and surface patterning tool drag printing (SDP). The minimum feature size of sub-1 μm and a print resolution of sub-2 μm is

achieved using these techniques. The printed micro-resistors have been found to be nearly 7 times less costly as compared with existing surface mount device (SMD) chip resistors used on printed circuit boards.

The third contribution of the thesis is the development of low-cost, simple and rapid process for fabrication of printed Schottky diodes based on drop-casted ZnO multiple or single nanowires (NWs) and micro-cantilever printed Ag contacts. The fabricated diodes have been applied for detection of CO_2, CO and NO_2 at room temperature with sensitivity ranging from 0.004 to 0.492 %/ppb and 0.146 to 14.9 %/ppm, for ZnO multiple NWs and ZnO single NWs based Schottky diode-sensors respectively. The fabricated sensors based on ZnO single nanowire show higher sensitivity as compared to gas sensors based on ZnO multiple nanowires for CO. All the fabricated gas sensors based on Schottky diode have an average response time of 30-60 seconds and an average recovery time of 1-5 minutes.

The fourth contribution of the thesis is the development of ZnO NW mat and ZnO single nanowire Schottky barrier field-effect transistors (SBFETs) with the help of MCP technology. The printed NW mat based FETs are applied as NO_2 sensor achieving an appreciable sensitivity of 1.127 %/ppb which is nearly twice the sensitivity of ZnO NW mat based Schottky diode based sensors for NO_2. Moreover, an analytical current model for ZnO single nanowire based field-effect transistor (FET) is developed. The analytical model is based on charge carrier distribution in a ZnO nanowire channel which has been modelled based on one-dimensional (1-D) density of states. Such simple mathematical models can help to understand the underlying physics and electronic transport phenomena for nanoscale devices which can help to improve the understanding of the gas sensing mechanism with variety of analytes.

Contents

List of Figures

List of Tables

List of Acronyms

AER	Average electrical resistance
AFM	Atomic force microscope
AgNP	Silver nanoparticles
ALD	Atomic layer deposition
AuNP	Gold nanoparticles
BBSD	Back-to-back Schottky diode
BHF	Buffered hydrofluoric acid
BQP	Bohm quantum-potential
CBD	Chemical bath deposition
CEC	Controlled environment chamber
CP	Contact pad
CVD	Chemical vapor deposition
DC	Direct current
DCPS	Direct current probe station
DI	De-ionised water
DIP	Dip-pen nanolithography
DMSO	Dimethyl sulfoxide
DOS	Density of states
EDS	Energy-dispersive X-ray spectroscopy
FESEM	Field emission scanning electron microscope
FET	Field effect transistor
FIB	Focussed-ion beam
IC	Integrated Circuit
IPT	Inkjet printing technology

IPA	Isopropyl alcohol
ITO	Indium tin oxide
JCPDS	Joint Committee on Powder Diffraction Standards
LIR	Local ink reservoir
LST-DI	Low surface tension-de-ionised water
MBE	Molecular beam epitaxy
MCP	Micro-cantilever printing
MCPT	Micro-cantilever based printing technology
MFC	Mass flow controllers
MOCVD	Metalorganic chemical vapour deposition
MOSFET	Metal-Oxide-Semiconductor Field-Effect Transistor
MPS	Molecular printing system
M-ZnO	Modified Zinc oxide
NW	Nanowire
NWB	Nanowire bridge
NWD	Nanowire dispersion
NWM	Nanowire mat
NWP	Nanowire powder
NWFET	Nanowire Field effect transistor
NW-μMD	Nanowire micro-mat diode
NW-μBD	Nanowire micro-mat bridge diode
PANI-ES	Polyaniline emaraldine salt
PCB	Printed circuit board
PDMS	Polydimethylsiloxane
PET	Polyethylene terephthalate
PEDOT:PSS	Poly(3,4-ethylenedioxythiophene) polystyrene sulfonate
PMMA	Poly(methyl methacrylate)
PMR	Printed micro-resistor
PPL	Polymer pen lithography
PTC	Positive temperature coefficient

PVA	Polyvinyl alcohol
PVP	Poly 4-vinylphenol
QCE	Quantum confinement effects
RFID	Radio frequency identification
SAED	Selected area electron-diffraction
SBFET	Schottky barrier field-effect transistor
SDP	Surface patterning tool drag printing
SDS	Sodium dodecyl sulfate
SEM	Scanning electron microscopy
SMF	Silicon micro-fabrication technology
SMD	Surface mount device
SMED	Single material electronic devices
SNW	Single nanowire
SOP	Spot overwrite printing
SP	Schrodinger-Poisson
SPT	Surface patterning tool
TFT	Thin film transistor
TGME	Triethylene glycol monoethyl ether
TSE	Tip scratch effect
UV	Ultra violet rays
U-ZnO	Unmodified Zinc oxide
VLS	Vapour-liquid-solid
XRD	X-ray diffraction
ZnO	Zinc oxide

1

Introduction

Contents

1.1 Introduction

It will not be out of place to mention that silicon has been probably the material of the 20^{th} century. Since the development of integrated circuit (IC) technology and metal-oxide-field effect transistors (MOSFETs), the electronic components, devices and circuits have been the building blocks of the daily use household items like computers, smartphones, micro-controllers and so on [1–5]. The silicon microelectronic fabrication (SMF) technology has been able to shrink the dimensions of MOSFETs as per the rate proposed by Moore's law [6]. The scaling ability of SMF technology has kept it growing every year. However, at present, the channel length of the MOSFETs is scaled down to sub-10 nm regime due to which the devices have to combat various types of short-channel effects [7] and the standard equations governing the semiconductor physics need modifications [8–10]. These issues have given a scope for considering various nanomaterials and nanostructures like metal-oxide semiconductor nanowires, graphene, carbon nanotubes, conductive polymers etc. to replace silicon as channel material specially in specific fields of application such as sensing, photovoltaics, display technology and so on [1, 11–13].

It is known that the SMF technology is most suitable for the development of ICs which requires thousands of silicon-based transistors to be fabricated in a single batch process [14]. Now, consider the fabrication challenges of non-silicon channel based discrete devices such as resistors, capacitors and field-effect transistors (FETs). The fabrication of any electronic device is incomplete without metal contact deposition. In most of the cases where the channel is a non-silicon material, the metal contact pads are usually fabricated using SMF technology which uses sophisticated and costly equipment and processes such as mask writing using photolithography, double-sided mask alignment, electron-beam lithography to develop the masks and thermal evaporation, RF sputtering etc. to deposit a certain thickness of metal layer [15–17]. As a result, the device fabrication process of non-silicon materials which depends on SMF technology becomes costly even for those specific applications like sensing, photovoltaics and so on, where only individual electronic components are primarily required. Moreover, the proper placement and integration of channel material with the two metal contacts also requires the usage of high-end processes like dielectrophoresis, site-selective molecular beam epitaxy (MBE), metalorganic chemical vapour deposition (MOCVD), focussed-ion beam/scanning electron microscopy (FIB/SEM). These processes are usually carried out at high temperatures and vacuum environment which in turn increases the fabrication cost even further [18–21].

This has led to the need of research efforts for development of alternative technologies which can fabricate the individual electronic components that can be employed to some specific application. Among such alternate technolgies, printed electronics has emerged as a highly active research area for the fabrication of low-cost, light-weight, large-area, flexible electronic devices on variety of substrates such as silicon, plastic, glass, polyethylene terephthalate (PET), polyvinyl alcohol (PVA), polydimethylsiloxane (PDMS), poly(methyl methacrylate) (PMMA), Indium tin oxide (ITO) coated PET and so on [2, 22, 23]. This technology is also related to wearable, flexible and paper electronics, for the fabrication of electronic components for specific applications and rapid prototyping [1, 2, 24–26].

1.2 Printed Electronics: Basics and Types

Printed electronics holds the potential to be a key technology in the upcoming miniaturised electronic industry. Printing facilitates integration of diverse and mutually incompatible materials on the same substrate, thus it is attractive for applications such as multi-component transistors and sensors [27, 28]. Moreover, this technique involves 'bottom-up' process which is much less wasteful than the standard 'top-down' microfabrication techniques involving etching and lift-off [29–35].

Being a low-cost and additive in nature, printing technology has been applied for the development of printed resistors, printed capacitor, printed FETs and printed memory-circuits [36–38]. Using these basic electronic components, numerous types of printed sensors, solar cells and radio-frequency identification (RFID) tags have been developed [1, 13, 30, 39–43]

The most common printing technologies are inkjet printing, gravure printing and screen printing. Inkjet printing is popular due to its simplicity, and it involves usage of inks with low viscosity (1-20 cP) without the need for binders which can destroy the functionality of electronic features. However, inkjet technology lacks in fine resolution, satellite-free precision and speed [37, 44–46]. Gravure printing is high speed and can produce patterns below 10 μm with low line edge roughness [24, 47], but this printing requires inks with high viscosity (40-60000 cP) [48]. Screen printing is a mature technique but it also requires inks with high viscosity (greater than 10000 cP) for stable print [27, 49, 50]. The operational procedure for each of above-mentioned printing technique has been detailed in following sub-sections.

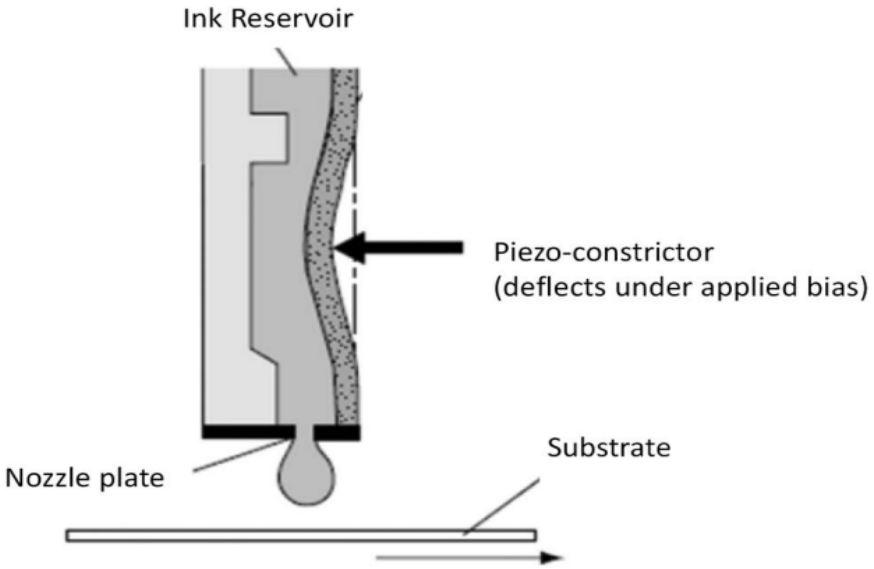

Fig. 1.1: Conceptual view of piezoelectric inkjet printing [1]

1.2.1 Inkjet printing

The inkjet printing utilizes a nozzle to eject the droplets by generating a pressure wave in an upstream chamber. The pressure wave is generated using several methods such as deformation of a piezoelectric membrane, thermal bubble formation and so on. In general, piezoelectric actuation has gained the peak attention in the field of printed electronics, owing to its compatibility with a wide range of inks and not exposing the ink to thermal stresses during the printing process. A conceptual view of inkjet printing is shown in Figure 1.1. Here, a pressure wave is induced within the ink reservoir by deflecting the piezo-constrictor by applying a voltage pulse to the constrictor, which causes it to deflect. A pressure wave in the ink is introduced as the constrictor deflects into the chamber and then backs out, which pushes the ink past the nozzle plate. The ink retracts when the constrictor pulls back and the droplet gets pinched off, and is expelled from the inkjet head. The expelled droplet travels downward, and hits the substrate. The voltage waveform is optimized to maximize the downward velocity of the expelled droplet to ensure stable jetting. The inkjet head never comes in contact with the substrate and this non-contact nature of inkjet printing reduces the risk of defects due to contacting of dust particles, etc. [1, 2, 39]

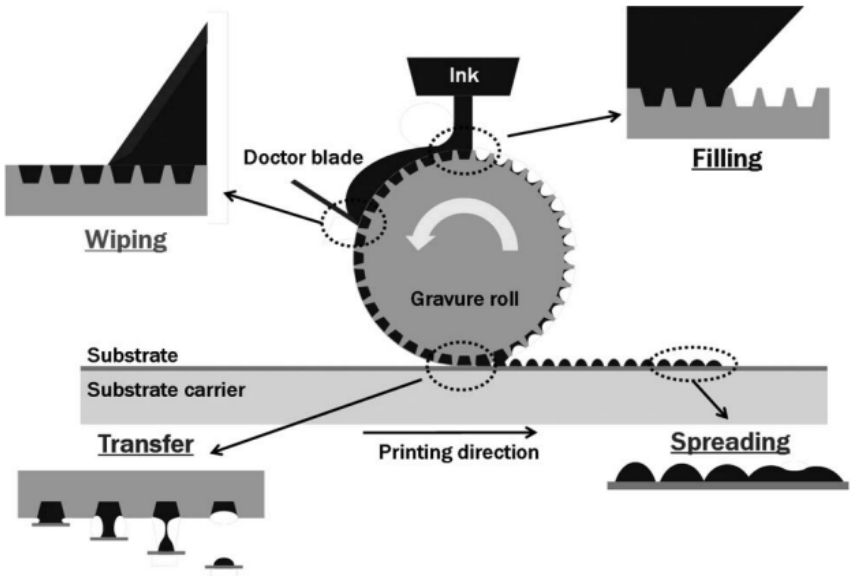

Fig. 1.2: Schematic of the gravure printing process [1, 2]

1.2.2 Gravure printing

In gravure printing, a hard metal cylinder is engraved with wells which are filled with ink and wiped using a doctor blade. The doctor blade removes any excess ink while keeping the wells fully filled. With the rolling of cylinder, ink is transferred to the substrate. Once the ink-transfer process is completed, the individual droplets of ink, dispensed from the gravure cells, spread on the substrate and dry to form the final pattern. The overall schematic of the gravure printing process is shown in Figure 1.2. Since the gravure printing is a contact printing, it shows excellent pattern fidelity and relative placement precision of individual drops. Eventually, it has been found that dispensing of the ink and its relative placement is purely a function of the quality of the cylinder engraving and also of the ink/cylinder/ substrate process optimization based on rheological properties of the ink [1, 2].

1.2.3 Screen printing

Screen printing is probably the most mature and old printing technology in which a viscous ink is “pressed" through a patterned screen using a squeegee [2]. In screen printing, a screen mask is used which typically consisting of a woven mesh, and a patterned stencil attached to the mesh. Ink to be printed is pressed on the screen mask by the squeegee and passes through the portions of the mesh that are not covered by the stencil material. Ink passing through the stencil openings is transferred over

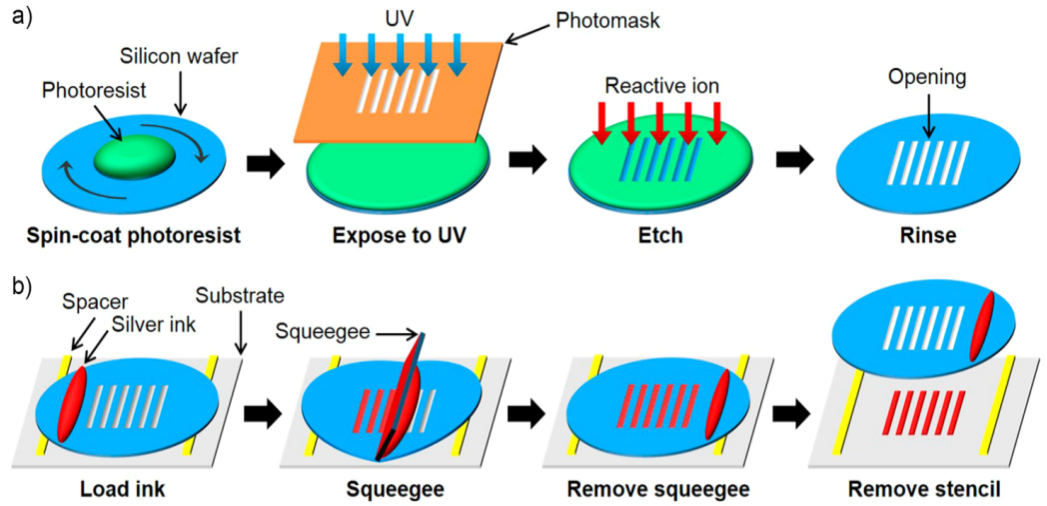

Fig. 1.3: (a)Schematic diagram for the preparation of a silicon stencil using photolithography techniques (b) Schematic diagrams illustrating the screen printing process using the silicon stencil and a silver ink [3]

the substrate to print the desired patterns. The screen printing technology is cost-effective and fast, however, the printed features lack fine resolution. Even if the stencils can be produced with fine line openings narrower than 40 μm, the wire of the mesh blocks the extremely fine openings and thus clog the ink to pass through the stencil, causing defects [2,3,51]. Figure 1.3 shows the schematic diagrams for silicon stencil preparation and screen printing steps for silver ink.

It is observed that the above mentioned printing techniques either require inks with very high viscosity, have poor print-resolution, have likelihood of defects and contamination from dust particles on the substrate or have relatively slow printing speed. Despite of appreciable progress in the area of printed electronics over the last decade, a tradeoff has been observed between the print-resolution and throughput of the printing process [1] as shown in Figure 1.4. Further, the lack of understanding of printing dynamics have resulted in poor pattern-shape control. Furthermore, most of these techniques are suitable mainly for high-volume production as they require moulds, screens and engravings to be made which involve high costs. An alternative for rapid prototyping of printed electronic circuitry could be a cantilever based additive printing technique with high precision and super-fine resolution which is introduced in the next section.

1.2.4 Other printing techniques

Apart from these three major printing techniques, there are other techniques also such as roll-to-roll nanoimprint lithography (R2R NIL) in which an imprint roller wrapped with a flexible mold is

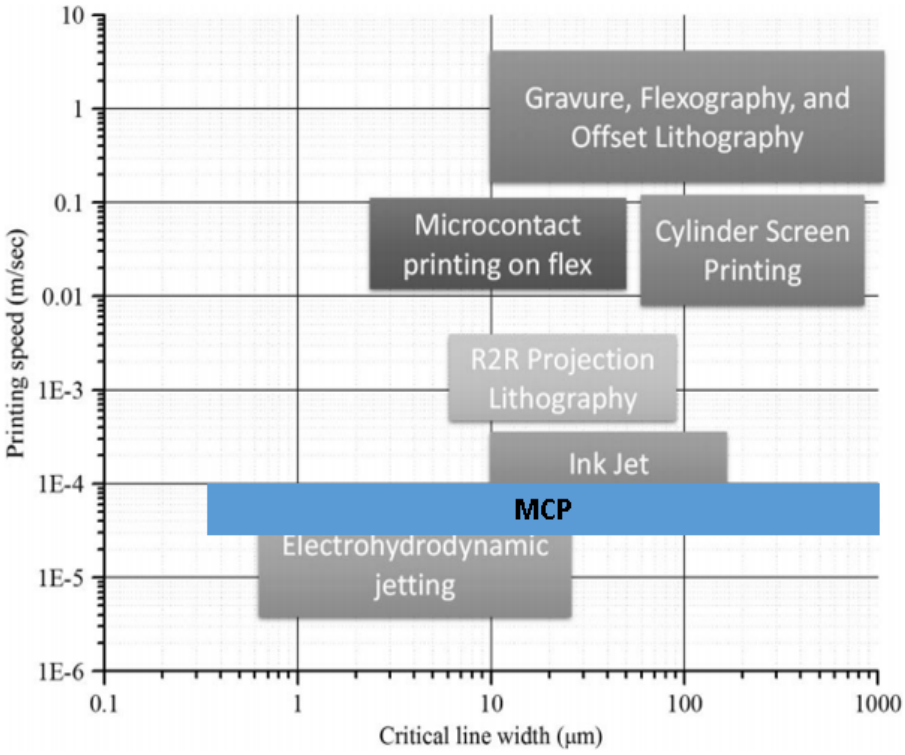

Fig. 1.4: Survey of the resolution versus throughput tradeoffs for different printing processes [1]

used to print onto a flexible substrate on a supporting roller instead of a flat plate. This technique has advantage of continuous process and higher throughput, however, it has challenges in process and stability control [52]. Electrodynamic jetting is another printing technology which is continuous as well as drop-on-demand printing having advantages of generating patterns smaller than the nozzle size because it performs the printing by pulling the ink rather than pushing the ink from the nozzle. However, this printing technology suffers the issue of low throughput [1,53]. Flexography is also another printing technique which has a major advantage that it can print on almost any kind of substrate, but faces poor ink control as it has an old inking system to control the ink-flow [54].

1.3 Micro-Cantilever Printing (MCP)

In this thesis work, micro-cantilever printing technology (MCP) is used to print electronic devices using the Nano eNabler^{TM} Molecular Printing System (MPS) [55]. MCP uses surface patterning tools (SPTs) that are fashioned after the probes of atomic force microscopes. A typical SPT contains a 2 mm x 2 mm sample reservoir and a 200 μm long micro-cantilever print head with inbuilt micro-channels as shown in Figure 1.5. A few microlitre volume of the ink to be printed is loaded onto the

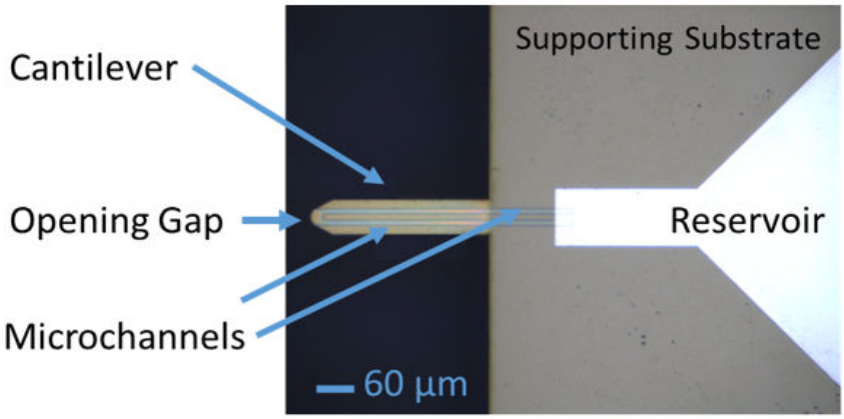

Fig. 1.5: Image of a '60R' SPT, where width of the micro-cantilever is 60μm and tip of the cantilever is rounded

reservoir [55]. The ink flows from the reservoir to the micro-cantilever tip through the micro-channel. The sample molecules or particles are printed by precisely positioning the piezo-controlled cantilever onto the substrate. This technology is similar to the inkjet printing technology, but its principal advantage over inkjet is that it can allow printing of features much closer to the ink particle size due to its low-volume loading technique, thereby offers feature-sizes in a much wider range of 0.5 to 1000 μm. It can also deliver more precise control on the print location with laser feedback. As MCP uses drop-by-drop printing, it is a slow technique but it can be operated in a dip-pen line drawing mode for increased speed and customised control of feature shape and size.

Moreover, MCP can be performed at room temperature and non-vacuum conditions, is maskless, eco-friendly and can print diverse nature of inks (metallic, semi-conductive organic, inorganic, polymers, polar and non-polar liquids, biological samples as proteins, nucleic acids and so on) directly at the targeted location on the substrate with a print-resolution of sub-2 μm. Tabel 1.1 describes the advantages and disadvantages of different printing methods.

1.4 Motivation

Additive manufacturing (printing) of micron-scale patterns of metal and semiconductor particles is receiving significant attention due to its potential as an inexpensive alternative to top-down fabrication of silicon microelectronic devices. However, printing of such devices needs an in-depth understanding of physico-chemical interactions between the liquid ink droplets and the substrate used for printing the devices. The paucity of detailed experimental studies in this area warrants a systematic investigation

Table 1.1: Table comparing advantages and disadvantages of different printing methods

Printing Technology	Advantages	Disadvantages
Inkjet	- uses low-viscosity inks (1-20 cP) - non-contact printing - inks are less prone to contamination - no need of binders	- lacks fine resolution - lacks satellite-free precision - drop placement has less accuracy - low print-speed
Gravure	- high-speed - low-line edge roughness - feature size scaling is good	- requires very high viscosity inks (40-60000 cP) - prone to defect and contaminations
Screen	- most mature print technology - cost-effective - fast	- polymer binders with ink requires - high viscosity ink required (10000 cP) - poor resolution
MCP	- best feature-to-particle size ratio - low viscosity inks required (10-18 cP) - wider print range - highly suitable for rapid prototyping - fine resolution of sub-2 μm - minimum feature size in sub-1 μm	- set-up time is high - requires rigourous cleaning of SPTs - faces spillover of ink

into the challenges involved in printing stable and reliable electronic devices.

Recognising MCP as a niche technique suitable for fabrication of customised micron and sub-micron scale electronic devices, theoretical and practical aspects of the technique that would be necessary to convert it into a reliable and reproducible technology have been explored in this work. Dispersions (inks) of nano-sized particles of polyaniline emaraldine salt (PANI-ES) and silver were initially chosen for this analysis, as these materials allow simple, versatile and relatively low-cost techniques for printing electronic devices [45,56–60]. This technique can be used for rapid design and execution of micro-devices for feasibility and proof-of-concept level testing.

1.5 Problem Definition

It is evident from the previous discussions that MCP technology offers a potential alternative not only to the standard silicon fabrication technology but also to the inkjet printing technology in terms of various parameters such as superfine resolution printing, flexibility of diverse nature of inks, wider range of printed feature size, relatively fast speed and probably the best feature size to ink-particle size ratio which dictates the quality of the printed structures. Therefore, to establish MCP as mainstream printing technology, research efforts have been carried out to optimize and analysis various physical, chemical and electrical parameters related to this printing technology and the expertise obtained from

such analysis has been utilized to print and fabricate micro-resistors of silver nanopartilces (AgNP), Schottky diodes using zinc oxide (ZnO) nanowires (NWs) mat and ZnO single NWs (SNW) with printed AgNP contact pads, and printed ZnO SNW transistors for gas sensing applications. The main objectives of the thesis can be listed as follows:

- Analysis and optimization of micro-cantilever printing of polyaniline and silver microstructures for electronic applications
- Fabrication and electrical characterization of printed micro-resistors (PMRs) of AgNPs using micro-cantilever printing technology
- Fabrication of back to back Schottky micro-diodes using MCP based AgNP film and ZnO Mutilple Nanowires for gas sensing applications
- Fabrication of MCP based Ag Contacts for ZnO Single-Nanowire Based Schottky Diodes as CO_2 and CO Sensors.
- Fabrication and analytical model development of MCP based ZnO Nanowire(s) based FETs for NO_2 detection

These research objectives are summarised in the following Table 1.2.

1.6 Thesis Outline

The thesis has been organized into seven chapters. The contents of each chapter can be briefly outlined as follows.

Chapter 1 is a generalized introduction chapter which details the fundamentals aspects of micro-cantilever printing technology and its comparison with other existing printing technologies along with motivation and organisation of the thesis work.

Chapter 2 describes the in-depth analysis of superfine-resolution printing of polyaniline and silver micro-structures for electronic applications. This chapter details the experimental procedures employed for substrate selection, printing and characterization of the features. Furthermore, this chapter deals with qualitative as well as quantitative study of various factors that determine the quality and stability of the printed features.

Chapter 3 describes the printing of micro-resistors of silver nanoparticles using three different printing techniques based on micro-cantilever based printing technology. The three techniques have

Table 1.2: Summary of research objectives

Research Objective	Targeted Device/ Structure	Materials	Substrates	Applications
Optimization of MCP technology, Printing of metallic and conductive polymer ink	Micro-spot arrays Micro-lines Squared pads	AgNP ink, PANI-ES ink	Glass (coverslip) SiO2/Si PET PVA@PET ITO@PET	Development of printing process
Fabrication of printed micro-resistors (PMRs), Electrical and material characterization of PMRs	Micro-Resistors	ChM: AgNP CM: AgNP	Glass SiO2/Si PET	Low-cost alternatives to SMD chip resistors on PCB boards
Fabrication of ZnO multiple NWs based Schottky diodes, Electrical and material characterization of diodes	Schottky diodes	ChM: ZnO NWM ChM: ZnO NWB CM: AgNP	SiO_2/Si	Low-cost gas sensors for CO_2, CO and NO_2 operating at RT
Fabrication of ZnO SNW based Schottky diodes, Electrical and material characterization of diodes, Analytical model development and device parameter extractions	Schottky diodes	ChM: ZnO SNW CM: AgNP	SiO_2/Si	Low-cost gas sensors for CO_2 and CO operating at RT
Fabrication of ZnO NW(s) FET, Analytical model development of SNW-FET	FETs	ChM: ZnO SNW ChM: ZnO NWM CM: AgNP	SiO_2/Si	Low-cost gas sensors for NO_2 operating at RT
NWM: Nanowire mat, NWB: Nanowire bridge, SMD: Surface-mount devices, PCB: Printed circuit boards, ChM: Channel material, CM: Contact material, RT: Room temperature				

been named as spot overwrite printing (SOP), dip-ink printing with spot overwrite printing (DIPSOP) and surface patterning tool drag printing (SDP). The fabrication process has been carried out over substrates like glass, silicon and polyethylene terephthalate (PET). A post-printing analysis has been carried out based on electrical characterization of the PMRs which shows SOP as the most preferred, DIPSOP as the most reliable and SDP as the fastest printing technique. The electrical characterization of the printed micro-resistors shows that their average resistance varies from few Ω to kΩ based on the print thickness. The printed resistors are single material electronic devices (SMED) as we have used only AgNP ink for complete fabrication of the device in order to avoid any interfacial mismatch and irregularities at the nano-scale. Moreover, the fabricated PMRs are smaller in size, have lower fabrication cost and consume less power as compared to the standard surface mount device (SMD) chip resistors and hence offer an effective alternative to be used as micro-chip resistors on printed circuit boards (PCBs).

Chapter 4 describes the usage of micro-cantilever printed silver nanoparticles (AgNP) contact pads for fabrication of ZnO nanowire (NW) Schottky diodes-based devices. The fabrication process is divided in two phases. In first phase, a ZnO NW mat based sensor is developed by simple drop-casting

techniques to first confirm the response of ZnO NWs to the pollutant gases. In the second phase, the sensor is optimised with the help of micro-cantilever printing technique by reducing the channel gap between the AgNP pads and forming a ZnO NW bridge having less density of NWs and a higher surface-to-volume ratio. The physical and chemical characterization of materials have been performed using various instruments like Field Emission Scanning Electron Microscope (FESEM), Energy-dispersive X-ray spectroscopy (EDS), X-ray Diffraction (XRD) while electrical characterization has been performed with the help of Keithley 4200A-SCS parametric analyzer [61]. These devices are further employed as sensors for detecting CO_2, CO and NO_2 in ppb range at room temperature. The goal is to develop a low-cost and simple process for rapid sensing of air pollutants at room temperature. The gas sensing experiments have been performed in a Controlled Environment Chamber (CEC) in which the gas-flow is controlled using mass flow controllers (MFCs) (Make: Alicat Scientific) [62]. The fabricated sensors show improved sensitivity towards all three gases as compared to earlier reported sensors.

Chapter 5 presents the fabrication of zinc oxide (ZnO) single-nanowire (SNW) based back-to-back Schottky diodes using micro-cantilever printed AgNP contact pads. ZnO SNWs have been placed on a SiO_2/Si surface by drop-casting an optimised dispersion of ZnO nanowires in de-ionised (DI) water. The micro-cantilever printing process has been used to overlap the surface of ZnO nanowire with AgNPs pads. The electrical response of the printed diodes have been verified with an analytical model based on thermionic emission theory. Printed-Schottky diodes have been fabricated with varying channel lengths of ZnO SNW and among them, the typical ideality factor is $\sim$ 2.4, the lowest Schottky barrier height of 0.21 eV for positive voltage sweep and 0.17 eV for negative voltage sweep, the I_{on}/I_{off} ratio in order of $\sim$ 10^3-10^4, the lowest series resistance of 30 kΩ and the fastest turn-ON voltage of 50 mV have been obtained. These ZnO SNW based Schottky diodes have been used for detection of air pollutants such as CO_2 and CO. ZnO nanowire dispersion is further optimized by adding sodium dodecyl sulfate (SDS) and acetic acid to form longer nanowires which ease the reproducibility and scaling of the fabrication process. The sensors demonstrate a wide gas-sensing range of 500 ppb to 500 ppm and 10 ppb to 9 ppm for CO_2 and CO respectively. A higher sensitivity of 4.01 %/ppm and 14.9 %/ppm is obtained for CO_2 and CO respectively. The fabricated sensors show a low response time mostly in a range of $\sim$ 5-10 s and recovery time in a range of $\sim$ 2-10 minutes. These sensors are stable within a relative humidity range of (15-75) %

Chapter 6 briefs the fabrication of ZnO NWM and SNW based SBFETs with the help of MCP

technology. The electrical characterization shows a n-type channel behaviour in both types of SBFETs. The conclusion drawn from the output and transfer curves of the fabricated SBFETs have been confirmed with respective C-V characteristics. The fabricated NWM-SBFETs have been applied to sense NO_2 at room temperature and it has been observed that ZnO NWM-SBFET based NO_2 sensors show nearly two times higher sensitivity for sub-10 ppb gas concentration range as compared to ZnO NWM-Schottky diode based sensors. Additionally, a surface potential based analytical drain current model for a depletion mode, back gated zinc oxide (ZnO) SNW field-effect transistor with a rectangular cross-section having channel length, width and thickness as 7 μm, 120 nm, 120 nm respectively. Nanowires are one-dimensional (1-D) structures, hence 1-D charge carrier concentration has been computed with the help of 1-D density of states (DOS) and Fermi -1/2 ($F_{-1/2}$) integral in order to include quantum confinement effects (QCEs) which are expected to effect the charge concentration and transport mechanism of the device with such nanoscale dimensions. Further, 1-D Poisson's equation has been solved to derive surface potential and surface depletion depth caused by adsorption of oxygen vacancies. The oxide capacitance of the nanowire has been utilized to express the effective charge in the nanowire channel. The drain current has been modelled with the help of surface potential and the effective charge of the nanowire channel. The current transport mechanism has been investigated for both depletion and accumulation cases with respect to the applied gate voltage. The model results have been verified with the published experimental results. The model approach developed in this section can be used for other methods and variants of current transport after proper modifications.

Chapter 7 presents a conclusive remarks for this work and a brief discussion on future scopes of this work.

2

Micro-Cantilever Printing of Polyaniline and Silver Microstructures: Analysis and Optimization

Contents

2.1 Introduction

In this chapter, super-fine resolution printing of two different kinds of materials have been demonstrated. Printing of PANI-ES is briefly explored for obtaining arrays of discrete conductive spots that may be useful for flextronics applications. Printing of silver nanoparticle (AgNP) is explored more thoroughly. Silver has a high conductivity over a wide range of temperatures, unlike organic conductors, and is therefore generally found to be suitable for hi-fidelity flexible printed devices despite its relatively higher cost. Therefore, printing and testing of micron-scale features made from silver is the chief focus of this work. Continuous line and 2-D patterns of silver were printed and fashioned into micro-resistors. Such 'monolithic' resistors find widespread applications in construction of monolithic ICs. Super-fine printing of silver can also be used towards chemoelectronic circuits with sensing abilities [56]. A wide variety of substrates such as silicon wafer, glass slide, PET sheet, ITO and PVA have been used in order to compare the compatibility between the ink and the substrates. A given ink cannot be printed over every type of substrate with the same level of integrity [27] due to different mutual adhesive interactions. Therefore, such comparison would be instructive for future development of the printing technology. In this report, analysis of the printing has been detailed in terms of concentration of the materials dispersed in the ink, particle size, evaporation rate of solvent, solvophilic or solvophobic nature of the substrate, effect of humidity variation along with the necessity of suitable pre-treatment and cleaning of SPTs and substrates. These parameters are extremely crucial for obtaining reproducible fine-resolution print of an ink over a particular substrate. Using the insights from this analysis, we have further demonstrated the printing of micrometer-scale printed patterns that can be used as monolithic resistors. To the best of our knowledge, there are no reports for monolithic printed resistors of silver using customised shapes at a low ratio of printed feature size to particle size using microcantilever based technique. The flow chart of the printing process has been provided in Figure 2.1.

2.2 Materials and Methods

This section contains the experimental procedures employed for substrate selection, printing and characterization of the features.

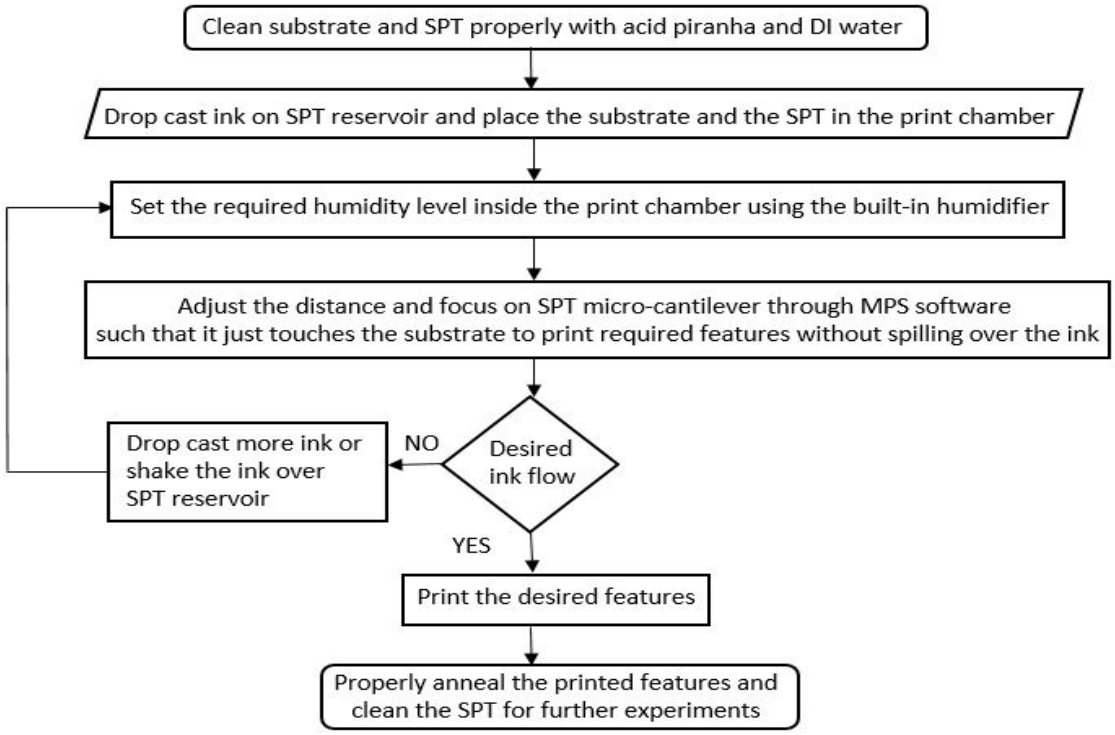

Fig. 2.1: Printing process flow chart

2.2.1 Selection of particle size of the sample material

The size of the particle of the material to be printed is limited by the channel-width of the micro-cantilever of the SPT. In case of 60R SPT used for these experiments, the channel-width is 10 μm. Both PANI-ES and AgNP used in these experiments were sourced commercially. The smallest available size in PANI-ES powder (Sigma Aldrich. Product No. 428329; particle size between 3-100 μm) was used. Upon dispersion in the desired solvent, larger particles were allowed to settle gravitationally in an eppendorf tube and the ink was drawn only from the upper portion of the tube. AgNP conductive ink (Sigma Aldrich, Product No. 736481; average particle size $<$ 50 nm, 30-35 wt.% dispersion of nanoparticles in triethylene glycol monoethyl ether (TGME), with specific resistivity near 2 $\mu\Omega$-cm) has been optimised for printing by the manufacturer, and was used as received. Dimethyl Sulphoxide (DMSO) was purchased from Merck India and used without further purification. Figure 2.2 (a,b) shows larger particle size of PANI-ES as compared to AgNP.

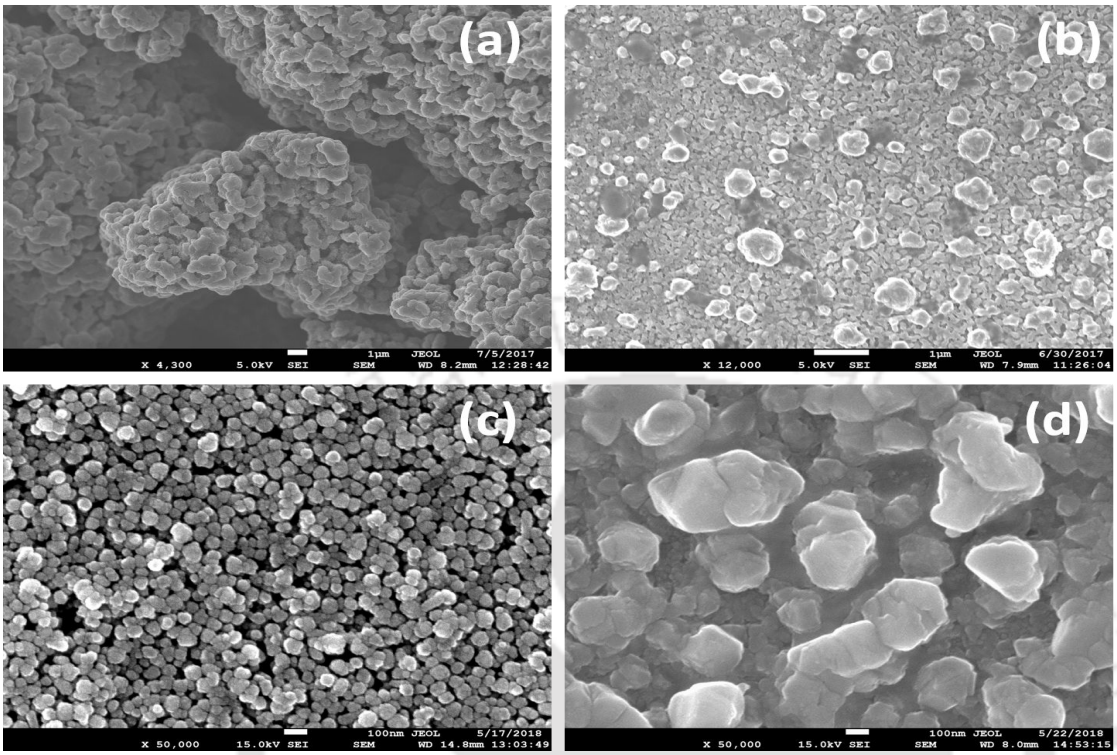

Fig. 2.2: (a) FESEM image of PANI-ES sample (b) FESEM image of AgNP ink sample (c) FESEM image of unannealed AgNP film (d) FESEM image of annealed AgNP film. Scale bar = 1 μm (a,b) and 100 nm (c,d)

2.2.2 Cleaning of SPTs and substrates

The SPTs and substrates were cleaned thoroughly before and after each set of experiments. The SPT was immobilised onto a PDMS-coated surface before cleaning, in order to avoid its movement and consequent damage to the micro-cantilever. During each cleaning step, 10 μl of acid piranha solution (H_2SO_4 mixed with H_2O_2 in 3:1 ratio) was placed carefully to cover the reservoir and the cantilever channel. After twenty minutes, the acid was removed using a micropipette, and 10 μl of de-ionised (DI) water was drop-casted onto the SPT. The water was replaced twice after 2 minutes soak. If necessary, the entire cleaning sequence was repeated till the channel was seen to be free of previous deposits under microscope. Finally, the SPT was dried under a gentle flow of dry nitrogen. Similar procedure was used for cleaning substrates. Immediately prior to printing, the clean SPT and substrates were exposed to UV-ozone treatment for 30 minutes. These procedures were found to be crucial for free flow of the optimized ink onto the substrate.

2.2.3 Preparation of PANI-ES ink suitable for printing

2.2.3.1 Solvent selection

Selection of suitable solvent is the first step for preparation of printing ink for a solid sample material. Solubility of PANI-ES in polar and non-polar solvents is low, hence homogeneous mixture of PANI-ES with solvent is denoted as dispersion [63]. Multiple solvents such as DI water, N-methyl-2-pyrrolidone, ethanol and DMSO were tested for obtaining a printable dispersion from PANI-ES. Based upon ease of dispersion, flow and vapour pressure, aqueous DMSO was selected to be the liquid medium for PANI-ES ink. The optimization of the solvent composition is detailed in the Results and Discussion section.

2.2.3.2 Concentration of the material within the inks

In ink-based printing systems, it is important to determine the optimal concentration of the dispersant material within the solvent matrix. In electronic devices, densely packed overlapping print features are necessary for obtaining good electrical conductivity, and this requires high concentration of the dispersant. However, for printing sub-micron scale features for ultra-miniaturised devices, the print-head size should also be extremely small. This requires a lower concentration of the dispersant, to avoid clogging the pore of the print-head. These conflicting requirements guide the minimum and maximum possible weight/volume ratio of the solid material and liquid medium in the ink. Following this guideline, optimal concentration of the ink was determined by systematically diluting the DMSO based PANI-ES formulation with DI water so as to obtain an uninterrupted flow for continuous printing. A custom-made silica substrate was used for the initial printing trials for obtaining the optimal PANI-ES ink composition. The printed patterns were inspected under a microscope for structural integrity, and the concentration that gave the smoothest features was noted.

2.2.4 Printing environment

The printing chamber is equipped with an ultrasonic humidifier and a PID controller module that is capable of spraying fine mist particles into the chamber to achieve uniform humidity values in the range of 40% - 90% RH. It was observed that the humidity in the chamber plays a crucial role in achieving optimal ink flow for printing. This is expected, because the vapour pressure of the solvent medium and the adhesion of the ink to the channels within the micro-cantilever are affected due to humidity. Typically, humidity was varied from the ambient humidity of the room (40%) to 58% RH

during the printing trials. The upper range of humidity was limited in order to avoid the printed patterns from merging into each other.

2.2.5 Selection of substrate

A range of substrates commonly used for modern microelectronic device testing were explored for their compatibility with the PANI-ES and AgNP inks. Initially, the rate of evaporation of the solvent medium from the printed substrate was compared by drop-casting 1 μl of each ink over three types of clean substrates - PET, silicon wafer and glass. Further, the PVA@PET was prepared by spin-coating 5% solution of PVA in DI water over the PET surface. The substrates were kept in ambient atmosphere until completely dry, in order to determine the rate of solvent evaporation. Subsequently, contact angle measurements between the ink and various substrates were performed using a goniometer (Model No. HO-IAD-CAM-01B) by dropping 1 μl of each sample over glass, silicon, PET, ITO and PVA surface. Humidity of the goniometer surface was also maintained at the same level where optimal printing could be achieved using a given ink.

2.2.6 Post-processing

After printing, the AgNP features on glass substrates were annealed at 200°C, with a ramp rate of 2°C per minute. The slow annealing assisted in binding the features to the glass as shown in Figure 2.2(d).

2.2.7 Characterisation of printed features

The printed features were imaged photographically using an in-built 700X camera in the MPS. Higher resolution images were obtained from a Field Emission Scanning Electron Microscope (FESEM) from JEOL (Model: JSM-7610F). The thickness of the monolithic resistors was measured using a Veeco DEKTAK 150 profilometer. Electrical resistance of the monolithic resistors was measured via Keithley 4200A-SCS Parametric Analyzer [61] attached to DC Probe Stations of Lakeshore cryotronics (Model: CPX) and EverBeing (Model: BD6). CPX probe station has a vacuum chamber equipped with temperature controller (Model 336), where liquid nitrogen is used for cooling the sample stage far below ambient conditions. The temperature was varied gradually in steps of 20 K from 200 K till 358 K at a vacuum level of $\sim 4.4\times 10^{-5}$ Torr, for measurement of I-V response as a test of reliability of the printed features. The sample was let to equilibrate for ten minutes at each temperature before the measurement.

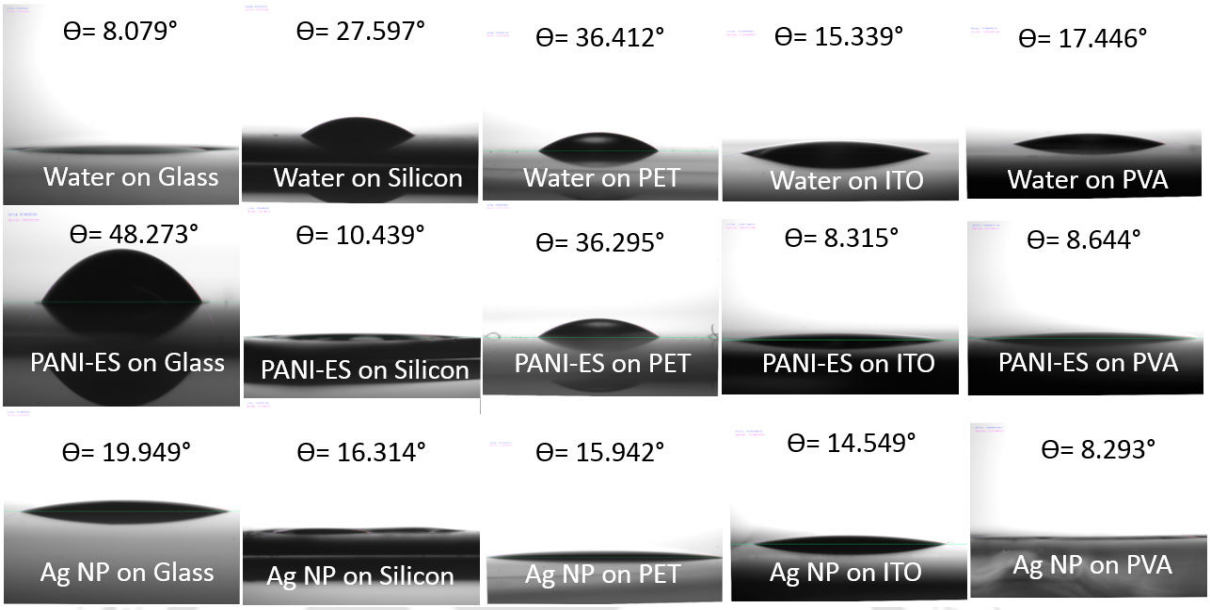

Fig. 2.3: Contact angle measurement for water, PANI-ES and AgNP over different substrates

2.3 Results and Discussion

This section deals with qualitative as well as quantitative study of various factors that determine the quality and stability of the printed features.

2.3.1 Concentration of PANI-ES ink suitable for printing

A commonly used composition of 5% w/v PANI-ES in dimethyl sulfoxide (DMSO) was used as the starting composition for printing features on custom-made Si substrates. However, this ink could not yield any patterns despite trials with different humidity levels. The reason for unsuitability of 5% PANI-ES in DMSO was attributed to aggregation of the conducting polymer within the dispersion that resulted in clogging of the 10 μm channel of the SPT. Upon subsequent dilution with DI water, the 30% v/v aqueous mixture of the 5% DMSO-based ink was found to be suitable for printing with MCP. This translates to a w/v concentration of 1.5% PANI-ES. At a lower concentration of 1%, the printed spots do not retain their continuous structure.

2.3.2 Selection of substrate

2.3.2.1 Solvent evaporation rate from substrate

Under given ambient conditions of temperature and humidity, the evaporation rate of solvent from the printed features on the substrate depends on dispersant-solvent interaction within the sample,

Table 2.1: Parametric analysis for 1.5% PANI-ES:DMSO and AgNP ink over different substrates

Parameter	1.5% PANI-ES:DMSO			AgNP ink		
	PET	Silicon	Glass	PET	Silicon	Glass
Drop Spreading	Second Fastest	Fastest	Slowest	Fastest	Second Fastest	Slowest
Drop Wetting Area	Second Largest	Largest	Smallest	Largest	Second Largest	Smallest
Evaporation Rate	Fast	Fast	Moderate	Moderate	Slow	Very Slow
Evaporation time	180 minutes	30 minutes	4 hours	2 days	2 days	10 days
Substrate Response	Moderately Solvophilic	Least Solvophilic	Most Solvophilic	Least Solvophilic	Moderately Solvophilic	Most Solvophilic

Table 2.2: Table for contact angle measurement results and solid-liquid adhesion energy, W_{SL}

Sample	Water					PANI-ES:DMSO					AgNP: TGME				
Substrate	Glass	Silicon	PET	ITO	PVA	Glass	Silicon	PET	ITO	PVA	Glass	Silicon	PET	ITO	PVA
Left Contact Angle	6.129°	25.877°	33.265°	13.943°	16.736°	44.185°	6.934°	36.563°	7.696°	8.455°	19.163°	18.314°	13.943°	14.783°	6.934°
Right Contact Angle	10.030°	29.316°	39.559°	16.736°	17.949°	52.361°	13.943°	36.027°	8.934°	8.833°	20.735°	14.314°	17.940°	14.315°	9.652°
Average Contact Angle	8.079°	27.597°	36.412°	15.339°	17.446°	48.273°	10.439°	36.295°	8.315°	8.644°	19.949°	16.314°	15.942°	14.549°	8.293°
γ_{LV} (N/m)	0.0728	0.0728	0.0728	0.0728	0.0728	0.053	0.053	0.053	0.053	0.053	0.040	0.040	0.040	0.040	0.040
W_{SL} (N/m)	0.1449	0.1373	0.1314	0.1430	0.1423	0.0883	0.1051	0.0957	0.1054	0.1053	0.0776	0.0784	0.0785	0.0787	0.0796

boiling point of the solvent, concentration of the ink and interactions of the ink with the ambient air and substrate. Due to the complex nature of these mutual interactions, it becomes hard to predict which substrate would be suitable for printing with a given ink. Therefore, the two inks were initially drop-casted on PET, silicon and glass, and kept in a dust-free chamber at ambient humidity of 50% RH and temperature of 23°C to directly observe their solvent evaporation rates. It was found that PANI-ES drops with aqueous DMSO solvent evaporate faster over all three substrates as compared to AgNP drops with TGME solvent, in correlation with the respective boiling points of the solvents (189°C and 256°C [64]). Complete solvent evaporation was the fastest over silicon and slowest over glass. The results of this experiment are tabulated in Table 2.1.

2.3.2.2 Ink-substrate adhesion via contact angle measurement

To quantify the results of the drop evaporation experiment, contact angle measurements of the two inks were performed on a wider range of substrates. Pure DI Water was used as a reference standard. An essential requirement of printing is that the printed droplet should adhere to the substrate firmly, without sliding away from the place where it was dropped by the printhead. This is facilitated if there are adhesive interactions between the substrate and the ink, i.e. when the substrate is solvophilic. However, if the substrate is excessively solvophilic, the printed droplet spreads across the surface,

jeopardizing the shape of the printed feature. If the substrate is highly solvophobic, the sample will remain stuck to the SPT and would not deposit on the substrate. Therefore, the substrate should be optimally balanced between solvophobic and solvophilic nature.

Contact angle measurements assist in gauging the adhesive response of the ink with a given substrate as it is being dropped from the print-head. Figure 2.3 contains the images from these measurements.

Thomas Young [65] expressed the contact angle of a liquid on a solid surface as

$$\gamma_{LV} \cos\theta = \gamma_{SV} - \gamma_{SL} \tag{2.1}$$

where, γ_{LV}, γ_{SV} and γ_{SL} represent the liquid-vapour, solid-vapour and solid-liquid interfacial tensions respectively. θ is the Young's contact angle. Using Dupre's equation, soild-liquid adhesion energy (wetting parameter) W_{SL} can be written as [66]

$$W_{SL} = \gamma_{SV} + \gamma_{LV} - \gamma_{SL} = \gamma_{LV}\,(1 + \cos\theta) \tag{2.2}$$

Table 2.2 shows adhesion energies for different cases calculated using contact angle values and γ_{LV} values from literature [67]. It is clear from the table that contact angle θ is inversely proportional to adhesion energy, W_{SL}. Therefore, lower the contact angle, higher will be the adhesion energy and hence the liquid will wet the solid surface more.

Based on the results of the solvent evaporation and contact angle experiments, PET and PVA@PET were chosen as the most suitable substrates for PANI-ES and glass was chosen to be the most suitable substrate for AgNP ink. Additionally, ITO coated PET was also explored for printing AgNP lines in one experiment, in order to test its suitability for flexible substrates. However, as seen further, the printed Ag features need to be annealed at temperatures higher than 200°C. The PET substrates are distorted at these temperatures, and therefore were not explored further.

2.3.3 Printing of PANI-ES micro-arrays on various substrates

Spots of 1.5% PANI-ES:DMSO with diameter ~ 20 μm at humidity of 47% were successfully printed over PET sheet. Circular Spots of diameter ~ 3 μm were printed on PVA surface with humidity of 55% as shown in Figure 2.4. The super-fine resolution capability of the MCP technique is evident from this result, as the feature size of 3 μm is equal to the average size of PANI-ES particles in the DMSO

based suspension. It is presumed that if smaller size particles are used as ink, the feature size can reach submicron levels.

2.3.4 Printing of continuous lines of silver over various substrates

With a thoroughly cleaned 60R SPT and a glass cover slip as substrate, a set of parallel lines of length $\sim$ 580 μm and width $\sim$ 65 μm could be printed with the as-purchased ink at a humidity level of 55-57% as shown in Figure 2.5. The lines retain their structural integrity for long periods of time. Further, super-fine resolution of the MCP printing technique in case of AgNP was established by printing individual elongated spots with width of $\sim$ 0.5 μm (Figure 2.6) and a pattern with smallest linewidth of 17 μm as shown in Figure 2.7. Considering the average AgNP size of 50 nm, the feature to particle size ratios are 10 and 340 in case of spots and linewidth respectively. To put these ratios in context, a comparative analysis of different printing methods using nanoparticle inks is presented in Table 7.1. The AgNP ink was also printed over ITO surface and lines with width $\sim$ 30 μm were printed at humidity $\sim$ 54% as shown in Figure 2.5.

2.3.5 Printing of monolithic resistors using AgNP conducting ink on glass substrate

Figure 2.8 shows the schematic of a model monolithic resistor. The advantage of a printed monolithic resistor is its reduced contact resistance. Also, the interface mismatch between contact pad and the channel is avoided in this device as the contact and channel region is fabricated with the same material. Two square shaped contact pads of Ag NP ink with length and width $\sim$ 200 μm were printed in about 15-20 minutes at 57% humidity with 60R SPT. In order to maintain good connectivity within the feature, partial overlap between successive print spots was ensured. After successful printing of contact pads, a AgNP line (channel) of length $\sim$ 100 μm and width $\sim$ 40 μm was printed to connect the two pads. In this way, a conducting line which can be treated as a resistor (named as R1) was printed.

As-printed resistor R1 was kept in ambient conditions for over 100 days for stability observation. During this time, the TGME solvent appeared to slowly evaporate from the substrate. Also, color difference appeared between outer edges and middle portion of contact pads due to the ubiquitous “coffee ring effect" [68]. This effect is detrimental to component stability. Further, measurement of I-V response show that R1 has average resistance $\sim$ 4.89 GΩ.

Therefore, controlled annealing close to the boiling point of TGME is required to make the feature

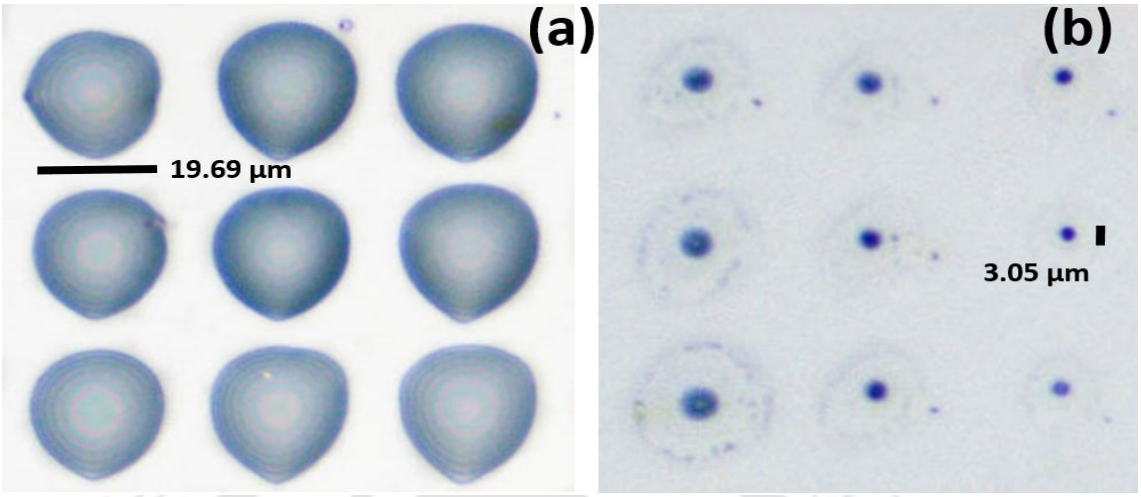

Fig. 2.4: Spots of 1.5% PANI-ES:DMSO on (a) PET sheet (b) PVA surface

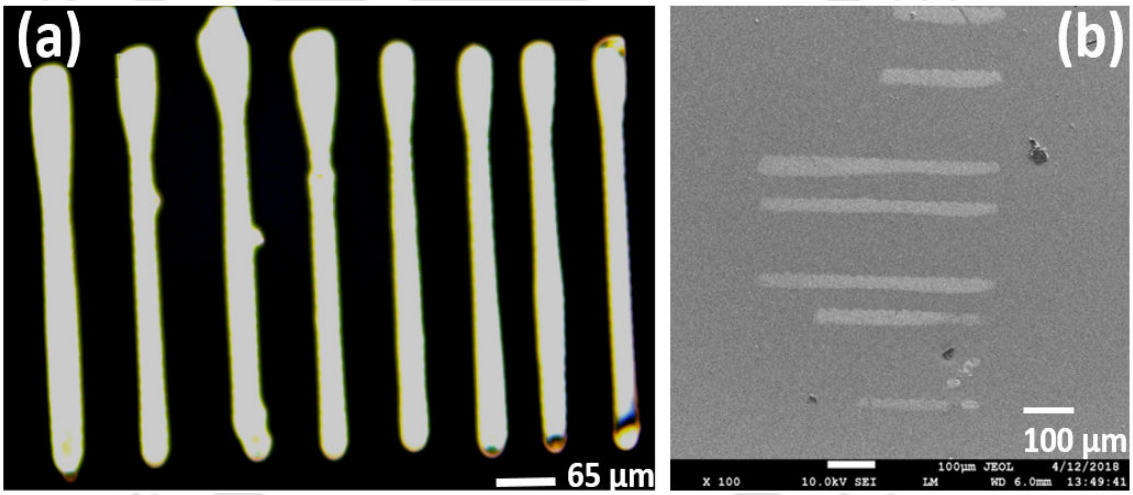

Fig. 2.5: (a) Optical image of parallel lines of AgNP ink over glass substrate (b) FESEM image of parallel lines of AgNP ink over ITO surface

electrically conductive, stable and reliable. Heating such small features suddenly at high temperature can expose them to high thermal stresses that can damage either the contact pads or the channel. The printed resistors were therefore gently annealed to avoid thermal stress. This post-processing procedure (refer sub-section F of section II) was followed on all further monolithic resistors printed using MCP.

It has been observed that a humidity level higher than 60% causes the ink from the reservoir to flow too fast onto the substrate. We have named this phenomenon as spillover. The blot on the substrate as a result of this spillover can itself be used as a reservoir of ink for further printing. The micro-cantilever tip can be dipped into the reservoir and prints can be achieved in a modified dip-pen printing technique, similar to dip-pen nanolithography (DPN) or polymer pen lithography (PPL) [69].

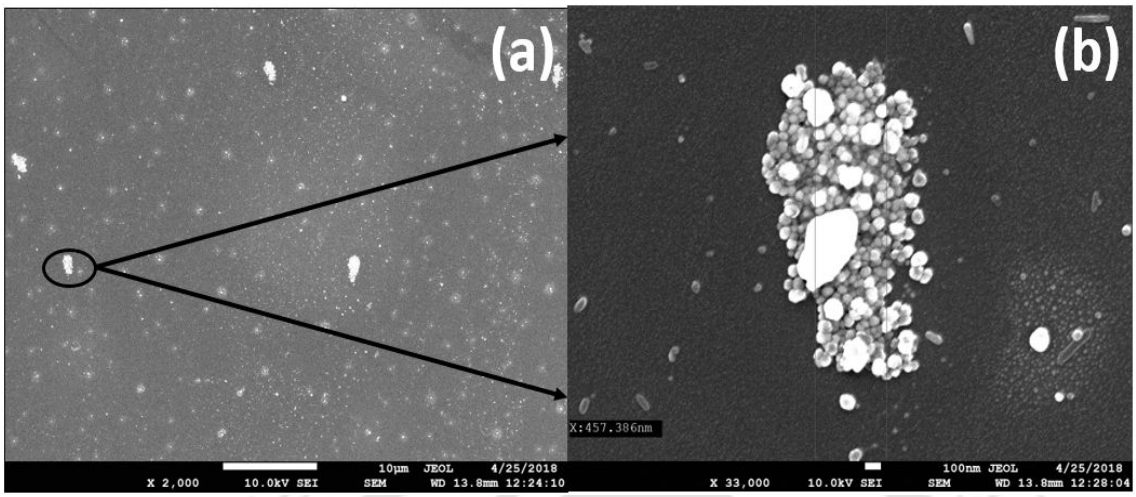

Fig. 2.6: (a) FESEM image of AgNP fine spots on glass. Scale bar = 10 μm (b) FESEM image of one of fine spots of AgNP with width $\sim$ 457 nm. Scale bar = 100 nm

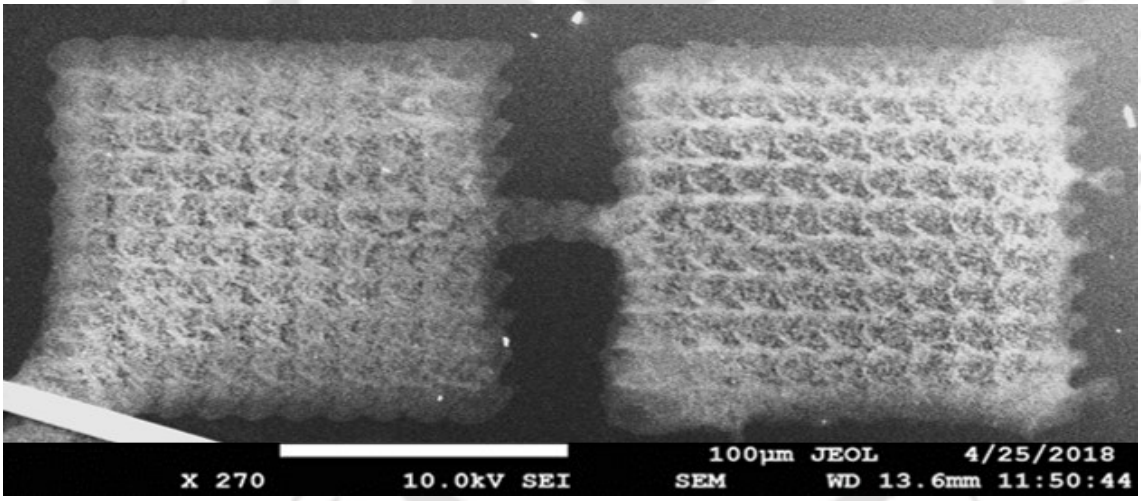

Fig. 2.7: FESEM image of AgNP pattern with smallest linewidth $\sim$ 17 μm on glass. Scale bar = 100 μm

However, disadvantage of such technique is the risk of drying the channel out between printing and dipping processes. Besides, uncontrolled spillover poses risk to the features that have been already printed on the substrate. Therefore, it can be concluded that 46-57% humidity range was suitable for the AgNP ink to maintain a fine flow of the ink to the micro-cantilever tip without spillover.

2.3.6 I-V characterisation of the printed resistors

This section deals with the I-V characterisation for the printed resistors. Multiple sets of monolithic resistors were printed and current-voltage characteristics of ten of these resistors were measured. Representative I-V responses of three of the resistors (R2, R3 and R4) are shown in Figure 2.9, where

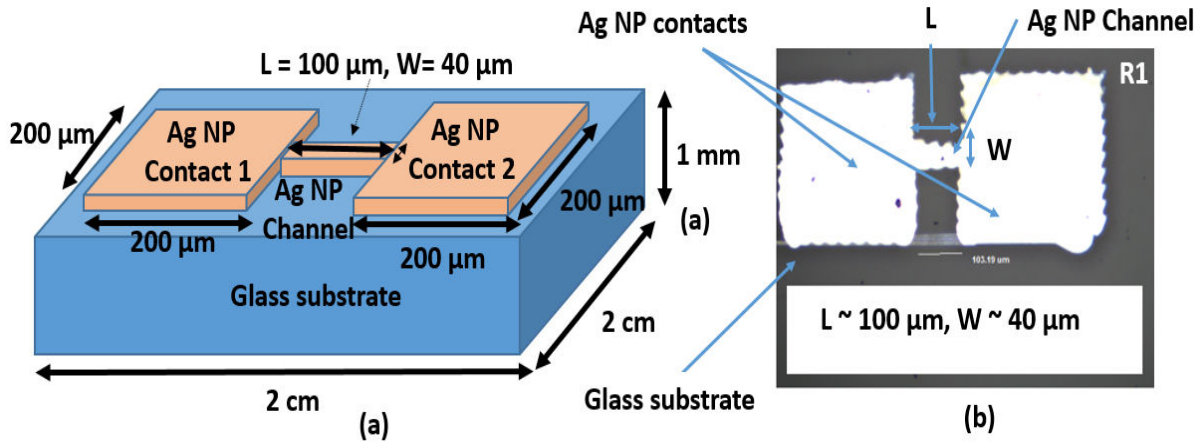

Fig. 2.8: (a) Schematic of the AgNP printed resistors (Dimensions shown in the figure are for R1 as an instance) (b) Top view of printed resistor R1

the current is normalized against cross-sectional areas of the channels and plotted as current density. The linear behaviour of the graph confirms the resistive nature of the printed feature.

Further, stability and reliability of the printed features was tested over extreme temperatures. Figure 2.10 shows the thickness normalised electrical performance of printed AgNP features from 200 K-358 K. It is observed that printed patterns are highly stable in this range and also show positive temperature coefficient (PTC) behaviour as expected from a AgNP thin film.

A brief summary of relevant characteristics of the ten resistors mentioned above is shown in Table 2.3. It can be seen that depending upon the length, width and thickness of the printed channel, the resistance of the feature can be controlled from a few tens of Ωs to a few KΩs.

2.3.7 Effect of thickness of printed devices

Thickness of a printed resistor would determine its electrical resistance, and consequently the range of current that flows through it. It is found that the MCP-printed resistors have thickness values near 100-350 nm and average resistance in order of few hundred Ω, whereas layers created as a result of spillover have thickness near 1-2 μm and average resistance less than 10 Ω for an applied voltage range of -0.5 V to 0.5 V at room temperature.

2.4 Mathematical model for current in printed resistors

The current model used to verify the experimental results for I-V of printed resistors has been expressed as

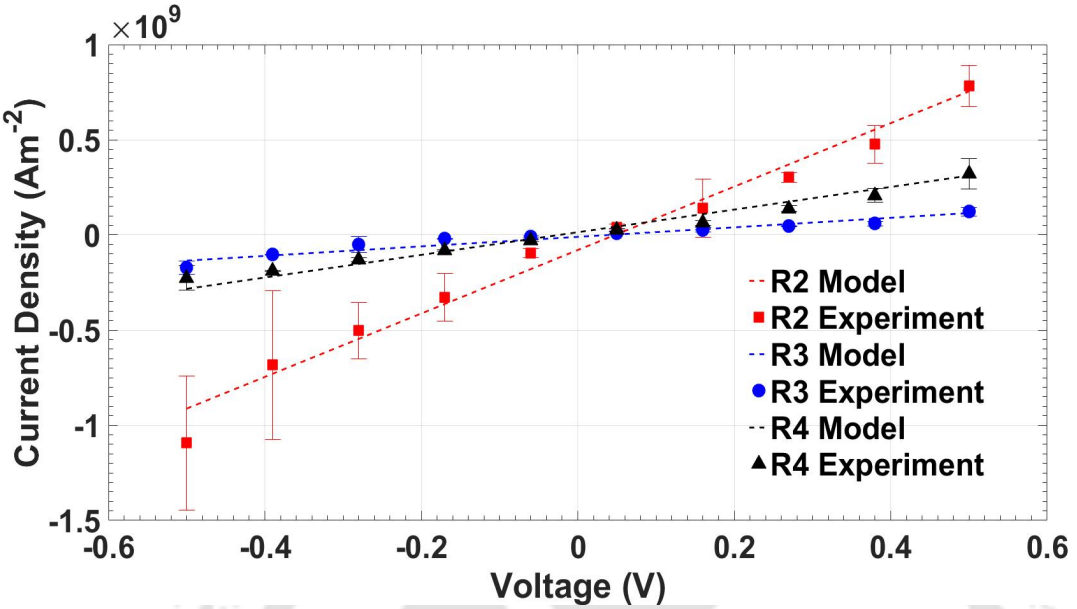

Fig. 2.9: Current density plot for resistive feature R2, R3 and R4

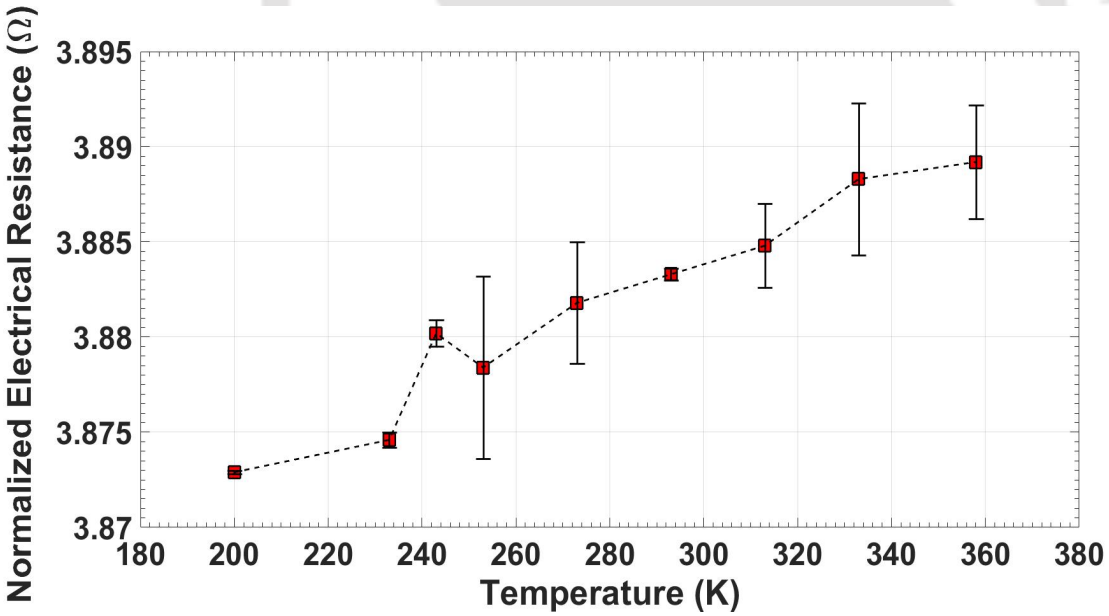

Fig. 2.10: Thickness normalized electrical performance of printed resistors over temperature

$$I = \frac{VWt\alpha}{\rho L} \Rightarrow J = \frac{I}{A} = \frac{V\alpha}{\rho L} \tag{2.3}$$

where, I and V are the current and applied voltage range, L and W are the length and width of the printed resistor, 't' is the thickness of the resistor, 'ρ' is the specific resistivity of the channel material and 'α' is the model fitting parameter to account for the variations in the conductivity of the printed

Table 2.3: A brief summary of printed resistors over glass using MCP

Feature	R1	R2	R3	R4	R5	R6	R7	R8	R9	R10
Approx. Length, Width (μm)	L = 100 W = 40	L = 100 W = 18	L = 100 W = 41	L = 200 W = 50	L = 200 W = 50	L = 200 W = 50	L = 200 W = 30	L = 350 W = 80	L = 80 W = 40	L = 120 W = 100
Avg. Thickness (nm)	140	350	300	353	386	360	302	64	65	140
Avg. Resistance	4.89 GΩ	120 Ω	448 Ω	131 Ω	224 Ω	100 Ω	86 Ω	4.6 KΩ	3.1 KΩ	600 Ω

resistors. J is the current density and A is the cross-sectional area of the printed resistors.

The value of 'ρ' used for model simulation is 2 $\mu\Omega$-cm as per datasheet [64]. It can be concluded from Figure 2.9 that model results are in close agreement with the experimental results.

2.5 Summary

In this chapter, micro-cantilever based precise printing approach was explored for printing customized micro-scale electronic components such as PANI-ES semiconductor arrays and Ag metal-nanoparticle based resistors. We have established that the MCP technique can provide a linewidth feature to particle size ratio of 340 for AgNP inks, which is five times finer than the typical inkjet printing ratios of 1800 [70, 71]. We have systematically presented the parameters that need to be evaluated for printing a novel material onto a given substrate. For example, for the particular combination of 60R SPT, AgNP ink and glass substrate, particle size of a few nanometers, ink viscosity below 20 cP, chamber humidity below 60% and an ink-substrate contact angle of about 20° were found to be the optimal conditions for achieving cohesive, stable printed features. Further, thickness of the printed features below 100 nm and linewidth about 80 μm and slow annealing at 200°C were necessary to achieve features with resistance values in kΩ range.

I-V characterisations show that printed resistors of AgNP ink have average resistance in order of few hundred Ω to few kΩ depending on the thickness of their printed channel with an applied voltage range of -0.5 V to 0.5 V. A simple current model was developed to verify the experimental results for I-V of the printed resistors. The model results show close agreement (R^2=0.9988) with the experimental results.

Our analysis has shown that the MCP technique is a unique method that is highly effective for printing on-demand patterns on a variety of substrates, using metallic or organic semiconductor inks. The MCP technique is applicable to printing of biomolecules, carbon based nanoparticles and polymers. The niche use of this technique can be found in rapid prototyping of precise monolithic electronic

circuitry elements such as resistors and transistors. It can also help for printing conductive polymer arrays with microscale spot sizes. The circuit elements so printed can be used as sensors for personalised biomedical and translational medicine applications.

3

Printed Micro-Resistors Using Silver Nanoparticles (AgNP)

Contents

3.1 Introduction

In this chapter, the insights gained from the fundamental analysis of different aspects of MCP, have been used for detailed printing, electrical characterization and analysis of AgNP micro-resistors using different modes of printing techniques based on MCP.

In recent years, printed electronics has emerged as a prominent alternative to the conventional photolithography based microelectronic fabrication technology to fabricate electronic devices such as resistors, capacitors, inductors, thin-film transistors (TFT), organic and in-organic field-effect transistors etc. [45, 58–60]. The electronic devices fabricated with printed electronics have been successfully applied in the field of sensors [72], RFID applications, displays, photovoltaics, electronic circuits and memory-device fabrication [30–35]. Among mainstream printing technologies, the inkjet printing technology (IPT) has attracted scientific community the most owing to its additive manufacturing process which can be carried out at low-cost [73], lower temperatures [58], non-vacuum environment [37,45,46]. Moreover, IPT is maskless technology [33], has reduced number of steps [58], is less wasteful [45] and eco-friendly [60].

To fabricate any electronic circuit, we need to fabricate the passive components like resistors, capacitors, inductors at the outset. There have been several reports on the fabrication of passive electronic components using IPT. Jung et al. [33] used IPT to print poly(3,4-ethylenedioxythiophene) polystyrene sulfonate (PEDOT: PSS) based resistors and have investigated the effect of additives and over-printing on the conductivity of the printed resistors. Garret et al. [37] used poly 4-vinylphenol (PVP) ink as a dielectric layer and AgNP ink as the conductor to fabricate inductors and capacitors using IPT. Similarly, Sternkiker et al. [38] demonstrated the manufacturing of inductor coils, capacitors and rectifying diodes using silver ink as conducting layer, PVP as a dielectric layer and PEDOT: PSS as a semi-conducting layer. In all the above reports, the emphasis was given on fabrication of either capacitor, inductor or diode but none of the reports detailed the fabrication of a printed resistor. Moreover, most of the printed features have dimensions in 'mm' range. There are few reports which discuss the various aspects related to the fabrication of printed resistors [33, 49, 58, 60, 74] but these printed resistors have dimensions in 'mm' range, focus more on device application and lack in-depth analysis for various physical and chemical parameters involved in the fabrication process. Therefore, being the basic element of electronic circuitry, the printed resistor fabrication area needs much higher attention from the research community.

In this work, we have utilised a micro-cantilever based printing technology (MCP) [22]. MCP like IPT is also an additive manufacturing technology which is processed at low cost, lower temperatures near room temperature, does not requires vacuum, is maskless and eco-friendly [2]. We have developed three different printing techniques within MCP named as SOP, DIPSOP and SDP. A detailed electrical characterisation based analysis has been reported for printed structures from each of printing techniques for comparison. Silver nanoparticle (AgNP) ink dispersion with average particle size of 50 nm have been utilized to print microstructures of size $\sim$ 50 μm over substrates like glass, polyethylene terephthalate (PET) and silicon. Moreover, we have used only AgNP ink for complete device fabrication in order to avoid any interfacial irregularities at the nano-scale. To the best of our knowledge, this for the first time that the printed micro-resistors of AgNP ink as a single material electronic device (SMED) has been reported to be fabricated using SOP, DIPSOP and SDP printing techniques based on micro-cantilever based printing technology.

The experiments are started by printing two square-shaped contact pads back to back and a rectangular channel of AgNP ink (used in chapter 1) connecting both contact pads over a cleaned coverslip glass substrate to act as a PMR with channel length and width being in μm regime. Such resistor has no issues of contact resistance and interface-mismatch, as contact pads and the main channel region, have been fabricated with the same material. Figure 3.1 shows fabrication steps of the proposed device using the top view of the optical image of PMR. The printed features are annealed gently till 200°C and their electrical characterization is performed using DC probe station (DCPS) as shown in Figure 3.1. The process of annealing is necessary for PMR fabrication as DC probing is carried out only for properly dried samples. The substrate is rinsed with de-ionised (DI) water and isopropyl alcohol (IPA) for two to three times and blow-dried with nitrogen. Before use, it is treated in UV/O_3 environment for 30 minutes for cleaning. The detailed printing process of SOP, DIPSOP and SDP based PMRs have been reported in Appendix A and conceptual diagrams of respective technique is shown in Figure 3.2 and Figure 3.3.

3.2 SOP, DIPSOP and SDP based AgNP PMRs

The fabrication of MCP based PMRs of AgNP is tried over various substrates such as silicon and PET but the best results are obtained for glass substrate. Figure 3.4 show the representative SOP, SDP and DIPSOP PMRs on glass after annealing and electrical characterization.

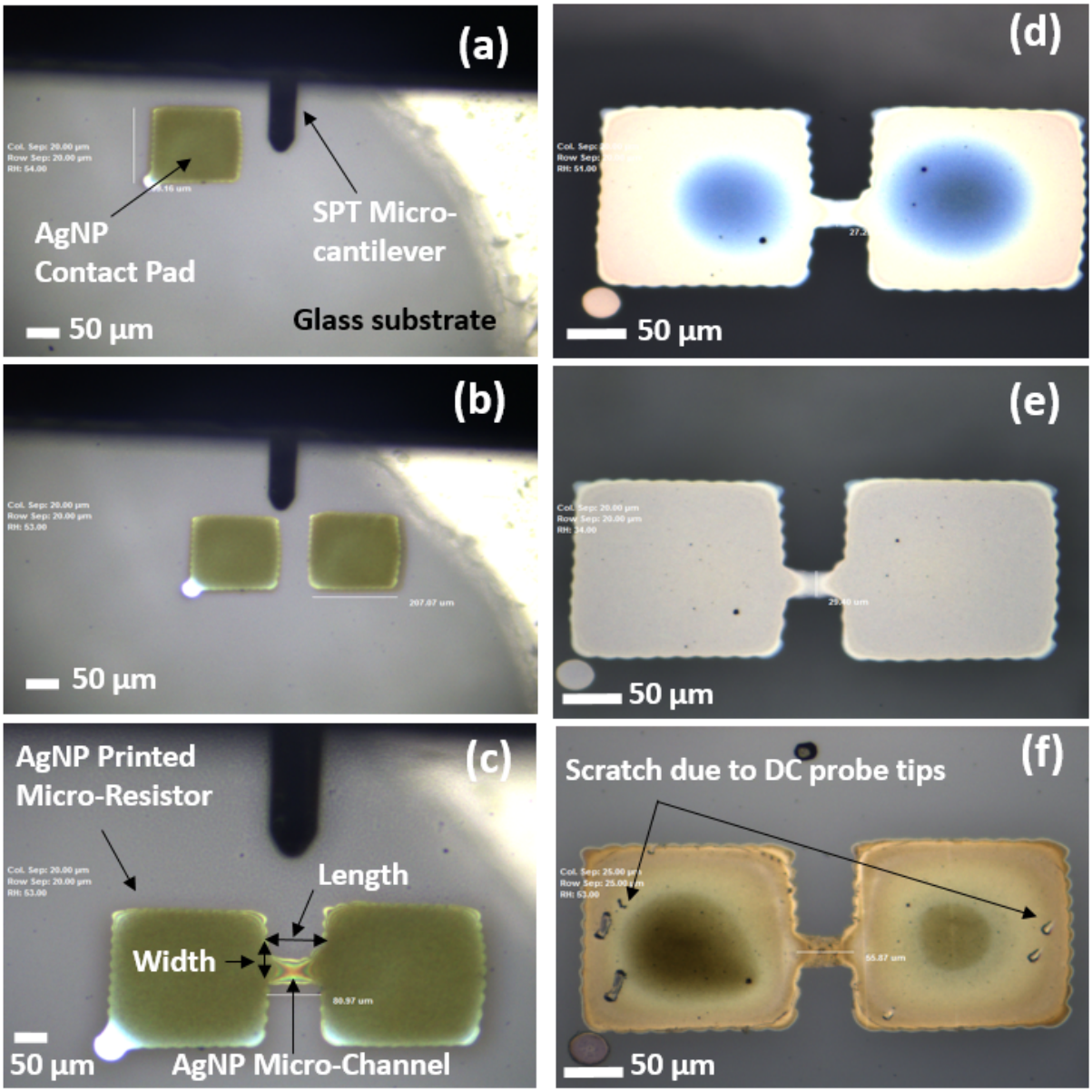

Fig. 3.1: Fabrication steps of the proposed PMR (a) Left electrode fabrication (b) Right electrode fabrication (c) AgNP channel bridging two electrodes to complete first level of PMR fabrication (d) PMR after 1 hour from printing (c) PMR after annealing (d) PMR after electrical characterization after 1 year

It is observed from Figure 3.1(f) and Figure 3.4(b,e and f) that proposed PMR show good structural stability even after 1 year from print. Table 3.1 details the minimum feature size and print resolution for different printing techniques as shown in Figure 3.5 and Figure 3.6 respectively.

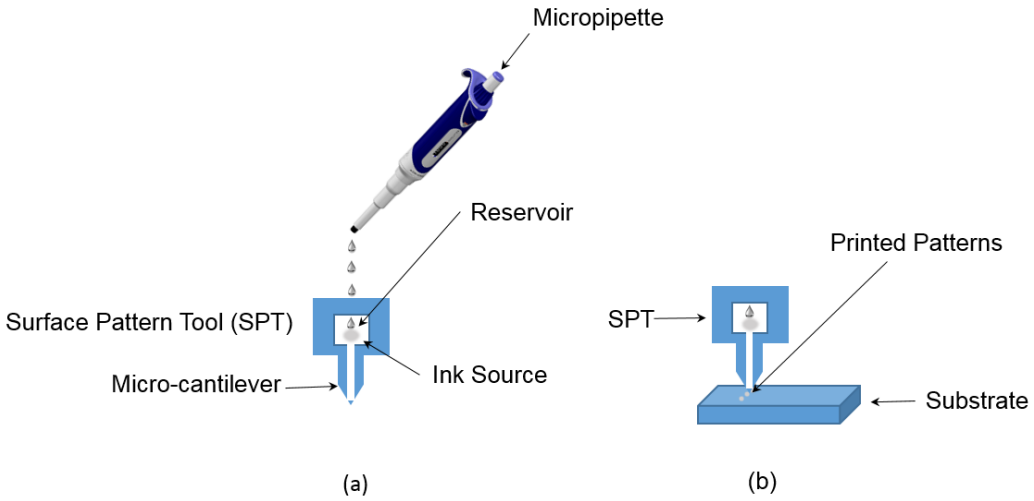

Fig. 3.2: (a and b) Schematic diagrams showing the printing steps of SOP

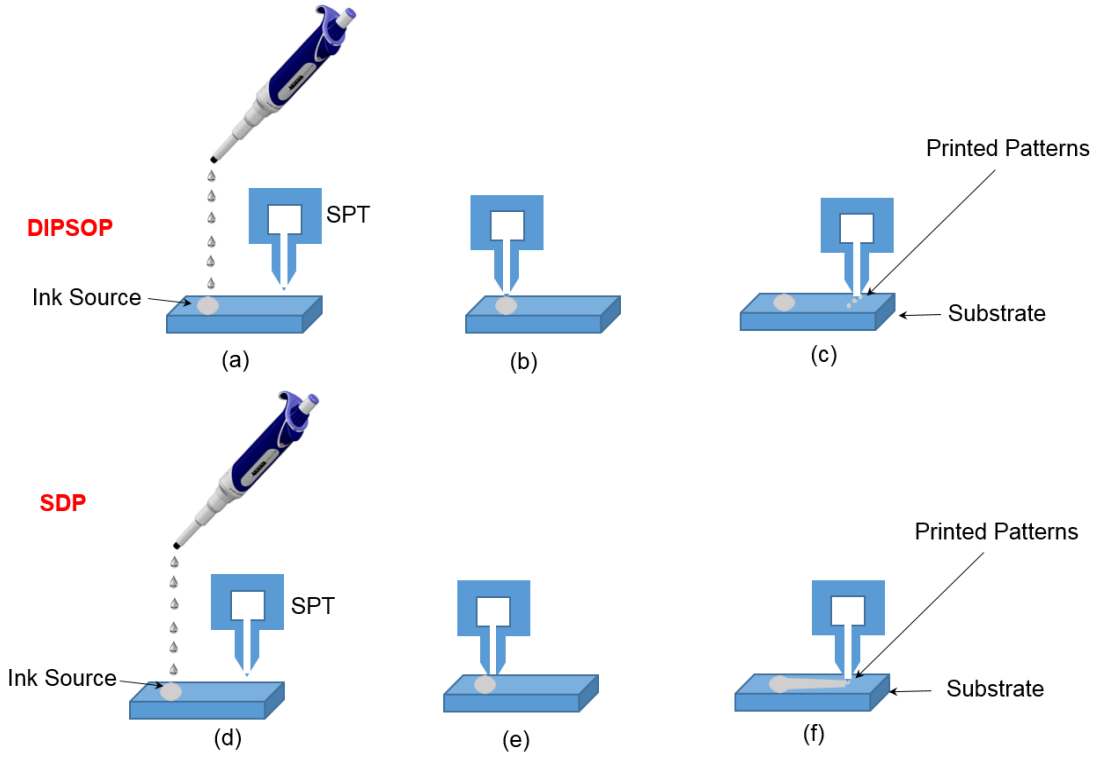

Fig. 3.3: (a,b and c) Schematic diagrams showing the printing steps of DIPSOP (d,e and f) Schematic diagrams showing the printing steps of SDP

3.2.1 Comparison between SOP, DIPSOP and SDP

The micro-resistors printed with SOP technique have lower edge roughness, proper thickness and dimensions in micro-to-nanometer regime with average electrical resistance, R varying in the range of few hundred ohms as seen in Table 7.2. SOP has a continuous supply of ink that can print comparatively

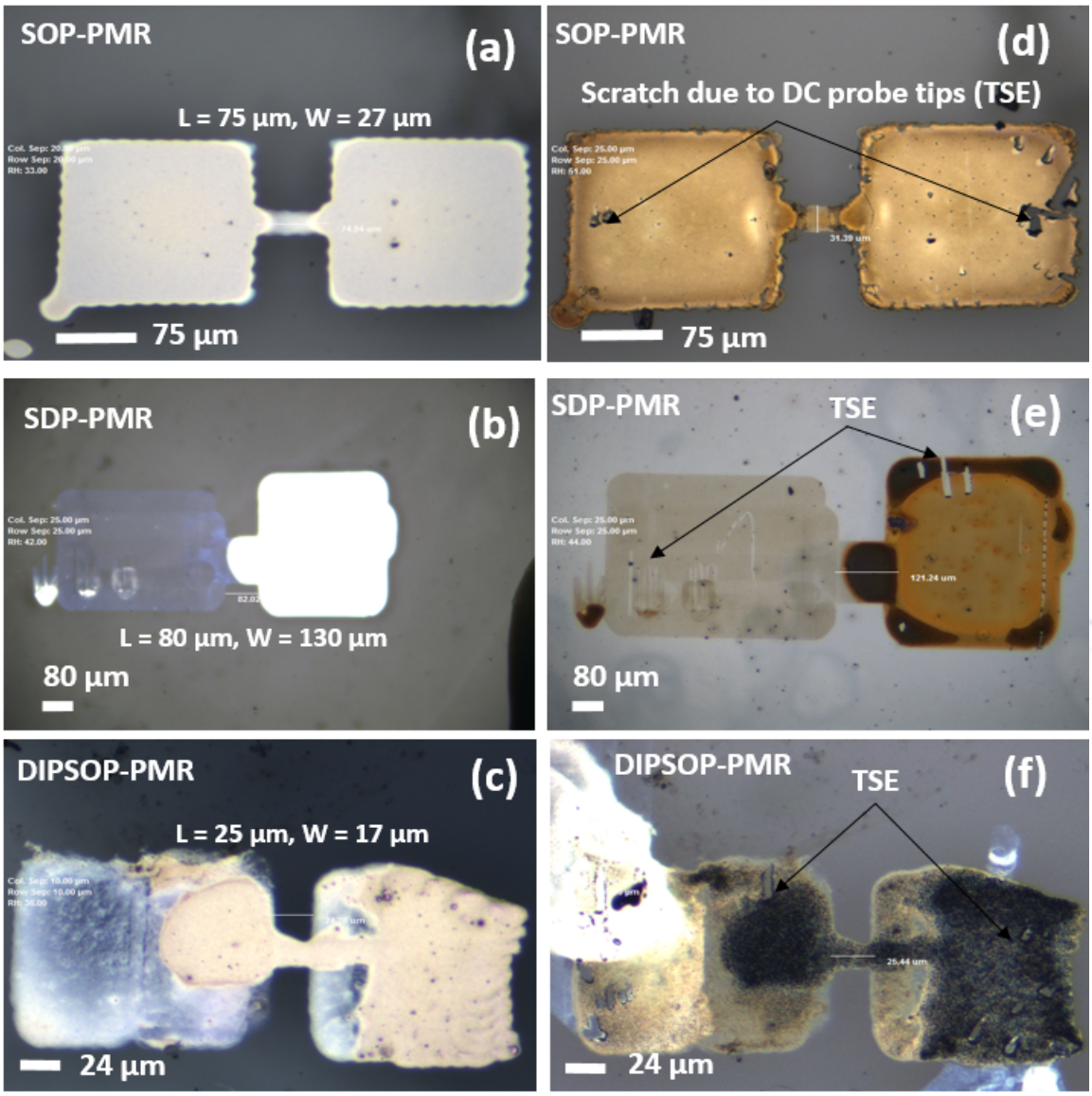

Fig. 3.4: Representative SOP, SDP and DIPSOP PMRs on glass (a, b and c) after annealing (d, e and f) after electrical characterization after 1 year from print

large number of PMRs in one go, once the ink starts flowing through the micro-cantilever channel in spite of being relatively slow. However, SOP can only be performed if the SPT micro-cantilever channel is properly cleaned and the ink satisfies certain physico-chemical pre-requisites. Moreover, SOP has the highest possibility of facing spillover of ink. On the other hand, DIPSOP is the most reliable printing technique as it ensures the repeatability of the printed structures. DIPSOP can be performed with almost any ink which can be withdrawn by SPT micro-cantilever. However, DIPSOP is the slowest among the three printing techniques because the structures printed using DIPSOP have larger edge roughness and the ink needs to be withdrawn from local ink reservoir at regular intervals. SDP print

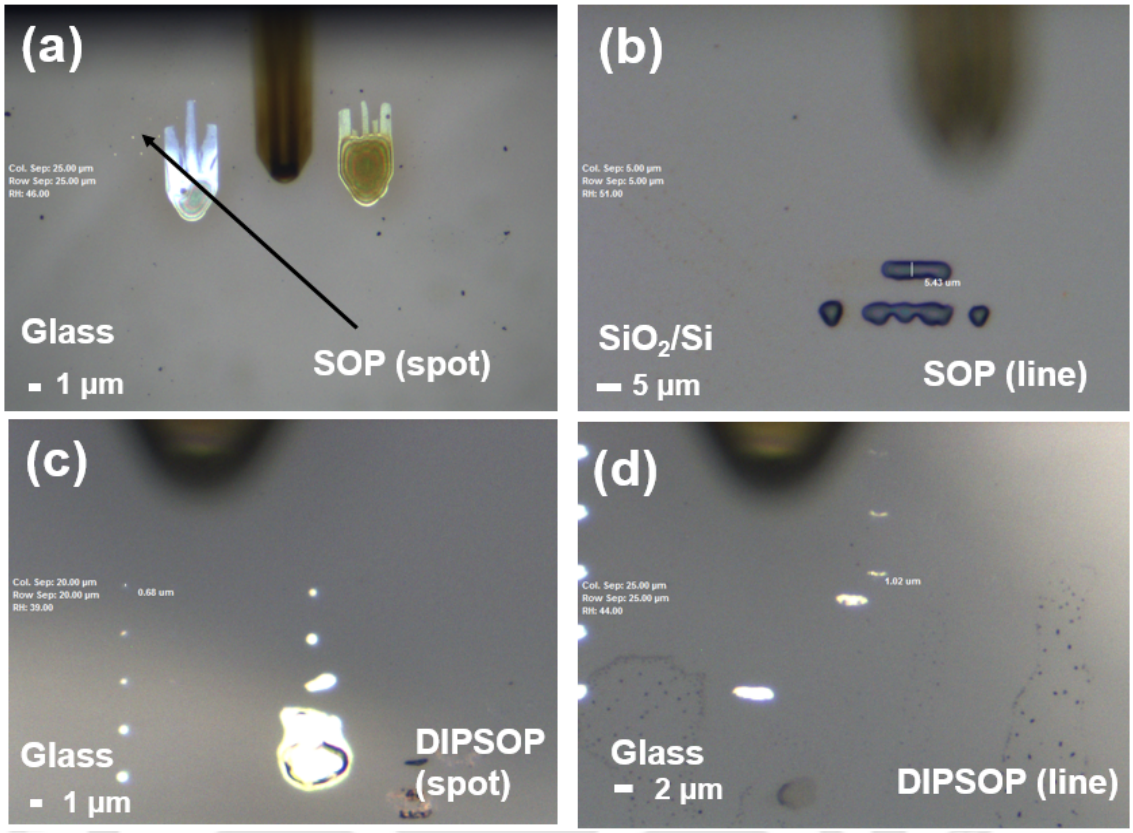

Fig. 3.5: Optical image showing minimum feature size for different printing methods (a) SOP-spot with dimensions near 0.46 μm (b) SOP-line with width near 5.43 μm (c) DIPSOP-spot with dimensions near 0.68 μm (d) DIPSOP-line with linewidth near 1.02 μm

Table 3.1: Table for minimum feature size and print resolution

	SOP	**DIPSOP**	**SDP**
Minimum Feature size (μm)	0.46 (S,G) 5.43 (LW,G)	0.68 (S, G) 1.02 (LW,G)	1.8 (LL,Si)
Print Resolution (μm)	1.9 (G)	1.92 (G)	1.8 (Si)

S: Spot, LW: Linewidth, LL: Length of line, G: Glass, Si: SiO_2/Si

technique has the advantage of printing features at a faster rate with low line edge roughness, however, it requires fast and constant ink flow rate which is very difficult to be maintained by SPT reservoir for a longer period owing to various physical and chemical limitations. Additionally, SDP has the least chances of spillover as it ensures that only micro-cantilever of the SPT touches the surface of the substrate.

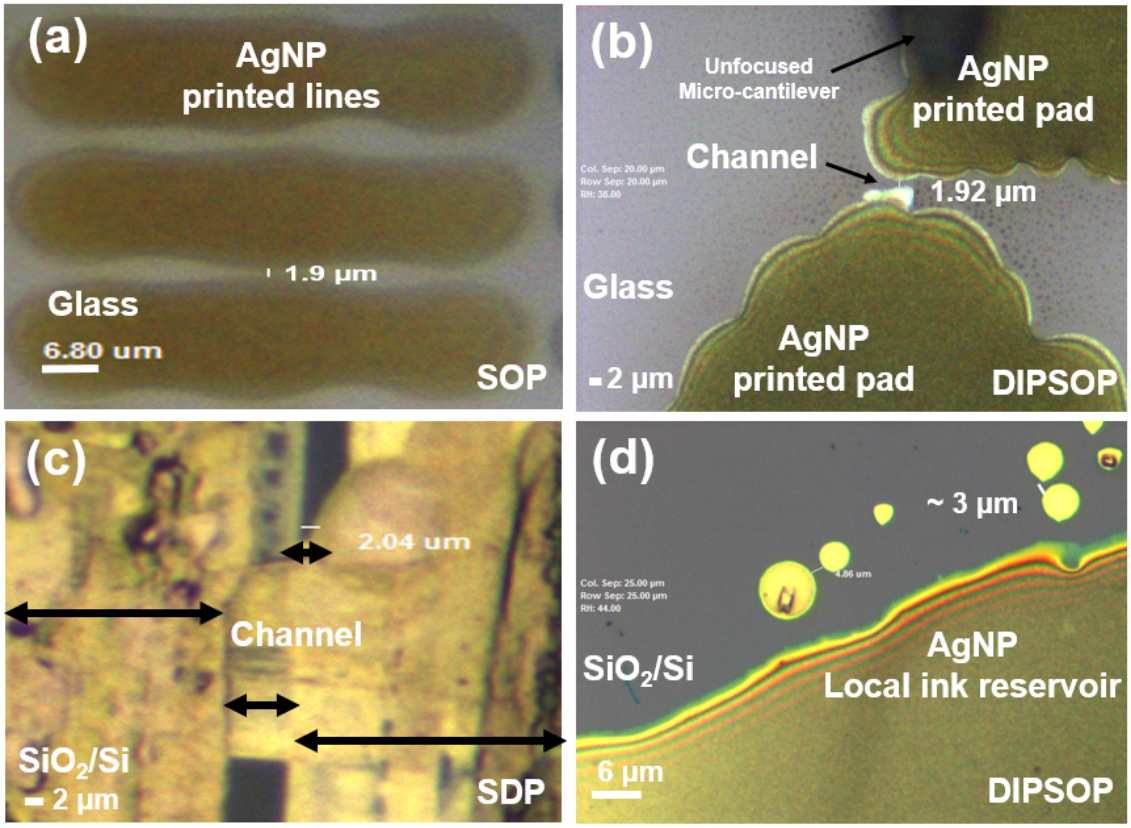

Fig. 3.6: Optical image showing printing resolution for different printing methods (a) printing resolution of 1.9 μm achieved by SOP on glass substrate (b) printing resolution of 1.92 μm achieved by DIPSOP on glass substrate (c) printing resolution of 1.8 μm achieved by SDP on SiO2/Si substrate (d) printing resolution of 3 μm achieved by DIPSOP on SiO2/Si substrate between two spots

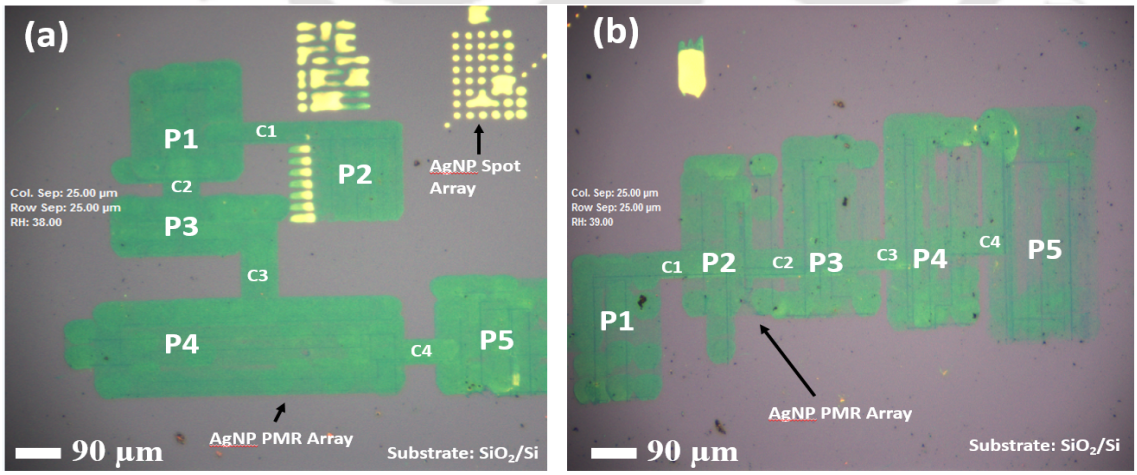

Fig. 3.7: SDP-PMR arrays of AgNP on SiO_2/Si substrate after annealing (a) Initial set of PMRs (b) Second set of PMRs. P1 to P5 are contact pad regions and C1 to C4 are PMR channel regions in both figures

Table 3.2: Surface roughness parameters, R_q and R_a for each printing method, number of printed layer, W and L

Analysis Parameters	Printing techniques			Number of Printed Layers			Channel width (W), L = 30 μm		Channel length (L), W = 30 μm	
	SDP	SOP	DIPSOP	1	3	5	W_1 = 12 μm	W_2 = 45 μm	L_1 = 106 μm	L_2 = 166 μm
R_q (nm)	12.1	18.7	30.5	30.5	31.6	36.9	83	93.4	31.8	33.8
R_a (nm)	8.83	14.1	24.3	24.3	25.5	29.5	67	76.3	25.6	24.7
Scan Range (μm × μm)	5 × 5	5 × 5	5 × 5	5 × 5	5 × 5	5 × 5	5 × 5	5 × 5	5 × 5	5 × 5
Substrate	SiO_2/Si	Glass	Glass	Glass	Glass	Glass	Glass	Glass	Glass	Glass

3.3 Results and Discussions

3.3.1 Effect of annealing on PMRs and Tip scratch effect (TSE)

Electrical characterisation is performed for a drop-casted AgNP layer and a SOP-PMR with channel length and width of 220 μm and 30 μm respectively, to analyse the effect of annealing on the electrical behaviour of the PMRs. Figure 3.10(a and b) show the I-V characteristics of drop-casted AgNP layer for a voltage linear sweep of ± 1 V, before and after annealing respectively. It is observed that the current increases from ± 2 μA to ± 0.1 A after annealing. Figure 3.10(c) shows that unannealed SOP-PMR is conducting, however, the current varies non-linearly with voltage. This is because the sample is not completely dried and liquid content results in sudden fall and rise in the current values. Figure 3.10(d) shows the I-V characteristics of SOP-PMR after optimized drying and annealing. It is observed that the process of annealing removes the non-linearities and improves the conductivity of the PMR.

It is observed that the printed ink of the unannealed resistors has weak adhesion to the glass substrate as the printed area which comes into the contact of the DC probe tips gets scratched during electrical characterization of these resistors. This phenomenon has been named as tip scratch effect (TSE) as seen in Figure 3.1(f) and Figure 3.4(b). Therefore, to avoid TSE, proper annealing of the printed structure is the foremost requirement. However, heating these micro-structures suddenly at higher temperatures can introduce thermal stress that can be detrimental to the device structure. Therefore, PMRs are annealed gently at a rate of 2°C per minute from 50°C till 200°C [22]. Further, the thickness of the printed feature needs to be high (> 1 μm) to avoid TSE. The non-uniform thickness caused by TSE can be minimized by proper selection and pre-treatment (like exposure to UV-ozone) of the substrate, through which its adhesiveness with the printed layer after annealing can be improved. Other solutions can be the deposition of multiple layers of the ink over the contact pads and the channel

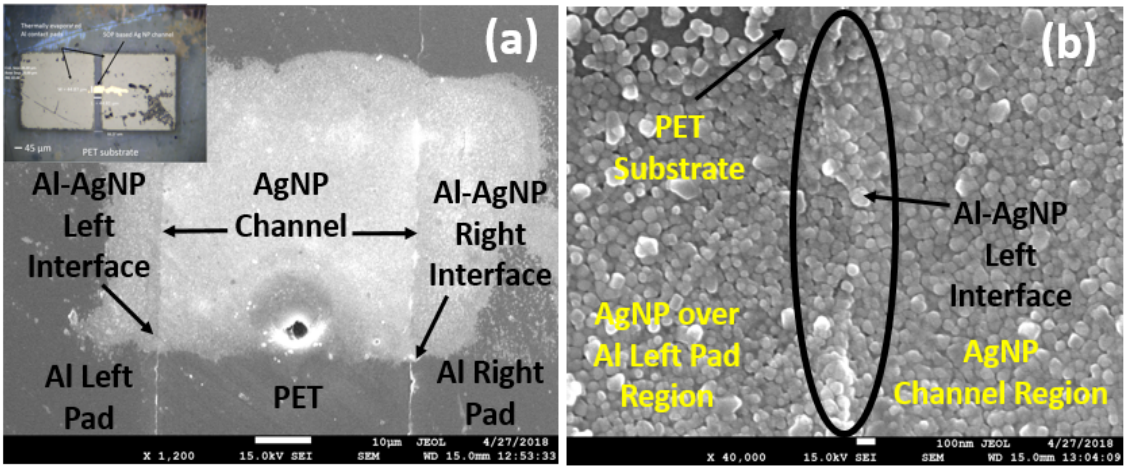

Fig. 3.8: (a) Field-emission scanning electron microscope (FESEM) image (Make: JEOL, Model: JSM-7610F) showing Al-AgNP interfaces along with AgNP channel region with a scale bar of 10 μm. Inset shows the optical image of PMR on PET (b) FESEM image showing the Al-AgNP left interface of (a) with a scale bar of 100 nm

region to increase the thickness of the printed structure to resist TSE or to fabricate the contact pads through silicon micro-fabrication technology and connect them using MCP based printing techniques as shown in Figure 3.8.

3.3.2 Methods for print-thickness control

It is important to control the thickness of printed features as their resistance is mostly determined by thickness. Print-thickness can be controlled by optimizing the position of micro-cantilever from the substrate using NanoWare software in such a way that micro-cantilever touches the substrate as per the requirement of thickness. The SPT micro-cantilever is made to hit the substrate hard to deploy a larger volume of ink if higher print-thickness is required while micro-cantilever has just to touch the substrate gently to deposit a thin layer of ink. The print-thickness can also be controlled by optimizing several other parameters such as substrate response to the ink particles, quality of ink in terms of its particle-size, viscosity, the evaporation rate of solvent, effect of printing environment [22]. For higher thicknesses, multiple deposition-annealing cycles can be carried out i.e. after a feature is printed and annealed, the printer can be used to re-deposit the ink on the exact same spot using the X-Y movement of stage. For further hardware modification, a micro-heater enabled stage can provide in-situ annealing to the printed features to make the process faster and more accurate. Moreover, there are different varieties of SPT with different widths of micro-channel such as 5 μm, 10 μm and 20 μm, which can be used to print features with controlled thickness once the above-mentioned parameters are optimized.

3.3.3 Analysis of uniformity of thickness for PMRs

The thickness of the PMRs is measured by a Veeco DEKTAK 150 profilometer. The analysis of uniformity of thickness for different printing techniques, is based on the surface roughness data obtained from Atomic Force Microscopy (AFM) [Make: Bruker]. Mutilple AFM scans are performed on the PMRs with different scan ranges like (50 X 50) μm, (20 X 20) μm, and (5 X 5) μm and the least value of the roughness parameter has been noted down. For this analysis, R_a (arithmetic average roughness) and R_q (root mean squared roughness) have been considered as parameters for surface roughness. Table 3.2 shows the least values of R_q and R_a for each printing method, the number of printed layer, W and L. It is observed that SDP-PMRs have the least surface roughness (i.e. highest uniformity of thickness) followed by SOP-PMRs. SDP technique performs the printing in one go and the micro-cantilever remains in continuous contact with the substrate and uniformly distributes the ink in the desired shape and size of the feature similar to polishing the substrate with the ink layers. On the other hand, the SOP technique prints continuous structures by partially overwriting a spot over the previous spot. As a result, some minor non-uniformity is introduced in the overlapped region between the two successive spots due to the diffusion of ink molecules in the two spots. However, in SOP mode, the ink supply through the micro-cantilever channels is not interrupted during the printing process. Hence, the ink-density is nearly uniform for each printed spot. However, in DIPSOP technique, the ink needs to be refilled after printing a certain number of spots and usually the ink-density decreases slightly with each printed spot. Therefore, least uniformity of thickness is achieved with DIPSOP technique comparatively. However, with optimization of physical and chemical properties of the ink and its interaction with the substrate, and several other parameters [22, 30, 33], surface roughness can be minimized. Figure 3.15 and Figure 3.16 shows the corresponding AFM images for different printing methods, different number of printed layers and different dimensions discussed above for uniformity of print-thickness respectively.

3.3.4 Electrical characterisation of AgNP printed micro-resistors

This section discusses the I-V characterisation for the above-printed micro-resistors. DC probe station of Lakeshore cryotronics (Model: CPX) and EverBeing (Model: BD6) was used along with Keithley 4200A-SCS Parametric Analyzer [61] to probe the printed resistors. Figure 3.9(a) shows the I-V characteristics of the spillover AgNP layer over the glass, SiO_2/Si and polyethylene terephthalate

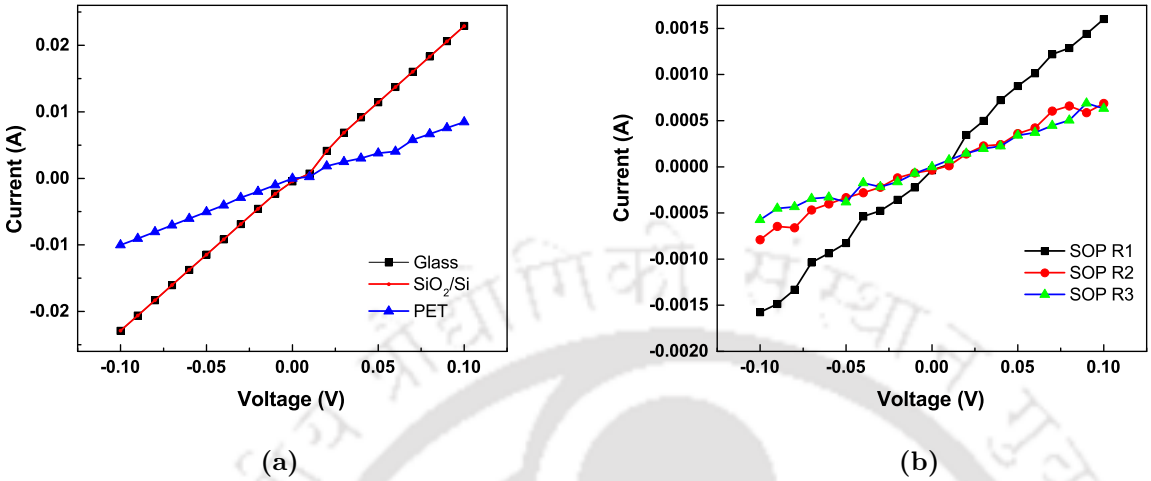

Fig. 3.9: (a) I-V characteristics of AgNP spill layer over different substrates (b) I-V characteristics of representative SOP-PMRs after annealing

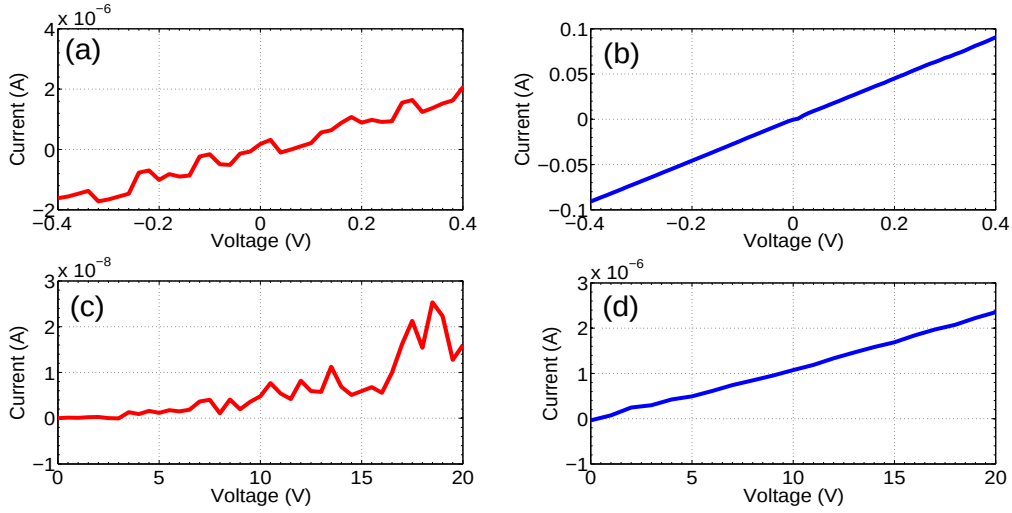

Fig. 3.10: I-V characteristics of drop-casted layer of AgNP ink on glass (a) before annealing (b) after annealing. I-V characteristics of SOP-PMR on glass (c) before annealing (d) after annealing

(PET). The I-V curve of AgNP spill layer on glass has been used as a reference to compare the I-V characteristics of the SOP, DIPSOP and SDP based PMRs on the glass. It has been measured that AgNP spill layer on glass has R of 4.4 Ω. The reason behind such low R and higher current of the AgNP spill layer is its higher thickness and surface uniformity. Figure 3.9(b) shows the I-V characteristics of SOP-PMRs on the glass substrate. It is observed that current varies in the range of -1.67 mA to 0.573 mA for an applied voltage linear sweep of ± 0.1 V while the measured R, varies in range of 94 Ω to 224 Ω. Figure 3.11(a) shows the I-V plot for SOP R4 for different levels of probe

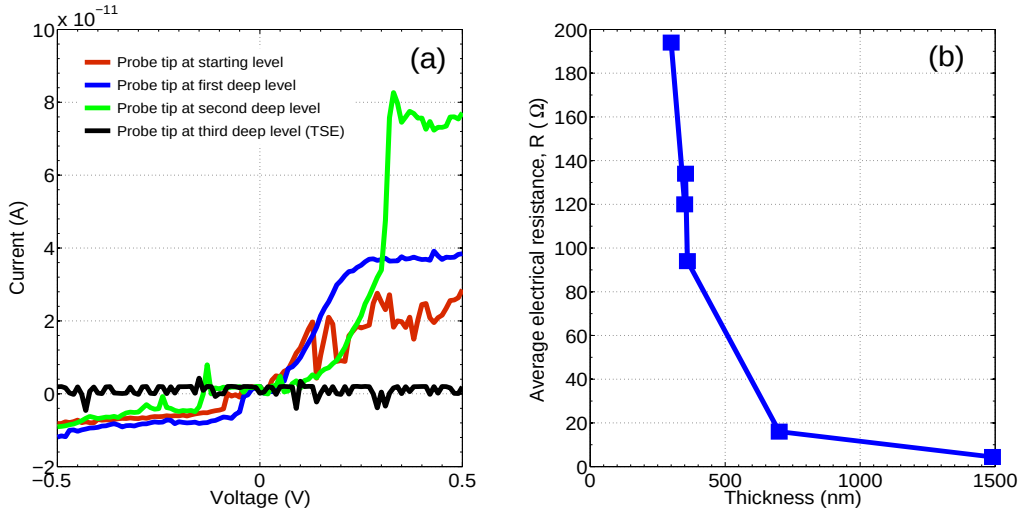

Fig. 3.11: (a) I-V characteristics of AgNP SOP R4 on glass surface at different levels of dc probe tip adjustment indicating a bad contact (b) Plot of measured average electrical resistance of PMRs against their thickness

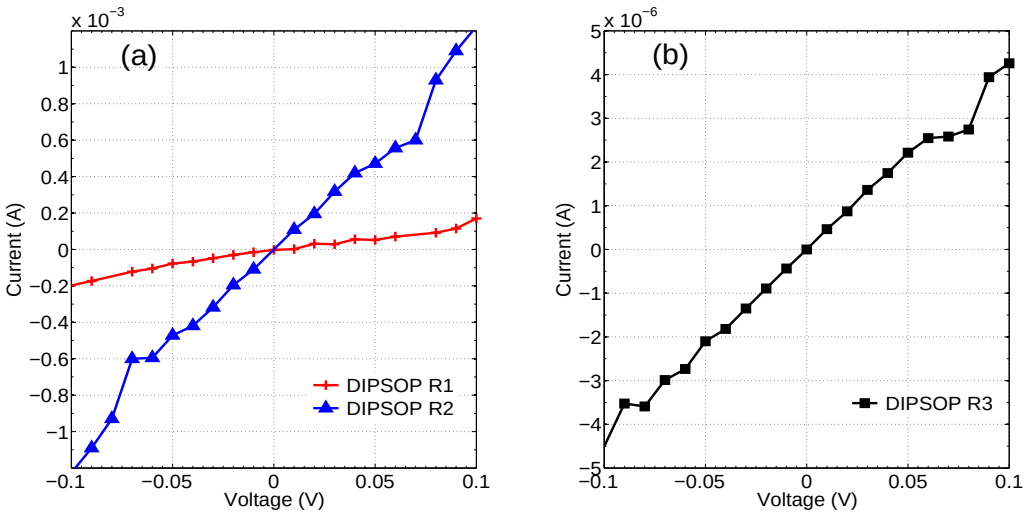

Fig. 3.12: I-V characteristics DIPSOP-PMRS after annealing

tip adjustment. It is observed that as the probe tip is forced more deep into the device, current initially increases but as the tip is forced further deep into the device, TSE occurs (Figure 3.13(a)) and device starts exhibiting non-conducting behaviour. Therefore, proper tip adjustment is also a crucial parameter to achieve the desired characteristics for the electrical characterization of a bare printed resistor. However, Figure 3.11(a) shows that current varies non-linearly with the applied voltage and gets saturated after a certain voltage in the first three cases which are free from TSE. The probable reason for such non-linear behaviour seems to be the non-uniform surface of the glass substrate and

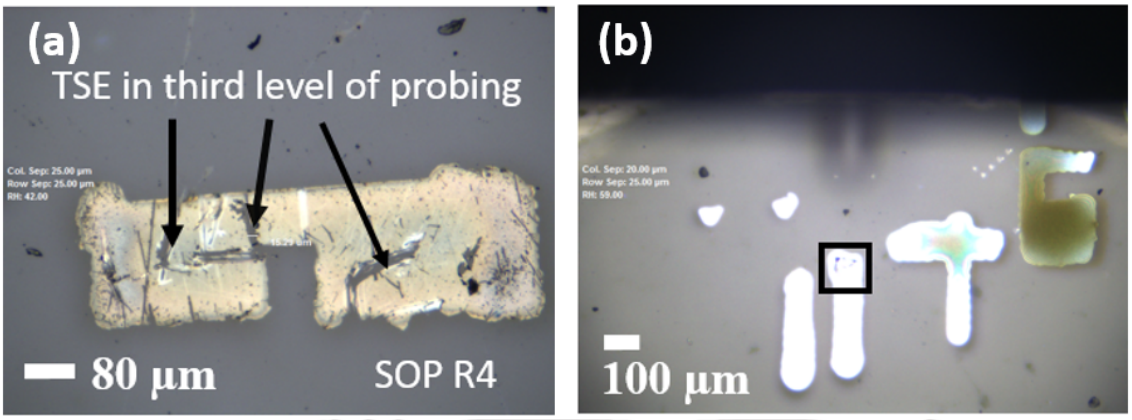

Fig. 3.13: (a) Optical image showing TSE effect seen in SOP R4 on glass in third level of probing (b) Optical image showing 'IITG' printed using SOP technique over glass substrate

PMR. Figure 3.13(b) shows the printing of 'IITG' using SOP technique over coverslip gass. The inset-region in Figure 3.13(b) has been used for study of surface uniformity of SOP-printed stucture after annealing. Figure 3.11(b) shows a combined plot of measured R of the PMRs against their thickness. It is verified that R decreases with increasing the print-thickness. The resistivity of PMRs on glass having R in Ω-range is computed using standard formula, $\rho = \mathrm{RWt/L}$, where R is the average electrical resistance, W is the channel width, L is the channel length and t is the print-thickness of PMR. The order of the resistivity is same for all the PMRs which is 10^{-5} Ω-m, with variation in magnitude from 1.22 to 5.4. This variation is observed probably due to higher surface roughness of the PMRs which results into the surface scattering of the charge carriers and subsequent variation in resistivity [75, 76].

Figure 3.12 shows the I-V characteristics of representative DIPSOP-PMRs. The measured R varies in range of 120 Ω and 194 Ω with a current variation of ± 0.2 mA to ± 1.2 mA for an applied voltage sweep of ± 0.1 V in DIPSOP R1 and DIPSOP R2. However, some PMRs such as DIPSOP R3 have comparatively higher R of 24 kΩ with a current variation of ± 0.004 mA for the same applied voltage range. The probable reason can be its thinner channel region and higher surface roughness. The SDP based printing technique is optimised and the ink is properly distributed over the two contact pads and the channel by the SPT micro-cantilever to achieve uniform thickness throughout the device. Figure 3.14 shows the electrical response of SDP R1. The current varies from ± 6 mA (with an R of 16 Ω) for a voltage linear sweep from ± 0.1 V. This result establishes SDP technique as a potential technique to print micro-structures of required dimensions and desired functionality. Moreover, the linear variation of current with applied voltage in the I-V plots of each printing technique validates our

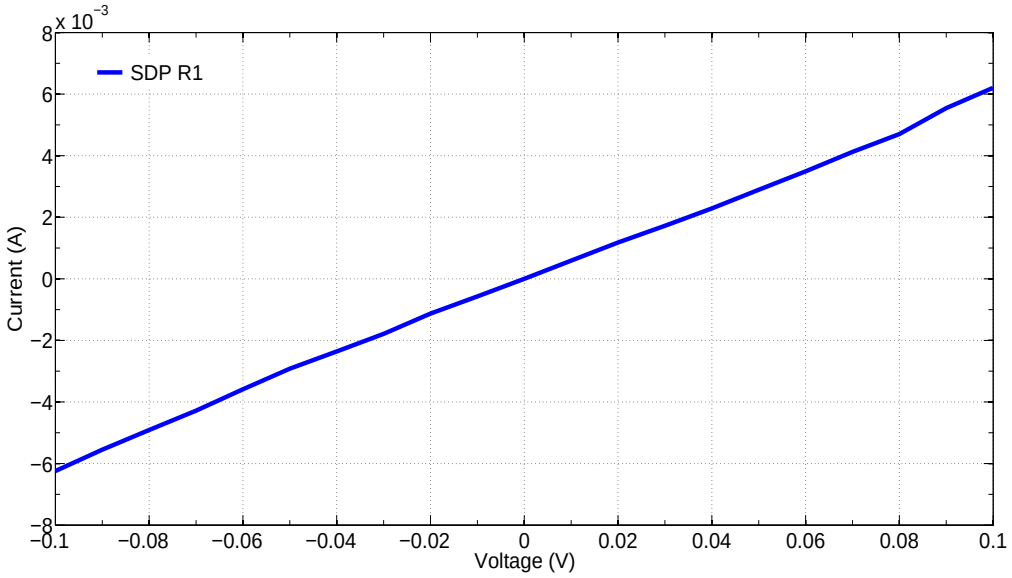

Fig. 3.14: I-V characteristics of SDP R1 on SiO_2/Si

Table 3.3: Table for comparison between standard SMD chip resistors and MCP based PMRs

Make and Model	Resistance	Length	Width	Thickness
Vishay CRCW e3 Series, Model: 1206	16 Ω	L ∼ 3.2 mm	W ∼ 1.6 mm	t ∼ 0.55 mm
SDP R4	**16 Ω**	**L ∼ 500 μm**	**W ∼ 200 μm**	**t ∼ 700 nm**
WALSIN WR06 Series, Model: 0603	93.1 Ω	L ∼ 1.6 mm	W ∼ 0.8 mm	t ∼ 0.45 mm
SOP R1	**94 Ω**	**L ∼ 475 μm**	**W ∼ 200 μm**	**t ∼ 360 nm**
TE CONNECTIVITY CPF-A Series, Model: 0603	120 Ω	L ∼ 1.55 mm	W ∼ 0.8 mm	t ∼ 0.45 mm
DIPSOP R2	**120 Ω**	**L ∼ 300 μm**	**W ∼ 120 μm**	**t ∼ 350 nm**
PANASONIC ERA6A Series, Model: 0805	133 Ω	L ∼ 2 mm	W ∼ 1.25 mm	t ∼ 0.5 mm
SOP R2	**134 Ω**	**L ∼ 450 μm**	**W ∼ 200 μm**	**t ∼ 353 nm**
MULTICOMP MCT05 Series, Model: 0805	196 Ω	L ∼ 2 mm	W ∼ 1.25 mm	t ∼ 0.55 mm
DIPSOP R1	**194Ω**	**L ∼ 190 μm**	**W ∼ 125 μm**	**t ∼ 300 nm**
MultiComp MCMR Series, Model: 0402	226 Ω	L ∼ 1 mm	W ∼ 0.5 mm	t ∼ 0.35 mm
SOP R3	**224 Ω**	**L ∼ 460 μm**	**W ∼ 200 μm**	**t ∼ 386 nm**

* L,W and t are overall device Length, Width and Thickness

claim to consider the printed structures as micro-resistors. When I-V measurements were performed after 1 year, a shift of few ohms was observed in R of PMRs which states that MCP based PMRs are electrically stable even after 1 year. A summary of fabricated and measured PMRs is presented in Table 7.2 where spill layer data has been presented as a reference for comparison. Since the printed contact pads are not sufficiently thick, the level of probing varies from one PMR to other PMR. Therefore, R varies somewhat inconsistently with the product of W/L ratio and t from one PMR to other as seen in Table 7.2.

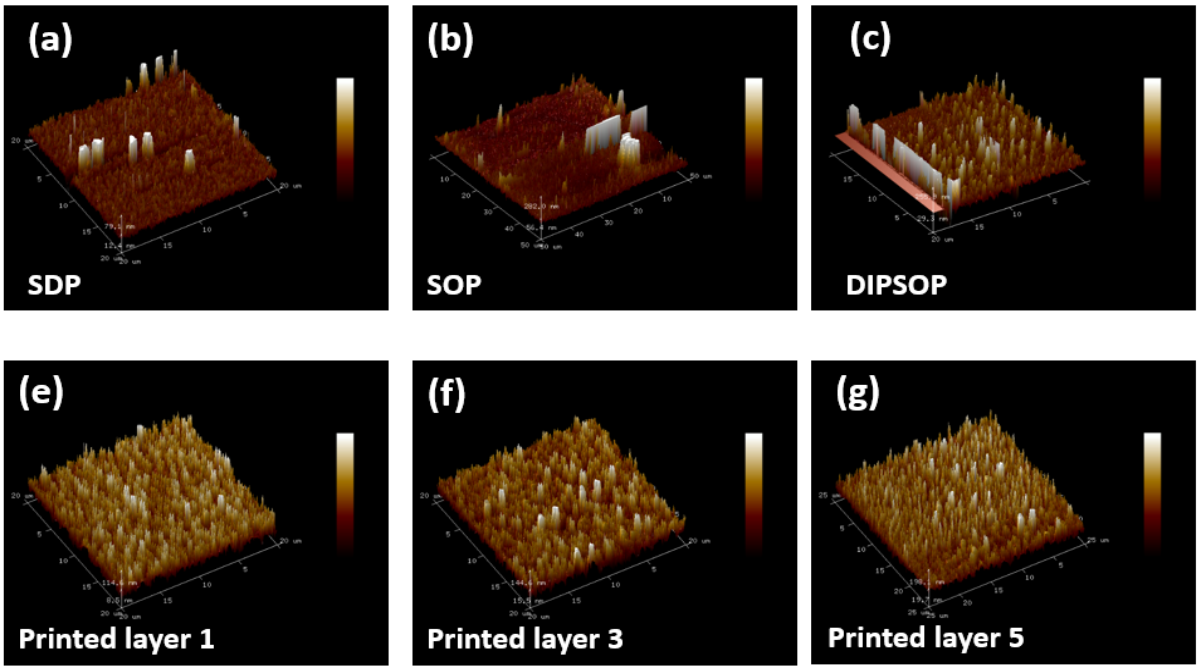

Fig. 3.15: AFM images for different printing methods and printed layers

3.3.5 Comparison between proposed and SMD Resistors

The proposed PMRs can be effectively used as SMD chip resistors on PCBs. Most of the standard SMD chip resistors available in the market have the size in 'mm' range, costs more than $ 0.014 per chip resistor and consume power more than 100 mW [77–79]. For instance, SMD chip resistor for 226 Ω (Make: MultiComp MCWR series, Model: 0402) has overall device length ∼ 1 mm, width ∼ 0.5 mm, thickness ∼ 0.35 mm, minimum unit price of $ 0.2424 (including the assembly cost and the fabrication cost of a SMD resistor) and a power rating of 62.5 mW [80–82]. Close to this chip resistor, our SOP R3 offers 224 Ω with overall device length ∼ 460 μm, width ∼ 200 μm, thickness ∼ 386 nm, and a unit price of ∼ $ 0.035041 (including the cost of ink and SPT) and excluding the overhead charges of electricity, labour charge, packaging and storage charge, shipping charge etc. Table 3.3 shows a comparison between standard SMD chip resistors available in market and MCP based PMRs fabricated in this work. The PMRs fabricated using MCP based printing techniques have smaller dimensions, are at least 7 times less costly and expected to consume less power due to their smaller size as compared to the standard SMD chip resistors. Additionally, PMRs fabrication can directly be carried out over PCBs to reduce the time-complexity of the fabrication process and to minimize the cost of assembly and packaging [83].

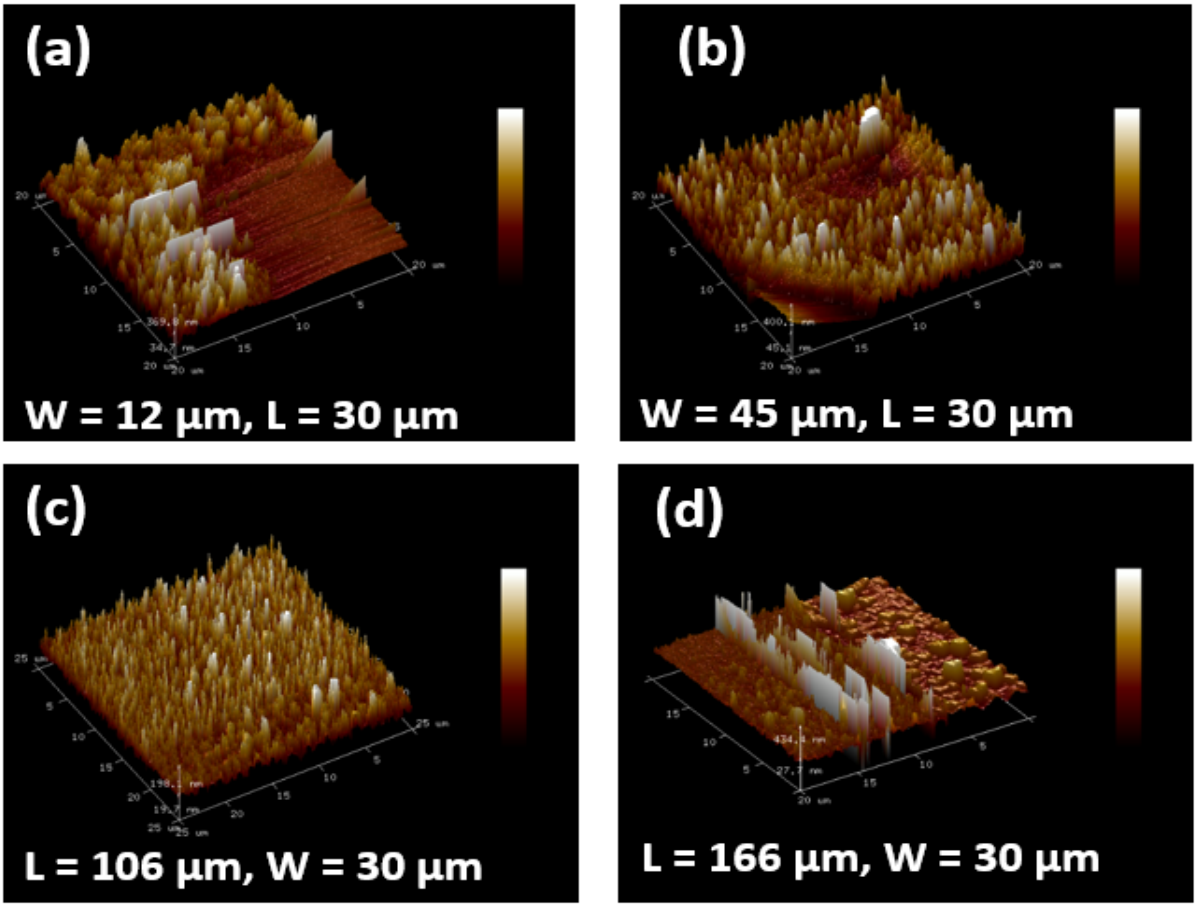

Fig. 3.16: (a, b) AFM images for different channel width (c, d) AFM images for different channel length

3.4 Summary

In this chapter, micro-cantilever based printing technology (MCP) has been optimized and utilized to print micro-resistors of AgNP ink with a particle size of 50 nm on a variety of substrates such as glass, silicon and PET. These PMRs are single material electronic devices as the core device is made up of AgNP only which in turn reduces the issues of interfacial mismatch. Three different printing techniques based on MCP have been developed which have been named as SOP, DIPSOP and SDP. The PMRs are found to be structurally and electrically stable even after 1 year of observation. Electrical characterization based analysis of PMRs on glass substrate shows that MCP can modulate the print thickness and W/L ratio of the AgNP PMRs to achieve $\sim$ 50 times higher R than the AgNP spill layer. Hence, it can be concluded that with proper optimization of print thickness and W/L ratio, the average resistance of the PMRs can be tuned to the desired level using MCP based printing techniques. SOP can print comparatively large number of PMRs in one go while DIPSOP is the most reliable and

SDP is the fastest printing technique. It was also found that proper annealing is a must before DC probing to avoid TSE and to achieve the required device characteristics. The analysis of surface roughness based on AFM scans reveals that SDP technique has the highest and DIPSOP technique has the least uniformity of thickness. Moreover, the minimum feature size of sub-1 μm and printing resolution of sub-2 μm has been achieved using these printing techniques. These printing techniques can be extended to fabricate micro-capacitors, field-effect transistors (FETs) etc. which can be applied in varied electronic applications in the field of sensors, displays, electronic circuits fabrication etc. The MCP based printing techniques can also be used to print structures with other kinds of ink which can be semi-conducting, conductive polymer, biological etc. in nature. The structures printed with such inks can also be tested for low-cost biosensors. Furthermore, these printing techniques can be utilized to functionalize a particular surface within a sub-5 μm regime at a targeted location. With numerous advantages and applicability in a variety of fields, MCP based printing technology is expected to be a potential and low-cost future technology for electronic device fabrication and can prove to be an effective alternative to the standard silicon microelectronic fabrication technology and inkjet-printing technology for specific applications.

4

ZnO Multiple Nanowires Based Printed-Schottky Diodes

Contents

4.1 Introduction

The expertise gained in printing of AgNP micro-structures on various substrates in the previous two chapters, has been used here to fabricate ZnO multiple nanowires-based Schottky diodes for sensing air pollutant gases such as CO_2, CO and NO_2. It is noteworthy tha the rapid increase in industrial growth has affected the environment around us adversely with air pollution being one of the major concerns. Therefore, the development of highly sensitive, selective and low-cost gas sensors is the need of the hour. Metal oxides have been one of the favourite sensing materials used for the fabrication of gas sensors for sensing air pollutants such as CO_2, CO and NO_2 [84–86]. Particularly, ZnO nanowires (NWs) have evolved as one of the most promising material for sensing air pollutants due to their higher sensitivity, ability to sense multiple gases, higher thermal and chemical stability, high surface-to-volume ratio

ZnO NW based sensors generally operate at higher temperatures which increases the power budget. Sinha et al. have reported CO sensing at 200 ppm using ZnO NW arrays at 250°C [87]. Ahn et al. have also reported NO_2 sensing at 225°C with a vertical network cluster of ZnO NW [88]. ZnO NWs are synthesized utilizing several methods, such as, chemical vapour deposition (CVD), electrospinning and deposited using pulsed laser deposition etc. which involve sophisticated equipment [89,90]. Hong et al. have reported the fabrication of comb-like ZnO nanostructures grown using a modified CVD method for CO sensing at room temperature [86]. Rakesh et al. have also reported room temperature detection of CO using Au decorated ZnO NW which have been grown using vapour-liquid-solid (VLS) method, where a vacuum furnace is involved [91]. Kannan et al. have explored CO_2 sensing properties of ZnO thin films which have been deposited using DC reactive magnetron [92]. The fabrication process in above reports is expensive, time-consuming and complex. Moreever, the metal contact pads are also typically deposited using costly shadow masks and spohisticated photolithography processes for electronic device fabrication [93]. Therefore, a simple, less expensive and rapid fabrication process is required for contact pad fabrication and deposition of ZnO NWs to develop devices that can sense pollutant gases at room temperature. In our previous works, we have already optimised the electrical properties of AgNP contact pads using micro-cantilever printing (MCP) over various substrates which have been used here as metal contacts for the fabrication of Schottky diode based gas sensors [22,36].

In this chapter, gas sensors based on Schottky diode have been proposed with a different fabrication approach which consists of two phases. In first phase, a small volume of ZnO NW dispersion (NWD) is

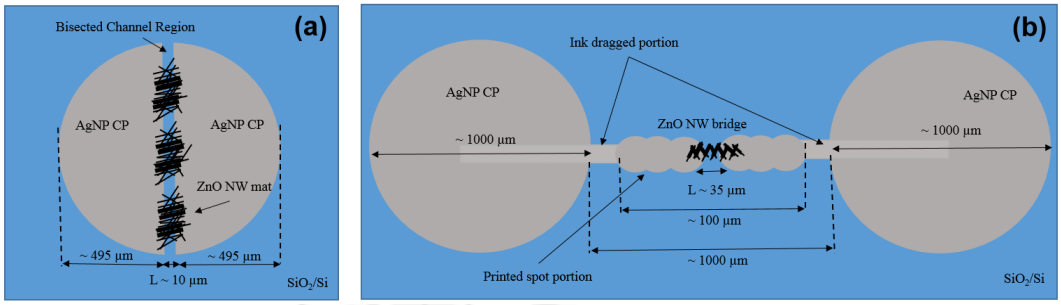

Fig. 4.1: Schematic diagram of (a) ZnO NW micro-mat diode (b) ZnO NW micro-bridge diode. L: Channel Length, CP: Contact pads, NW: Nanowire

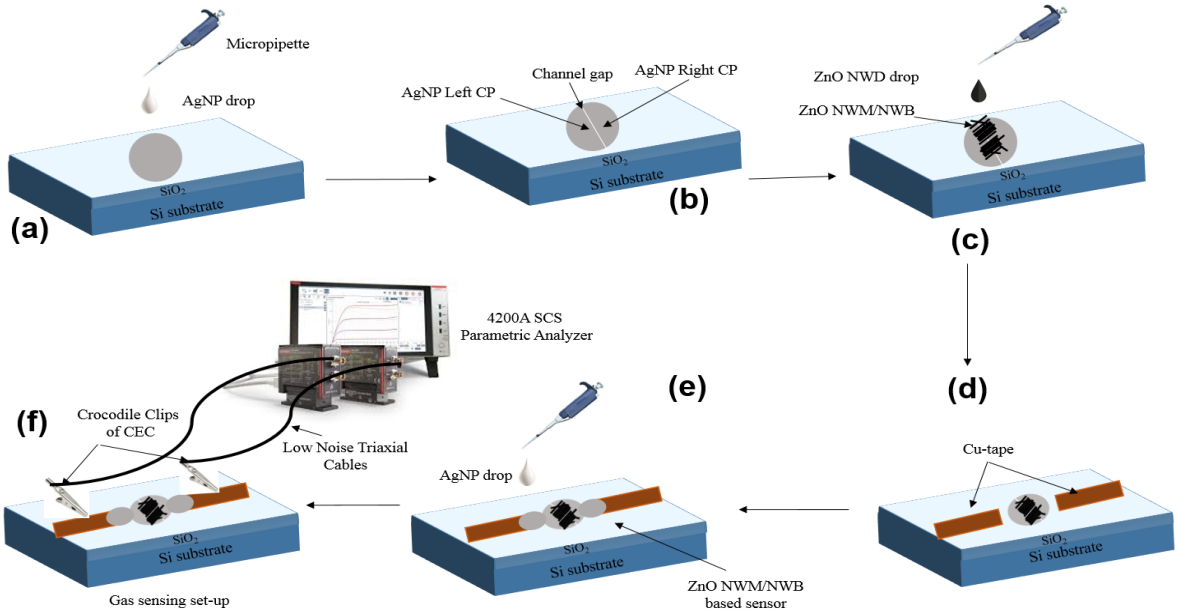

Fig. 4.2: Schematic showing complete flow diagram of ZnO NW-μMD/NW-μBD based sensor fabrication. For ZnO NW-μBD, the AgNP contact pads are printed in step (b) with rest of the steps being same

drop-casted over a gap (channel) between pre-drop-casted and annealed AgNP contact pads to deposit random and dense clusters of ZnO NWs, resembling the shape of a mat, at several places along the channel. This device has been named as ZnO NW-μMD. The core idea to develop ZnO NW-μMD is to verify the response of ZnO NWs to CO_2, CO and NO_2 in a simple and rapid way on the go. Once the response of NWs is verified satisfactorily, the device optimization has been performed by printing the AgNP contact pads using the MCP technique in the second phase [22,36]. The channel dimensions have been controlled and optimised via printing technique and a ZnO NW bridge like channel with less density of NWs is formed after drop-casting of ZnO NWD in DI water to improve the sensitivity and response time of the sensors. The optimised device is referred to as ZnO NW-μBD. A conceptual schematic diagram of these two devices is shown in Figure 4.2. Therefore, the sensor fabrication based

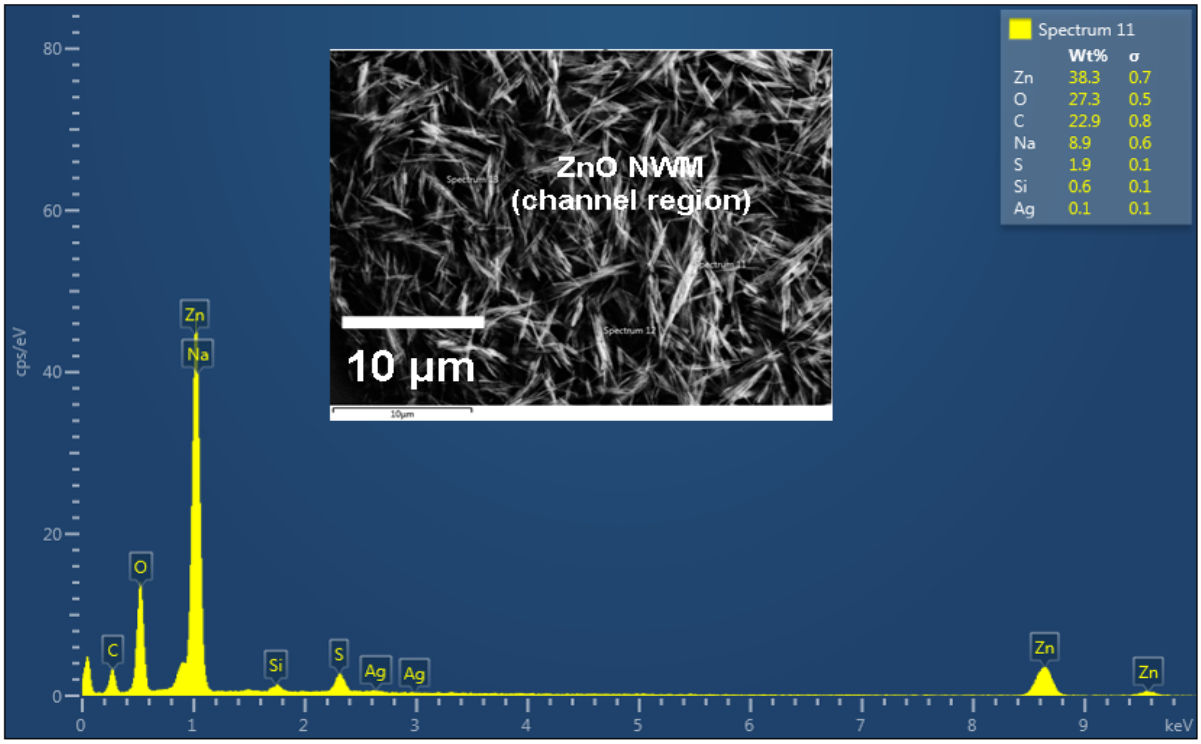

Fig. 4.3: EDS data for ZnO NW mat. Inset shows FESEM image of ZnO NW

on micro-cantilever printing technique offers a low-cost, room temperature, non-vacuum, and can be a potential alternative to the conventional gas sensor fabrication techniques which involve high-end equipment and have longer fabrication time. Probably, this is for the first time, micro-cantilever printed AgNP contacts for ZnO NW mat/NW bridge-Schottky diodes based gas sensor fabrication has been reported. The detailed fabrication steps are presented in Appendix B and C.

4.2 Gas sensing set-up

4.2.1 Contact modification in printed diodes

The fabricated contact pads have their dimensions in 'μm' regime ($\sim 500\ \mu$m). To test the fabricated devices as gas sensor, the contact pads dimensions need to be in 'mm' regime (> 2 mm) because gas sensing experiments have been performed in a Controlled Environment Chamber in which the gas-flow is controlled using mass flow controllers (MFCs) (Make: Alicat Scientific) which have a high reading accuracy of $\pm$ 0.4 % [62]. CEC uses crocodile clips to connect the sensor to electrical characterization equipment. If these clips are directly attached to the fabricated devices, they can scratch the contact pads. A copper (Cu) tape strip with a width of ~ 2 mm is pasted closely to both the AgNP contact pads

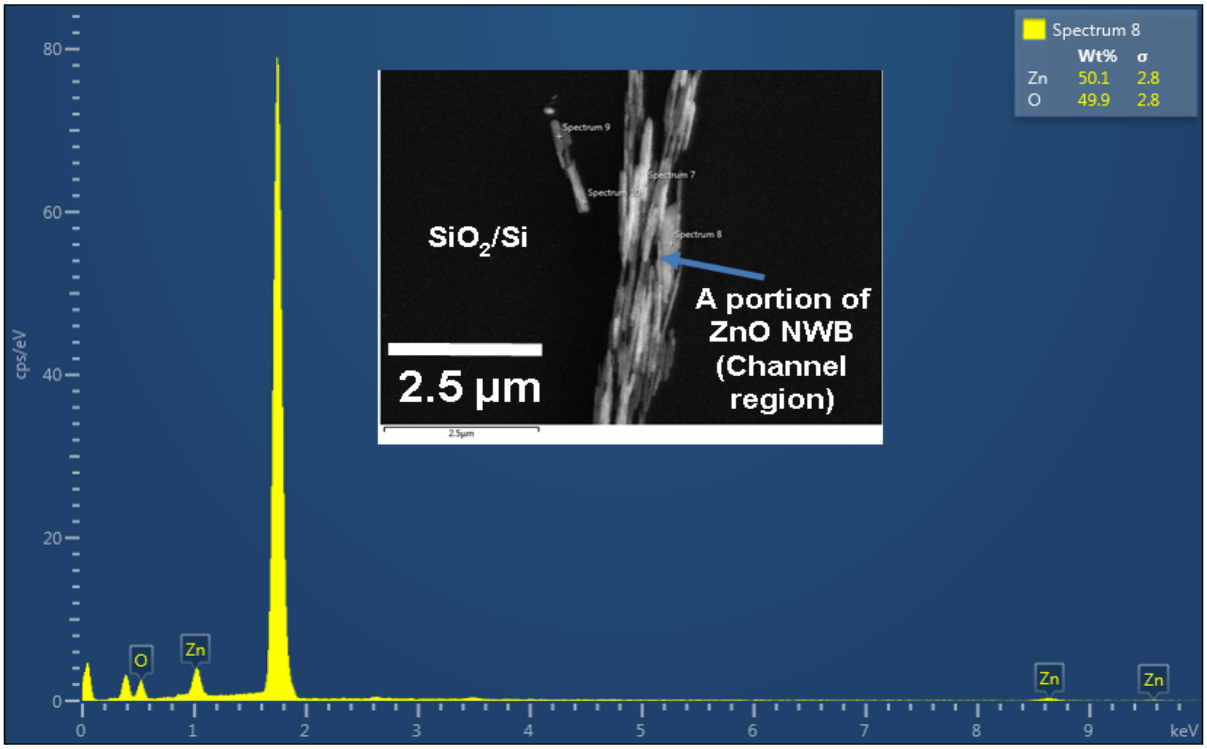

Fig. 4.4: EDS data for ZnO NW bridge. Inset shows FESEM images of a portion of channel region

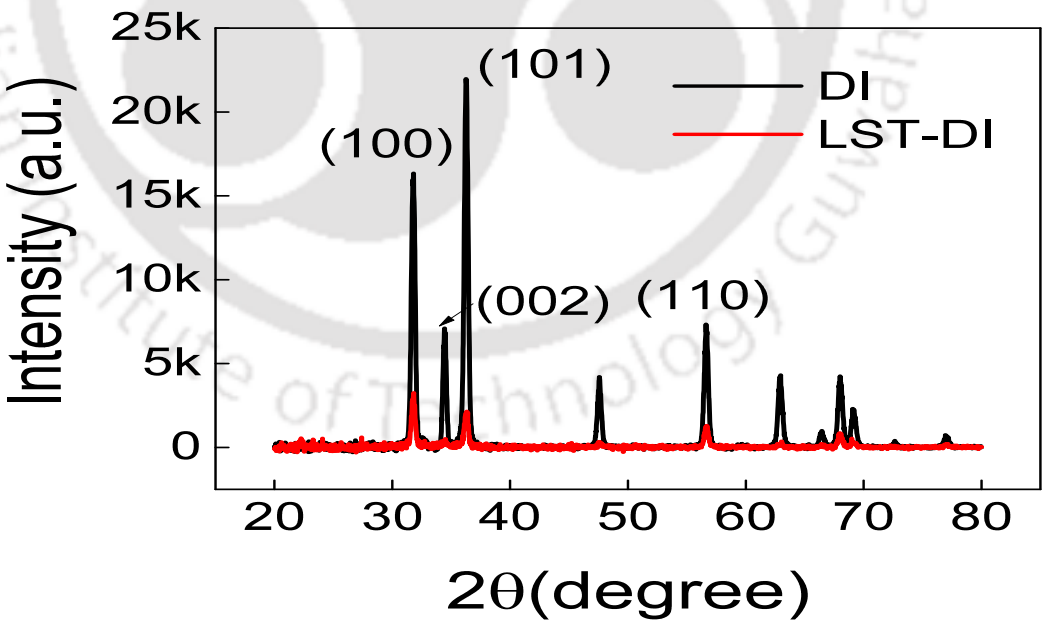

Fig. 4.5: XRD spectra for ZnO NWD in DI water and LST-DI water

to make the fabricated devices compatible with CEC. Further, to connect the Cu-tape to the AgNP contact pads, 1 μL of AgNP ink is drop-casted and annealed over the disconnected area between the tape and the contact pads. Figure C.1 shows the complete flow diagram of ZnO NW-μMD/NW-μBD

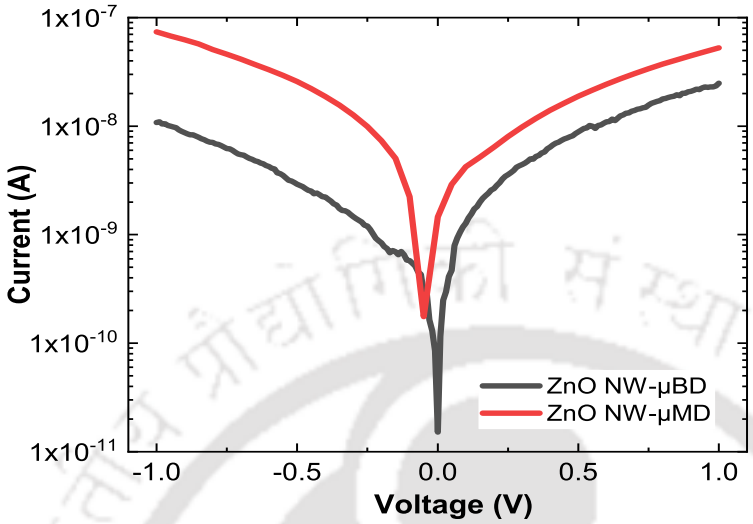

Fig. 4.6: Representative baseline semi-log I-V response of ZnO NW-μMD and ZnO NW-μBD

based gas sensor fabrication.

4.2.2 Gas sensing procedure

The sensor is placed in the gas sensing chamber (volume $\sim$ 9429 cm^3) in CEC and it is connected to Keithley 4200A-SCS parametric analyzer [61] using low-noise triaxial cables. The gas sensing chamber is set to vacuum first and then pressurized with dry nitrogen (N_2) and AER is measured for a particular voltage sweep. This AER is taken as a baseline resistance for calculating the response of the sensor and is represented as R_a. After that, the chamber is vacuumed and a new mixture of analyte and carrier gas is loaded into the chamber using Flow Vision MX^{TM} software [62] followed by electrical characterization. This step is repeated for every new mixing ratio. When the chamber is pressurized to the atmospheric pressure, this time is considered as a gas ON phase.

4.3 Results and Discussion

4.3.1 Characterization of fabricated devices

To observe the elemental composition of the channels, Energy-dispersive X-ray spectroscopy (EDS) [Make: Zeiss, Model: Sigma] was performed. Figure 4.3 shows the FESEM image of the ZnO NW mat in the channel region and its corresponding EDS spectra, which shows the weight % of 38.3%, 27.3%, 8.9% and 1.9% for Zinc (Zn), Oxygen (O), Sodium (Na) and Sulphur (S) respectively. Sodium

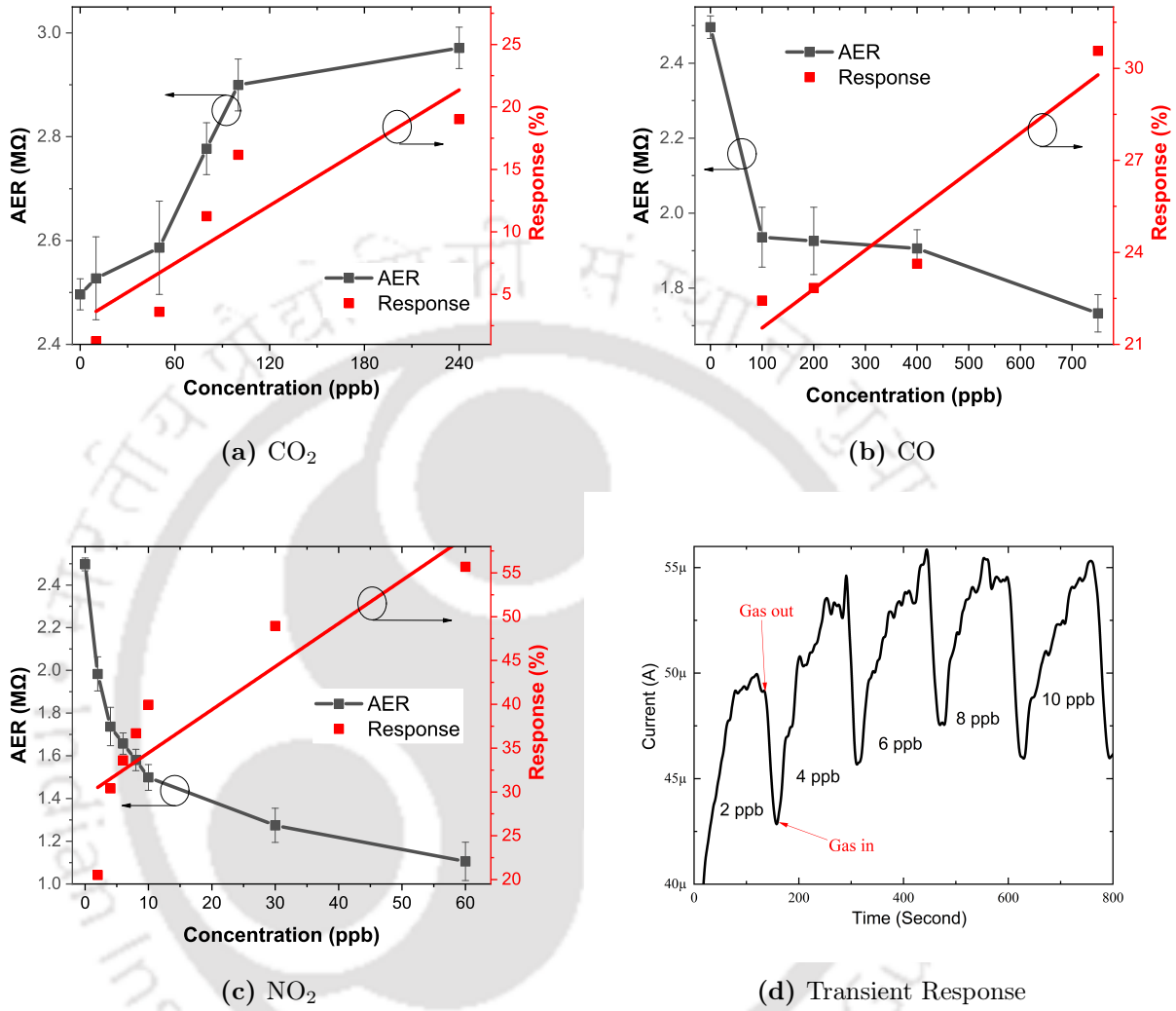

(a) CO_2 (b) CO

(c) NO_2 (d) Transient Response

Fig. 4.7: (a,b,c) AER variation with gas concentration and sensor response of ZnO NW-μMD based gas sensors (d) Transient response of ZnO NW-μMD based NO_2 sensor

and Sulphur presence in EDS spectra is due to the addition of SDS in DI water. It is reported that negative part of the SDS interacts with positive part of ZnO which affects the surface morphologies and aspect ratio of ZnO nanostructures. It is also mentioned that Na ions can act as shallow donors to ZnO nanostructures to affect the response of ZnO based sensors [94,95]. Similarly, Figure 4.4 shows the FESEM image of ZnO NW bridge in the channel region and its corresponding EDS spectra, which shows a weight % of 50.1% and 49.9% for Zn and O respectively.

Figure 4.5 shows the X-ray Diffraction (XRD) [Make: Rigaku, Model: Micromax-007HF] spectra of ZnO NWD in LST-DI water and DI water. It is observed that there are three major peaks present for 2θ value of 31.8°, 34.44° and 36.26° for ZnO NWD in DI water case which corresponds to ZnO

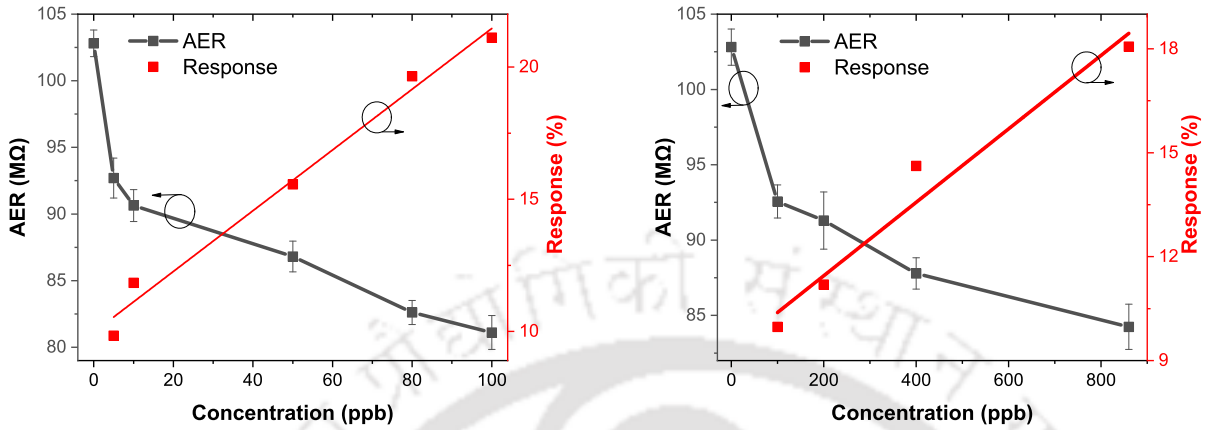

(a) CO_2 (b) CO

Fig. 4.8: AER variation with gas concentration and sensor response of ZnO NW-μBD based gas sensors

hexagonal wurtzite structure according to JCPDS database (36-1451) [96, 97]. It is also observed that two major peaks are present for 2θ value of 32.82° and 36.32° for ZnO NWD in LST-DI water case which also corresponds to ZnO wurtzite structure. However, the highest peak is observed for 2θ value of 36.26° and 32.82° for ZnO NWD in DI water and LST-DI water respectively. Moreover, the intensity ratio of the two major peaks in the two NWD cases is also different which indicates a difference in the lattice orientation of the ZnO NWs in the two cases. The shifts in the XRD data indicate that the sensing layer structure and crystal orientation is different for the two devices.

4.3.2 Electrical characterization of the fabricated devices

The I-V characteristics of the ZnO NW mat-based Schottky diode is shown in Figure 4.6. The slight shift in the symmetry of the I-V curves for negative and positive bias in Figure 4.6, is propably due to the fact that the ZnO NWs are drop-casted over the channel region and hence the contact uniformity may slightly differ in the two AgNP-ZnO NW interfaces. The formation of Schottky diode depends on the work function of the metal, interface properties of the metal-semiconductor junction, the thickness of the metal contact, the amount of voltage applied between the contacts, annealing process etc. [98–102]. However, there are only a few reports on the formation of Schottky diodes using AgNP contacts and ZnO NWs [103, 104].

4.3.3 ZnO NW-μMD based sensor response

The combination of three different gases have been chosen in order to perform a comparisonal analysis and to check the level of selectivity and sensitivity of Schottky diodes fabricated using ZnO nanowire mats or nanowire bridge structures for these three major air pollutants. The gas sensor response, R, is represented as

$$R = \frac{|R_g - R_a|}{R_a} \times 100\% \tag{4.1}$$

where R_g represents the AER for analyte gas for a particular concentration and R_a represents the baseline resistance of the device [97]. The sensitivity is calculated from the slope of the linearly fitted response curve [105].

Figure 4.7 (a, b, and c) show the AER variation and response curve of ZnO NW-μMD for CO_2, CO and NO_2 respectively. AER shows an increases tend with increasing CO_2 concentration implying CO_2 acts as an oxidizing gas to ZnO NWM and extracts electrons from its conduction band which leads to an increase in its AER. Contrary to this, AER shows a decreasing trend for CO and NO_2 indicating that these gases act as reducing agent to ZnO NW mat. CO_2 is expected to react with oxygen ions present on the lattice sites of ZnO NW bridge which results into the formation of neutral oxygen vacancies. These oxygen vacancies finally ionize to give the electron back to the conduction band of the ZnO and conductivity increases and AER decreases. This decreasing trend of AER with increasing CO is in agreement with the literature [87, 89, 106]. However, there in no readily available explanation for AER decreasing trend for NO_2. One strong possibility can be that ZnO NWs may get doped by Na of SDS to get converted to p-type and hence the AER trend is reversed as compared to n-type ZnO sensors [107]. F

The non-linearities observed in AER curves is due to the inclusion of baseline AER for each gas sensing case which results in a initial shift in slope of the AER variation curve gas concentrations. If the baseline AER is removed from these curves, AER variation with gas concentration is almost linear in most of the cases. Further, a sensitivity of 0.077 %ppb^{-1} for 10 to 240 ppb of CO_2, 0.004 %ppb^{-1} for 100 to 750 ppb of CO and 0.492 %ppb^{-1} for 2 to 60 ppb of NO_2 has been observed with ZnO NW-μMD. Figure 4.7(d) shows the representative transient response plot for NO_2 sensing using ZnO NW-μMD. Based on Figure 4.7(d), it is concluded that the sensor is reversible and a response time $\sim$ 30-40 s and a recovery time of $\sim$ 1 minute is obtained.

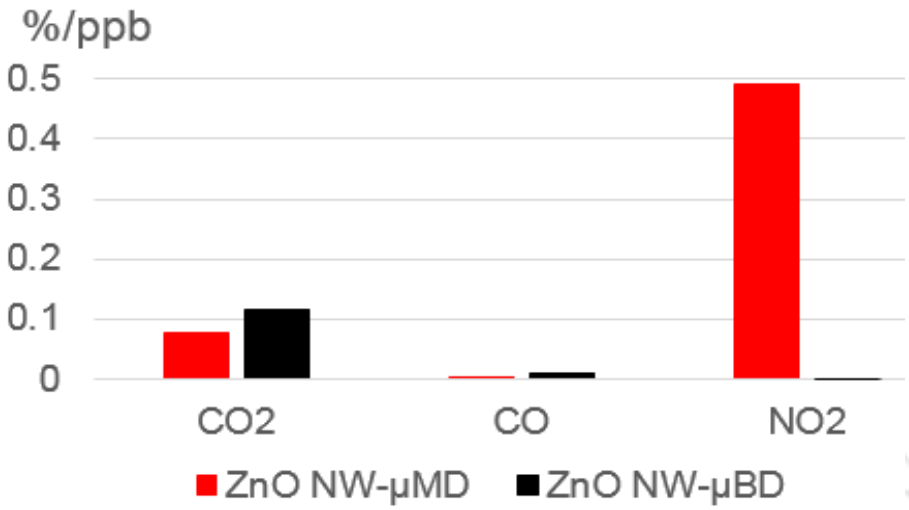

Fig. 4.9: Sensitivity comparison of ZnO NW-μMD and ZnO NW-μBD based sensors for different air pollutants

4.3.4 ZnO NW-μBD based sensor response

Figure 4.8(a, b) show the AER variation and response curve of ZnO NW-μBD for CO and CO_2 respectively. Here, a decreasing trend for AER is observed for both the gases which is in accordance with published reports [87, 105]. Therefore, both gases act as reducing agent for ZnO NW bridge. However, a minimal response is obtained for NO_2 using bridge. The probable reason can be the use of non-SDS ZnO dispersion for ZnO NW bridge device. Consequently, a sensitivity of 0.115 $\%ppb^{-1}$ for 5 to 100 ppb of CO_2 and 0.011 $\%ppb^{-1}$ for 100 to 860 ppb of CO is obtained using ZnO NW-μBD sensor. The limit of detection (LOD) has been calculated as

$$LOD = \frac{3 \times \sigma}{S} \tag{4.2}$$

where, σ represent the standard deviation of the AER and S is the sensitivity of the sensor. A LOD of 0.23 ppb for CO_2 and 9 ppb for CO has been obtained using ZnO NW-μMD and a LOD of 0.14 ppb for NO_2 has been obtained using ZnO NW-μMD. Figure 4.9 shows a mutual comparison between sensitivity of ZnO NW-μMD and ZnO NW-μBD based sensor for CO_2, CO and NO_2.

4.3.5 Gas sensing mechanism

Since both the sensors are based on Schottky diodes, the Schottky barrier height and Schottky contact area are expected to dominate the thermionic-emission based current transport through the

ZnO NW channel as shown in following equation [108]

$$I_{SD(TE)} = SA^*T^2e^{\frac{-q\phi_{SB}}{kT}}[e^{\frac{qV}{kT}} - 1] \tag{4.3}$$

where S is the area of the Schottky contact, A^* is the effective Richardson constant, T is the temperature, q is the unit electronic charge, k is the Boltzmann constant, V is the applied voltage, and ϕ_{SB} is the Schottky barrier height. The contact surface area of the ZnO NWs to the AgNP pads is small for ZnO NW bridge based-diode as compared to ZnO NW mat based-diode due to less density of NWs present at the interface. The ratio of contact circumference to contact area is therefore, large for ZnO NW bridge based-diode which amplifies the effect of gas molecules adsorbed at the interface by affecting the Schottky barrier height and hence the diode current [108]. Therefore, ZnO NW bridge is more sensitive to CO_2 and CO as Schottky contact dominates the sensing mechanism and make it feasible at room temperature. In case of NO_2, the defects and the presence of Na at the interstitial sites of ZnO NW mat as shallow donors dominate the sensing mechanism, which make ZnO NW mat based-diode more sensitive towards NO_2 as compared to ZnO NW bridge based-diode [94, 95, 109]. Moreover, Na can dope the ZnO NWs to p-type conduction at room temperature which can be a probable reason for room temperature detection of NO_2 [107]. However, consideration of other factors and further exploration is required to firmly establish the gas sensing mechanism. The fabricated sensors are low-cost devices as Ag contacts have been fabricated using MCP which is a room temperature, non-vaccum, additive manufacturing process, and ZnO NWs have been deposited via simple drop-casing techniques [36].

Table 4.1 shows response, sensitivity, response and recovery time for all the gas experiments performed along with a comparison of this work with other reported gas sensors. The fabricated sensors in this work show sufficiently higher sensitivity than the reported ones. Furthermore, most of the reports with high sensitivity either operate at higher temperature or have higher gas concentrations or use functionalized ZnO for gas sensing.

4.4 Summary

In this chapter, micro-cantilever printed AgNP contact pads based ZnO nanowire Schottky diodes-based gas sensors have been fabricated to sense three major air pollutants, CO_2, CO and NO_2 at room temperature. The sensor fabrication process has been optimised with the help of micro-cantilever

Table 4.1: Comparison of ZnO NW-μMD and ZnO NW-μBD gas based sensors with other reported sensors

Material	Device	Analyte Gas	Temperature (°C)	Gas Concentration	Sensitivity (%/ppb)	t_{res}	t_{rec}	Year	Ref.
ZnO TF	Resistor	CO_2	300	(500-10000) ppm	0.0000005	20 s	20 s	2014	[92]
ZnO:Ca NP	Resistor	CO_2	450	(0-10000) ppm	0.000008	~ 10 s	~ 10 s	2015	[97]
ZnO NFs	Resistor	CO_2	250	(200-1025) ppm	0.0001125	9-17 s	9-17 s	2019	[105]
ZnO NW-VN	Resistor	CO	250	200 ppm	0.000465	1 s	2 ms	2016	[87]
ZnO Comb-like NS	Schottky Diode	CO	RT	250 ppm	0.00032	~ 5 min	~ 2.5 min	2014	[86]
ZnO/ZnS Core-Shell NS	Resistor	NO_2	RT	(100-2400) ppb	0.353	~ 40 s	~ 15-20 s	2018	[110]
ZnO NR	Resistor	NO_2	RT	10 ppm	0.0278	~ 25 s	~ 25 s	2016	[111]
ZnO NW-μMD	Schottky Diode	CO_2	RT	(10-240) ppb	**0.077**	30-60 s	~ 1-2 min	2019	**[112]**
ZnO NW-μMD	Schottky Diode	CO	RT	(100-750) ppb	**0.004**	30-60 s	~ 2-5 min	2019	**[112]**
ZnO NW-μMD	Schottky Diode	NO_2	RT	(2-60) ppb	**0.492**	40-50 s	~ 1 min	2019	**[112]**
ZnO NW-μBD	Schottky Diode	CO_2	RT	(5-100) ppb	**0.115**	30 s	~ 1 min	2019	**[112]**
ZnO NW-μBD	Schottky Diode	CO	RT	(100-860) ppb	**0.011**	30-60 s	~ 1-2 min	2019	**[112]**

TF: Thin Film, NP: Nanoparticle, NFs: Nanoflakes, NS: Nanostructures, NR: Nanorod, VN: Verticle Network, HN: Horizontal Network, RT: Room Temperature

printing technique, through which the dimensions of the contact pads and the channel is controlled. The process of printing metal contacts reduces the cost of sensor fabrication, is additive, simple and comparatively fast. The optimised ZnO NW-μBD based sensors show a sensitivity of 0.115 $\%ppb^{-1}$ for 5 to 100 ppb of CO_2 and 0.011 $\%ppb^{-1}$ for 100 to 860 ppb of CO. ZnO NW-μMD sensor has shown the best sensitivity of 0.492 $\%ppb^{-1}$ for 2 to 60 ppb of NO_2. The response and recovery time of the sensors for all gases is in the range of 30-60 s and 1-5 minutes respectively. A LOD of 0.14 ppb for NO_2, 0.23 ppb for CO_2 and 9 ppb for CO has been obtained using fabricated sensors. Schottky contact is found to be the dominating parameter which is responsible for higher sensitivity and room temperature detection of the analyte gases.

5

ZnO Single Nanowire Based Printed-Schottky Diodes

Contents

In the previous chapter, ZnO multiple NW based devices were fabricated and used as gas sensors. However, it is evident from the previous discussions that ZnO NWM and NWB are dense clusters of multiple NWs clubbed together and hence it is difficult to determine exact count of NWs responsilbe for current transport. In other words, it is difficult to develop mathematical models for such mutiple NWs-based devices. One solution can be the development of electronic devices based on ZnO single NW (SNW) which has a definite dimension and additionally can improve the sensing parameters due to its higher surface-to-volume ratio. Therefore, this chapter details the fabrication and application of ZnO SNW based electronic devices. This chapter is divided into two parts. The first part refers the optimization of aqueous dispersions of ZnO NWs discussed in Appendix B to place well-separated ZnO SNWs on the substrate for single nanowire device fabrication. Once, ZnO SNWs are properly placed over the substrate, MCP technique has been employed to overlap the both sides of the selected ZnO SNW with AgNP metal contacts to fabricate ZnO SNW based Schottky diodes. The MCP-printed ZnO SNW Schottky diodes have been electrically characterised and the experimental results have been validated through a thermionic emission based analytical model and the subsequent discussions are presented. The second part of this chapter discusses the usage of ZnO SNW based Schottky diodes for sensing two major air pollutants CO_2 and CO.

5.1 Introduction

ZnO nanowires (NWs) are one-dimensional nanostructures with a larger surface-to-volume ratio, high thermal and chemical stability with less power consumption, higher electron mobility, compatiblity with modern device fabrication processes, having a long functional time, can be used as self-powered devices and so on [39, 108, 113]. ZnO SNW has been regularly used for the fabrication of Schottky diodes [18,19,108]. Kim et al. have used electron-beam evaporator and a shadow mask to deposit a thick layer of Ag to act as Schottky contact for ZnO NW based Schottky diode fabrication [103]. Das et al. have reported the growth of ZnO NWs on a c-plane sapphire substrates using a metalorganic chemical vapor deposition system utilizing Diethyl zinc and high purity oxygen as the Zn and O sources [101]. Hu et al. [108] have reported the growth of ZnO NWs using vapor-solid process and have used focused ion beam system to deposit Pt-Ga at one end of the ZnO NW for metal contact. Lee et al. report the direct contact-printing techniques for Schottky diode formation using ZnO SNW [17]. They use thermal evaporation for metal contact, the NWs are placed in the channel area using dielectrophoresis

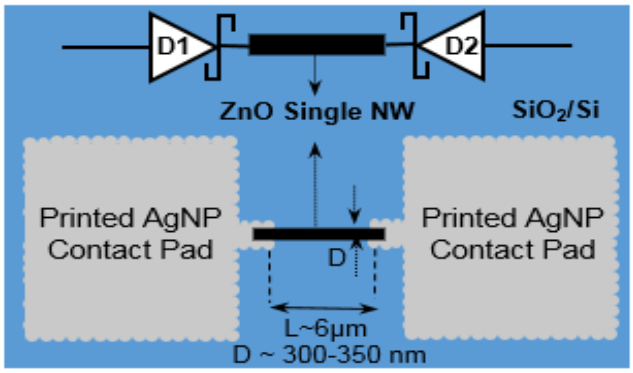

Fig. 5.1: Schematic diagram of ZnO SNW based Schottky diode. NW: Nanowire, L: Channel Length, D: NW diameter

and NW bridges are decaled on the substrate using decal-printing agents like polydimethylsiloxane (PDMS) layer.

It is observed that proper placement of metal contact pads over the ZnO channel material demands sophisticated technologies like electron-beam lithography, thermal evaporation, RF sputtering or focused ion beam/scanning electron microscopy (FIB/SEM), which makes the Schottky diode fabrication process costly [21,101]. Furthermore, ZnO SNWs are generally grown by site-selective molecular-beam epitaxy (MBE) or chemical vapour deposition (CVD) for diode fabrication, which increases the cost further [19]. In this chapter, ZnO SNW based Schottky diodes are fabricated by placing ZnO NWs on a clean SiO_2/Si substrate by dispersion drop-casting technique and AgNP contact pads have been printed directly over the ZnO SNW using micro-cantilever printing (MCP) technology [36]. MCP technology is additive which can directly deposit the contact pads over the targeted areas of SNWs in a controllable and rapid manner at room temperature and non-vacuum ambient. To the best of our knowledge, there are no reports on the fabrication of ZnO SNW based Schottky diodes using MCP technique. Figure 5.1 shows the conceptual schematic diagram of the proposed device.

5.2 Fabrication of ZnO SNW Schottky diode

5.2.1 Materials used

ZnO Nanowire powder (Product Id: 773999) and AgNP ink (Product Id: 736481) are procured from Sigma Aldrich. Ag is preferred over other metals as it is comparatively low-reactive, more stable and less expensive [93]. The optimized NW dispersion with 0.3 % w/v of ZnO nanowires in DI water is drop-casted over the SiO_2/Si substrate at a high temperature near 190°C to speed up the evaporation

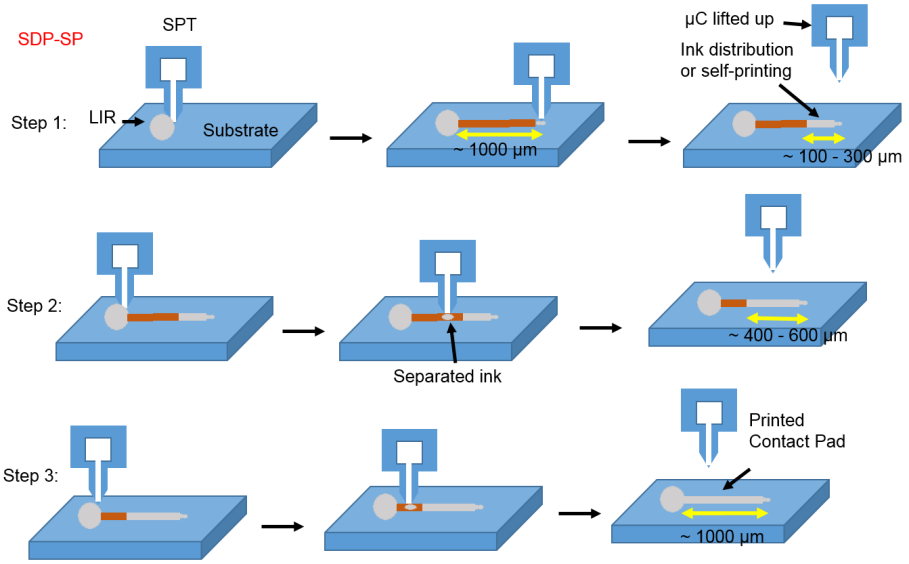

Fig. 5.2: Schematic diagrams showing the printing steps SDP-SP. LIR: Local ink reservoir, μC: Micro-cantilever

of DI water to avoid the agglomeration of NWs into random clusters due to high surface tension in DI water. The optimized ZnO SNWs solution helps to place the NWs at a reasonable distance on the substrate, which helps in targeting an SNW for printing metal contact pads to complete the device fabrication. AgNP contact pads are printed using MCP technology, which uses a molecular printing system (Make: BioForce Nanosciences) containing a surface patterning tool (SPT) consisting of a silicon micro-cantilever print-head [36, 55, 114]. The micro-cantilever has a 5-10 μm wide micro-channels through which the ink to be printed flows or is temporarily stored. The mechanism of AgNP contact printing is described in the following subsection.

5.2.2 AgNP Contact Pad fabrication

The micro-cantilever tip can be used to perform SPT drag printing (SDP) and dip-ink printing with spot overwrite printing (DIPSOP) [36]. The micro-cantilever is kept under UV/O_3 exposure for at least 30 minutes before using it for printing experiments. This turns the surface of micro-cantilever channels solvophilic to the AgNP ink to ensure that a large density of ink particles remain attached to it during the drag and dipping process [22, 112].

After selecting a ZnO SNW, $\sim$ 10 μL of AgNP ink is drop-casted as a local ink reservoir (LIR) $\sim$ 1000 μm away from one of the ends of the selected ZnO SNW. The micro-cantilever is positioned over the AgNP drop and slowly brought down using the coarse and fine z-axis control settings in NanoWare software installed with the printing system [55]. When the gap between the micro-cantilever and the

drop is less than 100 μm, then both get focussed together in an optical camera attached to the printing software. Further, the focus of the camera is re-adjusted to the tip of the micro-cantilever to avoid the spillover (proximity of micro-cantilever and drop may lead to the direct hit of whole surface pattering tool to the ink source).

SDP technique is used only for metal contact pads deposition where the micro-cantilever tip is dragged to a shorter length ($\sim$ 100 - 300 μm) in such a way that the dragged portion of the ink is not separated from the LIR. When the micro-cantilever tip is lifted up, the ink diffuses from LIR, which is a bigger ink-spot of average diameter near 1 to 2 mm containing a high volume of the ink. However, in this work, SDP is used to assist the targeted deposition of the metal ink to overlap the ZnO SNW properly. To achieve this, the micro-cantilever tip is made to deliberately touch the surface of the substrate being dipped in the LIR and is dragged to a longer length ($\sim$ 1000 μm) such that a small volume of ink is separated from the source LIR. When the micro-cantilever tip is lifted up gradually, the separated volume of the ink is uniformly distributed within a portion of the dragged area without touching the LIR due to the longer length and small volume of ink deposition. The above-mentioned process is repeated until the ink is uniformly deposited in the entire area dragged by the micro-cantilever tip. The complete printing mechanism is shown in Figure 5.2.

We have referred this phenomenon of uniform distribution of the separated ink (from the source LIR) throughout the SPT dragged region once the micro-cantilever tip is lifted up, as SDP assisted self-printing (SDP-SP) because the dynamics of the printing is totally governed by the volume of the separated ink, gradient of the ink density and the ink-substrate mutual interaction.

Utilizing SDP-SP, a rectangular contact strip of AgNP is printed, overlapping one end of the ZnO SNW. The overlap is achieved by stopping the drag of the ink closest possible to the ZnO SNW end (preferably $\sim$ 5 to 2 μm before NW) and allowing the ink to automatically diffuse and self-print the remaining distance with the help of high ink-density gradient between the micro-cantilever dragged region and the gap-region between the AgNP ink and ZnO SNW. The ink dragged by the micro-cantilever can also be placed directly over the SNW by gently touching its ends. The direct overlapping of ink is more feasible for SNW channel having length $>$ 10 μm. Then the entire substrate is annealed from 50°C to 200°C with a rate of 8°C/minute. To ensure proper connection between the contact pad and the SNW, two to three DIPSOP based AgNP micro-spots (average diameter $\sim$ 5-10 μm) are printed by ultra-fine positioning. The targeted hit region ensures that 1-2 μm of the

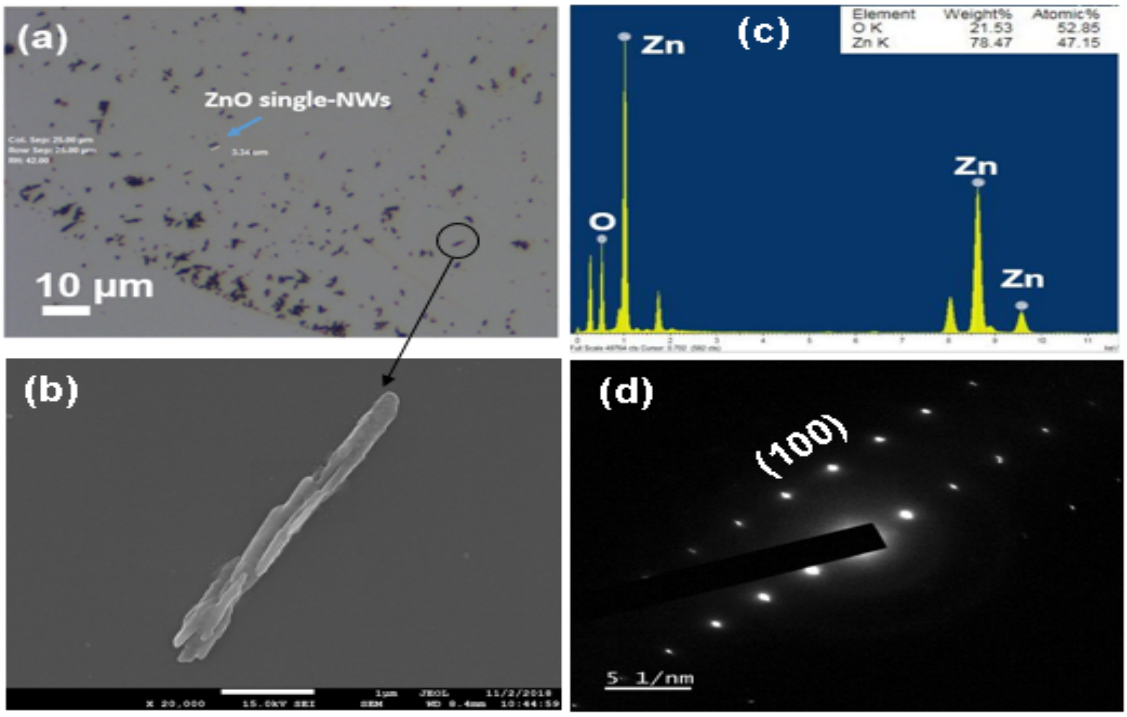

Fig. 5.3: (a) Optical image of dispersed ZnO SNWs on SiO_2/Si surface (b) FESEM image of ZnO SNW after annealing of drop-casted dispersion with a scale of 1 μm (c) EDS spectra of ZnO SNW (d) SAED pattern showing ZnO SNW as single crystalline material

peripheral region of the micro-spot touches the end of nanowire without completely drowning it with AgNP ink. The DIPSOP spots are annealed properly to complete the fabrication of one-side of metal contact. The above-mentioned steps are repeated to form the AgNP metal contacts to the other side of ZnO SNW. DIPSOP is used to thicken and strengthen the printed AgNP layer at the AgNP-ZnO SNW interface to avoid any chance of discontinuity in the AgNP printed layer and reduce the effect of contact resistance and surface defects at interface, on the electrical characteristics of the Schottky diodes.

There are modifications between our previous chapters and the present chapter, and their differences are briefly summarized in Table 5.1. The details of process development to accomplish the current device are shown in Figure 5.2.

Table 5.1: Comparison between our previous chapters and present chapter

Ref. Chapter	Chapter 3	Chapter 4	Current
Focus	Micro-cantilever based printing (MCP) process development	ZnO multiple nanowires as gas sensors	A device with ZnO single nanowire as channel
Contact pads	AgNP	AgNP	AgNP
Channel	AgNP	ZnO multiple nanowires	ZnO single nanowire
Devices	Micro-resistors	Back-to-back Schottky Diodes	Back-to-back Schottky Diodes
Process	Contact pads and channel printed using MCP modes aiming for single material devices	Contact pads: using SDP+DIPSOP Channel: Drop-casted ZnO multiple nanowires over contact pads, aiming for shorter channel lengths	Contact pads: using SDP-SP + DIPSOP Channel: ZnO single nanowire below contact pads, aiming overlapping between single nanowire and pads to reduce contact resistance
AER range (Fabricated devices)	16 Ω - 224 Ω	∼ 1 MΩ - 105 MΩ	91 kΩ - 671 kΩ
Application	Surface mount micro-resistors	Gas sensors	Single nanowire device

5.3 Results and Discussions

5.3.1 Material Characterization for ZnO SNWs

Figure 5.3(a) shows several ZnO SNWs dispersed over SiO_2/Si substrate in black colour wih random network of NWs at the periphery of the dispersion drop formed possibly due to coffee ring effect [68]. Figure 5.3(b) shows the magnified Field Emission Scanning Electron Microscope (FESEM) (Make: JEOL, Model: JSM-7610F) image of one of the dispersed and well-separated ZnO SNW with approximate length of 4 μm and a diameter (width) of $\sim$ 300-350 nm. The elemental composition in an individual ZnO NW is verified through Energy-dispersive X-ray spectroscopy (EDS) [Make: Zeiss, Model: Sigma] as shown in Figure 5.3(c). It is confirmed that ZnO SNW is a single-crystalline material with (100) being the dominant crystal plane as per the Selected area electron-diffraction (SAED) pattern shown in Figure 5.3(d). The ZnO SNW has hexagonal wurtzite structure and (100), (002) and (101) lattice planes [96, 112].

5.3.2 Electrical Characterization for printed Schottky diodes

The initial level electrical characterization of the Schottky diodes has been performed with the help of Keithley 4200A-SCS Parametric Analyzer and DC probe station [Make: EverBeing, Model: BD6]. However, it is observed that a slight disturbance in the probe tip contact, can result into shifts in I-V curves [36]. Therefore, to avoid such issues, the Schottky diode with printed AgNP contact pads is extended and connected to copper tape (Cu-tape) pasted on the same SiO_2/Si substrate as shown in Figure 5.4(a-d). The overall device is connected to Parametric Analyzer with the help of low-noise coaxial cables and crocodile clips as shown in Figure 5.4(e). Figure 5.5(a) shows the FESEM image of the fabricated Schottky diode structure with printed AgNP contact pads, ZnO SNW channel and

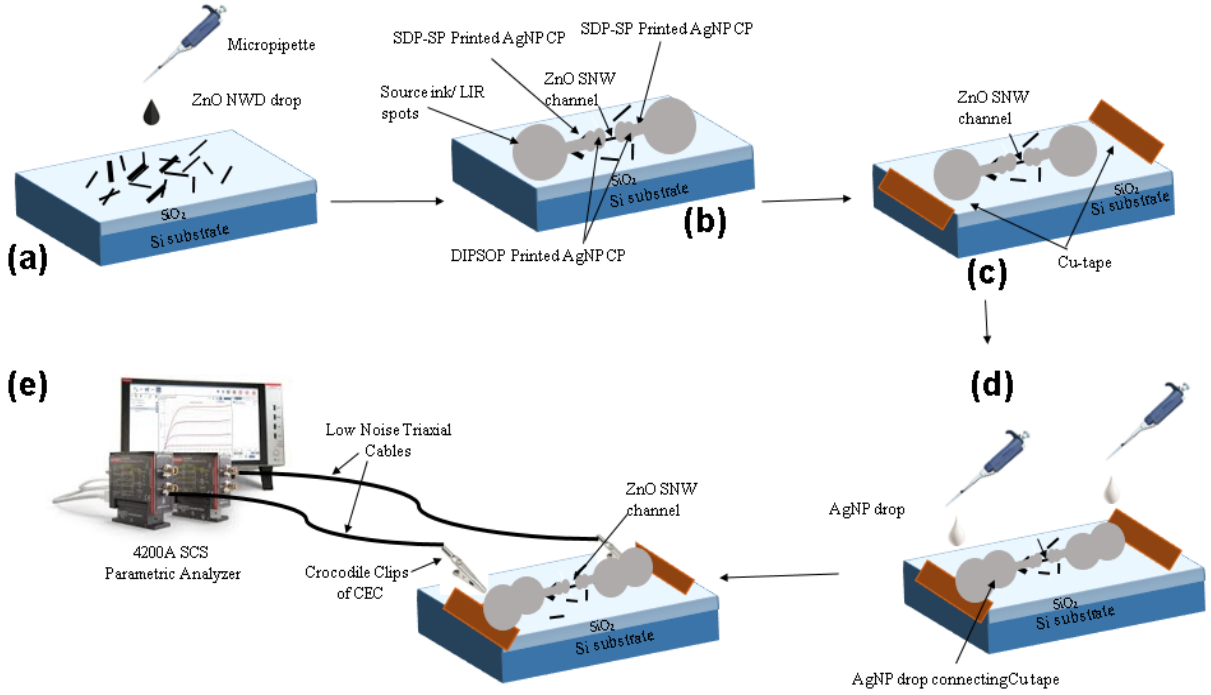

Fig. 5.4: Schematic showing complete flow of device fabrication process and electrical characterization set-up.(a) ZnO NWD drop-casting (b) AgNP CP formation on both sides of selected SNW using MCP techniques (c) Cu-tape attachment on substrate (d) Cu-tape connected to device metal CP (e) Device connected to parametric analyzer. NWD: Nanowire dispersion, CP: Contact pad

Cu-tape connections. Figure 5.5(b) shows the magnified FESEM image of ZnO SNW channel of length near 5 μm and diameter (width) $\sim$ 350 nm with DIPSOP printed AgNP contacts overlapped with both sides of ZnO SNW channel.

The I-V characteristics shown in Figure 5.6(a) depict the behaviour of back-to-back Schottky-contact devices [93, 103, 115, 116]. The experimental results have been verified by using thermionic emission diode current model represented as [117, 118]

$$I_{SDP,N} = SA^*T^2e^{\frac{-q\phi_{BP,N}}{kT}}[e^{\frac{-qV_{P,N}}{\eta kT}} - 1] \tag{5.1}$$

where, $I_{SDP,N}$ is the diode current, $\phi_{BP,N}$ is the Schottky barrier height for positive and negative voltage sweep, S is the Schottky contact area (1 μm length $\times$ 400 nm width), A* is the effective Richardson constant (8.6 A cm^{-2} K^{-2}), q is the elementary charge, k is the Boltzmann's constant, T is the absolute temperature (300 K), $V_{P,N}$ is the positive and negative voltage sweep, η is the ideality factor which is extracted as the slope of linear region of ln(I)-V plots for $V_{P,N} > 3kT$ [103] as shown in Figure 5.6(b). Using the Cheung and Cheung method [117], the $R_{sp,n}$ series resistance of the printed

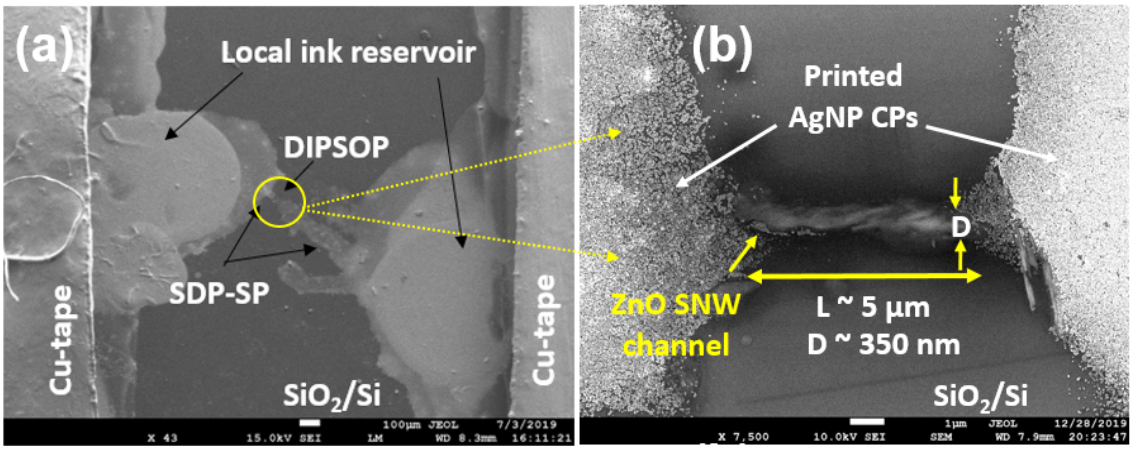

Fig. 5.5: (a) FESEM image of a representative complete Schottky diode with ZnO SNW channel, scale: 100 μm (b) Magnified FESEM image of the channel region with AgNP printed pads. L, D: Length, Diameter of ZnO SNW

Schottky diodes, for positive or negative applied bias, can be obtained as the slope of a linear portion of dV/dln(I) versus I (Figure 5.7(a)) with ηkT/q as the intercept as shown below

$$\frac{dV}{d(\ln I)} = \frac{\eta kT}{q} + I_{SDP}R_{sp} \tag{5.2}$$

The η obtained from the above equation is used to determine the diode barrier height with the help of following equation [117, 118]

$$H_{P,N}(I) = V_{P,N} - \frac{\eta kT}{q}\ln\frac{I_{SDP,N}}{SA^*T^2} = \eta\phi_{BP,N} + I_{SDP,N}R_{sp,n} \tag{5.3}$$

where, $\eta\phi_{BP,N}$ is the intercept of the above equation and $R_{sp,n}$ is the slope of this line (Figure 5.7(a)). The values of $R_{sp,n}$ extracted from H(I)-I plot can be used to verify the same extracted from dv/dln(I)-I plot and can be used to model the Schottky barrier height as follows:

$$\phi_{BP,N} = \frac{kT}{q}\ln\frac{SA^*T^2R_{sp,n}}{V_{P,N}} \tag{5.4}$$

Figure 5.7(b) shows the I-V curves for another printed diode (D4) for multiple runs to verify the repeatability of the proposed fabrication process. It is observed that I-V characteristics are consistent in each run which validates the repeatability of the printing process. Table 5.2 summaries the electrical parameters of three representative Schottky diodes (out of 20 printed devices) extracted using different methods. Table 5.3 shows the device count in the bracket given beside each electrical parameter for

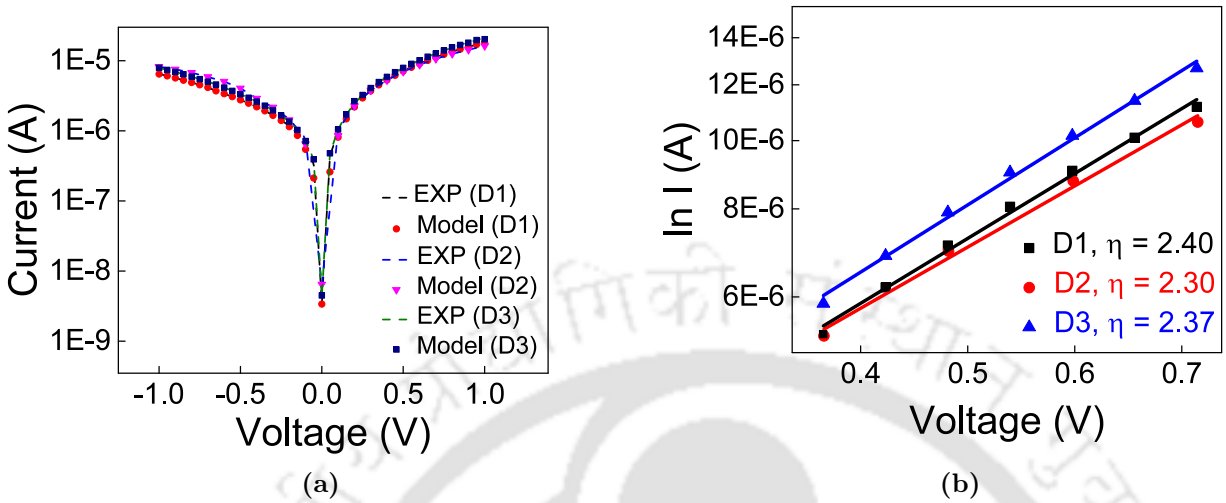

Fig. 5.6: (a) Semi-logarithmic I-V characteristics for three representative printed BBSDs along with model results (b) The ln(I)-V plots of printed diodes with straight lines as linear fit to the experimental data

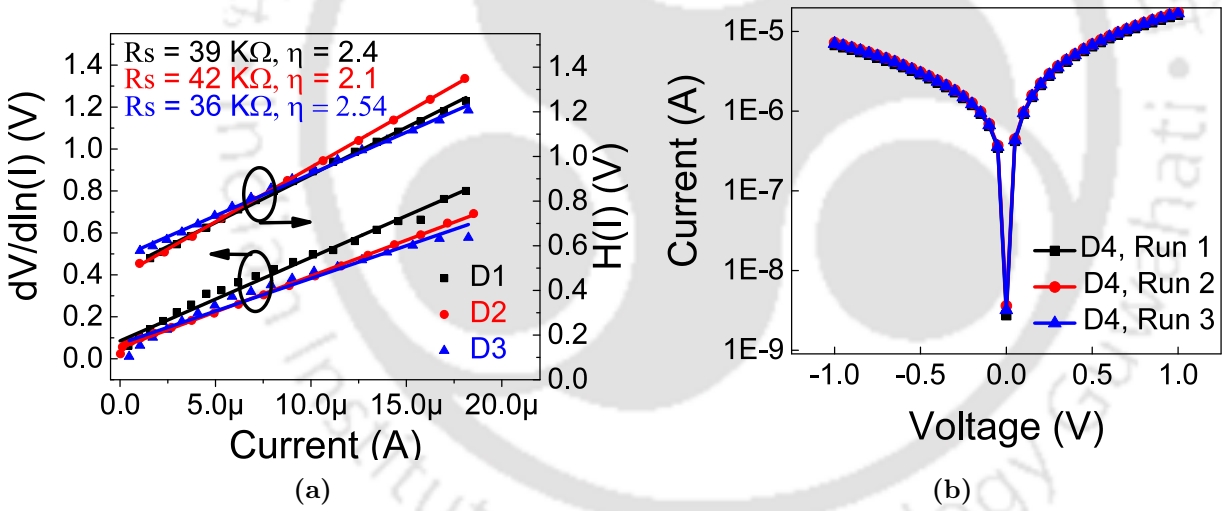

Fig. 5.7: (a) The dV/dln(I) vs. I and H(I) vs. I plots of printed diodes. Straight lines are linear fit to the experimental data (b) I-V curves under repeatable runs for D4

all the fabricated devices. It is observed in Table 5.2 that the electrical parameters extracted from the I-V characteristics of MCP based Schottky diodes are comparable to those reported earlier. Further, the barrier height of $\sim$ 0.17 eV, obtained for device D1 and D2 are in good match with the barrier height of $\sim$ 0.16 eV reported by Schottky-Mott model for Ag Schottky diodes [119]. These are not the best reported parameters as far as Schottky diodes are concerned, but this indicates the capability and applicability of MCP technology for the fabrication of electronic devices. However, MCP technology is in its emerging phase and needs further optimisation to improve the electrical parameters of the

Table 5.2: Electrical parameters for the micro-cantilever printed-Schottky diodes

Device	η_1, η_2	$R_{sn1,2}$ (kΩ)	$R_{sp1,2}$ (kΩ)	ϕ_{BN} (eV)	ϕ_{BP} (eV)	I_{on}/I_{off}	-ve Turn-ON voltage (mV)	+ve Turn-ON voltage (mV)	Applied Voltage (V)	Measured Current
D1	2.4, 2.4	NA, 180	38, 39	0.17	0.22	5326	50	50	± 1	-6.4 to 18 μA
D2	2.3, 2.1	NA, 140	34, 42	0.2	0.21	2492	100	100	± 1	-8.2 to 16 μA
D3	2.37, 2.54	NA, 107	30, 36	0.23	0.24	5041	50	50	± 1	-8 to 21 μA
[17]	2.02, 2.7	NA, NA	270, NA	NA	0.69	6.6×10^4	NA	75	± 1	~ 0.25 μA
[118]	2, 2.8	NA, NA	0.008, 0.006	NA	0.54	NA	NA	NA	± 1	0.005 to 0.05 A
[119]	1.2, NA	NA, NA	25	NA	0.78	10^4	NA	NA	- 1	- 0.2 μA
[115]	1.009, NA	NA, NA	NA, NA	0.42	0.41	NA	NA	NA	± 10	± 20 μA

$\eta_{1,2}$: ln(V)-I, dV/dln(I)-I; $R_{sn1,2}$ ($R_{sp1,2}$): Series resistance for negative (positive) voltage sweep from dV/ln(I)-I, H(I)-I;
ϕ_{BN} (ϕ_{BP}): Barrier height for negative (positive) voltage sweep

Table 5.3: Distribution of all fabricated devices based on different electrical parameters

Channel Length (μm)	η_1	ϕ_{BP} **(eV)**	R_{sp2} **(kΩ)**	I_{on}/I_{off}	**AER (kΩ)**
Sub-10 (12)	<2 (1)	0.2 - 0.25 (17)	<40 (9)	<4000 (2)	<130 (12)
10 - 15 (5)	2 - 2.5 (14)	>0.25 (3)	40 - 50 (10)	4000 - 10000 (13)	130 - 300 (5)
15 - 20 (3)	2.5 - 3 (3)		>50 (1)	>10000 (5)	>300 (3)
	>3 (2)				

printed devices.

Figure 5.8(a) shows the electrical behaviour of the D2 (as an representative) under two different polarity bias conditions where in first case, the voltage is swept from ± 5 V (Run 1) and then polarity is interchanged between the two contact pads and the voltage is swept from ± 5 V again (Run 2). It is observed that current behaviour and I_{on}/I_{off} ratio remains same in both runs which implies that the MCP technology is able to print metal contacts with uniform thickness and similar interface properties along the both ends of ZnO SNW channel. Figure 5.8(b) shows the I-V characteristics of D2 after 6 months which shows that the printed diodes are electrically stable and maintain the back-to-back Schottky behaviour. This in turn also implies that the printed metal contacts are also stable during this observation time with a slight (~ half-order) drop in the current density of the diode.

5.4 ZnO SNW Schottky diode-based gas sensors

5.4.1 Introduction

Many reports describe the usage of ZnO SNWs for the fabrication of Schottky diodes [19,108]. These reports focus on various aspects related to the device-physics such as modes of electronic transport, the

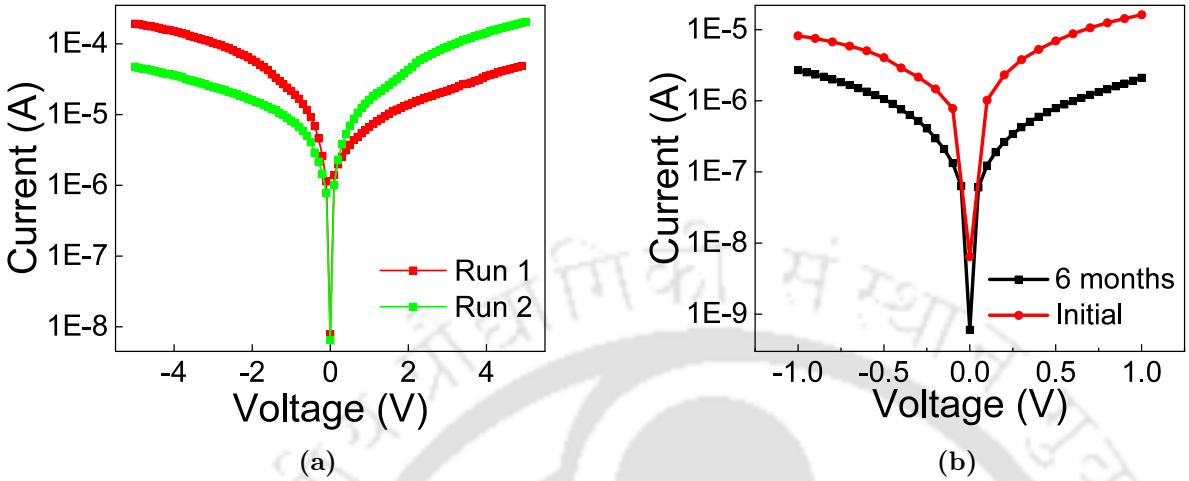

Fig. 5.8: (a) I-V response analysis under interchanged polarity bias conditions for D2 (b) I-V curve based comparison of D2 at initial stage and after 6 months of fabrication

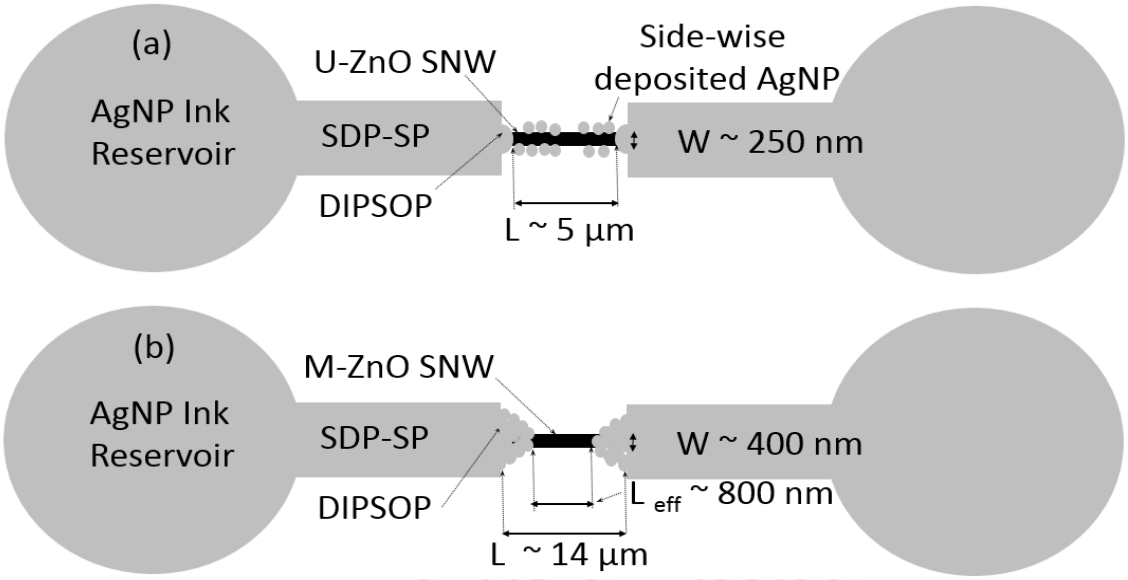

Fig. 5.9: Schematic diagram of Schottky diode based on (a) Unmodified ZnO (U-ZnO) SNW with side-wise deposited AgNP thin layer (b) Modified ZnO (M-ZnO) SNW. L: Channel Length, W: Channel Width or NW diameter.

on-off current ratio, metal-semiconductor interface analysis, resistive switching behaviour of ZnO SNW based-diodes etc. [102, 120, 121]. However, there are only a few reports about the usage of ZnO SNW based Schottky diodes for gas sensing applications. Lupan et al. have investigated the performance of single and multiple ZnO nanowire functionalized with Au nanoparticles for H_2 sensing [122]. Cardoza et al. have presented ZnO SNWs based gas sensors to detect low concentrations of hydrogen [123]. Rui et al. have shown excellent sensitivity and fast recovery time for Ammonia detection through resistive

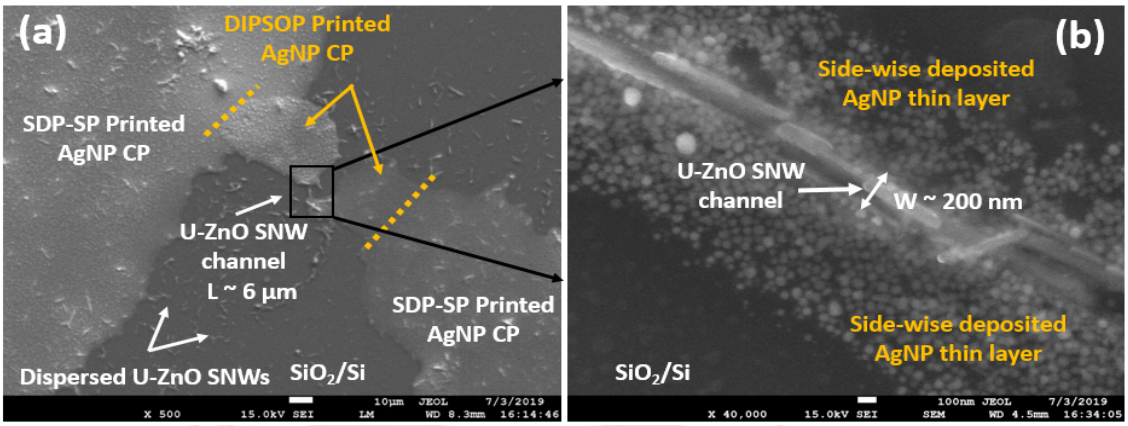

Fig. 5.10: (a) FESEM image of complete device with U-ZnO SNW channel shown in inset (e,f) Magnified FESEM image of U-ZnO SNW channel with side-wise deposited AgNP layer. CP: Contact pad

switching of ZnO nanowire [124]. Multiple ZnO nanowires based resistive devices have been used to detect CO_2 and CO [87, 125]. There are reports for NO_2 detection at 1 ppm using functionalized ZnO nanowires [126, 127]. Hong et al. have reported the fabrication of Schottky diodes based on comb-like ZnO nanostructures for CO sensing at RT [86]. Chen et al. have used facile hydrothermal route to grow ZnO nanowires to detect NO_2 in the range of 1-30 ppm at 250°C [128]. However, ZnO SNW based Schottky diodes have not been reported so far the detection of CO_2 or CO.

Schottky-contact based sensors have been reported to show a higher response ($\sim$ 4 times) than Ohmic-contacted sensors for CO detection at 275°C [129]. Hu et al. have also stated that the Schottky barrier at the contact area plays a key role in sensor response to the adsorbed gas molecules [108]. However, proper placement of metal contact pads to connect the ZnO SNW involves costly equipment and silicon microfabrication technologies like electron-beam lithography, thermal evaporation and so on.

In this work, ZnO SNW based Schottky diodes are fabricated by placing ZnO SNWs on a clean SiO_2/Si substrate by dispersion drop-casting technique and AgNP contact pads have been fabricated with micro-cantilever printing technology which is simple, rapid and cost-effective [36]. Figure 5.9 shows the conceptual schematic diagram of the proposed device. It is shown in this work, that ZnO SNW based Schottky diodes can sense CO_2 and CO at RT with higher sensitivity and a low response time. To the best of our knowledge, there are no reports on the fabrication of ZnO SNW based Schottky diodes using dispersion-processed and micro-cantilever printing techniques for detection of air pollutants at RT.

5.5 Materials and Methods

5.5.1 Fabrication of ZnO SNW Schottky diode using DI water as dispersion medium

ZnO Nanowire powder and AgNP ink are procured from Sigma Aldrich (Product Id: 773999, 736481). The specified average length and diameter of the as-purchased ZnO nanowire is 1 μm and 90 nm respectively. The AgNP ink is 30-35 wt.% dispersion of silver nanoparticles in triethylene glycol monoethyl ether. 3 mg of as purchased ZnO nanowire powder is added to 1 mL of DI water having a resistivity of 18.2 M-cm. 5 μL from the prepared ZnO nanowire dispersion is drop-casted over a clean SiO_2/Si substrate at a temperature near 180-190°C for proper dissemination of SNWs. Printing experiments are performed using a thermally grown silicon dioxide micro-cantilever as surface patterning tool [36, 130]. The micro-cantilever tip is deliberately dipped in a local ink reservoir and dragged to a longer length (∼1000 μm) separating a small volume of ink from the source. The separated volume of the ink is uniformly distributed over the dragged area when the tip is lifted up gradually. This technique of printing is referred to as surface patterning tool drag printing assisted self-printing (SDP-SP) [131]. The micro-cantilever is made to gently touch the upper periphery of the local ink reservoir to draw some ink into its channels and readily print the microspots by ultrafine positioning to reinforce the metal-nanowire interface. This technique of printing is referred to as dip-ink printing with spot overwrite printing (DIPSOP) [36, 131]

Figure B.2(a) shows the Field Emission Scanning Electron Microscope (FESEM)(Make: JEOL, Model: JSM-7610F) image of the complete device with printed AgNP contact pads with ZnO SNW channel of length near 6 μm and 200 nm with a thin discontinuous layer of AgNP deposited along the sides of ZnO SNW channel due to solvophilic response of ZnO SNW towards AgNP, as shown in Figure B.2(b). The typical diameter of a DIPSOP microspot is ∼ 5-10 μm and it is ensured that 1-2 μm of the peripheral region of the microspot touches the end of the ZnO SNW by targeting a proper hit region [131]. However, the non-uniformity of the substrate and the distance from which the micro-cantilever hits the substrate may result in misaligned printing and over-spread on the ink respectively, which can shift the periphery of the microspot ΔX μm further over the ZnO SNW, as shown in Figure 5.11. This increases the risk of short-circuit between metal pads if the length of ZnO SNW is < 10 μm. Therefore, a ZnO SNW with length > 10 μm ensures that there is no short-circuit between the metal pads in case of such variabilities. Table 5.4 presents a comparative analysis

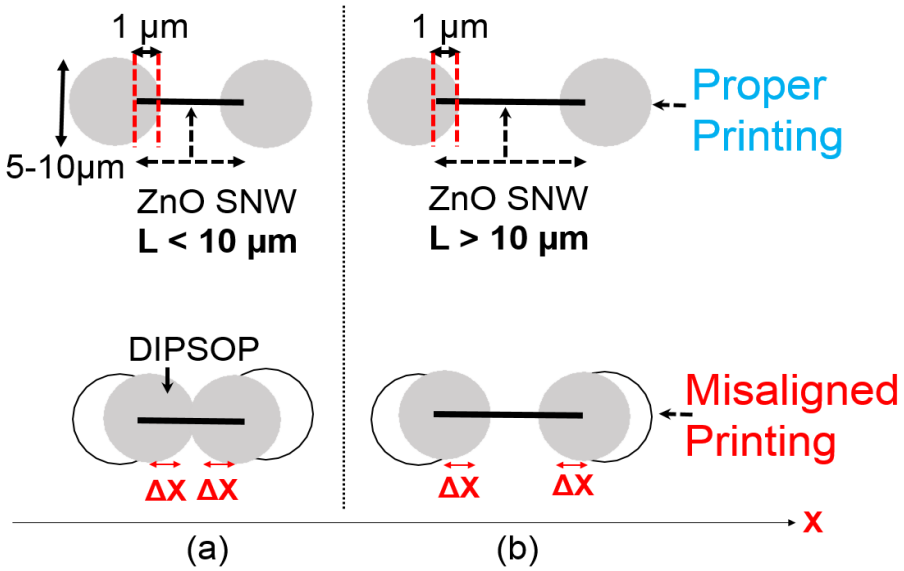

Fig. 5.11: Schematic showing (a) short-circuiting for ZnO SNW with L $<$ 10 μm (b) the prevention of short-circuiting by ZnO SNW with L $>$ 10 μm, in case of misaligned printing.

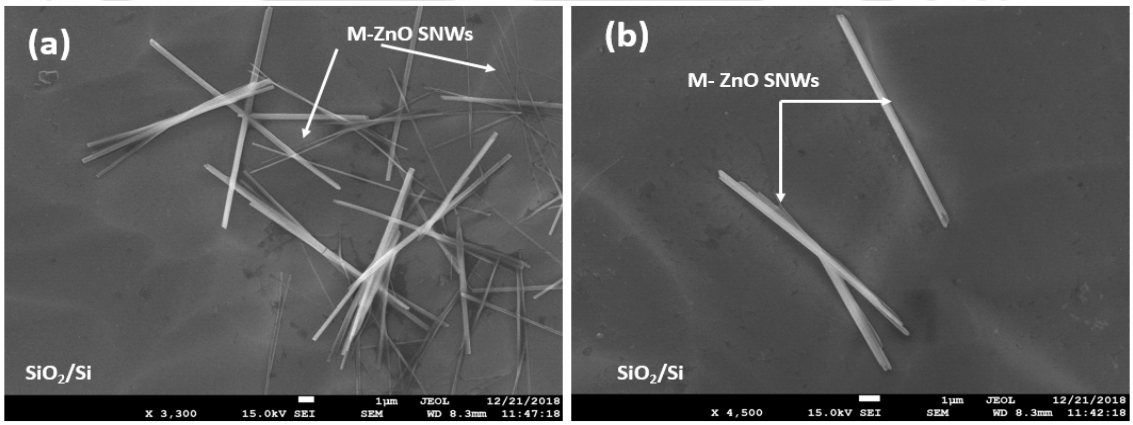

Fig. 5.12: Effect of acetic acid and SDS on morphology of M-ZnO SNWs (a) FESEM image showing cluster of M-ZnO SNWs of length $>$ 10 μm and width varying in range of $\sim$ 90 nm to 400 nm (b) FESEM image showing well separated M-ZnO SNWs

between different print set-ups and ZnO SNW dimensions to show the benefits of L $>$ 10 μm. The size and morphology of the SNWs dispersed in DI water is not modified. Hence, these are referred to as unmodified ZnO single nanowire (U-ZnO SNW).

5.5.2 Fabrication of ZnO SNW Schottky diode using SDS and acetic acid added DI water as dispersion medium

This section details the synthesis of ZnO SNWs with length $>$ 10 μm for the fabrication of Schottky diodes. With the inputs from the previous reports [94, 95, 132–134], 1 mg of SDS is added in 5 mL of DI water to lower down the surface tension of the solution to better disperse the clusters into smaller

Table 5.4: Comparative analysis between different print set-ups and ZnO SNW dimensions

Distance between micro-cantilever and the substrate	**DIPSOP Microspot Diameter(μm)**	**ZnO SNW (L < 10 μm)**	**ZnO SNW (L > 10 μm)**
30 μm (Hard Hit)	~10 μm	High chance of short-circuit (SC) and ink over-spread	Very less chance of SC
40 μm (Moderate Hit)	Between 5-10 μm	Less chance of SC, Optimized ink spread	No SC, Optimized ink spread
50 μm (Soft Hit)	~5 μm	Less chance of SC	No SC

aggregates of nanowires. Further, 1.2 mL of this solution is taken out separately, and 2 mg of ZnO nanowire powder is dispersed in it. This ZnO nanowire dispersion is treated with Vortex generator for proper mixing. 2 μL of this dispersion is added with the same amount of acetic acid and drop-casted on the SiO_2/Si substrate.

It is observed that the addition of acetic acid with the dispersion in equal proportion can separate the ZnO SNWs significantly and form longer (> 10 μm) ZnO SNWs, as shown in Figure C.2(a). The addition of acetic acid to the dispersion causes the following reaction sequence: (a) the acid partially dissolves the ZnO nanowires, and thus the droplet on the surface has Zn^{2+} ions as well as OH^- ions. Smaller nanowires in the dispersion would tend to dissolve faster (b) as the drop-cast solution is heated, the remaining larger nanowires act as seeding surfaces, and ZnO regrows. This enlarges the diameter and the length of the original nanowires. This process is known as dissolution-regrowth, and is limited by volume diffusion and solvent evaporation kinetics [135, 136]. Further, the size and orientation of the re-grown nanowire assemblies depends upon the concentration of the SDS. The addition of a higher concentration of acetic acid to dispersion (in 3:1 ratio) results in an enhanced separation between the ZnO SNWs as shown in Figure C.2(b). However, further addition of a higher concentration of acetic acid results in the complete or partial dissolution of ZnO SNWs in the acid. The SNWs synthesized using 3:1 ratio of acetic acid to ZnO nanowire dispersion convert into ZnO micro-particles when heated at higher temperatures, near 250 °C. This shows that ZnO SNWs synthesized using a higher concentration of acetic acid are not thermally stable and hence not suitable for sensing applications at higher temperatures. Therefore, mixing of acetic acid with the dispersion in 1:1 proportion is considered as the optimized concentration to fabricate ZnO SNW based devices for gas sensing applications. Since SDS and acetic acid modify the size and morphology of these ZnO

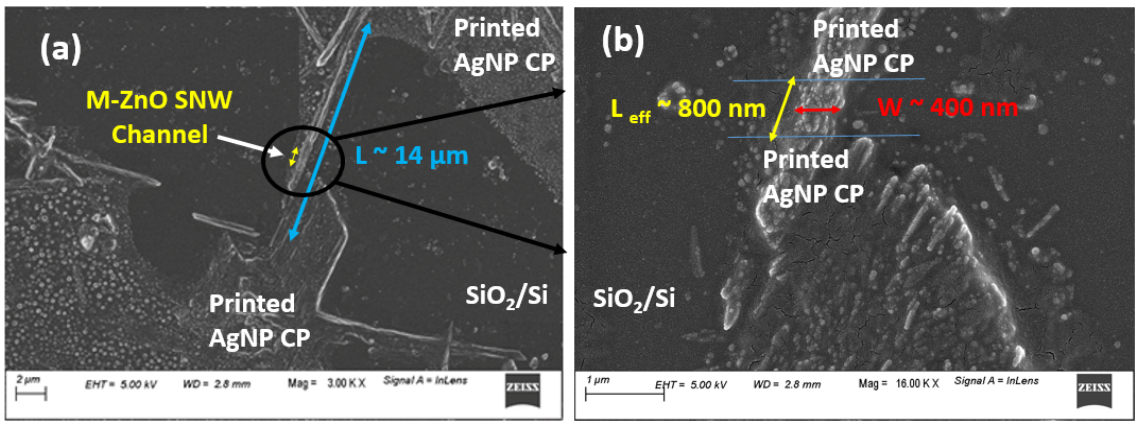

Fig. 5.13: (a) FESEM image of M-ZnO SNW channel based diode (b) Magnified FESEM image of (a) showing effective channel length L_{eff} as 800 nm.

SNWs, these are referred to as modified ZnO single-nanowires (M-ZnO SNWs).

Figure 5.13 (a) shows the FESEM image of M-ZnO SNW based diode and Figure 5.13 (b) shows the magnified image of (a). It is observed in Figure 5.13(b) that AgNP ink spreads over the entire ZnO SNW surface from its both ends after DIPSOP is performed. This indicates that solvophilic response of ZnO SNW to AgNP ink increases after acetic acid and SDS treatment. The ink-spread happening at the time of DIPSOP also reduces the effective length of the NW channel from $\sim$ 14 μm effectively to $\sim$ 800 nm (17.5 times), as shown in Figure 5.13(b). But the shorting of two contact pads is avoided due to longer SNW. Such a fabrication process is scalable as this self-assembly based metal deposition is controlled by optimizing the chemical and physical properties of the metal ink, proper placement of the DIPSOP spots at the metal-SNW interface after analysing the ink-diffusion rate through the ZnO SNW channel.

5.5.3 Sensor preparation and gas sensing conditions

The sensor fabrication process and gas sensing set-up is same as described in our previous papers [112, 137]. The gas sensing chamber is pressurised to atmospheric pressure maintaining the relative humidity (RH) below 1 % at RT for each cycle of sensing.

5.6 Results and Discussion

5.6.1 Characterization of ZnO SNW

Figure 5.14 shows the X-ray Diffraction (XRD) [Make: Rigaku, Model: Micromax-007HF] spectra of ZnO SNWs in three different dispersion media. Three major peaks are observed for 2θ value of 31.8°,

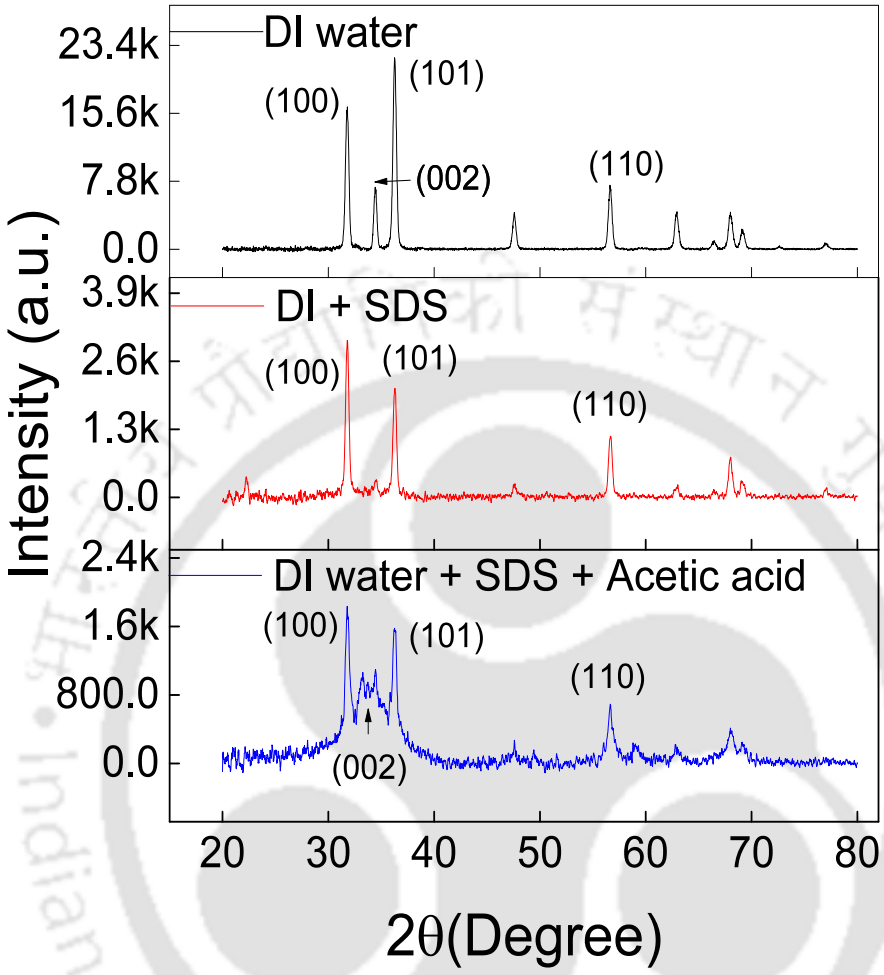

Fig. 5.14: XRD spectra for ZnO nanowires dispersed in various media

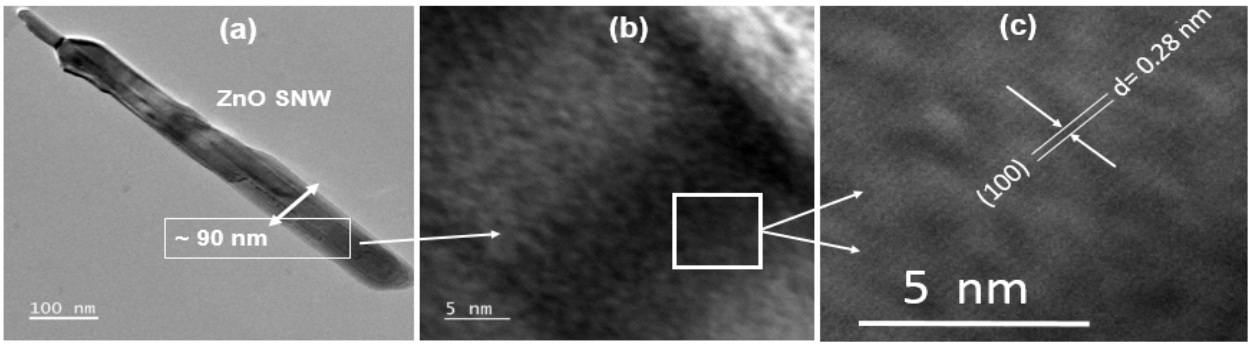

Fig. 5.15: (a) FETEM image of a ZnO SNW (b, c) FETEM images showing lattice planes and d-spacing of 0.28 nm corresponding to (100) plane

34.44° and 36.26° for ZnO SNWs dispersed in DI water which corresponds to ZnO hexagonal wurtzite structure and (100), (002) and (101) lattice planes respectively, according to the JCPDS database (36-1451) [96]. Similarly, the major peaks observed for ZnO SNWs dispersed in (DI water+ SDS)

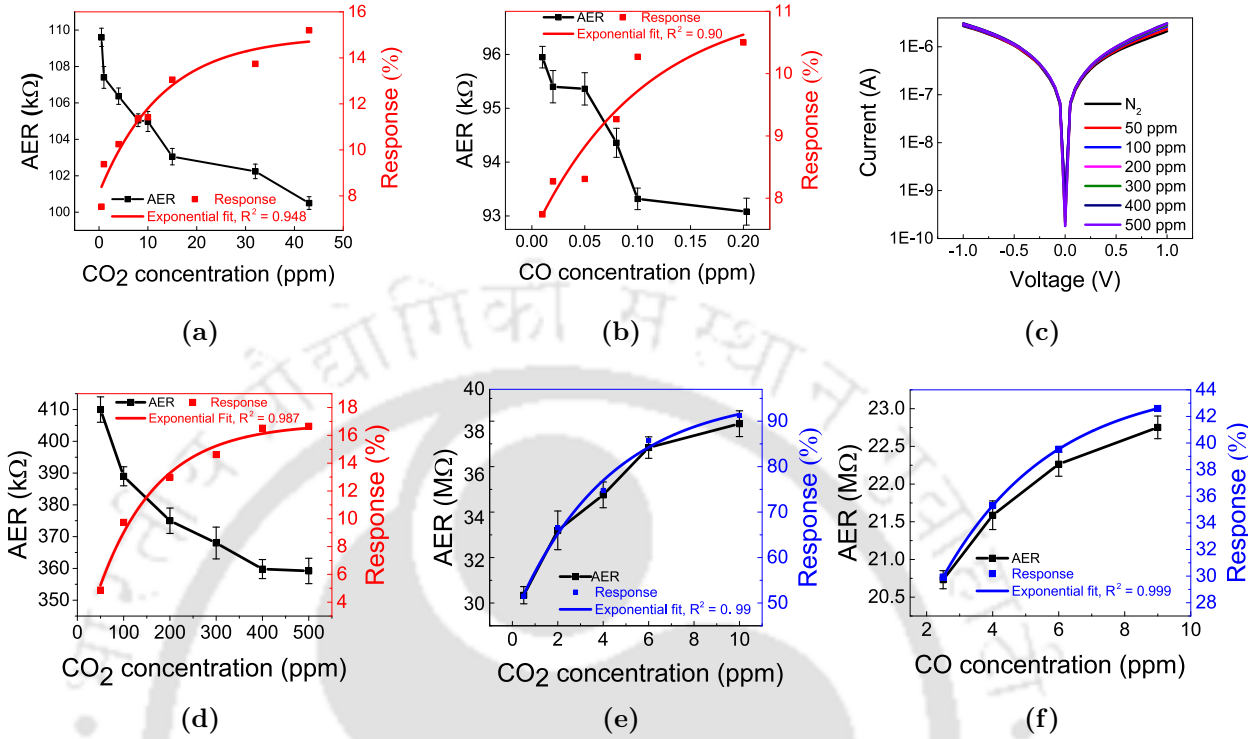

Fig. 5.16: (a) AER variation with CO_2 concentration and response of U-ZnO SNW diode-based sensor for lower concentration range of CO_2 (b) AER variation with CO concentration and response of U-ZnO SNW diode-based CO sensor (c) I-V response of U-ZnO SNW (d) AER variation with CO_2 concentration and response of U-ZnO SNW diode-based sensor for higher concentration range of CO_2 (e) AER variation with CO_2 concentration and response of M-ZnO SNW diode-based CO_2 sensor (f) AER variation with CO concentration and response of M-ZnO SNW diode-based CO sensor

and (DI water + SDS + Acetic acid) also correspond to ZnO hexagonal wurtzite structure. However, the absence of some of the peaks and decrease in the signal intensity hints towards treatment of ZnO SNWs with SDS, which may increase the active sites for analyte gas adsorption to improve the sensor response [132]. The peak broadening observed due to acetic acid reduces the crystallite size resulting in the increase of surface defects and produces non-uniform lattice strain in ZnO SNW.

Field Emission Transmission Electron Microscope (FETEM) [Make: JEOL, Model-2100F] images are taken for ZnO SNW dispersed in DI water. Figure 5.15(a) shows FETEM image of a ZnO SNW having a diameter of $\sim$ 90 nm and length $\sim$ 1 μm. Further, the spacing between two lattice planes (d-spacing) of 0.28 nm was measured form FETEM image as shown in Figure 5.15(b,c) which corresponds to (100) plane as per the JCPDS database (36-1451) [96].

The fabricated Schottky diodes are electrically characterized using Keithley 4200A-SCS parametric analyzer to verify their functionality [131].

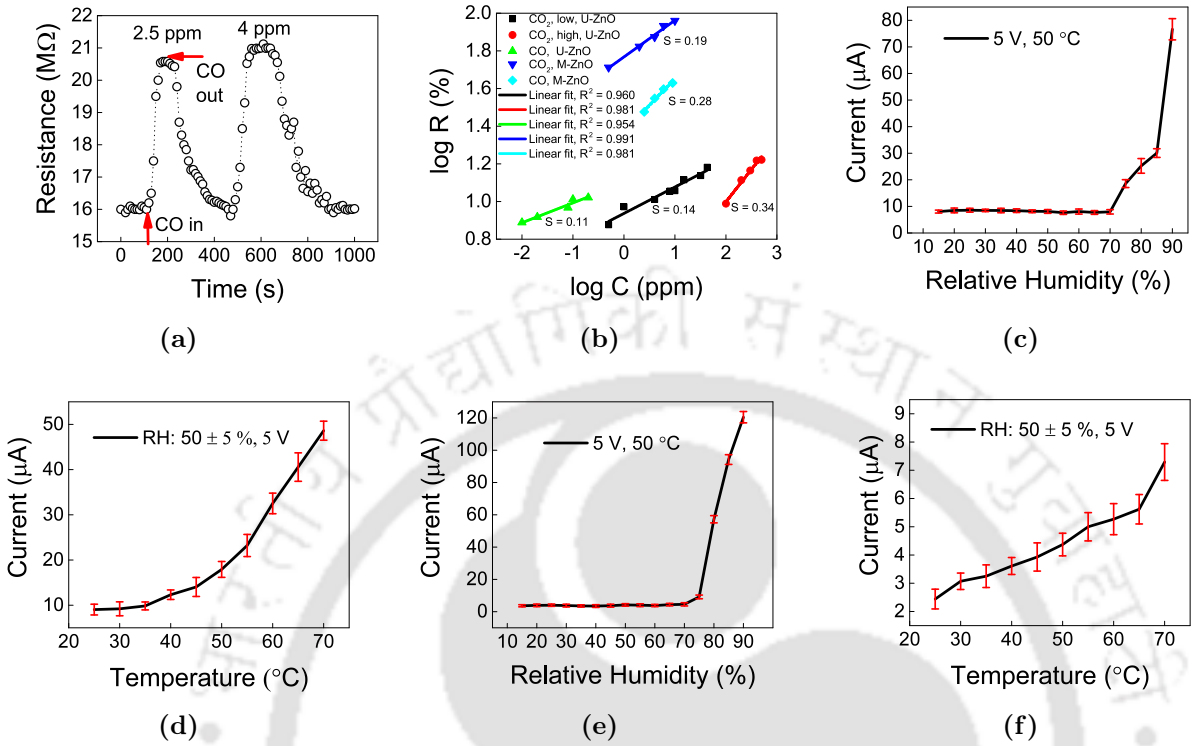

Fig. 5.17: (a)Approximated transient response of M-ZnO SNW diode-based CO sensor at RT (b) log S vs log C plots and their linear fit. U-ZnO SNW based diode current (c) under varying humidity (d) under varying temperature. M-ZnO SNW based diode current (e) under varying humidity (f) under varying temperature

5.6.2 Sensing response of U-ZnO SNW Schottky diode based sensor

Figure 5.16(a) shows the response curve of U-ZnO SNW based sensor for CO_2 for lower concentration range from 500 ppb to 43 ppm. A decreasing trend of average electrical resistance (AER) with CO_2 concentration is observed, which is in-line with previous reports [105, 138]. The gas sensor response, R, is represented as

$$R = \frac{|R_g - R_a|}{R_a} \times 100\% \tag{5.5}$$

where R_g represents the AER for analyte gas for a particular concentration and R_a represents the baseline resistance of the device [112]. The baseline resistance, R_a, is the average electrical resistance of the sensor when the gas-sensing chamber is pressurized to atmospheric pressure using the base (carrier) base N_2. Figure 5.16(b) shows that AER decreases with an increase in CO concentration for U-ZnO SNW based sensor, which is in-line with published reports [86, 91].

To observe the effect of O_2 present in the air on the response of our fabricated sensor, we pressurized the gas sensing chamber with 10% O_2. In the presence of 10% O_2, the sensitivity increases from 0.11 %/ppm to 0.32 %/ppm for U-ZnO SNW based CO sensor. The probable reasons for the increase in

this sensitivity can be the augmented chemisorption rate of O_2^- on the ZnO nanowire surface due to the presence of a larger number of oxygen molecules, which enhances the charge transfer rate between the nanowire surface and CO. Despite the improvement in the sensitivity, it is observed that selectivity of this sensor is suppressed in presence of 10% O_2 as the response of this sensor drops down from 11 % to 8.1 % for 0.2 ppm CO. Therefore, it can be concluded that the cross-sensitivity of the fabricated sensors is affected in the atmospheric air, which can be optimized for practical applications.

Figure 5.16(c) shows the I-V response of U-ZnO SNW based sensor and Figure 5.16(d) shows the AER variation and response of U-ZnO SNW based sensor for a higher concentration range of CO_2 from 50 ppm to 500 ppm. The decreasing AER trend as observed in the case of detection of lower CO_2 concentrations is also observed for higher CO_2 concentrations.

5.6.3 Sensing response of M-ZnO SNW Schottky diode based sensor

The M-ZnO SNW Schottky diode based sensor response towards CO_2 and CO is shown in Figure 5.16(e and f). Figure 5.16(e) shows that AER increases with an increase in the concentration of CO_2 using a M-ZnO SNW based sensor. A similar trend is reported in [92]. Figure 5.16(f) shows an increasing trend of AER with CO concentration for M-ZnO SNW based sensor similar to [139, 140]. The Figure 5.17(a) shows a representative transient response of this sensor for CO detection from 2.5 ppm to 4 ppm range. The Gas IN phase starts when the gas sensing chamber is pressurized to the atmospheric pressure with carrier and analyte gas and Gas OUT phase starts when the flow of the analyte gas is stopped [112]. This sensor shows a response time of 20-60 s and a recovery time of $\sim$ 5 minutes.

The response of sensors in the presence of different kinds of volatile organic compounds (VOCs) such as ethanol (C_2H_5OH), IPA (C_3H_8O), and Acetone (C_3H_6O) has also been analysed. It is found that SDS treatment makes M-ZnO SNW based sensor more selective towards air pollutants as compared to U-ZnO SNW based sensor as shown in the Table 5.6. The sensors also show stable electrical behaviour over a period of more than 1 year as there is a slight shift in their average electrical resistance.

5.6.4 Sensitivity calculation

The response (%) holds an empirical relationship with analyte gas concentration (C) given as [139]

$$R = AC^S \tag{5.6}$$

Table 5.5: Comparison of response of U-ZnO SNW and M-ZnO SNW based sensor upon exposure to different kinds of gases and VOCs at Room Temperature

U-ZnO SNW based sensor			**M-ZnO SNW based sensor**		
Analyte Gas	Gas Concentration (ppm)	Response (%)	Analyte Gas	Gas Concentration (ppm)	Response (%)
CO_2	43	**15.2**	CO_2	10	**91**
C_3H_8O	100	12	CO	9	43
CO	0.2	11	NO_2	10	17.8
NO_2	10	10.6	C_3H_8O	100	9.6
C_2H_5OH	100	9	C_2H_5OH	100	8.7
C_3H_6O	100	3.7	C_3H_6O	100	4.7

Table 5.6: Long-term electrical stability of the sensors

U-ZnO SNW based sensor			**M-ZnO SNW based sensor**		
Measurement	Voltage and Current Range	Average Resistance (kΩ)	Measurement	Voltage and Current Range)	Average Resistance(MΩ)
Initial	±1 V, -169 nA-20 μA	137	Initial	±5 V, -5 nA-14 μA	20
After 12 Months	(6-10) V, (33-85) μA	144	After 12 Months	±5 V, -2.5 nA-19 μA	21.5

where, A is a constant and âĂŸSâĂŹ gives the sensitivity of the sensor. Therefore, in accordance with Eqn.5.6, we have plotted log R (%) vs log C (ppm) which yields a straight line as shown in Figure 5.17(b). The slope of linear fit of this straight line gives the sensitivity in %/ppm of the fabricated sensors. The U-ZnO SNW based sensors show a sensitivity of 0.14 %/ppm, 0.34 %/ppm and 0.11 %/ppm for CO_2 low range, CO_2 high range and CO respectively. The M-ZnO SNW based sensors show a sensitivity of 0.19 %/ppm and 0.28 %/ppm CO_2 and CO respectively.

One of the reasons for high sensitivity shown by U-ZnO SNW based sensors for CO_2 can be the presence of side-wise deposited AgNP layer, that initially dissociates more of oxygen molecules to O_2^- which are chemisorbed on the ZnO SNW surface at RT [91, 138]. These oxygen ions interact with the analyte gas molecule and a higher electron transfer takes place in the ZnO SNWs resulting in an enhanced sensitivity. While the SDS treated M-ZnO SNW enabling interaction with CO molecules over a larger surface area can be possible reason for their higher sensitivity towards CO as compared to U-ZnO SNW based sensors.

Table 5.7: Comparison of U-ZnO SNW and M-ZnO SNW-AgNP based gas sensors with other reported sensors

Material	Device	Analyte Gas	Temperature (°C)	Gas conc. (ppm)	Sensitivity (%/ppm)	t_{res}	t_{rec}	Year	Ref.
50% La-loaded ZnO	Resistor	CO_2	400	5000	0.0035	90 s	38 s	2016	[141]
SnO_2âĂŞLaOCl	Resistor	CO_2	400	500-4000	0.0005	3-20 s	4-19 s	2012	[142]
Ga_2O_3 MNW	Resistor	CO	150	10-200	1	5 s	10 s	2014	[143]
ZnO MNW-VN	Resistor	CO	250	200	0.465	1 s	2 ms	2016	[87]
ZnO Nanoflakes	Resistor	CO_2	250	200-1025	0.1125	~ 9-17 s	~ 9-17 s	2019	[105]
CuO-ZnO film	Resistor	CO	325	10-500	0.6	~ 66 s	~ 331 s	2017	[139]
ZnO SNW	Schottky Diode	H_2	RT	500-2000	0.017	55 s	120 s	2019	[144]
ZnO MNW	Resistor	CO	RT	100-1000	0.02	~ 5 s	< 2 min	2017	[91]
U-ZnO SNW	Schottky Diode	CO_2	RT	0.5-43	0.14	~ 5-10 s	~ 5 min	2020	this work
U-ZnO SNW	Schottky Diode	CO_2	RT	50-500	0.34	~ 5-10 s	~ 5-10 min	2020	this work
U-ZnO SNW	Schottky Diode	CO	RT	0.01-0.2	0.11	~ 5-10 s	~ 2-4 min	2020	this work
M-ZnO SNW	Schottky Diode	CO_2	RT	0.5-10	0.19	~ 2-3 min.	~ 10 min.	2020	this work
M-ZnO SNW	Schottky Diode	CO	RT	2.5-9	0.28	~ 20-60 s	~ 5 min	2020	this work

MNW: Multiple nanowires, VN: Vertical network,

5.6.5 Effect of humidity and high temperature

The performance of both types of sensors is tested in varying RH and high-temperature conditions. A tightly closed chamber is heated to 50 °C to stabilize the RH at 15 %. DI water is flown into the chamber at a controlled rate to attain higher RH levels, maintaining the temperature constant at 50 °C [137]. Figure 5.17(c) shows that U-ZnO SNW based sensors show a stable performance in the RH range of (15-70) % after which there is a sharp increase in the sensor current most probably due to the presence of a large number of water molecules on the ZnO SNW surface [137]. The sensors performance is measured under higher temperatures by heating the chamber to 70 °C and maintaining the RH level within 50 ± 5 % with the help of a controlled flow of DI water. It is difficult to maintain the desired RH level when chamber temperature is increased above 70 °C with the existing instrumental set-up. Figure 5.17(d) shows an increase in U-ZnO SNW based sensor current with increasing temperature (a negative temperature coefficient behaviour) which validates the semi-conducting nature of the ZnO SNW channel. Similarly, Figure 5.17(e) shows that M-ZnO SNW based sensor is also stable within an RH range of (15-75) % and shows an negative temperature coefficient behaviour as observed in Figure 5.17(f).

5.6.6 Gas sensing mechanism for U-ZnO SNW based sensor

The CO_2 gas molecules interact with oxygen ions at the lattice sites of ZnO (${O_o}^X$) to form a meta-stable compound (CO_3), which lasts for a very short time, along with neutral oxygen vacancies (${V_o}^X$). The neutral oxygen vacancies ionize and transfer electrons back to the conduction band of the nanowire and hence, AER decreases. The reaction mechanism is presented as follows [138]

$$CO_2(ads) + O_o^X \leftrightarrow CO_3(gas) + V_o^X \tag{5.7}$$

$$V_o^X \leftrightarrow V_o^\bullet + e^- \tag{5.8}$$

where $V_o^\bullet$ is ionized oxygen vacancy.

It is observed that AER decreases with CO concentration which indicates that CO reacts with the adsorbed oxygen ions (O_2^-) on the nanowire surface and donates electrons to the conduction band of ZnO nanowire acting as a reducing agent [87, 145].

5.6.7 Gas sensing mechanism for M-ZnO SNW based sensor

The CO_2 gas molecules interact with adsorbed oxygen ions O_2^- and extracts the electrons from the conduction band of the nanowire, which results in a decrease of electron density at the nanowire surface and AER increases. Therefore, CO_2 acts as an oxidising gas for M-ZnO SNW based sensor. A brief reaction mechanism is mentioned below [92]

$$CO_2 + e^- \rightarrow {CO_2}^-{}_{(adsorbed)} \tag{5.9}$$

Figure 5.16(f) and Figure 5.17(a) show that AER increases with CO concentration similar to previous reports [139, 140]. The major factors that have affected the change in gas sensing mechanism are the treatment of M-ZnO SNW surface with SDS and the larger size of M-ZnO SNW, which affects the surface area to volume ratio. The sensing mechanism is also affected by the reduction of the crystallite size of SNW due to addition of acetic acid in the nanowire dispersion, which can increase the number of surface defects.

5.6.8 Room temperature sensing

The Schottky barrier height and Schottky contact area play a key role in RT gas sensing [108]. Since the contact area of ZnO SNW to the AgNP printed pads are very small, even a small amount of gas adsorption can influence the Schottky barrier height significantly which in turn results in a large variation in diode current passing through the ZnO SNW-AgNP interface. This eventually makes the sensors based on ZnO SNW Schottky diodes highly sensitive to the smaller concentration of analyte gases even at RT. Further, the high surface-to-volume ratio of SNW and presence of a higher number of defects such as oxygen vacancies on the surface of ZnO SNW may help to boost the RT detection of these gases by increasing their adsorption rate on the SNW surface resulting in a large charge transfer [146, 147].

Table 7.2 shows sensitivity, response and recovery time for all the cases discussed in this work

along with a comparison of this work with other reported literature. It is observed from Table 7.2 that sensing performance of fabricated sensors is comparable to the previously reported sensors.

5.7 Summary

This first part of this chapter focuses on the development of a novel fabrication technique for ZnO SNW based Schottky diodes by depositing AgNP contact pads via micro-cantilever based printing technology which is reproducible, highly controlled, low-cost and fast. Schottky diodes with ZnO SNW with length in range of $\sim$ 1-5 μm and diameter in the range of $\sim$ 90-250 nm have been fabricated. The typical ideality factor $\sim$ 2.4 is obtained among our fabricated devices which are comparable to the published results with an average barrier height of 0.18 eV and 0.21 eV for negative and positive voltage bias respectively which is in close proximity to what is predicted by Schottky-Mott model for Ag based Schottky diodes. The obtained series resistance is in range of 30-180 kΩ. The printed diodes also exhibit a fast turn-ON voltage of 50 mV and a higher I_{on}/I_{off} ratio $\sim 10^3$-10^4. The printed diodes are found to be electrically stable even after 12 months.

The second part of this chapter focuses on the usage of ZnO SNW Schottky diodes for the development of low-cost and rapidly fabricable gas sensors capable of detecting harmful air pollutants at RT. Two variants of ZnO SNW based Schottky diodes have been fabricated using micro-cantilever based printing and dispersion-processed techniques. Longer SNWs have been formed by adding the optimal concentration of SDS and acidic acid in ZnO SNW dispersion in DI water which helps to make the sensor fabrication process reproducible and scalable. U-ZnO SNW based sensor can sense CO_2 in the range of 500 ppb to 500 ppm. While the detection of CO_2 in ppm range is useful for air quality measurements, the ppb range detection of CO_2 indicates the detection limit of the device that can be useful in space applications and closed arena like coal-mines. U-ZnO SNW based sensors show a higher sensitivity of 0.34 %/ppm for CO_2 while M-ZnO SNW based sensors show a higher sensitivity of 0.28 %/ppm for CO. It is found that SDS treatment makes M-ZnO SNW based sensor more selective towards CO_2 and CO as compared to U-ZnO SNW based sensors. Schottky barrier height variation on gas adsorption, high surface-to-volume ratio and presence of a large number of surface defects in ZnO SNWs are expected to be primary reasons for making sensing feasible at RT.

6

ZnO Nanowire(s) Based Printed Field-Effect Transistors

Contents

6.1 Introduction

This chapter describes the fabrication of ZnO NW(s) based back-gated field-effect transistors and an analytical model to analyse and understand the mechanism of current transport in these transistors. The fabrication of back-gated FETs is achieved using ZnO NWM and ZnO SNW as channel material with MCP-printed AgNP contact pads as source and drain. The back-to-back Schottky diodes, fabricated in previous chapters, using ZnO NWM and ZnO SNW, are further modified to field-effect transistors by etching the native or grown layer of SiO_2 at the back side of the SiO_2/Si substrate using buffered HF (BHF). Therefore, these FETs are referred to as Schottky barrier FETs (SBFETs). After etching the back side oxide layer, AgNP ink has been drop-casted over the entire etched region and properly annealed to act as the gate-contact. The conceptual diagram of the fabricated FET is shown in Figure 6.1. The purpose of AgNP layer deposition at the back side of the substrate is to avoid any formation of possible Schottky-contact formation between the probing metal and the doped silicon substrate. Moreover, the drop-casted AgNP layer is expected to have less surface roughness as compared to the etched-out silicon surface which avoids any issues pertaining to contact resistance. The substrate used for FET fabrication is phosphorous doped (n-type) having a resistivity of 1-10 Ω-cm corresponding to a doping density of $\sim 5 \times 10^{14}$ to 5×10^{15} at 300 K with (100) orientation. The oxide thickness is 300 nm and total thickness of the substrate is 500 μm.

The motivation to fabricate printed-FET comes from the fact that the current flowing between source and drain terminals can be controlled using back-gate terminal and further it can be biased in different regions as per the demand of the application. FETs are known to have very high switching speed which establishes them as the back-bone for the integrated circuits (ICs) development. In order to develop MCP as potential technology for printing basic level circuits such as AND, OR gates, memory circuits and so on, the development and performance analysis of printed FETs is required. Moreover, in case of specific applications such as sensing, the printed-FETs are expected to improve the sensitivity and response of the sensors based on the shift in the threshold voltage after the introduction of the analyte [148]. Hence, FET-based sensors can be preferred option for cross-reactive gas sensing experiments [149].

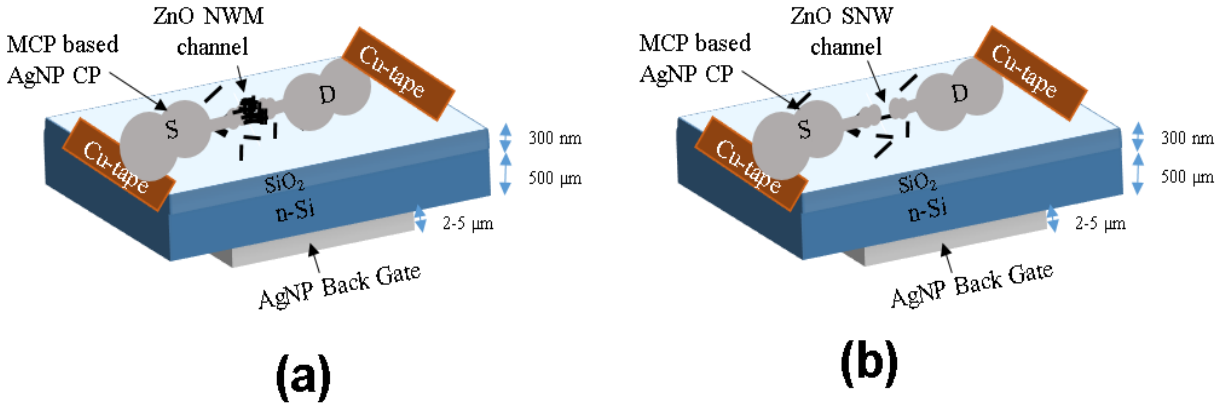

Fig. 6.1: Schematic digram of (a) ZnO NWM-SBFET (b) ZnO SNW-SBFET

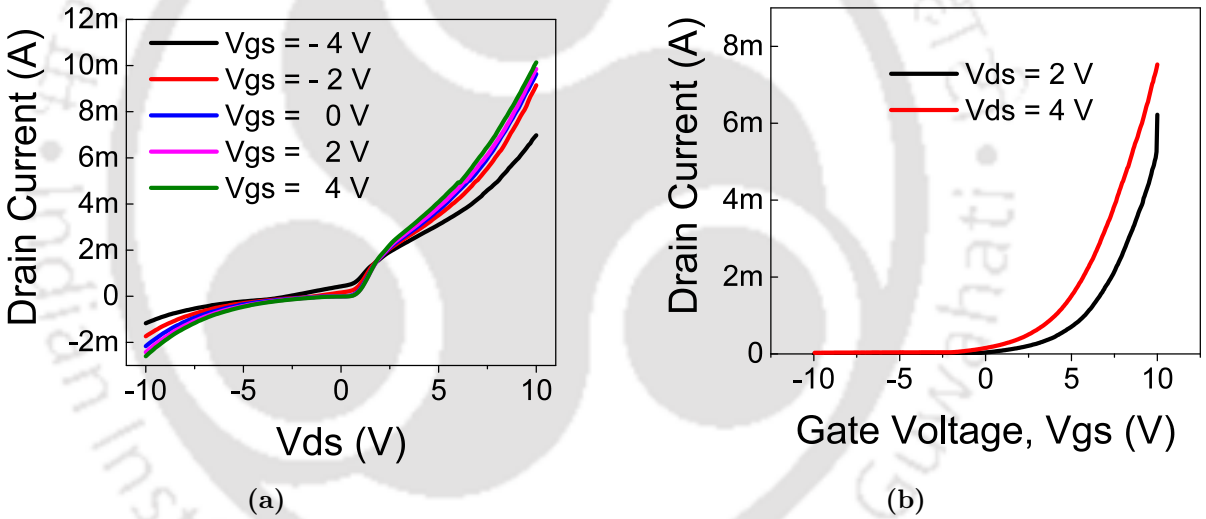

Fig. 6.2: I-V characteristics of ZnO NWM-SBFET (a) Output characteristics (b) Transfer characteristics

6.2 Electrical characterization of ZnO NWM-SBFET

The fabricated ZnO NWM-SBFETs are electrically characterized with the help of Keithley 4200A-SCS Parametric analyzer and low-noise cables with crocodile-clip end as reported in the previous chapters. Figure 6.2(a) represents the output characteristics of ZnO NWM-SBFET for a drain voltage (V_{ds}) range of ± 10 V with gate voltage (V_{gs}) varying from -4 V to 4 V. The exponential dependence of current over drain voltage, as seen in Figure 6.2(a) is probably due to the Schottky contact at the source and drain junctions. Figure 6.2(b) shows the transfer curves for this SBFET for V_{ds} of 2 V and 4 V. Both the I-V characteristics support the n-type semiconducting behaviour of ZnO NWM channel with a I_{on}/I_{off} ratio in order of 10^3. The n-type behaviour of the ZnO NW channel is also confirmed

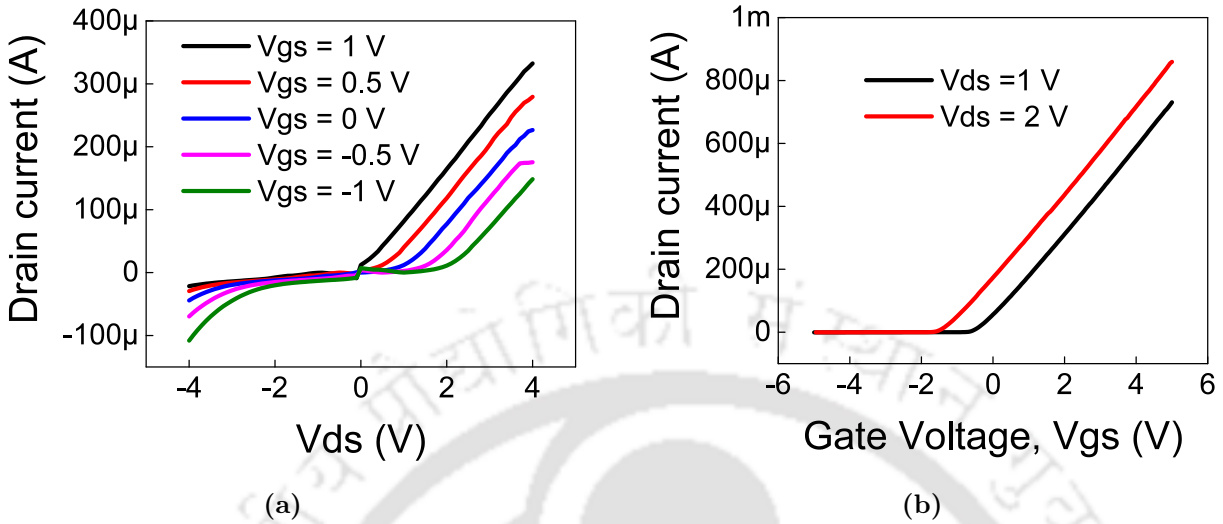

Fig. 6.3: I-V characteristics of ZnO SNW-SBFET (a) Output characteristics (b) Transfer characteristics

from the C-V characteristics measured for different frequencies as shown in Figure 6.4(a).

6.3 Electrical characterization of ZnO SNW-SBFET

Similar, to the previous subsection, this section presents a brief discussion on the electrical behaviour of ZnO SNW-SBFET. Figure 6.3(a) shows the output characteristics for a V_{ds} sweep of ± 4 V for a V_{gs} varying from -1 V to 1 V. Figure 6.3(b) shows the transfer characteristics for a V_{gs} sweep of ± 5 V for V_{ds} of 1 V and 2 V. These I-V curves also support n-type behaviour of the ZnO NW channel is also confirmed from the C-V characteristics as shown in Figure 6.4(b). However, a p-type semiconducting behaviour is also observed in Figure 6.3(a) for negative sweep of drain voltage with lower current density. The p-type conduction needs to be further validated. The possible reason can be the p-type doping of ZnO SNW by Na present in the SDS of ZnO NW dispersion, at room temperature as mentioned in Chapter 4 [107]. Also, to get a p-type ZnO NW is quite rare and p-type ZnO NWs are relatively less stable. Therefore, dominant semiconducting behaviour of channel is considered as n-type, in place of ambipolar transport, for this device.

The current density is decreased in the case of SNW-SBFET as compared to NWM-SBFET which is expected due to the decrease in the aspect-ratio (Width of NW channel/Length of the NW channel)of NW channel.

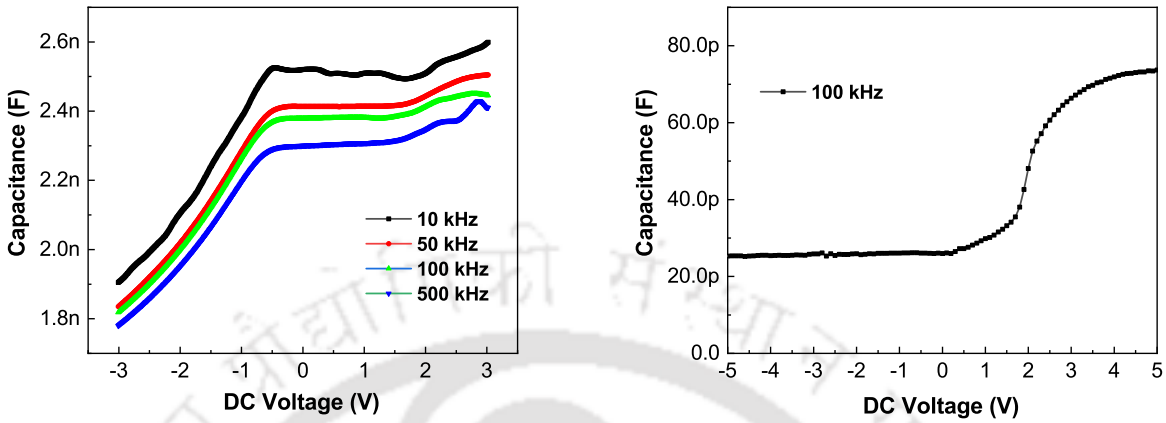

Fig. 6.4: C-V characteristics of (a) ZnO NWM-SBFET (b) ZnO SNW-SBFET

6.4 ZnO NWM-SBFETs as NO_2 sensor

The detection of NO_2 at room temperature is already reported by ZnO NWM based Schottky diodes in chapter four of this thesis where the AER decreased with the gas concentration. The ZnO NWM-SBFETs are also tested for NO_2 sensing. The sensing experiment is performed by sweeping the drain voltage from -5 V to 5 V with a step of 100 mV keeping gate voltage fixed as -2 V. The NO_2 concentration is varied from 2 to 100 ppb. It is found in Figure 6.5(a) that AER decreases with gas concentration in this case also which in a way validates the previous sensing results obtained with ZnO NWM Schottky diodes. A highest sensitivity of 1.127 (%/ppb) ($>$ 0.492 %/ppb of NWM diode) was obtained from the slope of the response curve the SBFET based sensor for NO_2 concentration range of 2 to 10 ppb as shown in Figure 6.5(b). This indicates that ZnO NWM-SBFET based NO_2 sensor is more sensitive to smaller concentrations of NO_2 as compared to ZNO NWM-Schottky diode based sensor at room temperature, non-vacuum conditions. These sensors also have a fast response and recovery time of $\sim$ 30-60 seconds.

6.5 Modeling of ZnO NWFET drain current

ZnO nanowires are quasi-one dimensional nanostructures which have received remarkable attention of researchers in past two decades due to their potential application in nanoscale device area such as field-effect transistors (FET) based sensors, solar cells, transparent displays, photodetectors etc. [150–152]. However, research related to the analytical modeling of electrical transport in 1-D nanowires,

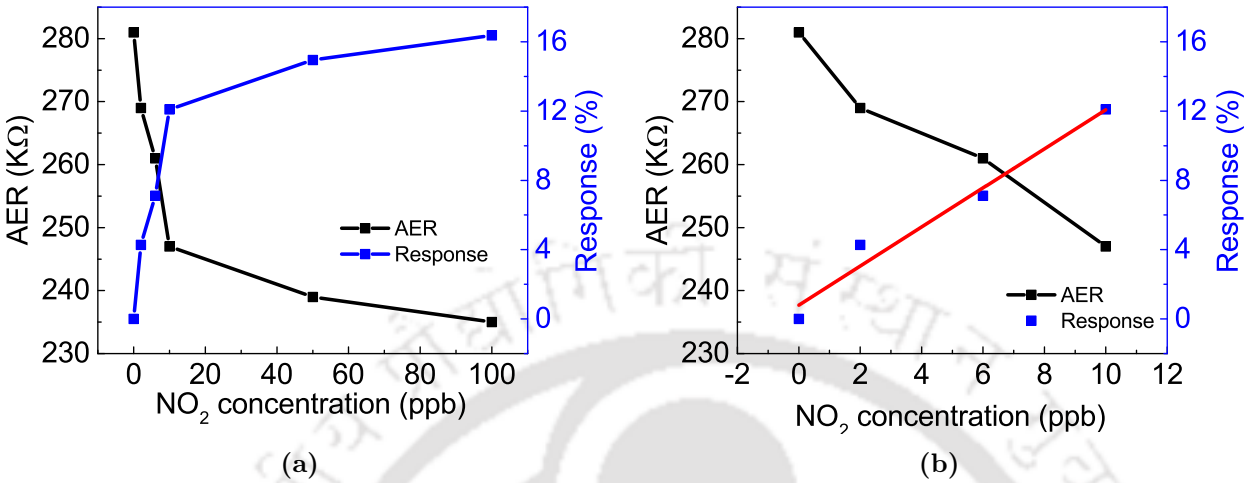

Fig. 6.5: AER variation and sensor response for ZnO NWM-SBFET based NO_2 sensor with varying gas concentration from (a) 2 to 100 ppb (b) 2 to 10 ppb

surface and channel potential, mobility, charge carrier concentration and surface depletion mechanism are still under exploration [153–158]. In this section a basic charge based modeling approach has been acquired to capture and understand the mechanisms related to the current transport in the ZnO NW channel by taking a n-type depletion model SNW MOSFET as an instance. The model approach developed in this section can be used for other methods and variants of current transport after proper modifications.

Since nanowires are 1-D nanostructures, standard equations which are used to model the solid-state physics of 3-D bulk devices like Poisson's equation, drift-diffusion equation, continuity equation need to be modified and QCEs are required to be included to properly model the current of a NWFET. In literature, there are reports available for NWFET current model but most of them use volume charge carrier concentration to develop the model and lack discussion regarding inclusion of quantum confinement effects. Yun et al. [159] have reported a compact analytical current model for a depletion mode n-type ZnO NWFET with bottom-gate structure where they have included current conduction mechanisms of NWFET operating under various bias conditions. Similarly, Soares et al. [160] have presented a model focused for chemical sensing based on single tin oxide (SnO_2) nanobelt FET. But, both of the reports have used bulk charge density and ther is no discussion regarding QCEs in their model. Anderi et al. [161] have reported current-voltage characteristics of single-nanobelt FET using well calibrated drift-diffusion model utilising $F_{1/2}$ integral. Andrew et al. [157] have reported an

analytical model for surface depletion in GaAs nanowires where they have also used $F_{1/2}$ integral to calculate the electron density. Both of these reports do not discuss the relevance of using $F_{1/2}$ integral with respect to QCEs and none of all the above reports have utilized 1-D DOS for expressing electron concentration inside 1-D nanowire channel.

In this section, surface potential and charge based based modeling approach has been used to develop a model for current in ZnO NWFET. The quantum confinement effect has been embedded in the model by deriving the charge carrier concentration in 1-D nanowire using 1-D DOS and $F_{-1/2}$ integral instead of $F_{1/2}$ because electron density in 1-D nanowire is closely related to $F_{-1/2}$ integral rather than $F_{1/2}$ integral [162]. In this way, we have determined the charge carrier concentration per unit channel length of 1-D nanowire which has been used to express the surface depletion depth, capacitance and the effective charge in the channel. Finally, surface potential model has been developed by solving 1-D Poisson's equation using bias dependent charge carrier concentration. Effective channel charge has been derived in terms of oxide voltage. Finally, drain current has been modelled with the help of surface potential and effective charge of the nanowire channel.

6.5.1 Structure used for Modeling

The schematic cross-sectional view of ZnO NWFET with a back gate structure is shown in Figure 6.6 [150, 159]. The cross-section of the nanowire used in this work is a square shape for simplicity [163]. ZnO nanowire is assumed to be n-type semiconductor due to presence of oxygen vacancies and zinc interstitials [152] while source and drain contacts are assumed to be ohmic in nature. Channel length is in 'x' direction while width of the channel is 'z' direction. The thickness of nanowire is in 'y' direction as shown in Figure 6.6. V_s, V_d and V_g are source, drain and gate voltages respectively while V_{fb} is the flat-band voltage. Source has been assumed grounded for model simplicity.

ZnO nanowires have significant surface-to-volume ratios as compared to their bulk counterparts. Therefore, surface defects like oxygen vacancies which are adsorbed at the nanowire surface act as electron acceptor and form O_2^-. This reduces the channel conductivity [150]. Poisson's equation has been solved to obtain the surface depletion depth expression which has been used to determine the effective width (W_{eff}) of the nanowire channel. (W_{eff}) has been used to calculate oxide capacitance (C_{ox}) which has been eventually utilized to model the effective charge (W_{eff}) in the channel to finally

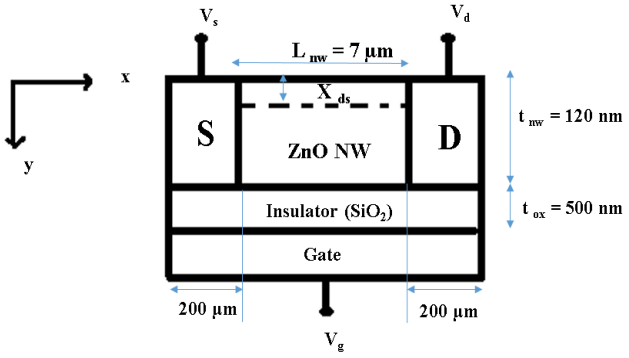

Fig. 6.6: Schematic cross-sectional view of ZnO NWFET

get a current model. The Poisson's equation in 1-D is given as

$$\frac{\partial^2 X}{\partial y^2} = \frac{-\rho}{\varepsilon_{nw}\varepsilon_0} \tag{6.1}$$

where ψ is the electric potential, ρ is the charge density and ε is the permittivity of ZnO nanowire. Solving Poisson's equation, we get an expression for surface depletion depth in ZnO NWFET as

$$X_{ds} = \sqrt{\frac{2\varepsilon_{nw}\varepsilon_o V_{bi}}{qn_L}} \tag{6.2}$$

where, V_{bi} is built-in potential or surface barrier height due to surface states [159]. $V_{bi} = 0.3$ V has been used for model simulation [150]. Here, n_v is the electron concentration per unit volume of the nanowire. It has been assumed that the nanowire is like a solid rectangular pipe which has been exposed to oxygen vacancies in all of its possible faces. Hence, surface depletion is supposed to occur in all the faces exposed to oxygen vacancies. In this report, n_v has been computed with the help of 1-D equilibrium electron density in the nanowire n_L. To compute n_L, standard quantum based approach in energy space has been used which involves Fermi function and 1-D density of states (DOS) in energy domain as described in Appendix C.

C_{ox} is the expressed with help of W_{eff} for rectangular cross-sections as [164]

$$C_{ox} = \frac{\varepsilon_{ox}\varepsilon_o W_{eff}\alpha}{t_{ox}} \tag{6.3}$$

where t_{ox} is the thickness of insulator, ε_{ox} is the permittivity of SiO_2, α is the parameter to account for capacitance variations in nanoscale device like 1-D nanowire as compared to bulk devices and

$W_{eff} = W_{nw} - 3X_{ds} - X_d$ where X_d is expressed as a function of gate voltage

$$X_{ds} = \sqrt{\frac{2\varepsilon_{nw}\varepsilon_o V_g}{qn_L}} \tag{6.4}$$

Moreover, the electron charge density is a also a function of bias. The voltage applied at the gate terminal can be distributed as

$$V_g = V_{ox} + V_{fb} + \psi_s \tag{6.5}$$

where, V_{ox} is the voltage dropped across the oxide. ψ_s is the surface potential and V_x is the potential along the channel close to oxide-nanowire interface. $V_x(x = 0) = 0$ V and $V_x(x = Lnw) = V_d$. The flat-band voltage, V_{fb} = -0.75 V has been computed based on following equation [165, 166]

$$V_{fb} = \frac{1}{q}\left[\varphi_{p^+Si} - \chi_{ZnO} - (E_c - E_f)_{ZnO}\right] - \frac{Q_i}{C_{ox}} \tag{6.6}$$

where, φ_{p^+Si} is the work function of degenerately doped p-type silicon substrate that is acting as back gate in our model structure, χ_{ZnO} is the electron affinity of ZnO, Q_i is the interface trapped charge density. φ_{p^+Si} = 5.05 eV, χ_{ZnO} = 4.35 eV, $Q_i = 8{\times}10^6\ cm^{-1}$ has been referred from [167], [168], [155] respectively. From (4), we can express oxide voltage in terms of gate voltage and surface potential which is turn can be used to express the effective charge in the nanowire channel as

$$Q_{eff} = C_{ox}(V_g - V_{fb} - \psi_s) \tag{6.7}$$

With the help of effective charge in the nanowire, the drain current can be modelled once we have the expression for surface potential in terms of terminal voltages and distance along the nanowire channel.

6.5.2 Model for surface potential

This section details the approach considered to model the surface potential in the nanowire channel with the help of Poisson's equation. In the first step, the 1-D electron charge density in the nanowire channel has been expressed as a function of bias through variation in the surface potential which corresponds to the bending of the bottom of conduction band according to the gate voltage applied. It is noteworthy that when $V_g{<}V_{fb}$, the electrons near the oxide-nanowire interface are repelled and a depletion region is formed as shown in Figure 6.7(a). Similarly, when $V_g{>}V_{fb}$ is applied, there is accumulation of electrons near the interface as shown in Figure 6.7(b). Therefore, for depletion case, the difference between fermi level and the conduction band minima ($E_f - E_c$) increase to ($E_f - E_c - q\psi_s$)

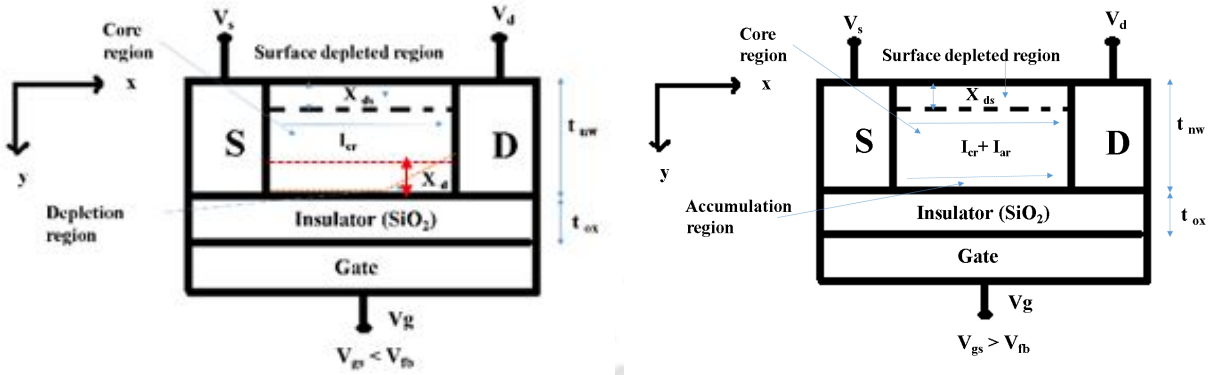

(a) (b)

Fig. 6.7: Cross-sectional view of ZnO NWFET when bottom surface of nanowire channel is (a) depleted (b) accumulated

and decreases to $(E_f - E_c + q\psi_s)$ for the accumulation case. Therefore, the electron charge density after the application of gate voltage can be expressed for both the cases (depletion, n_d and accumulation, n_a) as

$$\begin{aligned} n_d &\propto e^{\frac{-(E_c - E_f + q\psi_s)}{kT}} \Rightarrow n_d(V_g, V_d, x) = n_L e^{\frac{-q\psi_{sd}}{kT}} \\ n_a &\propto e^{\frac{-(E_c - E_f - q\psi_s)}{kT}} \Rightarrow n_a(V_g, V_d, x) = n_L e^{\frac{+q\psi_{sa}}{kT}} \end{aligned} \tag{6.8}$$

Surface potential can be expressed using 1-D Poissin's equation as follows

$$\frac{\partial^2 \psi_{s(d,a)}}{\partial x^2} = \frac{q n_{d,a}}{\varepsilon_{nw}\varepsilon_0} \tag{6.9}$$

Since the above equation is a second order non-homogeneous differential equation, its complementary and particular solutions are jointly given as

$$\psi_{sd}(x) = C_1 \cos(Bx) + C_2 \sin(Bx) + kT/q\delta \tag{6.10}$$

$$\psi_{sa}(x) = C_3 e^{Bx} + C_4 e^{-Bx} + kT/q\delta \tag{6.11}$$

where $B = \mathrm{q}^2 \mathrm{n}_L/\varepsilon_{nw}\varepsilon_0 kT$, δ is the smoothing factor given as -10q/kT, ψ_{sd}(x) and ψ_{sa}(x) are surface

potentials in depletion and accumulation case. Based on following boundary conditions

$$\begin{aligned} \psi_{s(d)}(x=0) &= \frac{qn_L X_d^2}{2\varepsilon_{nw}\varepsilon_0} \\ \psi_{s(a)}(x=0) &= 0 \\ \left.\frac{\partial \psi_{s(d,a)}}{\partial x}\right|_{x=0} &= 0 \end{aligned} \tag{6.12}$$

the coefficient values have been obtained as follows

$$\begin{aligned} C_1 &= -V_t \\ C_2 &= \frac{\psi - V_{ds} - V_t(1-\cos(BL_{nw}))}{\sin(BL_{nw})} \\ C_3 &= \frac{\psi - V_d - V_t(1-e^{-BL_{nw}})}{2\sinh(BL_{nw})} \\ C_4 &= -V_t - C_3 \end{aligned} \tag{6.13}$$

where $\psi = V_g$ - V_{fb} - V_{ox}. Now, once the expression for surface potential for both the cases have been obtained, we can model the drain current with the help of Q_{eff} as follow [169]

$$I_{ds} = \frac{\mu}{L_{nw}} \int_0^{V_d} Q_{eff}\ dV \tag{6.14}$$

The final expression for drain current in depletion and accumulation region is given as

$$I_{dep} = \frac{C_{ox}\mu_n}{L_{nw}} \left[(V_g - V_{fb} - \psi_{sd})V_d - \frac{V_d^2}{2} \right], \quad V_g < V_{fb} \tag{6.15}$$

$$\begin{aligned} I_{ac} &= \frac{C_{ox}(\mu_n + \mu_a)}{L_{nw}} \left[(V_g - V_{fb})V_d - \frac{V_d^2}{2} \right] \\ &\quad - \frac{C_{ox}\mu_n \psi_{sa} V_d}{L_{nw}}, \quad V_g \geq V_{fb} \end{aligned} \tag{6.16}$$

The total nanowire current is modelled as the sum of both the current components over their respective gate voltage range which is expressed as

$$I_{nw} = I_{dep} + I_{ac} \tag{6.17}$$

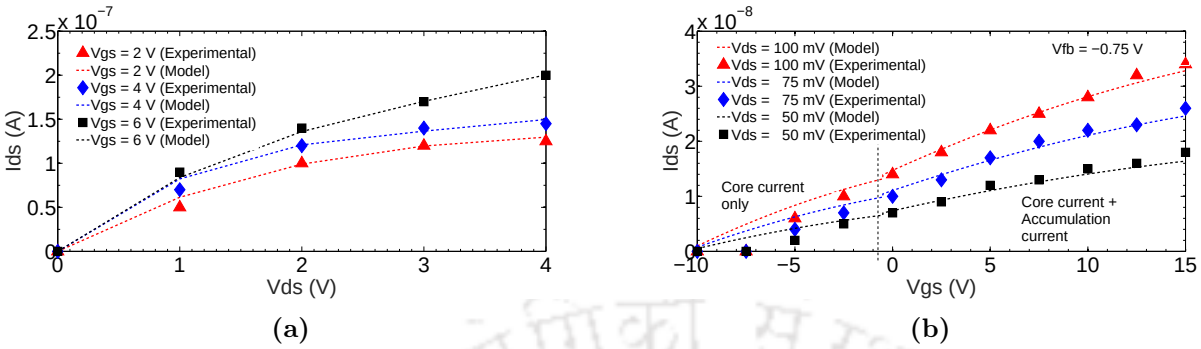

Fig. 6.8: (a) ZnO NWFET current for varying Vds (b) ZnO NWFET current for varying Vgs

6.5.3 Results and Discussion

The simulations have been performed for above current model referring the experimental values from [150] except μ_{cr} and μ_{ar} which are taken as 4.3 cm^2/Vs and 1 cm^2/Vs respectively as we have assumed rectangular cross-sectional nanowire in our model in place of cylindrical one. The parameters and their respective values used for analytical simulations are listed in Table 6.1. Figure 6.8(a) shows the current variation with drain voltage for V_{gs} = 2 V, 4 V and 6 V. Figure 6.8(b) shows nanowire current with varying gate voltage for different drain voltages such as 100 mV, 75 mV and 50 mV. It can also be derived from the current conduction mechanism discussed above that only core current is available during the depletion case as depletion region does not contributes mobile charge carriers for conduction. Though, in case of accumulation, we have core current added with the accumulation current. Hence, the drain current in the accumulation case is expected to be higher than that in the depletion case. This is evident from Figure 6.8(b) which shows an increase in the slope of drain current for $V_g > V_{fb}$. It is observed that the model results are in close agreement with the experimental results.

Also, calculation of N_{1D} gives a value near 4.6428 x 10^6 cm^{-1} which is very small as compared with the effective density of state value for 3-D bulk semiconductors which is in order of 10^{19} cm^{-3} [152]. Subsequently, the 1-D charge carrier concentration in nanowire channel is also expected to be very small as compared with volume charge carrier concentration. This argument correaltes with our idea to use 1-DOS to include the quantum confinement effect for a nanowire channel. Moreover, for a semiconductor to be non-degenerate, E_f-E_c < - $3k_B$T [170]. The computation of 1-D equilibrium electron density using n_f = -3 gives n_L = 2.47 x 10^7 cm^{-1} which is of same order as reported experimentally in [152]. This validates the approximation used for $F_{-1/2}$ integral for the computation of 1-D electron density.

Table 6.1: Table for model parameters and their values

Symbol	Description	Value	Unit
Eg (ZnO NW)	Electrical Bandgap	3.27	eV
m^* (ZnO NW)	Effective mass	0.39 m_0	Kg
ε_{nw}	Relative permittivity (ZnO)	8.7	-
ε_{SiO_2}	Relative permittivity (SiO_2)	3.9	-
t_{ox}	Insulator thickness	500	nm
t_{nw}	Nanowire thickness	120	nm
W_{nw}	Nanowire width	120	nm
L_{nw}	Nanowire length	7	μm
n_f	Coefficient for Fermi Integral	-3	-
β	Parameter to account for surface depletion depth	150	-
α	Parameter to account for capacitance variations	33	-

6.5.4 Summary

In this chapter, ZnO NWM and SNW based SBFETs have been fabricated with the help of MCP technology. The electrical characterization shows a n-type channel behaviour in both types of SBFETs The conclusion drawn from the output and transfer curves of the fabricated SBFETs have been confirmed with respective C-V characteristics. The ZnO NWM-SBFETs have been applied to sense NO_2 at room temperature and it has been observed that ZnO NWM-SBFET based NO_2 sensors show nearly two times higher sensitivity for sub-10 ppb gas concentration range as compared to ZnO NWM-Schottky diode based sensors.

Further, a surface potential based drain current model for a ZnO NWFET has been developed and model results are verified with experimental results. 1-D electron density has been modelled as a function of bias voltages using 1-D density of states (DOS) and an approximate solution of $F_{-1/2}$ integral. The core idea behind use of 1-D DOS instead of 3-D DOS and 1-D charge carrier concentration instead of volume charge carrier concentration is to include quantum confinement effects which are expected for a device with width and thickness near 100 nm. Furthermore, it has been observed that surface depletion depth caused by adsorbed oxygen vacancies is an important parameter for nanowire which significantly affects its channel conductivity by affecting the gate oxide capacitance. The model results for I_{ds}-V_{gs} show that current in accumulation case increases due to extra charge accumulation

near oxide-nanowire interface as compared to depletion case. This model also predicts a parabolic variation of surface potential near drain region of nanowire channel which is expected due to linear increase of depletion width caused by increased reverse bias. The model results are foud to be in close agreement with the experimental results. This current model can also be extended for degenerate ZnO NWFET where doping levels are very high by proper selection of n_f values. Further, inclusion of mobility model, effect of interface charge densities on the surface potential and inclusion of channel potential model in the present current model can improve the results.

7

Conclusions and Future Directions

Contents

7.1 Conclusion

The growing need of electronic devices in the field of sensors, biomedical and medicinal applications demands the development of alternative fabrication technologies which can be effectively used for proof-of-concept level testing and rapid prototyping at low costs. Printed electronics technology is emerging to serve the above purpose being additive and diverse in nature. This thesis contributes in the development of printed electronics by exploring and optimizing the various aspects of micro-cantilever based printing process for the fabrication of micro-resistors, micro-Schottky diodes, field-effect transistors and their application in the field of gas sensing and biological interactions. The major contributions of this work are summarised as follows.

- The initial phase of the thesis is focussed on the analysis and optimization of the micro-cantilever based printing process which utilises surface patterning tools (SPTs) with micro-cantilever (μC) with in-built micro-channels. Hence, this printing technique is referred as micro-cantilever based printing (MCP). MCP technique has been compared with other printing technologies such as inkjet printing, gravure and screen printing as shown in Table 7.1. MCP is an additive manufacturing technology which is processed at low cost, room temperature, does not require masks or vacuum environment and is eco-friendly. MCP generally requires inks with low viscosity (below 20 cP), particle size as low as possible, solvents having slow evaporation rate, substrate which show optimal solvophilic or solvophobic response towards the inks, ambient humidity in the range of 40-60 % etc. Further, low ratios of printed feature-size to suspended particle-size have been obtained for PANI-ES and AgNP ink which are nearly five times finer than typical inkjet printing ratios as shown in Table 7.1. The various physico-chemical parameters which play a vital role in printing of stable and reliable structures such as suitable ink concentration in the solvent, proper selection of the substrate with which the ink has good adhesion, ink-substrate interactions via contact-angle measurement, selection of proper solvent and particle-size of the ink, printing environment, annealing, cleaning of SPTs etc. have been studied, analysed and optimised. Multiple arrays of micro-spots of PANI-ES have been printed on flexible substrates like PET, PVA@PET. Monolithic resistors of AgNP have been printed using MCP having average electrical resistance in the order of few hundred ohms to a few kilo-ohms depending on their print thickness.

- The MCP technology has been further explored to fabricate printed micro-resistors (PMRs) in

Table 7.1: A comparison between different printing methods

Printing Method	Viscosity (cP)	Feature Size (μm)	Ink Particle Size (nm)	Feature to Particle Size Ratio	Material	Reference	Year
Inkjet	-	100 (Line)	50	2000	Ag NP	[70]	2012
	10-18	90 (Spot)	50	1800	Ag NP	[171]	2017
	9-11	10 (Line), 3 (Spot)	5.5	1800 (Line), 545 (Spot)	Au NP	[71]	2005
Gravure	60000	121	1900	63	Ag NP	[48]	2016
Screen	10000	22	5	4400	Ag NP	[49]	2015
MPS	**10-18**	**0.5 (Spot), 17 (Line)**	**50**	**10 (Spot), 340 (Line)**	**Ag NP**	**[22]**	**2018**
	10-18	**3 (Spot)**	**3000**	**1 (Spot)**	**PANI-ES**	**[22]**	**2018**

three different printing modes based on MCP. These printing modes are based on the way the μC is utilized to draw the ink from the ink-source and deploys the ink on the substrate during the printing process. These modes have been named as spot spot overwrite printing (SOP), dip-ink printing with spot overwrite printing (DIPSOP) and surface patterning tool drag printing (SDP). SOP has higher print capability as it can print large number of structures in one go. DIPSOP has highest print-probability as it can print those inks also which do not fulfil the printing pre-requisites completely and therefore DIPSOP is the most reliable printing mode. SDP is the fast printing mode and can print structures having the least surface roughness. The PMRs are single material electronic devices as they contain only AgNP ink and hence reduce the issues of contact resistance and interfacial mismatch. Moreover, it has been found that these PMRs are structurally and electrically stable even after 1 year. These PMRs are comparable with SMD chip resistors available in the market with lower fabrication cost. Implementing these three different modes of MCP, a print resolution of sub-2 μm and minimum feature size of sub-1 μm has been achieved. Table 7.2 summarises the PMRs printed via three modes of MCP.

- Schottky micro-diodes have been fabricated through a low cost, simple and rapid fabrication process using μC printed AgNP layer (thickness $<$ 400 nm) and dispersion-casted ZnO NWs as semiconductor channel material for a channel length $\sim$ 35 μm. To control the dimensions of the channel, first SDP and later DIPSOP mode of MCP has been applied. The electrical characterization of printed micro-diodes (PMDs) verify their Schottky behaviour. The PMDs have been used as sensors for air pollutant gases such as CO_2, CO and NO_2 at room temperatures. The best sensitivity of 0.492 (% ppb^{-1}) for NO_2 is achieved.

- The ZnO NW dispersions have been further optimized with the addition of SDS or SDS combined with Acetic acid such that maximum number of separated and countable single nanowires and

Table 7.2: A brief summary of fabricated and measured resistors

Feature	Substrate	Channel Length, Width (μm)	Average Print Thickness, t	Printing Technique	Voltage Range (V)	Current Range (mA)	Average Resistance, R	Resistivity (Ω-m)$\times 10^{-5}$
SOP R1	Glass	L=75, W=27	360 nm	SOP	$\pm$ 0.1	-1.67 to 0.883	94 Ω	1.22
SOP R2	Glass	L=50, W=37	353 nm	SOP	$\pm$ 0.1	-0.79 to 0.687	134 Ω	3.50
SOP R3	Glass	L=60, W=27	386 nm	SOP	$\pm$ 0.1	- 0.573 to 0.631	224 Ω	3.89
DIPSOP R1	Glass	L=30, W=45	300 nm	DIPSOP	$\pm$ 0.1	$\pm$ 0.2	194 Ω	5.40
DIPSOP R2	Glass	L=25, W=17	350 nm	DIPSOP	$\pm$ 0.1	$\pm$ 1.2	120 Ω	2.86
SDP R1	Silicon	L=50, W=75	700 nm	SDP	$\pm$ 0.1	$\pm$ 6	16 Ω	1.68
Spill Layer	Glass	L=60, W=170	1.49 μm	Spillover	$\pm$ 0.1	$\pm$ 23	4.4 Ω	1.86
Spill Layer	Silicon	L=1500, W=950	2.15 μm	Spillover	$\pm$ 0.1	$\pm$ 23	4.4 Ω	0.59
Spill Layer	PET	L=2500, W=2500	2 μm	Spillover	$\pm$ 0.1	$\pm$ 10	10.9 Ω	2.18

least number of dense nanowire clusters get drop-casted on the substrate. MCP has been used to place AgNP contact pads over the surface of a ZnO single NW (ZnO SNW) to fabricate micro-cantilever printed single nanowire based Schottky diodes. These diodes have been applied to sense CO_2 and CO at room temperature achieving a maximum sensitivity of 14.9 (% ppm^{-1}) for CO and 1.71 (% ppm^{-1}) for CO_2 with a response time range of 5 s - 3 minutes and a recovery time range of $\sim$ 2 - 10 minutes with gas concentration down to 500 ppb for CO_2 and 10 ppb for CO. The measured I-V results of the fabricated diodes are also verified via a simple Schottky diode current model based on thermionic emission theory.

- In the last phase of the thesis work, MCP based ZnO SNW Schottky barrier field-effect transistors (SBFETs) have been fabricated by printing the source and drain with AgNP ink and tuning the current through ZnO SNW channel via a n^+-Si/AgNP back gate. The output, transfer and C-V curves of the SBFETs support a n-type conduction in the ZnO SNW channel. These printed FETs can sense NO_2 at 2 ppb to 100 ppb level with a response and recovery time in range of 30-60 seconds. An simple analytical model has been developed to understand the nature of transport in such SBFETs. This model is based on estimation of carrier charge density in the ZnO SNW channel using 1-D Density of States. The model is validated with published experimental results.

  Table 7.3 presents the complete summary of fabricated and applied devices and structures.

7.2 Future Directions

The major theme of this thesis has been the exploration and development of MCP to fabricate reliable and practically efficient electronic components and devices that can offer an potential alternatives for silicon micro-fabrication based devices in terms of cost and simplicity of fabrication. However,

there are various future aspects related to this research area which are presented as follows.

- **Scaling of MCP technology and device aspects** The present thesis focuses on the development of discrete electronic components such as micro-resistors, Schottky diodes and FETs. However, the MCP technology can be scaled to fabricate basic logics gates, memory circuits and other integrated circuits having dimensions in micrometer regime. The Schottky contacts have been printed using the combination AgNP/ZnO/AgNP in this thesis and have been a prime focus with respect to the device perspective. However, the ohmic contacts can also be fabricated using the MCP technology by selection of proper metal with appropriate work function like Pt, Ti or Au or by doping the ZnO NW channel, p-type or n-type with respect to the work function of the metal, which helps the formation of ohmic contacts instead of Schottky one. Further, these ohmic contacts based devices can be used to print conventional FETs in place of SBFETs. The effect of Schottky contacts on the C-V characteristics of the SBFETs can be analysed in detail. The ZnO SNW-SBFET based gas sensors can be developed to sense NO_2 and other pollutant gases. Moreover, fabrication of p-type ZnO SBFETs along with n-type ZnO SBFETs can be important in development of complementary circuits such as inverter, other logic and memory circuits.

- **Printing of biomolecules, polymers and nanomaterials** The insights obtained from the analysis and optimization of MCP process using AgNP ink can be used to print other kinds of ink like AuNPs, carbon-dots etc. Moreover, the printing techniques can be extended to deposit biomolecules such as DNA, biological entities like E-coli bacteria, different kinds of viruses for their quantification based on electrical characterization. The μC printing based technology can be used and studied for selective-area functionalisation where ink can be deposited at the targeted locations in μm regime. Usually, polymer printing is challenging using MCP due to thin dimensions of μC channels. Polymer particles generally agglomerate and clog the flow of the polymer ink. An extensive research can be carried out on the development of suitable polymer inks with optimized solvents that can reduce the rate of agglomeration and facilitate the polymer-ink flow through the micro-channels of μC. The printing of diverse nature of inks can be performed over flexible substrate like PET, PVA or PMMA coated PHP sheets and also on paper to fabricate electronic components that can be applied in the field of flexible, wearable and paper electronics. In the present thesis, ZnO NWs have been drop-casted over the substrate using ZnO

NWDs. However, various mechanisms and synthesis procedures can be explored to print ZnO NWs using MCP. Such experiments will require the NWs to flow through the micro-channels of μC. To control and direct the movement of ZnO NWs through the μC channels, some sort of extra capillary-push or electromagnetic field excitation based flow mechanisms can be analysed and developed. The MCP printed Schottky diodes and SNW SBFETs can be tested for sensing other gases like hydrogen, VOCs to analyse the selectivity of the sensors. The ZnO NW channel can also be functionalised with suitable material to improve its selectivity. Further, the effect of humidity and temperature variations on the performance of sensors can be analysed.

- **Device modeling and stability analysis** The basic current model for SNW SBFET can be further improved by developing the model for channel surface potential using Poisson's equation. Standard quantum confinement models like Schrodinger-Poisson (SP) solver model, Bohm quantum-potential (BQP) model, Landauer current expression can be utilised to account for carrier transport in the nanowire channel. The other devices than PMRs fabricated using MCP like Schottky diodes, SBFETs and gas sensors developed using these devices can also be analysed for structural, electrical and functional stability and reliability. The NW gas sensor sensitivity and stability models can also be developed based on NW current and surface potential models. The discussed drain current model assumes ohmic contacts and it can be modified by combing the effect of Schottky contact to model the actual current in the fabricated FETs.

Table 7.3: Complete summary of fabricated devices and their applications

Chapter	Fabricated Devices/ Structures	Technology	Substrates	Results
2	Micro-spots (μS), Micro-lines (μL), Printed micro-resistors (PMRs)	MCP-SOP	Glass (coverslip)	AgNP μS on glass (D $\sim$ 0.5 μm), AgNP micro-line on glass (W $\sim$ 17 μm), AgNP PMR on glass (average length $\sim$ 158 μm, average width $\sim$ 51 μm, average thickness $\sim$ 258 nm, AER $\sim$ 244 Ω)
			PVA@PET	PANI-ES μS (D $\sim$ 3 μm),
			PET	PANI-ES μS (D $\sim$ 20 μm),
3	Micro-spots (μS), Micro-lines (μL), Printed micro-resistors (PMRs)	MCP-SOP	Glass	AgNP μS (D $\sim$ 0.46 μm), * Print resolution: 1.9 μm
			SiO2/Si	AgNP μS (D $\sim$ 0.46 μm), AgNP micro-line (W $\sim$ 5 μm)
		MCP-DIPSOP	Glass	AgNP μS (D $\sim$ 0.68 μm), AgNP micro-line (W $\sim$ 1.02 μm, * Print resolution: 1.9 μm
		MCP-SDP	SiO_2/Si	AgNP micro-line (L $\sim$ 1.8 μm), Print resolution: 1.8 μm
4	ZnO NW-Micro-mat Schottky diode , CO_2, CO, NO_2 sensors	MCP-SDP, MCP-DIPSOP, Drop-casting	SiO_2/Si	* NWs over the metal CP Sensitivity $\sim$ 0.492 %/ppb (NO_2), T_{res} $\sim$ 30-60 sec, T_{rec} $\sim$ 60 sec, * Room temperature operation
	ZnO NW-Micro-bridge Schottky diode, CO_2, CO, NO_2 sensors	MCP-SDP, MCP-DIPSOP, Drop-casting	SiO_2/Si	Sensitivity $\sim$ 0.115 %/ppb (CO_2), T_{res} $\sim$ 30 sec, T_{rec} $\sim$ 1 min, LOD: 0.14 ppb (NO_2), 0.23 ppb (CO_2), 9 ppb for CO, * Room temperature operation.
5	U-ZnO SNW Schotky diode, CO_2 and CO sensors	MCP SDP-SP, MCP-DIPSOP	SiO_2/Si	* Metal CP printed over SNW * SNW L $\sim$ 4-5 μm, D$\sim$ 300-350 nm * Schottky diode parameters: Average barrier height: 0.18 eV to 0.21 eV Series resistance: 30-180 k Ω I_{on}/I_{off} $\sim$ 10^4 * Sensing parameters: Sensitivity $\sim$ 14.9 %/ppm (CO), T_{res} $\sim$ 5-10 sec (all three gases), T_{rec} $\sim$ 2-4 min (CO) * Room temperature operation.
	M-ZnO SNW Schotky diode, CO_2 and CO sensors	MCP SDP-SP, MCP-DIPSOP	SiO_2/Si	Sensitivity $\sim$ 4.01 %/ppm (CO_2), T_{res} $\sim$ 20-60 sec (CO), T_{rec} $\sim$ 5 min (CO) * Room temperature operation.
6	ZnO NWM-SBFET, NO_2 sensor	MCP SDP-SP, MCP DIPSOP	SiO_2/Si	* Device parameters from I-V: n-type channel conduction I_{on}/I_{off} $\sim$ 10^3 * Device parameters from C-V: n-type channel conduction * Sensor results Sensitivity $\sim$ 1.127 %/ppb (NO_2) * Room temperature operation .
	ZnO SNW-SBFET	MCP SDP-SP, MCP DIPSOP	SiO_2/Si	* Device parameters: dominant n-type channel transport (CV and I-V), I_{on}/I_{off} $\sim$ 10^3 * Room temperature operation.
D: Diameter, W: Width, CP: Contact pads, T_{res}: Response time, T_{rec}: Recovery time				

A

Printing of SOP, DIPSOP and SDP based AgNP PMRs

Contents

A.1 Printing of SOP, DIPSOP and SDP based AgNP PMRs

In the first MCP based printing technique, a continuous structure like a line or a square with a certain length, width and thickness is printed by partial overwriting of every single spot of the ink over the previous spot as shown in Figure 3.1. Therefore, this technique has been named as spot overwrite printing (SOP). There are various conditions in which the flow of the ink to the substrate is restricted during the print experiments. The ink has to satisfy certain physical and chemical criteria such as particle-size (as small as possible), viscosity (as close to that of water i.e 1 cP), evaporation point (higher preferred) etc [22] to attain a proper flow through the channel of micro-cantilever. Moreover, the ink flow is restricted even if the micro-cantilever channel of the SPT is not properly cleaned and contains the dried-up particles of the ink used in the previous printing experiments. DIPSOP printing technique is an effective solution for such conditions. This is because, in this printing technique, we first drop cast extremely small amount ($\sim$ 0.2-0.5 μL) of AgNP ink on the substrate which acts as a local ink reservoir (LIR). Thereafter, the SPT micro-cantilever is made to just touch the upper periphery of this reservoir to avoid the spillover of the ink. In doing so, the SPT draws some ink into its micro-cantilever channel and readily prints the spots or the designed structure with the help of NanoWare software installed in Molecular printing system (MPS) from Nano eNabler [22, 130] MPS where the array printing can be customised. When the ink gets over, the SPT is again dipped in the source drop and re-draws some ink and carry forwards the printing process. Since the SPT is dipped in the source drop, this printing technique has been referred to as dip-ink printing with spot overwrite printing (DIPSOP). This technique is slow but guarantees the flow of the ink from micro-cantilever of the SPT. DIPSOP is analogous to the ancient technique of writing using quill pens.

The third technique prints the structures by dragging the surface patterning tool (SPT) micro-cantilever, which acts as a reservoir for the ink, continuously like a tip of a pen to draw straight lines, rectangles or square shaped features with low line edge roughness. We have named this printing technique as SPT drag printing (SDP). SDP can be performed either by drop-casting the ink over the SPT reservoir, making the micro-cantilever of SPT to properly touch the substrate surface and then dragging the micro-cantilever to print the desired structure or by dipping the micro-cantilever into a local ink spot and dragging the ink with the micro-cantilever to the print targeted design. In both cases, the ink needs to be properly spread over the contact pads and channel region by gradually lifting the micro-cantilever which is in contact with the substrate and allowing the ink stored in the

micro-channel to come out and spread uniformly by itself (self-printing). The interesting fact is that the ink coming out of micro-cantilever channel after the drag spreads only in the dragged region due to cohesive forces acting between the ink molecules. It can be observed in Figure 3.4(B) that the left contact pad in SDP-PMR seems to have less print thickness as compared to the pad at the other end based on color texture. It is so because the SPT drag process has been performed from left to right direction. When the drag process is stopped in the middle of the right contact pad, there is an outflow of ink from the micro-channel of the cantilever due to accumulated capillary force during the SPT drag process which spreads an extra ink throughout the whole right contact pad. The ink also gets spread in the channel of SDP-PMR as well. This extra flow of ink results in the gain of extra thickness where the ink has spread. To balance the thickness, the extra ink needs to be properly distributed among the two contact pads and the channel of SDP-PMRs by dragging the SPT in the middle of each contact pad and lifting the micro-cantilever gradually from the surface of the substrate.

Figure 3.7(a) shows SDP-PMR array of AgNP over SiO_2/Si substrate after annealing. It is observed in Figure 3.7(a) that the printed array has uniform thickness without any discontinuity because there is no colour change observed in the printed array. However, in Figure 3.7(b), the second printed array lacks uniform thickness due to non-uniformity and discontinuity in the flow rate of the ink from the reservoir to the tip of the micro-cantilever after printing the first set of PMR array. The core reason behind such non-uniformity in the flow rate is the higher speed of SPT drag which increases the ink demand for printing. The SPT reservoir is unable to meet this demand rate due to intrinsic limitations for the ink flow rate which is based on certain parameters like the viscosity of the ink, the particle size of the ink, agglomeration rate of the particles inside the ink, micro-channel width of the micro-cantilever of SPT, surface uniformity etc. Hence, these parameters need to be optimised to get a constant and faster ink flow rate for a longer period to print continuous features.

B

Optimization of ZnO NW dispersions for SNW device fabrication

Contents

B.1 Introduction

In this work, we report the optimization of ZnO NW dispersion in de-ionized (DI) water such that the drop-casted quantity of the dispersion contains maximum number of distinguishable and individual NWs and least number of ZnO NW clusters. To observe the effect of surfactant, acid and base on the separation tendency of clustered ZnO NWs, sodium dodecyl sulfate (SDS), acetic acid and ammonium hydroxide has been added to the original dispersion in DI water in various concentrations and a comparisonal analysis has been presented. Moreover, the effect of annealing temperature and annealing rate has also been discussed with each case to observe the thermal and structural stability of drop-casted ZnO NWs. Such drop-casting technique of ZnO NW in DI based dispersions is a low-cost, easier, faster, more controllable technique as compared to the conventional techniques utilized for fabrication of ZnO SNW devices. Therefore, such technique has a promising potential to be applied in the fabrication of single nanowire based electronic devices in general.

Zinc oxide (ZnO) nanowires (NWs) have been deeply researched due to their unique and attractive material properties which are being employed in the field of electronics, optics, energy-harvesting and so on [172–174]. ZnO NWs are generally synthesized over the substrate using vapour-liquid-solid (VLS) method with the help of chemical vapour deposition (CVD), laser ablation method, atomic layer deposition (ALD), hydrothermal or solvothermal techniques and so on [175–181]. However, most of the avove-mentioned methods use some kind of catalyst or auxiliaries that leads to residual contamination of ZnO NWs [175].

Therefore, more efficient method of ZnO NW synthesis requires a contamination-free process that does not alters the original properties of a NW. Shih et al. have reported the synthesis of a ZnO single NW (SNW) using a Ti-assisted CVD in order to avoid catalytic contamination which can control the dimensions of NWs with the help of a diffusion phenomena taking during the fabrication process [175]. Lupan et al. have reported the low-temperature solution based synthesis of Au-modified ZnO NWs with diameter varying in the range of 10-100 nm [181]. Similarly, Galan et al. have used atomic layer deposition (ALD) to grow ZnO seed layers followed by chemical bath deposition (CBD) of ZnO NWs to produce uniform single crystal ZnO NWs in low-cost [182]. Naif et al. have reported a low-temperature hydrothermal technique for ZnO NW reproduction and have studied the effect of growth duration time, growth temperature, zinc precursor concentration etc. on the morphology of ZnO NWs [183]. Lupan et al. have reported the integration of a single NW or a single microwire

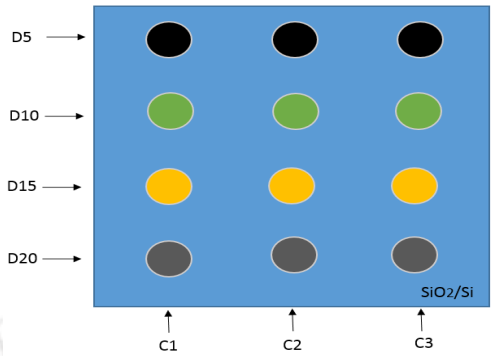

Fig. B.1: Schematic of ZnO dispersion drops with varying solvent concentration over silicon surface

on the chip by employing metal maskless nano depositions in the dual beam focussed electron/ion beam instrument [184]. However, it is observed that in most of the reports that the growth of ZnO NWs is either affected by catalytic-contamination or there is always a need of series of sophisticated equipments which increases the fabrication time and processing complexity and most of the times, need a high processing temperature.

In this work, we have proposed a novel method of separation of dense and random clusters of NWs into highly separated and distinguishable single NW entities. For this, we have utilised a commercial ZnO NW powder and have prepared an optimized dispersion of ZnO NWs using de-ionized (DI) water as dispersion medium, which when drop-casted over the substrate, randomly spreads highly separated ZnO SNWs that can be identified and targeted for metal-contact formation via a simple microscopic-visual inspection. Once the ZnO SNWs are properly placed on the SiO_2/Si surface, then the metal-contacts can be directly printed overlapping the two sides of a selected ZnO SNW using MCP technique [36] to fabricate two-terminal (micro-resistors, diodes) and three-terminal devices such as field-effect transistors (FETs), which can be further deployed for some sensing applications. Further, the effect of acid and base addition to DI water based nanowire-dispersion on the morphology of ZnO SNW is also investigated.

B.2 Dispersion Preparation

ZnO Nanowire powder (NWP) is procured from Sigma Aldrich (Product Id: 773999). Since we have ZnO NW in powder form, we need to find some technique to separate thousands of NWs which are clubbed together in powder form to get a single (or at least countable) NWs and place them at targeted locations for our device fabrication. Basically, the ZnO NW being our channel material, it is

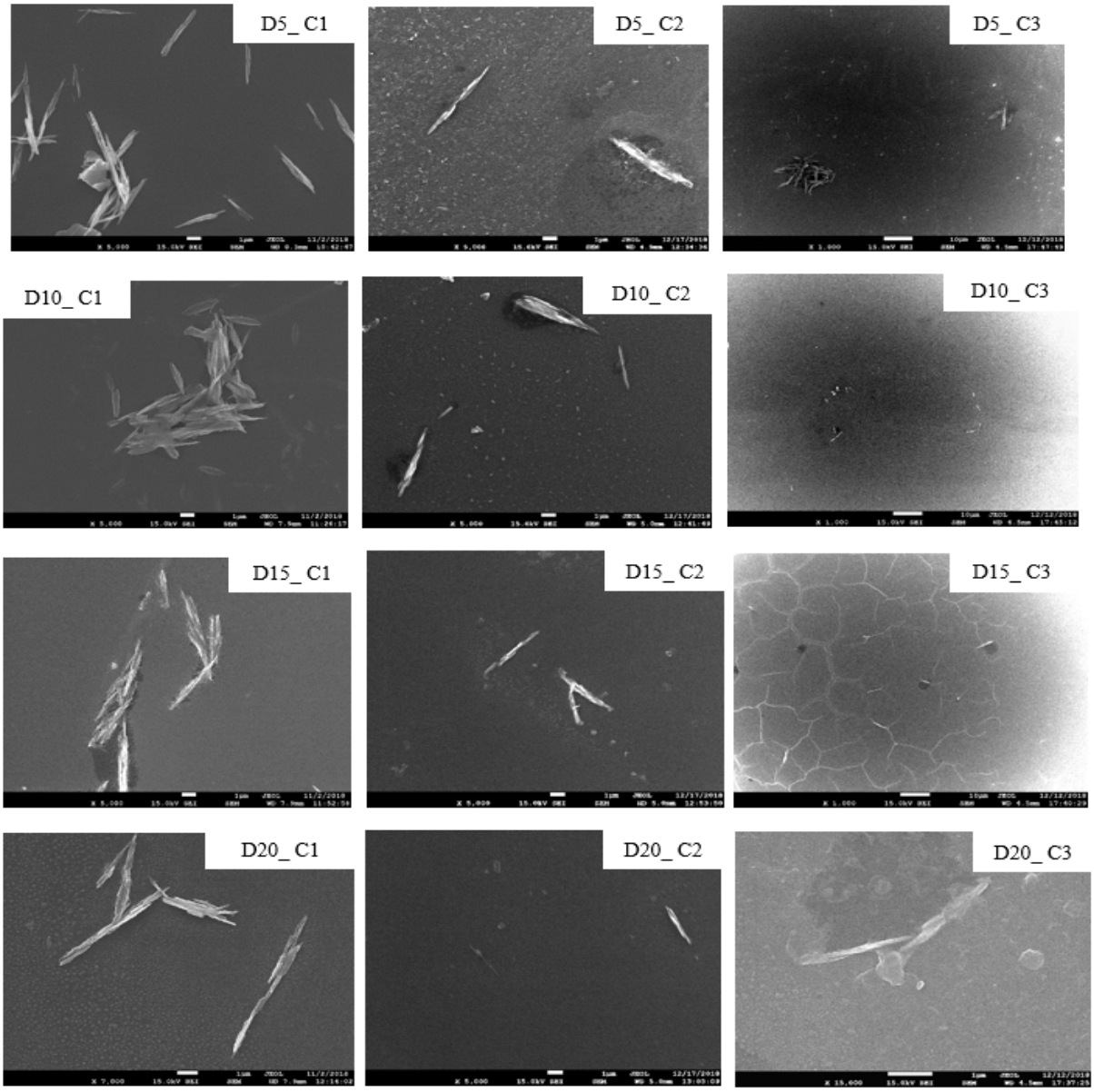

Fig. B.2: FESEM image showing separation tendency of ZnO NWs in four different concentrations of dispersions of ZnO NWs in DI water added with SDS

targeted to be placed in the channel (gap) between the two electrodes such that it can properly bridge the gap between the two electrodes and connect them properly. To separate ZnO NWs, one of the preferred methods will be to make a solution or dispersion of ZnO NWP and drop cast the same over desired location. Generally, ZnO NWP is not soluble in many solvents except some acids. Moreover, acids evaporate fast and also need more precaution during experimentation. Therefore, experimenting with ZnO NW dispersions drops is preferred here over ZnO NW solutions.

1 mg of ZnO NWP was taken and dispersed in four different concentrations (5 mL, 10 mL, 15

Table B.1: Count of distinguishable and separated individual ZnO NWs entities in each dispersion drops

Drop columns/ ZnO dispersions	C1	C2	C3
D5 (5 mL)	9	2	10
D10 (10 mL)	3	4	7
D15 (15 mL)	2	3	6
D20 (20 mL)	1	2	2

mL and 20 mL) of low surface tension de-ionized (LST-DI) water. For convenience, we have named four dispersions as D5, D10, D15 and D20 respectively. A low surface tension DI water (LST-DI) was prepared by dissolving 1 mg of sodium dodecyle sulfate (SDS) in each DI water sample. Each of four dispersions were treated with vortex generator for 5 minutes for proper mixing of components and 0.5 μL of each dispersion was drop casted at three different locations over a cleaned silicon substrate as shown in Figure C.1. In this way, three different columns of dispersion drops were casted on silicon substrate as shown in Figure C.1 as C1, C2 and C3. This sample was annealed till 210°C with a ramp rate of 2°C/min starting from 60°C. The so annealed sample was imaged with field-emission scanning electron microscope (FESEM) from JEOL (Model: JSM-7610F) to observe the presence of ZnO NWs in each of dispersion drops. SDS helps to reduce the surface tension of the water [185–187] and hence resist the agglomeration rate of NWs resulting in a improved level of NWs separation as shown in Figure B.3.

All the FESEM images are taken near the centre of each drop. Images which are taken at least with 1000X for all columns were considered for comparison and analysis for each drop. It is observed that number of ZnO NWs over the imaged surface decreases as the concentration of the LST-DI water increases in accordance with the level of dilution. Hence, D5 contains maximum number of ZnO NWs while D20 contains least number of ZnO NWs. In D5, we also observe small clusters of NWs as sown in Figure B.2. Also, it is observed that NWs get agglomerated due to annealing to form random nanowire clusters. It is observed that two or more than two smaller ZnO NWs get stacked over each another to form a bigger single ZnO nanowire with length $\sim$ 5 to 10 μm. Moreover, D20 comes out as the best dispersion to be used for further experimentations for device fabrication. Table 1 shows the count of completely separated and easily distinguishable ZnO SNWs entities in each column of all four dispersions. It has been observed that C1 and C3 show a continuous decline in the count of a ZnO SNW as the amount of LST-DI water is increased from 5 mL to 20 mL which hints to the

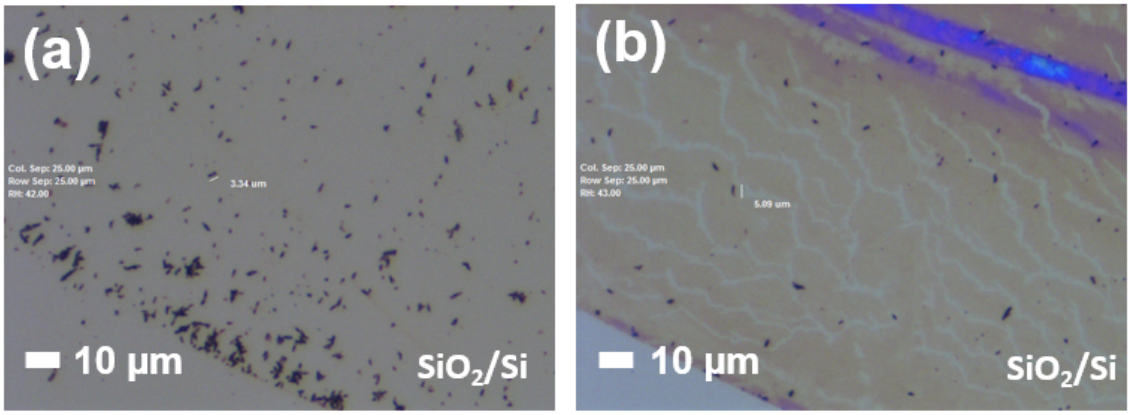

Fig. B.3: Optical image showing a portion of ZnO NW dispersion drop in (a) DI water only (b) DI water + SDS after heating. ZnO NWs are in black colour

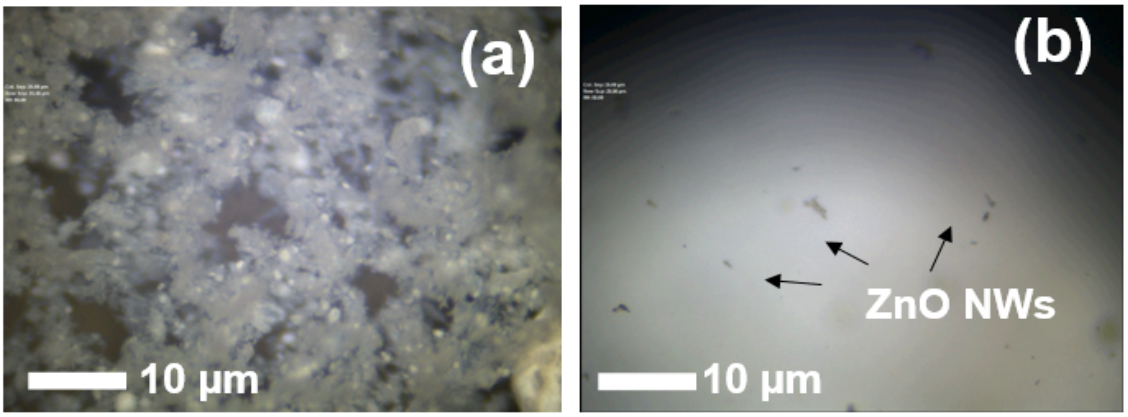

Fig. B.4: Optical image showing a portion of 2 μL drop-casted ZnO NW dispersion (a) without acetic acid (b) with acetic acid in 1:1 proportion

fact that ZnO NWs show higher separation tendency with increased dispersion medium concentration i.e. higher dilution ratio. The probable reason can be the increase in the repulsive force exerted by water molecules on the ZnO NWs. Moreover, C2 also shows a decreasing trend in the count of ZnO NW like C1 and C3 for D10, D15 and D20 except for D5 case where the scanned area needs to be changed for better results. Further, to achieve the target of distributing separated-single nanowires over the substrate, a rapid annealing, direct heat treatment or addition of other materials such as acids or base to the DI water based NW dispersion is expected to give improved results as it provides less time for water molecules to interact with ZnO NWs and hence reduces the chances of corresponding agglomeration.

B.2.1 Results and Discussion

B.2.2 Effect of acid addition to ZnO NW dispersion in LST-DI water

When ZnO NW powder is dispersed in LST-DI water, all the powder particles got agglomerated and assembled at one place which showed that water molecules exert repulsive force on ZnO NWP particles which created the assembly of larger and agglomerated ZnO NW clusters as shown in Figure C.2(a). Therefore, to achieve higher degree of NW separation, mixing acids in ZnO NW dispersion in LST-DI can be a viable option [133, 134]. DI water molecules show repulsive response to ZnO NWs and acetic acid molecules are expected to attract the NWs. Therefore, adding acids in optimal concentration to LST-DI water is expected to result in a dispersion system where ZnO NWs will experience two different types of forces (one repulsive and other attractive) which will help them to remain separated.

For this experiment, LST-DI water is prepared simply by adding 1 mg of SDS to 5 mL of DI water. ZnO NW dispersion is by prepared by adding 2 mg of ZnO NW powder in 1200 ÂţL of LST-DI water. The reason to experiment with a very small concentration of ZnO NW dispersion in 'μL' level as compared to previous 'mL' level is to keep the density of ZnO NWs high so that the effect of acids can be observed clearly. 2 μL of above prepared ZnO NW dispersion was drop-casted on to a cleaned silicon substrate and initial image is captured with camera of Material Printing System (MPS) [55]. The drop-casted ZnO NW dispersion is in white colour as seen from naked eyes. Then, 2 μL of acetic acid, hydrochloric acid (HCl) and sulphuric acid (H_2SO_4) is added to the already drop-casted ZnO NW dispersion to keep the proportion same (1:1). It is observed that (H_2SO_4) dissolves ZnO NWs in all the proportions. HCl also partially dissolves ZnO NWs, however, these NWs turned into micro-particles when heated at $\sim$ 220°C as shown in Figure B.5.

When acetic acid is added in 1:1 proportion with NW dispersion, it is observed that within few seconds, the white colour of the dispersion changed to colourless and transparent like LST-DI water as shown in Figure C.2(b). The agglomerated and dense NW clusters got fragmented into smaller and highly separated ZnO NW clusters and the ZnO NW dispersion seemed almost transparent which confirms expected separation tendency between ZnO NWs as hypothesised by us earlier. The ZnO SNW with length $<$ 10 μm are almost invisible at this scale as shown in Figure C.2(b). After drop-casting 0.5 μL of above composition on a silicon substrate and heating immediately at 120°C resulted into the formation of long ($>$ 10 μm), sharp-edged and highly separated nanowires and micro-wires are formed as shown in Figure B.6. Further, acetic acid was added in different volume proportions such as

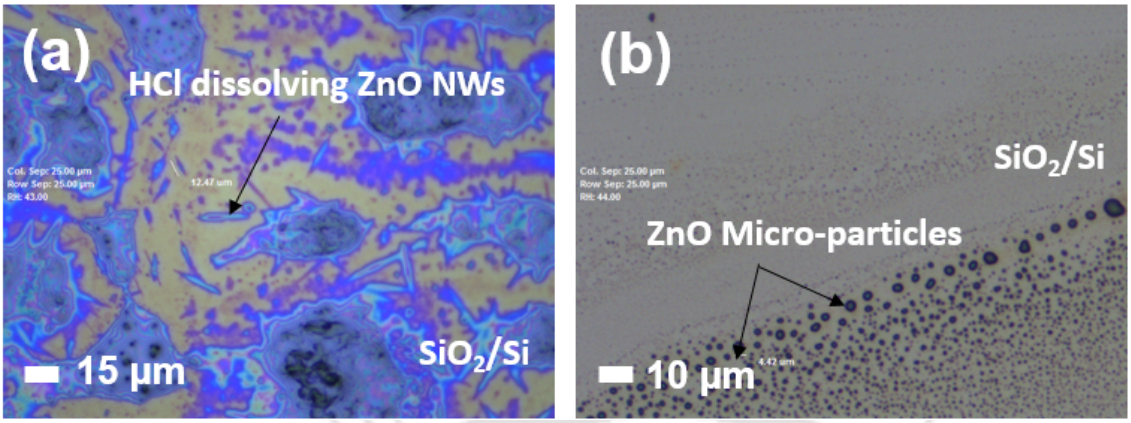

Fig. B.5: Optical image showing (a) HCl partially dissolving ZnO NWs (b) NWs converted to micro-particles at high temperatures

1:1 (0.5 μL acetic acid in 0.5 μL of NW dispersion), 1:10 (0.5 μL acetic acid in 5 μL of NW dispersion) and 1:40 (0.5 μL acetic acid in 20 μL of NW dispersion) as shown in Figure B.7. It is observed that acetic acid addition to ZnO NW dispersion in different proportion is resulting long and sharp-edged NWs and therefore, has capability to modulate the morphology of already synthesized ZnO NWs due to its different pH range as compared to H_2SO_4 or HCl [133, 134, 188, 189]. The acetic acid dissolved all the ZnO NWs in those dispersions in which SDS was not added. This is a strong evidence that the it is the combination of acetic acid and SDS in proper ratios, that is mainly responsible for the creation of long, sharp-edged and highly distinguishable ZnO NWs [190, 191]. However, the dispersion containing acetic acid also converts nanowires and micro-wires into ZnO micro-particles when exposed to high temperatures near $\sim$ 220°C as shown in Figure B.7(f).

B.2.3 Effect of base addition to ZnO NW dispersion in LST-DI water

To observe the effect of adding base (higher pH substance) on the morphology and separation tendency of ZnO NWs, 0.5 μL of ammonium hydroxide (NH_4OH) was added in 0.5 μL (1:1), 10 μL (1:20) and 20 μL (1:40) of ZnO aqueous dispersion (1 mL DI water + 3 mg ZnO NW powder). As observed from the optical images taken from MPS microscope, NH_4OH shows no tendency to either dissolve the NWs or separate them. It forms a ring of ZnO NW mat-cluster of width near 25-50 μm with small, single and unmodified ZnO NWs scattered randomly along the periphery of the ring as shown in Figure B.8. The width of NW cluster ring increases from $\sim$ 32 μm to 60 μm as shown in Figure B.8(a,b).

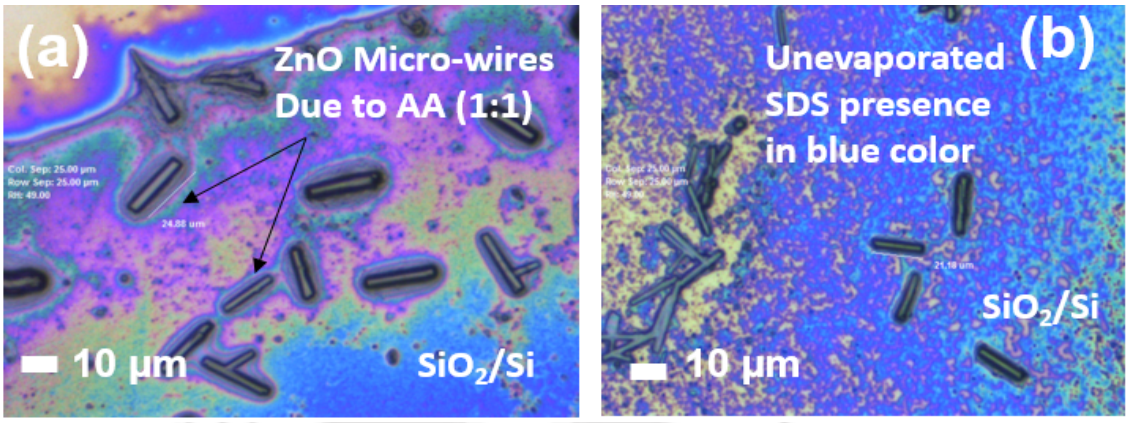

Fig. B.6: Optical image showing sharp and long ZnO micro-wires formation after acetic acid addition in 1:1 (a) at periphery of drop (b) in middle portion of drop. AA: Acetic acid

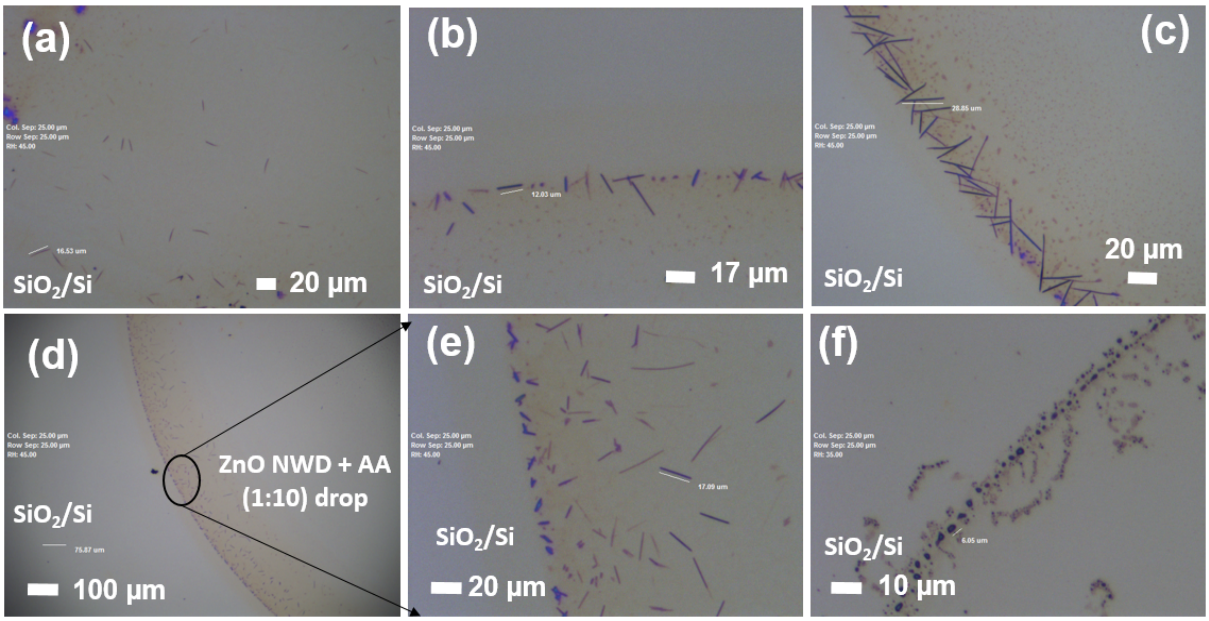

Fig. B.7: Optical image showing sharp and long ZnO micro-wires formation after acetic acid addition in (a) 1:1 (a) 1: 10 (c) 1:40 proportion (d) 1:10 drop periphery (e) zoomed-in image of encircled region in (d) (f) ZnO nanowires converting to micro-particles at higher temperatures. AA: Acetic acid NWD: NW dispersion

B.2.4 Effect of annealing temperature and annealing rate

To observe the thermal stability of ZnO NWs in general, the earlier sample drops (without any acid or base) in LST-DI based dispersions are heated to first 180 °C and then to 220°C. The ZnO NWs are thermally stable and their morphological properties are retained till 220°C as shown in Figure B.9. However, it is also observed that SDS (as seen in blue color in Figure B.9(a) and Figure B.8) evaporates at temperatures near 220°C. Further, NW dispersion added with NH_4OH is also annealed to 180°C to

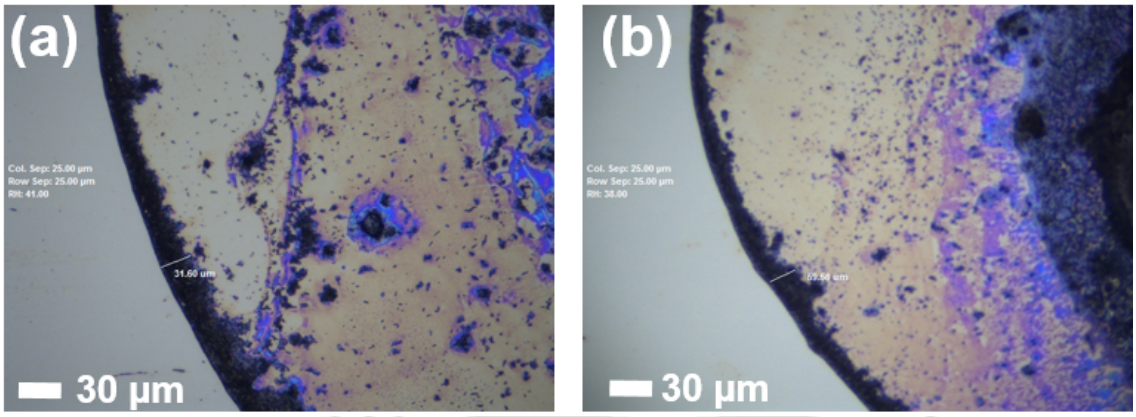

Fig. B.8: Optical image showing formation of ZnO NW mat-cluster ring after NH_4OH addition to ZnO NW aqueous dispersion in (a) 1:20 (b) 1: 40 after heating the drop at 180°C

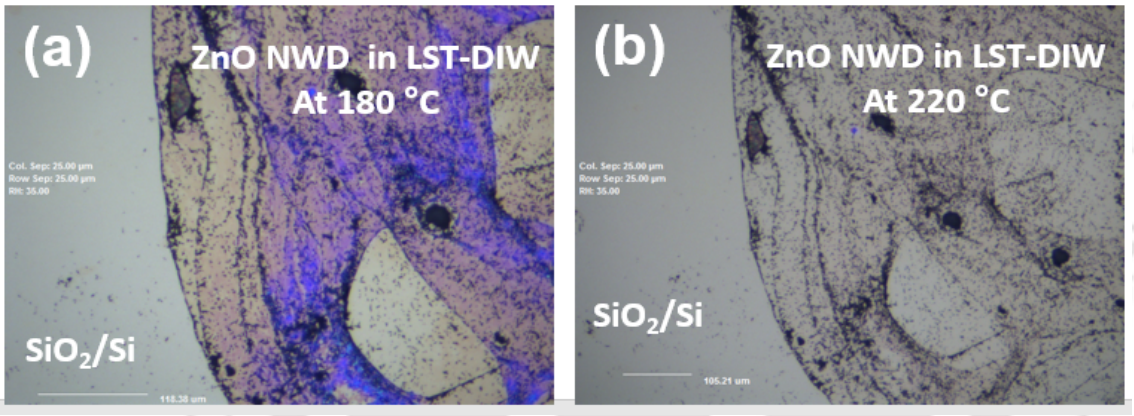

Fig. B.9: Optical image showing effect of annealing temperature on ZnO NWs at (a) 180 °C (b) 220°C

220°C for 5 minutes and was found that there is no effect of NH_4OH on the morphology of ZnO NWs as observed in the case of acids which converted ZnO nanowires/microwires to ZnO micro-particles.

It is not only the optimized concentration of acetic acid and SDS addition in ZnO NW aqueous dispersion helps the formation of long, sharp-edged NWs but also the annealing rate. In first case, when acetic acid is added in proper proportion and annealing is started from 80°C, it is observed that acetic acid dissolves most of the ZnO NWs completely. However, when a direct annealing is done at 120°C to the NW dispersion in LST-DI, immediately after the addition of acetic acid drop, the formation of long, sharp-edged and highly separated NWs takes place.

Figure B.10 and Figure B.11 show the initial stage development of printed micro-resistors of ZnO SNW using MCP technology [36] and the I-V characteristics of a printed resistor and diode of ZnO NW respectively, after the optimization of ZnO NW dispersion is achieved.

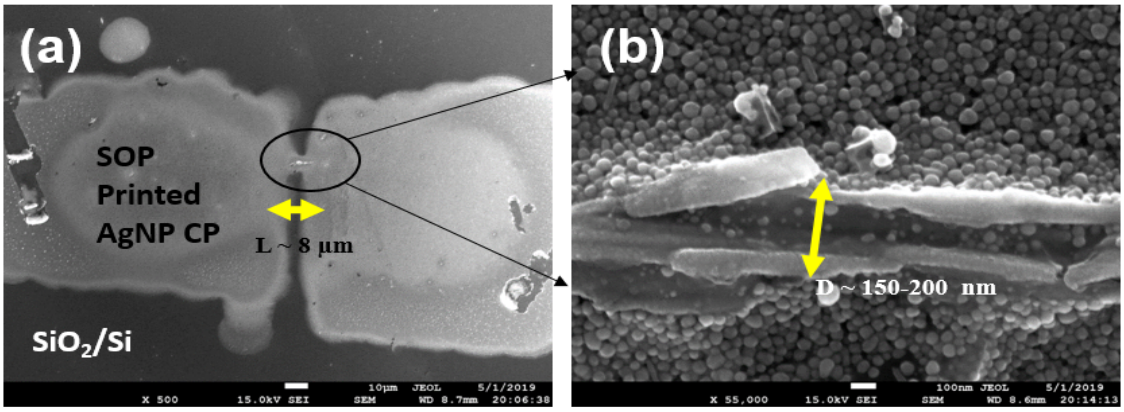

Fig. B.10: FESEM image of (a) a printed micro-resistor of ZnO NW/AgNP, scale of 10 μm (b) magnified images of ZnO NW/AgNP channel region, scale of 100 nm. SDS present in blue color in (a)

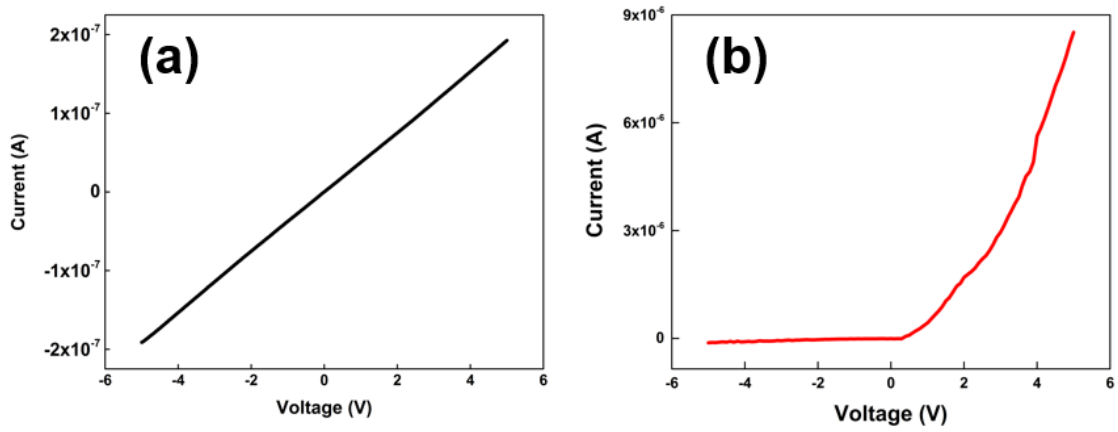

Fig. B.11: I-V characteristics of (a) printed micro-resistor (b) printed Schottky diode of ZnO NW/AgNP

B.3 Summary

This work focus on the development of optimization techniques for ZnO NW aqueous dispersion for distribution of highly separated and distinguishable ZnO NWs and reduction of ZnO NW random cluster formation, for the fabrication of single nanowire based electronic devices. For this purpose, effect of different kind of materials such as SDS (surfactant), acetic acid (acid), NH_4OH (base), annealing temperature and annealing rate has been analysed with respect to the morphological changes and the separation tendency of ZnO NWs. It is observed that SDS reduces surface tension of DI water increasing the dispersibilty of NWs and formation of long, sharp-edged single NWs. Acetic acid with SDS in 1:40 to 1:1 proportion with ZnO NW aqueous dispersion, for ZnO NWD drop-casted volume upto 5 μL, is optimized for ZnO Single NW formation. It is observed that HCl turn NW to micro-

particles at high temperature and H_2SO_4 dissolve ZnO NWs completely. ZnO NW micro-mat is formed by addition of ammonium hydroxide in ZnO NW dispersion in LST-DI water. The ZnO NWs show appreciable, thermal and structural stability, at temperatures $\sim 220°C$ and immediate heating of drop-casted dispersion with acetic acid at 120°C helps to form long, sharp-edged, single and highly separated ZnO NWs.

C

ZnO multiple and single NW based Schottky diode fabrication

Contents

C.1 ZnO NW-μMD fabrication

For the preparation of ZnO NWD, ZnO Nanowire powder is procured from Sigma Aldrich (Product Id: 773999). DI water having a resistivity > 18 MΩ-cm is used as a dispersion medium. To improve the dispersibility of the ZnO NWs and lower the surface tension of DI water, 0.24 mg of Sodium Dodecyl Sulfate (SDS) is added in 1.2 mL of DI water. The dispersing medium is referred to as low surface-tension de-ionised water (LST-DI water). Finally, 2 mg of ZnO nanowire powder is added to the above dispersion.

1 μL of AgNP ink is drop-casted over a cleaned SiO_2/Si substrate and annealed from 60°C to 200°C with a rate of 2°C/minute. The annealed AgNP drop is bisected with a sharp edge cutter to achieve achannel gap varying from 10 to 50 μm followed by drop-casting of 0.5 μL of ZnO NWD over the channel region at 190°C. The drop-casting is carried out at higher temperature to evaporate DI water immediately to avoid its interaction with AgNP contact pads in order to keep them intact with the SiO_2/Si surface and to transfer only the ZnO NWs over the channel. The evaporation of aqueous solutions of SDS depends on various parameters such as concentration of SDS in DI water, hydrophobic or hydrophilic nature of substrate, the mutual interaction of surfactant to the substrate etc. [187, 192]. Even if the drop-casting is carried out at higher temperatures, the NWD is not completely evaporated before it touches the AgNP CPs surface. This in-turn results into formation of multiple small droplets region of NWD which seem to have a higher surface tension that tends the NWs to club together to form random and highly dense clusters of nanowires which have been referred to as ZnO nanowire mat. It is noteworthy that several mat-like structures, similar to what is shown in Figure C.1(a), are deposited in the channel area. This, in turn, increases the effective channel width of the device and provides a larger surface area for the gas molecules to interact. Figure C.1(b,c) shows the Field Emission Scanning Electron Microscope (FESEM)(Make: JEOL, Model: JSM-7610F) image of the interface regions between AgNP CPs and ZnO NW mat. It is observed in Figure C.1(b,c) that ZnO NWs are well placed above the CPs.

C.2 ZnO NW-μBD fabrication

To control the channel dimensions and optimize the fabrication process, ZnO NWD has been prepared in DI water only and AgNP contact pads are printed using MCP. Two distinct large spots of AgNP ink with a separation of $\sim$ 1mm, are placed on a cleaned SiO_2/Si surface and the micro-

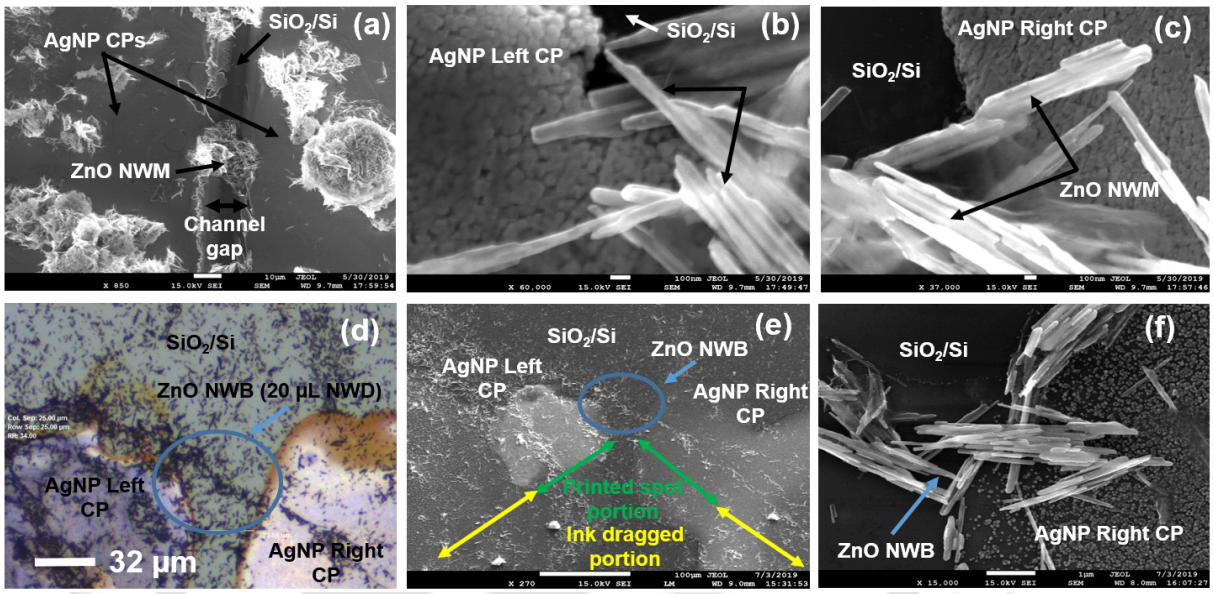

Fig. C.1: (a) FESEM image of a portion of ZnO NW-μMD. Scale: 10 μm (b) AgNP left CP interface region with ZnO NW mat (NWM). Scale: 100 nm (d) AgNP right CP interface region with ZnO NWM. Scale: 100 nm (d) Optical image ZnO NW-μBD with a channel length and width $\sim$ 35 μm and 10 μm (e) FESEM images of ZnO NW-μBD with AgNP CPs and ZnO NW bridge (NWB). Scale: 100 μm (f) FESEM image of right interface region between AgNP CPs and ZnO NWB. Scale: 1 μm

cantilever tip position is adjusted just to touch the upper peripheral surface of one of the spots to drag it closer to the other spot. The similar cantilever-dragging process is applied from the side of other spot to reduce the gap to $\sim$ 100 μm. When micro-cantilever drags the ink, some ink from the spot diffuses in its micro-channel through which the gap between the two spots is further reduced to $\sim$ 35 μm by multiple printing and overwriting of a micro-spot over another micro-spot [36]. The printed structures are annealed in the same manner as reported earlier in this section. The printed micro-spots act as the AgNP contact pads for the device as shown in Figure C.1(d). Further, 3 mg of ZnO NW powder is dispersed in 1 mL of DI water to prepare ZnO NWD. The SiO_2/Si substrate with AgNP contact pads is gradually heated to 190°C and 20 μL of NWD is drop-casted over the channel region to bridge the two contact pads. This device has been referred to as ZnO nanowire bridge (NWB) as shown in Figure C.1(d). Figure C.1(e) shows the FESEM image of ink dragged portion and printed spot portion of the contact pads along with ZnO NWB. It is clear from Figure C.1(f) that ZnO NWs are properly interfaced with AgNP contact pads. Thus, the DI water dispersion medium lowers the process time, makes it simpler and cost-effective.

C.3 U-ZnO SNW based Schottky diode fabrication

Ag is preferred over other metals as it is comparatively low-reactive, more stable and less expensive [93]. The optimized NW dispersion (Appendix B) with 0.3 % w/v of ZnO nanowires in DI water is drop-casted over the SiO_2/Si substrate at a high temperature near 190°C to avoid the agglomeration of NWs into random clusters due to high surface tension in DI water. The optimized ZnO SNWs solution helps to place the NWs at a reasonable distance on the substrate, which helps in targeting an SNW for printing metal contact pads to complete the device fabrication. AgNP contact pads are printed using MCP technology, which uses a molecular printing system (Make: BioForce Nanosciences) containing a surface patterning tool (SPT) consisting of a silicon micro-cantilever print-head [36, 55]. The micro-cantilever has a 5-10 μm wide micro-channels through which the ink to be printed flows or is temporarily stored. The micro-cantilever is typically 200 μm long and 30-60 μm wide. AgNP contact pads have been printed using SPT drag printing (SDP) and dip-ink printing with spot overwrite printing (DIPSOP) modes of micro-cantilever printing (MCP) technology [36].

The micro-cantilever tip can be used to perform SPT drag printing (SDP) and dip-ink printing with spot overwrite printing (DIPSOP) [36]. A schematic diagram showing the step-by-step process of DIPSOP and SDP technique is illusterd in Figure 3.3(a, b, and c) and Figure 3.3(d, e, and f), respectively. The micro-cantilever is kept under UV/O_3 exposure for at least 30 minutes before using it for printing experiments to make the surface of micro-cantilever channels solvophilic to the AgNP ink to ensure that a large density of ink particles remain attached to it during the drag and dipping process [22]. After selecting a ZnO SNW, $\sim$ 10 μL of AgNP ink is drop-casted as a local ink reservoir (LIR) $\sim$ 1000 μm away from one of the ends of the selected ZnO SNW. The micro-cantilever is positioned over the AgNP drop and slowly brought down using the coarse and fine z-axis control setting in NanoWare software installed with the printing system [55]. Initially, the focus of an optical camera attached to the printing software is to set much down the microcantilever to focus the drop and the SiO_2/Si substrate. When the gap between the micro-cantilever and the drop reaches less than 100 μm, then both get focussed together. Further, the focus is re-adjusted to the tip of the micro-cantilever to avoid the spillover (proximity of micro-cantilever and drop may lead direct hit of whole surface pattering tool to the ink source). Fine z-axis control is used to move down slowly until the tip touches the AgNP drop peripheral region. When the micro-cantilever touches the upper surface of AgNP drop, ink particles diffuse inside its vacant micro-channels which reflects the solvophilic nature

of the cantilever. The micro-cantilever in touch with the ink-drop is dragged very slowly towards the targeted end of the ZnO SNW to a certain length ($\sim$ 500-600 μm). Then the micro-cantilever is slowly lifted to allow the ink captured inside its micro-channels to come out and get distributed over the dragged strip [36]. Dragged strip area acquires ink from LIR and thus results in a self-printing of contacts; the technique can be referred to as SDP assisted self-printing (SDP-SP).

Utilizing SDP-SP, a rectangular contact strip of AgNP is printed, overlapping one end of the ZnO SNW. The overlap is achieved by stopping the drag of the ink $\sim$ 2 to 5 μm before the ZnO SNW end and allowing the ink to automatically diffuse and self-print the remaining distance with the help of high ink-density gradient between the micro-cantilever dragged region and the gap-region between the AgNP ink and ZnO SNW of the substrate. Then the entire substrate is annealed from 50°C to 200°C with a rate of 8°C/minute. If the overlap does not occur at the ZnO SNW interface region, two to three DIPSOP micro-spots of average diameter $\sim$ 5-10 μm are printed by ultra-fine position. The micro-spots ensures the targeted hit region such that 1-2 μm of the peripheral region of the DIPSOP micro-spot touches the end of ZnO SNW without completely drowning the ZnO SNW with AgNP ink. The DIPSOP spots are annealed properly to complete the fabrication of one-side of metal contact. The steps, as mentioned earlier, are repeated to form the AgNP metal contacts to the other side of ZnO SNW.

To increase the scalability and ease of reproducibility of abovementioned printing technique, ZnO SNWs of longer lengths ($>$ 10 μm) can be synthesized. It is relatively easy to print metal contact-pads with longer SNWs using SDP-SP and DIPSOP processes without any concerns of misalignment of micro-cantilever contact with the substrate or shorting between two metal pads. Therefore, following section discuss the fabrication of longer ZnO SNWs with help of acetic acid and SDS in optimized proportions with the ZnO dispersion DI water.

C.4 M-ZnO SNW based Schottky diode fabrication

Jang et al. have reported the synthesis of ZnO nanowires and nanorods with controlled morphologies and aspect ratio in low-temperature hydrothermal conditions with the help of different forms of dodecyl sulfate, such as, sodium dodecyl sulfate (SDS) [95]. Choi et al. have also reported about the effect of SDS on the growth of ZnO particles by introducing doping of Na ions and improvement in the crystallinity and photoluminescence of fabricated ZnO nanostructures [94]. Similarly, Edinger et

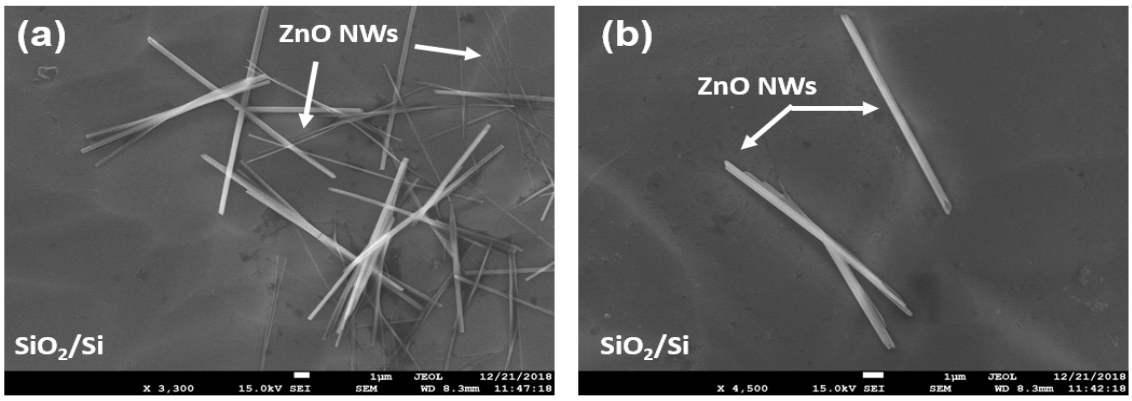

Fig. C.2: Effect of acetic acid and SDS on morphology of ZnO NW (a) FESEM image showing formation of ZnO single-NWs with length > 10 μm and width varying in range of ~ 90 nm to 400 nm after addition of 1:3 acetic acid in ZnO NW dispersion in DI water and SDS (b) FESEM image showing improved separation between two ZnO NWs

al. have investigated the effect of Acetic acid on the growth rate, morphological and electro-optical properties of ZnO thin films and have found that Acetic acid favoured (001)-textured films and has an influence on the roughness and grain-size of the ZnO film [133]. Jiao et al. have also shown that Acetic acid has a great effect on the physical properties of ZnO thin films by enhancing their growth rate and modifying the surface morphology [134].

With the inputs from the above reports, 1 mg of SDS is added in 5 mL of DI water to lower down the surface tension of the solution. Further, 1.2 mL of this solution is taken out separately, and 2 mg of ZnO nanowire powder is dispersed in it. This ZnO NW dispersion is treated with Vortex generator for proper mixing. For simplicity, the ZnO NW dispersion in SDS-added DI water is abbreviated as low surface-tension nanowire dispersion (LST-NWD). 2 μL of this dispersion is added with the same amount of Acetic acid and drop-casted on the SiO_2/Si substrate. It is observed that the addition of Acetic acid with LST-NWD in equal proportion can separate the individual ZnO NWs significantly and form longer (> 10 μm) ZnO NWs, having low-edge roughness, as shown in Figure C.2(a). It shows a small cluster of individual and longer ZnO NWs with lengths > 10 μm and width near 200-400 nm after addition of Acetic acid in 1:1 ratio with LST-NWD. To further decrease the width of above ZnO NWs, more Acetic acid is added in 3:1 ratio (6 μL of Acetic acid in 2 μL of LST-NWD). The addition of higher concentration of Acetic acid results in ZnO single-NWs with width near 100 nm and length greater than 10 μm with appreciable separation among individual nanowires as shown in Figure C.2(a, b). However, further addition of a higher concentration of Acetic acid results in the complete or partial dissolution of ZnO NWs in the acid. The ZnO SNWs synthesized using 3:1 ratio of

Acetic acid to LST-NWD got converted into ZnO micro-particles when heated at higher temperatures, near 250 °C. This shows that ZnO SNWs synthesized using a higher concentration of Acetic acid are not thermally stable and hence not suitable for sensing applications at higher temperatures. Therefore, 1:1 concentration of Acetic acid and ZnO NW dispersion in SDS-added DI water is considered as the optimized concentration to fabricate ZnO single-NW based devices for gas sensing applications. Since SDS and Acetic acid modify the structure of these ZnO NWs, these are referred to as Modified ZnO single nanowires (M-ZnO SNWs).

D

Electron density computation

Contents

D.1 Computation for 1-D electron density using 1-D DOS for a ZnO SNW

The electron density per unit length in a 1-D nanowire semiconductor can be written in energy space as [162]

$$n_L = \int_{Ec}^{\infty} f(E) D_{1d}(E) dE \tag{D.1}$$

where, $D_{1d}(E)$ is density of states in 1-D semiconductors like nanowire and is given as [162]

$$D_{1d}(E) = \frac{\sqrt{2m*}}{\pi\hbar} \sqrt{\frac{1}{E - E_c}} \tag{D.2}$$

and m^* is the effective mass of electrons in ZnO NW which is generally given as m^*= 0.39 m_e, where m_e is electron rest mass. Here, f(E) is the Fermi function given as

$$f(E) = \frac{1}{1 + e^{E - E_f/k_B T}} \tag{D.3}$$

where, E_c is the conduction band energy, 'k_B' is the Boltzmann constant, E_f is fermi level and T is the temperature in Kelvin. Putting (4,5) in (3), we get n_L as follow

$$n_L = \frac{\sqrt{2m^*}}{\pi\hbar} \int_{Ec}^{\infty} \frac{dE}{\sqrt{E - E_c}(1 + e^{E - E_f/k_B T})} \tag{D.4}$$

Now, total electronic energy E can be expressed as follows assuming parabolic relation between electron energy and momentum

$$E = E_c + \frac{\hbar^2 k^2}{2m^*} \tag{D.5}$$

where, $\hbar^2$ is reduced plank's constant given as $\hbar^2$=h/2π, 'k' is the wave number. From above equation, we can express wave number 'k' in terms of energy as

$$k = \frac{\sqrt{2m^*(E - E_c)}}{\hbar} \tag{D.6}$$

Now, integrating for n_L in terms of 'k', we can write its expression as

$$n_L = \frac{\sqrt{2m^* k_B T}}{\pi\hbar} \int_{0}^{\infty} \frac{\varepsilon^{-1/2} d\varepsilon}{1 + e^{\varepsilon - n_f}} \tag{D.7}$$

where, ε and n_f are given as

$$\varepsilon = E - E_c/k_B T \tag{D.8}$$

$$n_f = E_f - E_c/k_BT \tag{D.9}$$

Final expression for n_L can be written as

$$n_L = N_{1D}F_{-1/2}(n_f) \tag{D.10}$$

where, N_{1D} is the effective density of states in 1-D nanowire and $F_{-1/2}(n_f)$ is the Fermi-Dirac integral of order -1/2. These are expressed as follows

$$N_{1D} = \frac{1}{\hbar}\sqrt{\frac{2m^*k_BT}{\pi}} \tag{D.11}$$

$$F_{-1/2}(n_f) = \frac{1}{\sqrt{\pi}}\int_0^\infty \frac{\varepsilon^{-1/2}d\varepsilon}{1+e^{\varepsilon-n_f}} \tag{D.12}$$

Since exact analytical solution for $F_{-1/2}$ integral is not possible, we have used approximate solution of $F_{-1/2}(n_f)$ integral as given below [162]

$$F_{-1/2}(n_f) = e^{n_f} \tag{D.13}$$

Hence, final expression of n_L can be written as

$$n_L = N_{1D}e^{nf} \tag{D.14}$$

Bibliography

[1] V. Subramanian, J. Cen, A. de la Fuente Vornbrock, G. Grau, H. Kang, R. Kitsomboonloha, D. Soltman, and H. Tseng, "High-speed printing of transistors: From inks to devices," *Proceedings of the IEEE*, vol. 103, no. 4, pp. 567–582, April 2015.

[2] V. Subramanian, J. B. Chang, A. de la Fuente Vornbrock, D. C. Huang, L. Jagannathan, F. Liao, B. Mattis, S. Molesa, D. R. Redinger, D. Soltman *et al.*, "Printed electronics for low-cost electronic systems: Technology status and application development," pp. 17–24, 2008.

[3] W. J. Hyun, S. Lim, B. Y. Ahn, J. A. Lewis, C. D. Frisbie, and L. F. Francis, "Screen printing of highly loaded silver inks on plastic substrates using silicon stencils," *ACS Applied Materials & Interfaces*, vol. 7, no. 23, pp. 12 619–12 624, June 2015, doi:10.1021/acsami.5b02487.

[4] I. technology roadmap for semiconductors (ITRS), 2015. [Online]. Available: http://www.itrs2.net/itrs-reports.html

[5] L. Zhang, "Silicon process and manufacturing technology evolution: An overview of advancements in chip making." *IEEE Consumer Electronics Magazine*, vol. 3, pp. 44–48, 2014.

[6] G. Moore, "MooreâĂŹs law," *Electronics Magazine*, vol. 38, no. 8, p. 114, 1965.

[7] C. Hu, "Modern semiconductor devices for integrated circuits," vol. 2, 2010.

[8] A. Dasgupta, A. Agarwal, and Y. S. Chauhan, "Unified compact model for nanowire transistors including quantum effects and quasi-ballistic transport," *IEEE Transactions on Electron Devices*, vol. 64, no. 4, pp. 1837–1845, 2017.

[9] S. Datta, "Electronic transport in mesoscopic systems," 1997.

[10] M. G. Ancona and G. J. Iafrate, "Quantum correction to the equation of state of an electron gas in a semiconductor," *Phys. Rev. B*, vol. 39, pp. 9536–9540, May 1989, doi:10.1103/PhysRevB.39.9536.

[11] C. Wang, L. Yin, L. Zhang, D. Xiang, and R. Gao, "Metal oxide gas sensors: sensitivity and influencing factors," *Sensors*, vol. 10, no. 3, pp. 2088–2106, 2010.

[12] G. Natu, Z. Huang, Z. Ji, and Y. Wu, "The effect of an atomically deposited layer of alumina on nio in p-type dye-sensitized solar cells," *Langmuir*, vol. 28, no. 1, pp. 950–956, 2012, doi:10.1021/la203534s.

[13] A. C. Arias, J. Daniel, B. Krusor, S. Ready, V. Sholin, and R. Street, "All-additive ink-jet-printed display backplanes: Materials development and integration," *Journal of the Society for Information Display*, vol. 15, no. 7, pp. 485–490, June 2007.

[14] T. S. M. C. (TSMC), 2019. [Online]. Available: https://www.tsmc.com/english/dedicatedFoundry/technology/7nm.htm

[15] Z. Fan and J. G. Lu, "Chemical sensing with ZnO nanowire Field-Effect Transistor," *IEEE Transactions on Nanotechnology*, vol. 5, no. 4, pp. 393–396, July 2006.

[16] T. I. Lee, W. J. Choi, K. J. Moon, J. H. Choi, J. P. Kar, S. N. Das, Y. S. Kim, H. K. Baik, and J. M. Myoung, "Programmable direct-printing nanowire electronic components," *Nano Letters*, vol. 10, no. 3, pp. 1016–1021, 2010.

[17] T. I. Lee, W. J. Choi, J. P. Kar, Y. H. Kang, J. H. Jeon, J. H. Park, Y. S. Kim, H. K. Baik, and J. M. Myoung, "Electrical contact tunable direct printing route for a Zno nanowire schottky diode," *Nano Letters*, vol. 10, no. 9, pp. 3517–3523, Sep 2010, doi:10.1021/nl101684c.

[18] C. S. Lao, J. Liu, P. Gao, L. Zhang, D. Davidovic, R. Tummala, and Z. L. Wang, "ZnO nanobelt/nanowire schottky diodes formed by dielectrophoresis alignment across Au electrodes," *Nano Letters*, vol. 6, no. 2, pp. 263–266, Jan 2006, doi:10.1021/nl052239p.

[19] Y. W. Heo, L. C. Tien, D. P. Norton, S. J. Pearton, B. S. Kang, F. Ren, and J. R. LaRoche, "Pt / ZnO nanowire Schottky diodes," *Applied Physics Letters*, vol. 85, no. 15, pp. 3107–3109, Aug 2004, doi:10.1063/1.1802372.

[20] H. Sheng, S. Muthukumar, N. W. Emanetoglu, and Y. Lu, "Schottky diode with Ag on (112ĬĎ0) epitaxial ZnO film," *Applied Physics Letters*, vol. 80, no. 12, pp. 2132–2134, 2002.

[21] O. Lupan, V. Postica, T. PauportÃĭ, M. Hoppe, and R. Adelung, "UV nanophotodetectors: A case study of individual Au-modified ZnO nanowires," *Sensors and Actuators A: Physical*, vol. 296, pp. 400 – 408, Sep 2019, doi:10.1016/j.sna.2019.07.040.

[22] V. K. S. Yadav, G. Natu, and R. Paily, "Analysis of superfine-resolution printing of Polyaniline and Silver microstructures for electronic applications," *IEEE Transactions on Components, Packaging and Manufacturing Technology*, vol. 8, no. 9, pp. 1678–1685, Sep. 2018, doi:10.1109/TCPMT.2018.2854629.

[23] J. Arrese, G. Vescio, E. Xuriguera, B. Medina-Rodriguez, A. Cornet, and A. Cirera, "Flexible hybrid circuit fully inkjet-printed: Surface mount devices assembled by silver nanoparticles-based inkjet ink," *Journal of Applied Physics*, vol. 121, no. 10, p. 104904, March 2017, doi:10.1063/1.4977961.

[24] M. Magliulo, M. Mulla, M. Singh, E. Macchia, A. Tiwari, L. Torsi, and K. Manoli, "Printable and flexible electronics: from tfts to bioelectronic devices," *Journal of Materials Chemistry C*, vol. 3, no. 48, pp. 12 347–12 363, 2015.

[25] Y. Yang and W. Gao, "Wearable and flexible electronics for continuous molecular monitoring," *Chem. Soc. Rev.*, vol. 48, pp. 1465–1491, March 2019, doi:10.1039/C7CS00730B.

[26] D. TobjÃűrk and R. ÃŰsterbacka, "Paper electronics," *Advanced Materials*, vol. 23, no. 17, pp. 1935–1961, March 2011, doi:10.1002/adma.201004692.

[27] J. Perelaer, P. J. Smith, D. Mager, D. Soltman, S. K. Volkman, V. Subramanian, J. G. Korvink, and U. S. Schubert, "Printed electronics: the challenges involved in printing devices, interconnects, and contacts based on inorganic materials," *Journal of Materials Chemistry*, vol. 20, no. 39, pp. 8446–8453, 2010.

[28] J. Daniel, "Printed electronics: Technology, challenges and applications," Sept. 8-10,2010.

[29] J. Zhou, T. Ge, and J. S. Chang, "Printed electronics: Effects of bending and a self-compensation means," *IEEE Transactions on Circuits and Systems I: Regular Papers*, vol. 64, no. 3, pp. 505–515, 2017.

[30] V. Subramanian, P. C. Chang, J. B. Lee, S. E. Molesa, and S. K. Volkman, "Printed organic transistors for ultra-low-cost RFID applications," *IEEE Transactions on Components and Packaging Technologies*, vol. 28, no. 4, pp. 742–747, Dec 2005, doi:10.1109/TCAPT.2005.859672.

[31] S. Koskinen, L. PykÃďri, and M. MÃďntysalo, "Electrical performance characterization of an inkjet-printed flexible circuit in a mobile application," *IEEE Transactions on Components, Packaging and Manufacturing Technology*, vol. 3, no. 9, pp. 1604–1610, Sep. 2013.

[32] Y. Li, M. Misra, and S. Gregori, "Printing green nanomaterials for organic electronics," *IEEE Transactions on Components, Packaging and Manufacturing Technology*, vol. 8, no. 7, pp. 1307–1315, July 2018.

[33] S. Jung, A. Sou, E. Gili, and H. Sirringhaus, "Inkjet-printed resistors with a wide resistance range for printed read-only memory applications," *Organic Electronics*, vol. 14, no. 3, pp. 699 – 702, 2013.

[34] R. Ramakrishnan, N. Saran, and R. J. Petcavich, "Selective inkjet printing of conductors for displays and flexible printed electronics," *Journal of Display Technology*, vol. 7, no. 6, pp. 344–347, June 2011.

[35] H. Marien, M. S. J. Steyaert, E. van Veenendaal, and P. Heremans, "Analog building blocks for organic smart sensor systems in organic thin-film transistor technology on flexible plastic foil," *IEEE Journal of Solid-State Circuits*, vol. 47, no. 7, pp. 1712–1720, July 2012.

[36] V. K. S. Yadav, G. Natu, and R. Paily, "Fabrication and electrical characterization of printed micro-resistors of silver nanoparticles using micro-cantilever based printing technology," *IEEE Transactions on Components, Packaging and Manufacturing Technology*, pp. 1–1, 2019, doi:10.1109/TCPMT.2019.2954079.

[37] G. McKerricher, J. G. Perez, and A. Shamim, "Fully inkjet printed rf inductors and capacitors using polymer dielectric and silver conductive ink with through vias," *IEEE Transactions on Electron Devices*, vol. 62, no. 3, pp. 1002–1009, March 2015.

[38] C. Sternkiker, E. Sowade, K. Y. Mitra, R. Zichner, and R. R. Baumann, "Upscaling of the inkjet printing process for the manufacturing of passive electronic devices," *IEEE Transactions on Electron Devices*, vol. 63, no. 1, pp. 426–431, Jan 2016.

[39] Z. Fan, J. C. Ho, T. Takahashi, R. Yerushalmi, K. Takei, A. C. Ford, Y.-L. Chueh, and A. Javey, "Toward the development of printable nanowire electronics and sensors," *Advanced Materials*, vol. 21, no. 37, pp. 3730–3743, Sep 2009, doi:10.1002/adma.200900860.

[40] V. Subramanian, J. M. Fréchet, P. C. Chang, D. C. Huang, J. B. Lee, S. E. Molesa, A. R. Murphy, D. R. Redinger, and S. K. Volkman, "Progress toward development of all-printed rfid tags: materials, processes, and devices," *Proceedings of the IEEE*, vol. 93, no. 7, pp. 1330–1338, 2005.

[41] T. Sekitani, Y. Noguchi, U. Zschieschang, H. Klauk, and T. Someya, "Organic transistors manufactured using inkjet technology with subfemtoliter accuracy," *Proceedings of the National Academy of Sciences*, vol. 105, no. 13, pp. 4976–4980, Feb 2008, doi:10.1073/pnas.0708340105.

[42] M. G. Mabeck, J.T., "Chemical and biological sensors based on organic thin-film transistors," *Anal Bioanal Chem*, no. 384, p. 343âĂŞ353, Aug 2006, doi:10.1007/s00216-005-3390-2.

[43] P. Kopola, T. Aernouts, R. Sliz, S. Guillerez, M. Ylikunnari, D. Cheyns, M. VÃďlimÃďki, M. Tuomikoski, J. Hast, G. Jabbour, R. MyllylÃď, and A. Maaninen, "Gravure printed flexible organic photovoltaic modules," *Solar Energy Materials and Solar Cells*, vol. 95, no. 5, pp. 1344 – 1347, May 2011, doi:10.1016/j.solmat.2010.12.020.

[44] W. R. Cai, Y. Q. Chen, Y. Liu, X. Jin, Y. Q. Deng, Y. Z. Zhang, J. Zhang, H. Yan, W. L. Gao, J. Mei, and W. M. Lau, "Fabrication of copper electrode on flexible substrate through Ag^{+}- based inkjet printing and rapid electroless metallization," *IEEE Transactions on Components, Packaging and Manufacturing Technology*, vol. 7, no. 9, pp. 1552–1559, Sept 2017.

[45] Y. Li, L. Lan, S. Hu, P. Gao, X. Dai, P. He, X. Li, and J. Peng, "Fully printed top-gate metalâĂŞoxide thin-film transistors based on scandium-zirconium-oxide dielectric," *IEEE Transactions on Electron Devices*, vol. 66, no. 1, pp. 445–450, Jan 2019.

[46] R. Tao, H. Ning, J. Chen, J. Zou, Z. Fang, C. Yang, Y. Zhou, J. Zhang, R. Yao, and J. Peng, "Inkjet printed electrodes in thin film transistors," *IEEE Journal of the Electron Devices Society*, vol. 6, pp. 774–790, 2018.

[47] H. A. D. Nguyen, J. Lee, C. H. Kim, K.-H. Shin, and D. Lee, "An approach for controlling printed line-width in high resolution roll-to-roll gravure printing," *Journal of Micromechanics and Microengineering*, vol. 23, no. 9, p. 095010, 2013.

[48] K.-H. Shin, H. A. D. Nguyen, J. Park, D. Shin, and D. Lee, "Roll-to-roll gravure printing of thick-film silver electrode micropatterns for flexible printed circuit board," *Journal of Coatings Technology and Research*, vol. 14, no. 1, pp. 95–106, Jan 2017.

[49] W. J. Hyun, S. Lim, B. Y. Ahn, J. A. Lewis, C. D. Frisbie, and L. F. Francis, "Screen printing of highly loaded silver inks on plastic substrates using silicon stencils," *ACS Applied Materials & Interfaces*, vol. 7, no. 23, pp. 12 619–12 624, 2015.

[50] E. K. Choi, J. Park, B. S. Kim, and D. Lee, "Fabrication of electrodes and near-field communication tags based on screen printing of silver seed patterns and copper electroless plating," *International Journal of Precision Engineering and Manufacturing*, vol. 16, no. 10, pp. 2199–2204, Sep 2015.

[51] D. Erath, A. FilipoviÄĞ, M. Retzlaff, A. K. Goetz, F. Clement, D. Biro, and R. Preu, "Advanced screen printing technique for high definition front side metallization of crystalline silicon solar cells," *Solar Energy Materials and Solar Cells*, vol. 94, no. 1, pp. 57 – 61, 2010, 17th International Materials Research Congress 2008.

[52] N. Kooy, K. Mohamed, L. T. Pin, and O. S. Guan, "A review of roll-to-roll nanoimprint lithography," *Nanoscale research letters*, vol. 9, no. 1, p. 320, 2014.

[53] K.-H. Choi, A. Khan, H.-C. Kim, K. Rahman, K.-R. Kwon, N. M. Muhammad, and Y.-H. Doh, "Electro-hydrodynamic inkjet-micro pattern fabrication for printed electronics applications," 2011.

[54] Accessed: May 5, 2019. [Online]. Available: https://en.wikipedia.org/wiki/Collagen

[55] *BioForce Nanosciences*, Accessed: April 10, 2019. [Online]. Available: www.bioforcenano.com

[56] Y. Yan, S. C. Warren, P. Fuller, and B. A. Grzybowski, "Chemoelectronic circuits based on metal nanoparticles," *Nature Nanotechnology*, vol. 11, pp. 603–608, 2016.

[57] D. McManus, S. Vranic, F. Withers, V. Sanchez-Romaguera, M. Macucci, H. Yang, R. Sorrentino, K. Parvez, S.-K. Son, G. Iannaccone *et al.*, "Water-based and biocompatible 2d crystal inks for all-inkjet-printed heterostructures," *Nature Nanotechnology*, vol. 12, no. 4, pp. 343–350, 2017.

[58] B. J. Kang, C. K. Lee, and J. H. Oh, "All-inkjet-printed electrical components and circuit fabrication on a plastic substrate," *Microelectronic Engineering*, vol. 97, pp. 251 – 254, 2012.

[59] T. Kawase, H. Sirringhaus, R. H. Friend, T. Shimoda *et al.*, "Inkjet printed via-hole interconnections and resistors for all-polymer transistor circuits," *Advanced Materials*, vol. 13, no. 21, p. 1601, 2001.

[60] S. M. Bidoki, J. Nouri, and A. A. Heidari, "Inkjet deposited circuit components," *Journal of Micromechanics and Microengineering*, vol. 20, no. 5, p. 055023, 2010.

[61] "Keithley 4200-SCS manual," *Keithley, Cleveland, OH, USA*, 2003.

[62] *Alicat Scientific*, Accessed: August 21, 2019. [Online]. Available: https://www.alicat.com/models/flow-vision-software/

[63] D. Wessling, "Berhard," conductive polymer/solvent systems: Solutions or dispersions?", zipperling kessler/ormecon chemie, dated 1996, article from the internet," 2001.

[64] "Silver Dispersion/Dimethyl Sulfoxide," *Sigma Aldrich (Merck) Pvt. Ltd.*, Accessed: April 10, 2019. [Online]. Available: https://www.sigmaaldrich.com/india.html

[65] Young.T, "An essay on the cohesion of fluids," *Philos. Trans. R. Soc. Lond.*, vol. 95, no. 65, 1805.

[66] B. N. Sahoo, K. Balasubramanian, and M. Sucheendran, "Thermally triggered transition of superhydrophobic characteristics of micro- and nanotextured multiscale rough surfaces," *The Journal of Physical Chemistry C*, vol. 119, no. 25, pp. 14 201–14 213, 2015.

[67] S. A. Markarian and A. M. Terzyan, "Surface tension and refractive index of dialkylsulfoxide + water mixtures at several temperatures," *Journal of Chemical & Engineering Data*, vol. 52, no. 5, pp. 1704–1709, 2007.

[68] D. Soltman and V. Subramanian, "Inkjet-printed line morphologies and temperature control of the coffee ring effect," *Langmuir*, vol. 24, no. 5, pp. 2224–2231, 2008.

[69] F. Huo, Z. Zheng, G. Zheng, L. R. Giam, H. Zhang, and C. A. Mirkin, "Polymer pen lithography," *Science*, vol. 321, no. 5896, pp. 1658–1660, 2008.

[70] E. S. Park, J. Jeon, V. Subramanian, and T. J. K. Liu, "Inkjet-printed microshell encapsulation: A new zero-level packaging technology," pp. 357–360, Jan 2012.

[71] K. Murata, J. Matsumoto, A. Tezuka, Y. Matsuba, and H. Yokoyama, "Super-fine ink-jet printing: toward the minimal manufacturing system," *Microsystem Technologies*, vol. 12, no. 1, p. 2, Oct 2005.

[72] F. Hsiao and Y. Liao, "Printed micro-sensors for simultaneous temperature and humidity detection," *IEEE Sensors Journal*, vol. 18, no. 16, pp. 6788–6793, Aug 2018.

[73] M. Vaseem, K. M. Lee, A.-R. Hong, and Y.-B. Hahn, "Inkjet printed fractal-connected electrodes with silver nanoparticle ink," *ACS Applied Materials & Interfaces*, vol. 4, no. 6, pp. 3300–3307, 2012.

[74] V. Correia, K. Mitra, H. Castro, J. Rocha, E. Sowade, R. Baumann, and S. Lanceros-Mendez, "Design and fabrication of multilayer inkjet-printed passive components for printed electronics circuit development," *Journal of Manufacturing Processes*, vol. 31, pp. 364 – 371, 2018.

[75] S. Dutta, K. Sankaran, K. Moors, G. Pourtois, S. Van Elshocht, J. BÃűmmels, W. Vandervorst, Z. TÅŚkei, and C. Adelmann, "Thickness dependence of the resistivity of platinum-group metal thin films," *Journal of Applied Physics*, vol. 122, no. 2, p. 025107, 2017.

[76] H. Wei and H. Eilers, "From silver nanoparticles to thin films: Evolution of microstructure and electrical conduction," *arXiv preprint arXiv:1105.2608*, 2011.

[77] *Electronic notes*, Accessed: April 10, 2019. [Online]. Available: www.electronic-notes.com

[78] *Element 14*, Accessed: April 10, 2019. [Online]. Available: www.electronic-notes.com

[79] *Vishay Intertechnology*, Accessed: April 10, 2019. [Online]. Available: www.vishay.com

[80] *MultiComp Farnell*, Accessed: April 10, 2019. [Online]. Available: https://uk.farnell.com/b/multicomp

[81] "Silver Dispersion/Dimethyl Sulfoxide," *Sigma Aldrich (Merck) Pvt. Ltd.*, Accessed: May 5, 2019. [Online]. Available: https://www.sigmaaldrich.com/india.html

[82] *Bittele Turn-Key PCB Assembly*, Accessed: September 30, 2019. [Online]. Available: https://www.7pcb.com/blog/surface-mount-smt-assembly-cost-china.php

[83] D. C. S. Wai, R. Lim, M. R. N. B. Damalerio, W. Chen, and M. Cheng, "Development of a flexible printed multi-functional sensor platform for medical applications," in *2018 IEEE 20th Electronics Packaging Technology Conference (EPTC)*, Dec 2018, pp. 464–467.

[84] F. Juang, "Ag additive and nanorod structure enhanced gas sensing properties of metal oxide-based CO_2 sensor," *IEEE Sensors Journal*, vol. 19, no. 12, pp. 4381–4385, June 2019.

[85] C. Lee, H. Lee, and Y. Chiu, "Performance improvement of nitrogen oxide gas sensors using Au catalytic metal on Sno2/Wo3 complex nanoparticle sensing layer," *IEEE Sensors Journal*, vol. 16, no. 21, pp. 7581–7585, Nov 2016.

[86] H.-D. Zhang, Y.-Z. Long, Z.-J. Li, and B. Sun, "Fabrication of comb-like ZnO nanostructures for room-temperature CO gas sensing application," *Vacuum*, vol. 101, pp. 113 – 117, 2014.

[87] M. Sinha, R. Mahapatra, B. Mondal, T. Maruyama, and R. Ghosh, "Ultrafast and reversible gas-sensing properties of ZnO nanowire arrays grown by hydrothermal technique," *The Journal of Physical Chemistry C*, vol. 120, no. 5, pp. 3019–3025, 2016.

[88] M.-W. Ahn, K.-S. Park, J.-H. Heo, J.-G. Park, D.-W. Kim, K. J. Choi, J.-H. Lee, and S.-H. Hong, "Gas sensing properties of defect-controlled ZnO-nanowire gas sensor," *Applied Physics Letters*, vol. 93, no. 26, p. 263103, 2008.

[89] D. Zhang, S. Chava, C. Berven, S. K. Lee, R. Devitt, and V. Katkanant, "Experimental study of electrical properties of ZnO nanowire random networks for gas sensing and electronic devices," *Applied Physics A*, vol. 100, no. 1, pp. 145–150, Jul 2010.

[90] H. Wu, D. Lin, R. Zhang, and W. Pan, "ZnO nanofiber Field-Effect Transistor assembled by electrospinning," *Journal of the American Ceramic Society*, vol. 91, no. 2, pp. 656–659, 2008.

[91] R. K. Joshi, Q. Hu, F. Alvi, N. Joshi, and A. Kumar, "Au decorated Zinc Oxide nanowires for CO sensing," *The Journal of Physical Chemistry C*, vol. 113, no. 36, pp. 16 199–16 202, 2009.

[92] P. K. Kannan, R. Saraswathi, and J. B. B. Rayappan, "CO_2 gas sensing properties of DC reactive magnetron sputtered ZnO thin film," *Ceramics International*, vol. 40, no. 8, Part B, pp. 13 115 – 13 122, 2014.

[93] A. Y. Polyakov, N. B. Smirnov, E. A. Kozhukhova, V. I. Vdovin, K. Ip, Y. W. Heo, D. P. Norton, and S. J. Pearton, "Electrical characteristics of Au and Ag Schottky contacts on n-ZnO," *Applied Physics Letters*, vol. 83, no. 8, pp. 1575–1577, June 2003, doi:10.1063/1.1604173.

[94] K. Choi, T. Kang, and S.-G. Oh, "Preparation of disk shaped ZnO particles using surfactant and their PL properties," *Materials Letters*, vol. 75, pp. 240–243, 2012.

[95] J.-H. Jang, J. H. Park, and S.-G. Oh, "Effects of Dodecyl Sulfate Anionic surfactants on the crystal growth of ZnO through hydrothermal process," *J. Ceram. Process. Res*, vol. 10, pp. 783–790, 2009.

[96] *International Centre for Diffraction Data (ICDD)*, Accessed: Jan 09, 2020. [Online]. Available: http://www.icdd.com/pdfsearch/

[97] R. Dhahri, M. Hjiri, L. E. Mir, E. Fazio, F. Neri, F. Barreca, N. Donato, A. Bonavita, S. G. Leonardi, and G. Neri, "ZnO:Ca nanopowders with enhanced CO_2 sensing properties," *Journal of Physics D: Applied Physics*, vol. 48, no. 25, p. 255503, may 2015, doi:10.1088/0022-3727/48/25/255503.

[98] K. Kim, H. Kwak, H. Cho, M. Meyyappan, and C. Baek, "Design guidelines for high sensitivity ZnO nanowire gas sensors with Schottky contact," *IEEE Sensors Journal*, vol. 19, no. 3, pp. 976–981, Feb 2019.

[99] L. J. Brillson and Y. Lu, "ZnO Schottky barriers and Ohmic contacts," *Journal of Applied Physics*, vol. 109, no. 12, p. 121301, 2011.

[100] R. T. Tung, "The physics and chemistry of the Schottky barrier height," *Applied Physics Reviews*, vol. 1, no. 1, p. 011304, 2014.

[101] S. N. Das, J.-H. Choi, J. P. Kar, K.-J. Moon, T. I. Lee, and J.-M. Myoung, "Junction properties of Au/ZnO single nanowire Schottky diode," *Applied Physics Letters*, vol. 96, no. 9, p. 092111, Feb 2010, doi:10.1063/1.3339883.

[102] Y. S. Puzyrev, X. Shen, C. X. Zhang, J. Hachtel, K. Ni, B. K. Choi, E.-X. Zhang, O. Ovchinnikov, R. D. Schrimpf, D. M. Fleetwood, and S. T. Pantelides, "Memristive devices from ZnO nanowire bundles and meshes," *Applied Physics Letters*, vol. 111, no. 15, p. 153504, 2017.

[103] H. Kim, H. Kim, and D.-W. Kim, "Silver Schottky contacts to α-plane bulk ZnO," *Journal of Applied Physics*, vol. 108, no. 7, p. 074514, Aug 2010, doi:10.1063/1.3493261.

[104] V. K. S. Yadav, S. Roy, G. Natu, and R. Paily, "Fabrication of back to back Schottky micro-diodes using Silver nanoparticle film and Zinc Oxide nanowire mat for biological interactions," *IEEE TENCON*, 2019.

[105] S. Kanaparthi and S. G. Singh, "Chemiresistive sensor based on Zinc Oxide nanoflakes for CO_2 detection," *ACS Applied Nano Materials*, vol. 2, no. 2, pp. 700–706, 2019.

[106] W. An, X. Wu, and X. C. Zeng, "Adsorption of O_2, H_2, CO, NH_3, and NO_2 on ZnO nanotube:âĂĽ a density functional theory study," *The Journal of Physical Chemistry C*, vol. 112, no. 15, pp. 5747–5755, 2008.

[107] C.-L. Hsu, B.-Y. Jhang, C. Kao, and T.-J. Hsueh, "Uv-illumination and Au-nanoparticles enhanced gas sensing of p-type Na-doped ZnO nanowires operating at room temperature," *Sensors and Actuators B: Chemical*, vol. 274, pp. 565 – 574, 2018.

[108] Y. Hu, J. Zhou, P.-H. Yeh, Z. Li, T.-Y. Wei, and Z. L. Wang, "Supersensitive, fast-response nanowire sensors by using Schottky contacts," *Advanced Materials*, vol. 22, no. 30, pp. 3327–3332, Aug 2010, doi:10.1002/adma.201000278.

[109] Nugraha, A. G. Saputro, M. K. Agusta, B. Yuliarto, H. K. Dipojono, and R. Maezono, "Density functional study of adsorptions of CO2, NO2and SO2 molecules on Zn(0002) surfaces," *Journal of Physics: Conference Series*, vol. 739, p. 012080, aug 2016.

[110] R. Borgohain, R. Das, B. Mondal, V. Yordsri, C. Thanachayanont, and S. Baruah, "ZnO/ZnS core-shell nanostructures for low-concentration NO_2 sensing at room temperature," *IEEE Sensors Journal*, vol. 18, no. 17, pp. 7203–7208, Sep. 2018.

[111] Y. Xia, J. Wang, X. Li, D. Xie, D. Zhou, L. Xiang, and S. Komarneni, "Nanoseed-assisted rapid formation of ultrathin ZnO nanorods for efficient room temperature NO_2 detection," *Ceramics International*, vol. 42, no. 14, pp. 15 876 – 15 880, 2016.

[112] V. K. S. Yadav, T. T. Daniel, and R. P. Paily, "Gas sensors based on drop-casted ZnO nanowires and micro-cantilever printed Ag contacts," *IEEE Sensors Journal*, vol. 20, no. 9, pp. 4951–4958, May 2020, doi:10.1109/JSEN.2020.2964600.

[113] S. Xu, Y. Qin, C. Xu, Y. Wei, R. Yang, and Z. Wang, "Self-powered nanowire devices," *Nature nanotechnology*, vol. 5, pp. 366–73, March 2010, doi:10.1038/nnano.2010.46.

[114] J. L. H. C. M. S. V. G. D. E. H. Juntao Xu, Michael Lynch, "Microfabricated quill-type surface patterning tools for the creation of biological micronano arrays," *Biomedical Microdevices*, vol. 6, p. 117âĂŞ123, June 2014, doi:10.1023B:BMMD0000031748.13353.10.

[115] A. J. Chiquito, C. A. Amorim, O. M. Berengue, L. S. Araujo, E. P. Bernardo, and E. R. Leite, "Back-to-back schottky diodes: the generalization of the diode theory in analysis and extraction of electrical parameters of nanodevices," *Journal of Physics: Condensed Matter*, vol. 24, no. 22, p. 225303, 2012, doi:10.1088/0953-8984/24/22/225303.

[116] M. Shafiei, J. Yu, R. Arsat, K. Kalantar-zadeh, E. Comini, M. Ferroni, G. Sberveglieri, and W. Wlodarski, "Reversed bias Pt / nanostructured ZnO schottky diode with enhanced electric field for hydrogen sensing," *Sensors and Actuators B: Chemical*, vol. 146, no. 2, pp. 507 – 512, April 2010, doi:10.1016/j.snb.2009.12.028.

[117] S. K. Cheung and N. W. Cheung, "Extraction of Schottky diode parameters from forward currentâĂŘvoltage characteristics," *Applied Physics Letters*, vol. 49, no. 2, pp. 85–87, May 1986, doi:10.1063/1.97359.

[118] X. Zhang, J. Zhai, X. Yu, L. Ding, and W. Zhang, "Fabrication and characterization of flexible Ag/Zno Schottky diodes on polyimide substrates," *Thin Solid Films*, vol. 548, pp. 623 – 626, Dec 2013, doi:10.1016/j.tsf.2013.09.090.

[119] M. W. Allen, M. M. Alkaisi, and S. M. Durbin, "Metal schottky diodes on Zn-polar and O-polar bulk ZnO," *Applied Physics Letters*, vol. 89, no. 10, p. 103520, Sept 2006, doi:10.1063/1.2346137.

[120] Y. Yang, X. Zhang, M. Gao, F. Zeng, W. Zhou, S. Xie, and F. Pan, "Nonvolatile resistive switching in single crystalline Zno nanowires," *Nanoscale*, vol. 3, pp. 1917–1921, 2011.

[121] J. J. Yang, D. B. Strukov, and D. R. Stewart, "Memristive devices for computing," *Nature nanotechnology*, vol. 8, no. 1, p. 13, 2013.

[122] O. Lupan, V. Postica, T. PauportÃĺ, B. Viana, M.-I. Terasa, and R. Adelung, "Room temperature gas nanosensors based on individual and multiple networked au-modified ZnO nanowires," *Sensors and Actuators B: Chemical*, vol. 299, p. 126977, 2019.

[123] M. N. Cardoza-Contreras, J. M. Romo-Herrera, L. A. RÃŋos, R. GarcÃŋa-GutiÃĺrrez, T. A. Zepeda, and O. E. Contreras, "Single ZnO nanowire-based gas sensors to detect low concentrations of hydrogen," *Sensors*, vol. 15, no. 12, pp. 30 539–30 544, 2015.

[124] R. Zhang, W. Pang, Z. Feng, X. Chen, Y. Chen, Q. Zhang, H. Zhang, C. Sun, J. J. Yang, and D. Zhang, "Enabling selectivity and fast recovery of ZnO nanowire gas sensors through resistive switching," *Sensors and Actuators B: Chemical*, vol. 238, pp. 357 – 363, 2017.

[125] R. Dhahri, S. Leonardi, M. Hjiri, L. E. Mir, A. Bonavita, N. Donato, D. Iannazzo, and G. Neri, "Enhanced performance of novel Calcium/Aluminum co-doped Zinc Oxide for CO_2 sensors," *Sensors and Actuators B: Chemical*, vol. 239, pp. 36 – 44, 2017.

[126] S. Zhao, Y. Shen, P. Zhou, F. Hao, X. Xu, S. Gao, D. Wei, Y. Ao, and Y. Shen, "Enhanced NO_2 sensing performance of ZnO nanowires functionalized with ultra-fine In_2O_3 nanoparticles," *Sensors and Actuators B: Chemical*, vol. 308, p. 127729, 2020.

[127] X. Chen, Y. Shen, P. Zhou, S. Zhao, X. Zhong, T. Li, C. Han, D. Wei, and D. Meng, "NO_2 sensing properties of one-pot-synthesized ZnO nanowires with Pd functionalization," *Sensors and Actuators B: Chemical*, vol. 280, pp. 151 – 161, 2019.

[128] X. Chen, Y. Shen, W. Zhang, J. Zhang, D. Wei, R. Lu, L. Zhu, H. Li, and Y. Shen, "In-situ growth of ZnO nanowire arrays on the sensing electrode via a facile hydrothermal route for high-performance NO_2 sensor," *Applied Surface Science*, vol. 435, pp. 1096 – 1104, 2018.

[129] E. Comini, "Metal oxide nanowire chemical sensors: innovation and quality of life," *Materials Today*, vol. 19, no. 10, pp. 559 – 567, 2016.

[130] *BioForce Nanosciences*, Accessed: April 10, 2019. [Online]. Available: www.bioforcenano.com

[131] V. K. S. Yadav, S. Raveesh, T. T. Daniel, and R. Paily, "Microcantilever printed back-to-back zno single-nanowire schottky diodes," *IEEE Transactions on Electron Devices*, vol. 67, no. 8, pp. 3309–3314, Aug 2020, doi:10.1109/TED.2020.3002733.

[132] S. Zhao, Y. Shen, X. Yan, P. Zhou, Y. Yin, R. Lu, C. Han, B. Cui, and D. Wei, "Complex-surfactant-assisted hydrothermal synthesis of one-dimensional ZnO nanorods for high-performance ethanol gas sensor," *Sensors and Actuators B: Chemical*, vol. 286, pp. 501 – 511, 2019.

[133] S. Edinger, J. Bekacz, M. Richter, R. Hamid, R. Wibowo, A. PeiÄĞ, and T. Dimopoulos, "Influence of the acetic acid concentration on the growth of Zinc oxide thin films prepared by spray pyrolysis of aqueous solutions," *Thin Solid Films*, vol. 594, pp. 238 – 244, 2015.

[134] B. Jiao, X. Zhang, C. Wei, J. Sun, Q. Huang, and Y. Zhao, "Effect of Acetic acid on Zno:in transparent conductive oxide prepared by ultrasonic spray pyrolysis," *Thin Solid Films*, vol. 520, no. 4, pp. 1323 – 1329, 2011.

[135] X. Liu, Z. Jin, Z. Liu, K. Yu, and S. Bu, "Nanostructured ZnO films obtained by a basic erosion method," *Applied surface science*, vol. 252, no. 24, pp. 8668–8672, 2006.

[136] S. Bu, C. Cui, Q. Wang, and L. Bai, "Growth of ZnO nanowires in aqueous solution by a dissolution-growth mechanism," *Journal of Nanomaterials*, vol. 2008, pp. 1–5, 2008.

[137] T. T. Daniel, S. Majumder, V. K. S. Yadav, and R. Paily, "Magnetite based resistor for nitric oxide detection," *IEEE Sensors Journal*, pp. 1–1, 2020.

[138] Y. Xiong, Q. Xue, C. Ling, W. Lu, D. Ding, L. Zhu, and X. Li, "Effective CO_2 detection based on laocl-doped SnO_2 nanofibers: Insight into the role of oxygen in carrier gas," *Sensors and Actuators B: Chemical*, vol. 241, pp. 725 – 734, 2017.

[139] A. Ghosh, T. Schneller, R. Waser, and S. Majumder, "Understanding on the selective carbon monoxide sensing characteristics of copper oxide-zinc oxide composite thin films," *Sensors and Actuators B: Chemical*, vol. 253, pp. 685 – 696, 2017.

[140] M.-R. Yu, R.-J. Wu, and M. Chavali, "Effect of PtâĂŹ loading in ZnO-CuO hetero-junction material sensing carbon monoxide at room temperature," *Sensors and Actuators B: Chemical*, vol. 153, no. 2, pp. 321 – 328, 2011.

[141] Y.-J. Jeong, C. Balamurugan, and D.-W. Lee, "Enhanced CO_2 gas-sensing performance of ZnO nanopowder by La loaded during simple hydrothermal method," *Sensors and Actuators B: Chemical*, vol. 229, pp. 288 – 296, 2016.

[142] D. D. Trung, L. D. Toan, H. S. Hong, T. D. Lam, T. Trung, and N. V. Hieu, "Selective detection of Carbon Dioxide using LaOCl-functionalized SnO_2 nanowires for air-quality monitoring," *Talanta*, vol. 88, pp. 152 – 159, 2012.

[143] S. H. Park, S. H. Kim, S. Y. Park, and C. Lee, "Synthesis and CO gas sensing properties of surface-nitridated Ga_2O_3 nanowires," *RSC Adv.*, vol. 4, pp. 63 402–63 407, 2014.

[144] S. N. Das, J. P. Kar, J.-H. Choi, T. I. Lee, K.-J. Moon, and J.-M. Myoung, "Fabrication and characterization of ZnO single nanowire-based hydrogen sensor," *The Journal of Physical Chemistry C*, vol. 114, no. 3, pp. 1689–1693, 2010.

[145] S. Chang, "Oxygen chemisorption on tin oxide: Correlation between electrical conductivity and epr measurements," *Journal of Vacuum Science and Technology*, vol. 17, no. 1, pp. 366–369, Aug 1980, doi:10.1116/1.570389.

[146] Y. Wei, C. Chen, G. Yuan, and S. Gao, "Sno2 nanocrystals with abundant oxygen vacancies: Preparation and room temperature no2 sensing," *Journal of Alloys and Compounds*, vol. 681, pp. 43 – 49, 2016, doi:10.1016/j.jallcom.2016.04.220.

[147] B. Manna, S. Acharyya, I. Chakrabarti, and P. K. Guha, "Graphene oxide wrapped hollow sno2 sphere for room temperature formaldehyde sensing: An insight through computational analysis experimental study," *IEEE Transactions on Electron Devices*, vol. 67, no. 9, pp. 3767–3774, 2020.

[148] B. Sharma and J.-S. Kim, "Mems based highly sensitive dual fet gas sensor using graphene decorated pd-ag alloy nanoparticles for h_2 detection," *Scientific reports*, vol. 8, no. 1, p. 5902, 2018.

[149] T. Yoshizumi and Y. Miyahara, "Field-effect transistors for gas sensing," *Intechopen*, vol. 194, pp. 85 – 88, June 2017, doi:10.5772/intechopen.68481.

[150] Z. Fan, D. Wang, P.-C. Chang, W.-Y. Tseng, and J. G. Lu, "ZnO nanowire field-effect transistor and oxygen sensing property," *Applied Physics Letters*, vol. 85, no. 24, pp. 5923–5925, 2004.

[151] S. J. Pearton, D. P. Norton, L. C. Tien, and J. Guo, "Modeling and fabrication of ZnO nanowire transistors," *IEEE Transactions on Electron Devices*, vol. 55, no. 11, pp. 3012–3019, 2008.

[152] Z. Fan and J. G. Lu, "Chemical sensing with ZnO nanowire field-effect transistor," *IEEE Transactions on Nanotechnology*, vol. 5, no. 4, pp. 393–396, 2006.

[153] Q. H. Li, Q. Wan, Y. X. Liang, and T. H. Wang, "Electronic transport through individual ZnO nanowires," *Applied Physics Letters*, vol. 84, no. 22, pp. 4556–4558, 2004.

[154] Y. W. Heo, L. C. Tien, D. P. Norton, B. S. Kang, F. Ren, B. P. Gila, and S. J. Pearton, "Electrical transport properties of single ZnO nanorods," *Applied Physics Letters*, vol. 85, no. 11, pp. 2002–2004, 2004.

[155] Y. Shao, J. Yoon, H. Kim, T. Lee, and W. Lu, "Temperature dependence of electron transport in ZnO nanowire field effect transistors," *IEEE Transactions on Electron Devices*, vol. 61, no. 2, pp. 625–630, 2014.

[156] D. S. Kim, J.-P. Richters, R. Scholz, T. Voss, and M. Zacharias, "Modulation of carrier density in ZnO nanowires without impurity doping," *Applied Physics Letters*, vol. 96, no. 12, p. 123110, 2010.

[157] A. C. E. Chia and R. R. LaPierre, "Analytical model of surface depletion in GaAs nanowires," *Journal of Applied Physics*, vol. 112, no. 6, p. 063705, 2012.

[158] Y. Heo, D. Norton, L. Tien, Y. Kwon, B. Kang, F. Ren, S. Pearton, and J. LaRoche, "ZnO nanowire growth and devices," *Materials Science and Engineering: R: Reports*, vol. 47, no. 1, pp. 1 – 47, 2004.

[159] Y. S. Yu, S. H. Lee, J. H. Oh, H. J. Kim, S. W. Hwang, and D. Ahn, "A compact analytical current conduction model for a depletion-mode n-type nanowire field-effect transistor with a bottom-gate structure," *Semiconductor Science and Technology*, vol. 23, no. 3, p. 035025.

[160] A. J. Soares and R. J. Perry, "Modeling and simulation of a single tin dioxide nanobelt FET for chemical sensors," *IEEE Sensors Journal*, vol. 10, no. 2, pp. 235–242, 2010.

[161] P. Andrei, L. Fields, J. Zheng, Y. Cheng, and P. Xiong, "Modeling and simulation of single nanobelt SnO_2 gas sensors with FET structure," *Sensors and Actuators B: Chemical*, vol. 128, no. 1, pp. 226 – 234, 2007.

[162] R. Kim and M. Lundstrom, "Notes on Fermi-Dirac Integrals," *ArXiv e-prints*.

[163] H.-Y. Cha, H. Wu, M. Chandrashekhar, Y. C. Choi, S. Chae, G. Koley, and M. G. Spencer, "Fabrication and characterization of pre-aligned gallium nitride nanowire field-effect transistors," *Nanotechnology*, vol. 17, no. 5, p. 1264, 2006.

[164] A. Dasgupta, A. Agarwal, and Y. S. Chauhan, "Unified compact model for nanowire transistors including quantum effects and quasi-ballistic transport," *IEEE Transactions on Electron Devices*, vol. 64, no. 4, pp. 1837–1845, April 2017.

[165] R. K. Baruah and R. P. Paily, "A dual-material gate junctionless transistor with high- k spacer for enhanced analog performance," *IEEE Transactions on Electron Devices*, vol. 61, no. 1, pp. 123–128, 2014.

[166] B. G. Streetman, *Solid State Electronic Devices*, 1990.

[167] "Experimental measurement of work function in doped silicon surfaces," *Solid-State Electronics*, vol. 54, no. 1, pp. 8 – 13, 2010.

[168] D. Song and B. Guo, "J. phys. d: Appl. phys." vol. 42, p. 025103, 2009.

[169] B. C. Paul, R. Tu, S. Fujita, M. Okajima, T. H. Lee, and Y. Nishi, "An analytical compact circuit model for nanowire fet," *IEEE Transactions on Electron Devices*, vol. 54, no. 7, pp. 1637–1644, July 2007.

[170] R. F. Pierret, "Semiconductor device fundamentalss," *Prentice Hall, New York*, 1995.

[171] J. Vaithilingam, M. Simonelli, E. Saleh, N. Senin, R. D. Wildman, R. J. M. Hague, R. K. Leach, and C. J. Tuck, "Combined inkjet printing and infrared sintering of silver nanoparticles using a swathe-by-swathe and layer-by-layer approach for 3-dimensional structures," *ACS Applied Materials & Interfaces*, vol. 9, no. 7, pp. 6560–6570, 2017.

[172] Y. Zhang, M. K. Ram, E. K. Stefanakos, and D. Y. Goswami, "Synthesis, characterization, and applications of zno nanowires," *Journal of Nanomaterials*, vol. 2012, p. 22, 2012.

[173] Z. W. Pan, Z. R. Dai, and Z. L. Wang, "Nanobelts of semiconducting oxides," *Science*, vol. 291, no. 5510, pp. 1947–1949, 2001.

[174] G. Poulin-Vittrant, A. S. Dahiya, S. Boubenia, K. Nadaud, F. Morini, C. Justeau, and D. Alquier, "Challenges of low-temperature synthesized Zno nanostructures and their integration into nano-systems," *Materials Science in Semiconductor Processing*, vol. 91, pp. 404 – 408, 2019.

[175] P.-H. Shih and S. Wu, "Growth mechanism studies of ZnO nanowires: Experimental observations and short-circuit diffusion analysis," *Nanomaterials*, vol. 7, no. 7, p. 188, 2017.

[176] H. Y. Shih, T. T. Chen, Y. C. Chen, T. H. Lin, L. W. Chang, and Y. F. Chen, "Size-dependent photoelastic effect in ZnO nanorods," *Applied Physics Letters*, vol. 94, no. 2, p. 021908, 2009.

[177] M. H. Huang, S. Mao, H. Feick, H. Yan, Y. Wu, H. Kind, E. Weber, R. Russo, and P. Yang, "Room-temperature ultraviolet nanowire nanolasers," *Science*, vol. 292, no. 5523, pp. 1897–1899, 2001.

[178] J. Wang, B. Weng, P. Larson, and Y. Liu, "Synthesis and characterization of self-assembled ZnO nanoarrays on hybrid structural fibers," *Surfaces and Interfaces*, vol. 16, pp. 188 – 193, 2019.

[179] M.-H. Jung and M.-J. Chu, "Synthesis of hexagonal zno nanodrums, nanosheets and nanowires by the ionic effect during the growth of hexagonal zno crystals," *J. Mater. Chem. C*, vol. 2, pp. 6675–6682, 2014.

[180] Y. Chu, L. Wan, X. Wang, and J. Zhang, "Synthesis and characterization of ZnO nanowires by solvothermal method and fabrication of nanowire-based ZnO nanofilms," pp. 366–369, Aug 2012.

[181] O. Lupan, V. Postica, N. Wolff, J. Su, F. Labat, I. Ciofini, H. Cavers, R. Adelung, O. Polonskyi, F. Faupel, L. Kienle, B. Viana, and T. PauportÃĽ, "Low-temperature solution synthesis of au-modified ZnO nanowires for highly efficient hydrogen nanosensors," *ACS Applied Materials & Interfaces*, vol. 11, no. 35, pp. 32 115–32 126, 2019.

[182] A. Galan-Gonzalez, A. Gallant, D. A. Zeze, and D. Atkinson, "Controlling the growth of single crystal ZnO nanowires by tuning the atomic layer deposition parameters of the ZnO seed layer," *Nanotechnology*, vol. 30, no. 30, p. 305602, may 2019.

[183] N. A. Alshehri, A. R. Lewis, C. Pleydell-Pearce, and T. G. Maffeis, "Investigation of the growth parameters of hydrothermal zno nanowires for scale up applications," *Journal of Saudi Chemical Society*, vol. 22, no. 5, pp. 538 – 545, 2018.

[184] O. Lupan, V. Cretu, V. Postica, M. Ahmadi, B. R. Cuenya, L. Chow, I. Tiginyanu, B. Viana, T. PauportÃĽ, and R. Adelung, "Silver-doped zinc oxide single nanowire multifunctional nanosensor with a significant enhancement in response," *Sensors and Actuators B: Chemical*, vol. 223, pp. 893 – 903, 2016, doi:10.1016/j.snb.2015.10.002.

[185] W. KwieciÅĎski, T. Segers, S. van der Werf, A. van Houselt, D. Lohse, H. J. W. Zandvliet, and S. Kooij, "Evaporation of dilute sodium dodecyl sulfate droplets on a hydrophobic substrate," *Langmuir*, vol. 35, no. 32, pp. 10 453–10 460, 2019.

[186] M. D. Doganci, B. U. Sesli, and H. Y. Erbil, "Diffusion-controlled evaporation of Sodium Dodecyl Sulfate solution drops placed on a hydrophobic substrate," *Journal of Colloid and Interface Science*, vol. 362, no. 2, pp. 524 – 531, 2011.

[187] D. Ramimoghadam, M. Z. B. Hussein, and Y. H. Taufiq-Yap, "The effect of Sodium Dodecyl Sulfate (SDS) and cetyltrimethylammonium bromide (CTAB) on the properties of ZnO synthesized by hydrothermal method," *International Journal of Molecular Sciences*, vol. 13, no. 10, pp. 13 275–13 293, 2012.

[188] R. Biswal, A. Maldonado, J. Vega-Pérez, D. Acosta, and M. De La Luz Olvera, "Indium doped zinc oxide thin films deposited by ultrasonic chemical spray technique, starting from zinc acetylacetonate and indium chloride," *Materials*, vol. 7, no. 7, pp. 5038–5046, 2014.

[189] A. Maldonado, R. Asomoza, J. CaÃśetas-Ortega, E. Zironi, R. HernÃąndez, R. PatiÃśo, and O. Solorza-Feria, "Effect of the ph on the physical properties of ZnO:In thin films deposited by spray pyrolysis," *Solar Energy Materials and Solar Cells*, vol. 57, no. 4, pp. 331 – 344, 1999.

[190] H. wa Yu, J. Wang, X. an Yan, J. Wang, P. fei Cheng, and C. juan Xia, "Effect of surfactants on the morphology and photocatocatalytic properties of ZnO nanostructures," *Optik*, vol. 185, pp. 990 – 996, 2019.

[191] H. Usui, "The effect of surfactants on the morphology and optical properties of precipitated wurtzite ZnO," *Materials Letters*, vol. 63, no. 17, pp. 1489 – 1492, 2009.

[192] W. KwieciÅĎski, T. Segers, S. van der Werf, A. van Houselt, D. Lohse, H. J. W. Zandvliet, and S. Kooij, "Evaporation of dilute Sodium Dodecyl Sulfate droplets on a hydrophobic substrate," *Langmuir*, vol. 35, no. 32, pp. 10 453–10 460, 2019.

List of Publications

Journal Publications

1. V. K. S. Yadav, G. Natu and R. Paily, “Analysis of Superfine-Resolution Printing of Polyaniline and Silver Microstructures for Electronic Applications," IEEE Transactions on Components, Packaging and Manufacturing Technology, vol. 8, no. 9, pp. 1678-1685, Sept. 2018, DOI: 10.1109/TCPMT.2018.2854629.

2. V. K. S. Yadav, G. Natu and R. Paily, “Fabrication and Electrical Characterization of Printed Micro-Resistors of Silver Nanoparticles Using Micro-Cantilever Based Printing Technology," IEEE Transactions on Components, Packaging and Manufacturing Technology, vol. 10, no. 1, pp. 57-64, Jan. 2020, DOI: 10.1109/TCPMT.2019.2954079.

3. V. K. S. Yadav, Thomas T. Daniel and R. Paily, “Gas Sensors Based on Drop-Casted ZnO Nanowires and Micro-Cantilever Printed Ag Contacts," IEEE Sensors Journal, vol. 20, no. 9, pp. 4951-4958, 1 May 2020, DOI: 10.1109/JSEN.2020.2964600.

4. V. K. S. Yadav, S. Raveesh, T. T. Daniel and R. Paily, “Microcantilever Printed Back-to-Back ZnO Single-Nanowire Schottky Diodes," IEEE Transactions on Electron Devices, vol. 67, no. 8, pp. 3309-3314, Aug. 2020, DOI: 10.1109/TED.2020.3002733.

5. Thomas T. Daniel, S. Majumder, V. K. S. Yadav and R. Paily, “Magnetite Based Resistor for Nitric Oxide Detection," IEEE Sensors Journal,vol. 20, no. 22, pp. 13341-13348, 15 Nov. 2020, DOI: 10.1109/JSEN.2020.3005398.

6. V. K. S. Yadav, Thomas T. Daniel, S. Raveesh and R. Paily, “Room Temperature Air Pollutants Sensors Using Printed ZnO Single-Nanowire Schottky Diodes,"IEEE Transactions on Nanotechnology, vol. 20, pp. 338-345, 2021. DOI: 10.1109/TNANO.2021.3071320.

7. S. Raveesh, V. K. S. Yadav and Roy Paily, “CuO Single-Nanowire Based White-Light Photodetector, " IEEE Electron Device Letters, vol. 42, no. 7, pp. 1021-1024, July 2021. DOI: 10.1109/LED.2021.3081627.

8. Thomas T. Daniel, V. K. S. Yadav, Gayatri Natu and Roy Paily,“Fully Printed Inorganic Schottky Diode, " IEEE Electron Device Letters , vol. 42, no. 8, pp. 1212-1215, August 2021. DOI: 10.1109/LED.2021.3086849.

9. S.Raveesh, V.K.S. Yadav, Thomas T. Daniel and Roy Paily, “CuO Single-Nanowire-Based Devices for Volatile Organic Compounds (VOCs) Detection," IEEE Sensors Journal, 2021(Under Review).

10. V. K. S. Yadav, S. Raveesh, Thomas T. Daniel, and R. Paily, “Printed ZnO Nanowire Schottky Barrier Field-Effect Transistors," IEEE Transactions on Electron Devices (Under preparation)

11. V. K. S. Yadav, Thomas T. Daniel, and R. Paily, “Magnetite Microspheres Diode Based Hydrogen Sensor,"IEEE Sensors Journal (Under preparation).

12. V. K. S. Yadav, Anil P. Bidkar, S.S. Ghosh and R. Paily, “Electrical Mode of Quantification for E-Coli Bacteria Using ZnO Nanowires Based Electronic Devices," ACS Sensors (Under Preparation).

13. U. Kerketta, Thomas T. Daniel, V. K. S. Yadav and Roy P. Paily, “Room Temperature Hydrogen Gas Sensing Using Zn2TiO4 Thin Film, " SN Applied Sciences (Submitting).

14. S. Raveesh, V. K. S. Yadav and Roy Paily, “Solution-Processed Devices: In-Plane Capacitor and Schottky FET," IEEE Transactions on Electron Devices (Submitting).

15. Reena Dey, Emlin E. Abraham, V.K.S. Yadav, Thomas T. Daniel and R. Paily,“VOCs sensor based on functionalized reduced graphene oxide/para polyphenylenediamine," IEEE Sensors Letters (Submitting).

16. Thomas T Daniel, V. K. S. Yadav, Blessy and R. Paily, “Room Temperature H2 Detection Using MnFe2O4 Based Diode," ACS Sensors (Under Preparation).

17. Thomas T Daniel, V. K. S. Yadav, S. Mazumder, J.R. Palathinkal and R. Paily, “Hydrogen Sensing at Room Temperature Using SeFe2O3 Based Diode," IEEE Sensors Journal (Under Preparation).

Conference Publications

1. V.K.S. Yadav, Roy Paily, “Effect of pH Variations on Zinc Oxide (ZnO) Nanowire Dispersions," In: Mallick P.K., Meher P., Majumder A., Das S.K. (eds) Electronic Systems and Intelligent Computing, Lecture Notes in Electrical Engineering, vol. 686. pp 949-955, 2020, Springer Nature Singapore. Online ISBN 978-981-15-7031-5.

2. V.K.S. Yadav, Thomas T. Daniel and R. Paily, “Electrical Characterization and Analytical Modeling of ZnO Single-Nanowire Based Schottky Diode," 6th International Conference on Advanced Nanomaterial and Nanotechnology (ICANN 2019), IIT Guwahati, India, December 18-21, 2019.

3. V.K.S. Yadav and R. Paily, “Optimization of Zinc Oxide (ZnO) Nanowire Dispersion for Single Nanowire Device Fabrication," XXth International Workshop on Physics of Semiconductor Devices (IWPSD), Kolkata, India, December 17-20, 2019. (Accepted)

4. V.K.S. Yadav, S. Roy. G. Natu and R. Paily, “Fabrication of Back to Back Schottky Micro-Diodes Using Silver Nanoparticle Film and Zinc Oxide Nanowire Mat for Biological Interactions," IEEE TENCON, Kochi, India, October 17-20, 2019.

5. V.K.S. Yadav, G. Natu and R. Paily, “Fabrication and Electrical Characterization of Voltage Dependent Micro-Resistors (Micro-Varistors) Using Silver Nanoparticle and Zinc Oxide Nanowire Film," NWNTD, IIT Guwahati, India, February 2019.

6. V.K.S. Yadav, G. Natu and R. Paily, “Electrical Characterization of Nano-Level Printed Resistors of Silver Nanoparticles for Sensing Applications," Research Conclave, Indian Institute of Technology Guwahati, Assam, India, March, 2018.